

学位論文

ALMA Observations Revealing Disk Formation

in Early Phases of Star Formation

(ALMA を用いた星形成初期段階における

円盤形成の研究)

平成28年12月博士（理学）申請

東京大学大学院理学系研究科

天文学専攻

麻生 有佑

Abstract

The main purpose of my PhD thesis is to unveil formation process of circumstellar disks based on observations with Atacama Large Millimeter/submillimeter Array (ALMA) during its Cycle 0, 1, and 3. I, together with my collaborators, have investigated disk formation process from different points of view in the three Cycles of ALMA observations. First, dynamics of the protostellar disk and envelope around the Class I protostar TMC-1A has been investigated. Keplerian rotation is identified within 100 AU around the protostar by analyses with the position-velocity diagram with a cut across its outflow direction. Infall motion in the envelope around the Keplerian disk has also been discussed. Secondly, structures of the protostellar disk envelope around the Class 0/I protostar L1527 IRS has been investigated. Two dimensional distributions of continuum visibility in the uv plane are analyzed for the disk for the first time. This analysis suggests that a density jump between the disk and the envelope. Importantly, the radius of the disk estimated from the visibility analysis is consistent with the one kinematically determined. Finally, in order to extend my research on disk formation into earlier phases of star formation, objects that would be considered to be younger than the two protostars studied earlier have been searched in Serpens Main cluster with infrared observations (*Spitzer*, *Herschel*) as well as radio observations (SMA, ALMA); as a result, a first hydrostatic core (FHSC) candidate, SMM11a, is newly identified in the region. These results and discussion suggest the following four aspects of the disk formation in the course of the protostellar evolution; (1) the overall structure of the envelope changes from spherical ones to flattened ones as protostellar evolution proceeds; (2) sizes of disks increase as the central stellar mass in-

creases; (3) infall motions in envelopes are slower than the free-fall yielded by the central stellar mass; (4) disks around protostars are kinematically and structurally similar to those around T Tauri disks.

要旨

私の学位論文の主たる目的は、ALMA を用いた Cycle 0、1、3 の期間の観測結果にもとづき星周円盤の形成過程を明らかにすることである。私は共同研究者とともにそれぞれの Cycle の観測結果をもとに異なる視点から円盤形成を研究した。第一の研究では、速度勾配や回転速度と半径の関係といった観測量をもとに原始星周囲のケプラー円盤とエンベロープが力学的に切り分けられ、Class I 原始星である TMC-1A 周囲の円盤とエンベロープの力学が調べられた。第二の研究では連続波のビジビリティを用いて、TMC-1A よりも若い Class 0/I 原始星 L1527 IRS 周囲の円盤とエンベロープの構造が調べられた。この研究ではビジビリティを方位角方向に平均化することなく、その二次元分布が原始星円盤に対して初めて可視化して調べられた。この解析はケプラー円盤とエンベロープの間の密度ジャンプに注目することで、輝線観測に基づいた力学のみならず連続波観測に基づいた構造からも円盤とエンベロープを切り分けられることを示唆する。この解析はエンベロープ内のインフォール速度とも関係している。最後の研究では、円盤形成に関する私の研究を原始星よりも若い段階へと拡張する足がかりとして、ALMA と SMA を用いた電波観測に加えて *Spitzer* と *Herschel* という赤外線観測の結果も用いて、Serpens Main クラスターの探査を行い、同領域にこれまで同定されていなかったファーストコア候補 SMM11a を同定した。これらの結果と議論から、(1) エンベロープはファーストコアから原始星初期の段階に至る間に扁平になる、(2) 原始星円盤の大きさは中心星質量とともに成長する、(3) エンベロープ内のインフォール速度は自由落下よりも遅い、(4) 原始星円盤は力学的にも構造的にも T タウリ円盤に近い特徴を持つ、という四つの示唆が得られた。

Contents

Abstract	i
1 General Introduction	2
1.1 STAR FORMATION	2
1.1.1 Evolutional Phases in Star Formation	3
1.1.2 Observational Studies of Star Formation	5
1.1.3 Kinematics in Star Formation	18
1.2 DISK FORMATION IN EARLY PHASES	27
1.2.1 Importance and Problems	27
1.2.2 Related Methods in Previous Works	30
1.2.3 This Thesis	33
2 ALMA CYCLE 0 OBSERVATIONS OF TMC-1A	35
2.1 ABSTRACT	35
2.2 INTRODUCTION	36
2.3 ALMA OBSERVATIONS	37
2.4 RESULTS	39
2.4.1 Continuum and ^{12}CO	39
2.4.2 $\text{C}^{18}\text{O } J = 2 - 1$	44
2.5 ANALYSIS	49
2.5.1 C^{18}O Velocity Gradient	49
2.5.2 Rotation Profile	52

2.5.3	Rotating Disk Models	54
2.6	DISCUSSION	60
2.6.1	Velocity Gradient along the Disk Minor Axis	60
2.6.2	Nature of The Infall Motion	62
2.6.3	Magnetic Pressure and Tension	68
2.6.4	A Possible Scenario of the Keplerian Disk Formation	69
2.7	CONCLUSIONS	75
2.8	APPENDIX	77
2.8.1	Analytic Consideration of Our Method to Derive Rotational Profiles from Observed PV Diagrams	77
2.8.2	Comparison between the Flattened and Spherical Envelope Models	80
3	ALMA CYCLE 1 OBSERVATIONS OF L1527 IRS	83
3.1	ABSTRACT	83
3.2	INTRODUCTION	84
3.3	ALMA OBSERVATIONS AND DATA REDUCTION	86
3.4	RESULTS	88
3.4.1	220 GHz Continuum	88
3.4.2	C ¹⁸ O J=2-1	91
3.5	ANALYSIS	95
3.5.1	Rotation Profile	95
3.5.2	Structures of the Keplerian Disk	98
3.6	DISCUSSION	108
3.6.1	Possible Origin of the Surface Density Jump	108
3.6.2	Structures of the C ¹⁸ O gas disk	110
3.7	CONCLUSIONS	114
3.8	APPENDIX	116
3.8.1	Shallower Index for Outer Envelope	116

4	ALMA CYCLE 3 OBSERVATIONS OF SERPENS MAIN CLUSTER	118
4.1	ABSTRACT	118
4.2	INTRODUCTION	119
4.3	SAMPLES AND ALMA OBSERVATIONS	121
4.3.1	Samples	121
4.3.2	ALMA Observations and Data Reduction	123
4.4	RESULTS	126
4.4.1	ALMA 1.3-mm continuum and ^{12}CO line	126
4.4.2	Near and Mid-infrared emission	133
4.5	DISCUSSION	137
4.5.1	^{12}CO outflows	138
4.5.2	C^{18}O abundance	143
4.5.3	Continuum visibility	147
4.5.4	Possibility of Second Core	153
4.6	CONCLUSION	155
5	CONCLUSIONS	158
	Acknowledgments	162
	References	164

List of Figures

1.1	Representative points in PV diagrams derived by Yen et al. (2013)	31
1.2	Representative points in the $\log R - \log V$ plane derived by Yen et al. (2013)	32
1.3	Azimuthally averaged visibility in Jørgensen et al. (2009) and Looney et al. (2003)	33
2.1	Continuum emission map of TMC-1A	40
2.2	Moment 0 and 1 maps of the ^{12}CO ($J = 2 - 1$) emission in TMC-1A . .	42
2.3	PV diagrams of the ^{12}CO ($J = 2 - 1$) emission in TMC-1A along the outflow axes ($\text{PA} = -17^\circ$)	43
2.4	Moment 0 and 1 maps of the C^{18}O ($J = 2 - 1$) emission in TMC-1A . .	45
2.5	Channel maps of the C^{18}O ($J = 2 - 1$) emission in TMC-1A	48
2.6	Maps of blueshifted and redshifted emission of C^{18}O ($J = 2 - 1$) emission in TMC-1A	50
2.7	2D mean positions of the C^{18}O ($J = 2 - 1$) emission in TMC-1A	50
2.8	PV diagrams of the C^{18}O ($J = 2 - 1$) emission in TMC-1A	51
2.9	Mean positions of the PV diagram along the major axis plotted on $\log R - \log V$ plane	54
2.10	Channel maps of the best-fit model and the residual	58
2.11	Distribution of the reduced χ^2 in terms of the inclination angle of the disk	59
2.12	Comparisons of the observations and models with infall motions	64
2.12	(Continued)	65

2.13	Correlation among bolometric temperature, $L_{\text{bol}}/L_{\text{submm}}$, central proto-stellar masses, and sizes of Keplerian disks	71
2.14	The dependency of the normalized mean position on the normalized beam width	80
2.15	Comparison FE and SE model A/D	82
3.1	Continuum emission map of L1527 IRS	90
3.2	Integrated intensity map and mean velocity map of the $\text{C}^{18}\text{O } J = 2 - 1$ emission in L1527 IRS	92
3.3	Channel maps of the $\text{C}^{18}\text{O } J = 2 - 1$ emission in L1527 IRS	94
3.4	Position Velocity diagrams of the $\text{C}^{18}\text{O } J = 2 - 1$ emission in L1527 IRS	96
3.5	Mean positions of the PV diagram along the major axis plotted on a $\log R - \log V$ plane	97
3.6	Continuum visibility averaged over scans	100
3.7	The observed continuum visibility and models with different S_{damp}	105
3.8	The observed continuum image, the best-fit model, and the residual	106
3.9	Comparison of C^{18}O moment 0 maps integrated over $ V > 2.0 \text{ km s}^{-1}$	112
3.10	The same figures as Figure 3.9but the model has enhancement of C^{18}O abundance	113
3.11	Comparison of the continuum and C^{18}O observations and the alternative model with $p_{\text{env}} = 0.5$, $S_{\text{damp}} = 0.08$, and $\alpha = 0.6$	117
4.1	JCMT 850- μm contour map of Serpens Main cluster overlaid on Herschel 70- μm image	122
4.2	Four parts of SMA mosaicking observations overlaid on Herschel 70 μm images	123
4.3	ALMA 1.3-mm continuum, ^{12}CO line, <i>Spitzer</i> 24 μm , and <i>Herschel</i> 70 μm maps toward SMM11a	128
4.4	The same figure as Figure 4.3but toward SMM4a	130

4.5	The same figure as Figure 4.3but toward SMM9d	131
4.6	The same figure as Figure 4.3but toward SMM9a	132
4.7	The same figure as Figure 4.3but toward SMM2 condensation	133
4.8	SEDs of the ALMA 1.3-mm sources	135
4.9	Position Velocity diagram of the $^{12}\text{CO } J = 2 - 1$ emission in SMM11a .	141
4.10	Integrated intensity map and mean velocity map of the $\text{C}^{18}\text{O } J = 2 - 1$ emission in SMM11a	144
4.11	Channel maps of the $\text{C}^{18}\text{O } J = 2 - 1$ emission in SMM11a	146
4.12	Position Velocity diagram of the $\text{C}^{18}\text{O } J = 2 - 1$ emission in SMM11a across the outflow axes (P.A.=-15.5°)	147
4.13	Continuum visibility averaged over scans	150
4.14	The same figures of the Class 0 protostar B335	151
4.15	Comparison of visibility distributions	152
4.16	Comparison of SEDs with the same distance	154
5.1	Summary of this thesis	160

List of Tables

2.1	Summary of the observational parameters (TMC-1A)	39
2.2	Fixed and free parameters of the model fitting (TMC-1A)	56
2.3	Parameters of Keplerian disks around protostars	72
2.3	Parameters of Keplerian disks around protostars	73
3.1	Summary of the ALMA observational parameters (L1527 IRS)	88
3.2	Fixed and Free Parameters of the Model Fitting (L1527 IRS)	103
4.1	Summary of the ALMA observational parameters (Serpens)	125
4.2	ALMA 1.3-mm sources	136
4.3	Comparison of outflow properties of SMM11a and known FHSC candidates.	142

Chapter 1

General Introduction

This chapter is divided into two sections. In Section 1.1 the field of star formation is widely reviewed. In the field this thesis focuses on disk formation in early phases of star formation, which is introduced in more detail in Section 1.2.

1.1 STAR FORMATION

Stars are highly concentrated gas clumps radiating by nuclear fusion reaction of hydrogen, helium, and other atoms in the clumps. They are the most fundamental component of various astronomical objects, such as nebulae and galaxies. Formation process of stars is basic process of galaxy formation and a part of its sub process, planetary formation, is closely related to human being's origin, the Earth. These facts imply that star formation underlies other astronomical fields and thus revealing the process would be one of the most important tasks in astronomy.

Stars are classified into main sequence stars, brown dwarfs, red giants, white dwarfs, and so on based on their characteristics and evolutionary phases. It is known in our Galaxy that about one third of stars is multiple stars and $\sim 90\%$ of stars are forming as members of clusters (Lada & Lada, 2003). Their mass widely ranges; ones with $0.08-2 M_{\odot}$, $2-8 M_{\odot}$, and $> 8 M_{\odot}$ are classified into low mass-, intermediate mass-, and high mass stars, respectively. The first boundary is defined from the limit above which stars have no outer

convective zones related to magnetically mediated accretion (Simon et al., 2002) while the second boundary is defined from the limit above which stars can produce the type II supernova (Zinnecker & Yorke, 2007). Stars with higher mass show shorter time scales of evolution and the time scales of high mass stars are on the order of 10 Myr. In addition to the short time scales, the number of high mass star is much smaller than that of lower mass stars. In contrast low mass stars show longer time scales and more number of samples. The low mass stars are, therefore, the best targets in order for us to investigate star formation process in detail. Stars form mainly by gravitationally collapse. Spontaneous gravitational collapse mainly produces low mass stars in isolated system, such as bok globules (e.g., B335) while high mass stars are known to form in clustering star forming regions. It has also been reported that star formation can also be triggered by cloud-cloud collision or other kinds of shock motion, such as interaction of supergiant shells (Fujii et al., 2014), which might be important to understand star formation comprehensively.

1.1.1 Evolutional Phases in Star Formation

Theoretical studies have provided a widely accepted scenario to generate a star and a planet system similar to the solar system. First, a molecular cloud isothermally collapsed, forming a dense core with heat capacity ratio γ higher than 4/3. The efficiency of radiative cooling decreases because of the high heat capacity ratio and adiabatic collapse begins, forming a first hydrostatic core. This collapse is called first collapse. When the central temperature reaches 2000 K, dissociation of molecular hydrogen causes the second isothermal collapse and eventually a protostar, or a second core, forms in the innermost region. Ambient material becomes a dynamically collapsing, or infalling, envelope around the protostar, while the first core changes into a disk in Keplerian rotation, which is called protoplanetary disk. The system subsequently evolves into a main-sequence star and planets are form (Kokubo & Genda, 2010). Those objects before the main sequence are called young stellar objects (YSOs). Particularly the YSOs dominated by a protoplanetary disk

and a central star are called T Tauri stars while the younger YSOs are called protostars. The protoplanetary disks are widely known as a place for planet formation (Hayashi et al., 1985; Howard, 2013).

The first phase, molecular cloud, is classified by its size. The largest molecular clouds have sizes on a few 100 pc scale and are called complexes or giant molecular clouds. Their number density of molecular hydrogen ranges from 100 to 1000 cm^{-3} ; an example is Orion Molecular Cloud. Molecular clouds on 10 pc scales are called infrared dark clouds. Their number density of molecular hydrogen is similar to those of complexes; an example is Taurus Molecular Cloud. High density regions in molecular clouds are called dense cores and have sizes on 0.1–1 pc scales and number density of molecular hydrogen ranges from 10^4 to 10^6 cm^{-3} (e.g., L1527). It is also known that molecular clouds exhibit filament structures; the formation process of molecular clouds are discussed both observationally and theoretically (Inutsuka et al., 2015).

At the beginning point of star formation, the presence of first hydrostatic cores are theoretically expected and theoretical studies predict that their temperature, size, mass, and lifetime to be $\sim 1000 \text{ K}$, $\sim 5 - 100 \text{ AU}$, $0.01 - 0.1 M_{\odot}$, and $\sim 500 - 5 \times 10^4 \text{ yr}$, respectively. There is still, however, no determinative observational results of first hydrostatic cores. Very Low Luminosity Objects (VeLLOs) and PACS Bright Red Sources (PBRs) are considered to be strong candidates of first hydrostatic cores in observational studies.

In contrast to first hydrostatic cores, YSOs after protostars have been observationally identified in numerous studies. Previous observational studies show that protostars have large mass accretion rates around $10^{-6} M_{\odot} \text{ yr}^{-1}$. For this reason protostars are also defined from observational points of view as YSOs where more than half of luminosity is fed by mass accretion, i.e., releasing gravitational energy. Protostars are also theoretically defined based on the dissociation of molecular hydrogen. Central stars in the protostellar phase cannot be observed in optical wavelength because they are embedded in protostellar envelopes on a few 1000 AU scales.

The envelopes are dissipated as time goes on and the central stars become visible in optical wavelength in the T Tauri phase. T Tauri stars have similar effective temperature to main-sequence stars, whereas their luminosity is brighter than that of main-sequence stars because their sizes are larger than those of main-sequence stars. Nuclear fusion reaction does not occur in the T Tauri phase and their main energy source is releasing gravitational energy by gradually collapse.

1.1.2 Observational Studies of Star Formation

Molecular clouds can be observationally identified by dust extinction in optical wavelength. The first survey of molecular clouds was CfA Survey in 1980's, which observed CO molecular lines with a $\sim 7'$ angular resolution, showing CO emission associated with giant molecular clouds with the mass range of $10^{4-6} M_{\odot}$. *Herschel* space telescope detected filamentary structures, such as Pipe, Aquila, and Taurus, indicating that such filaments are ubiquitous in interstellar medium. Such filamentary structures are also reproduced in Magnetohydrodynamics (MHD) simulations. Previous observations show that those filaments have a typical size of 0.1 pc and that the sizes of molecular clouds are positively correlated with their velocity dispersion (Larson's law), where the sizes are ~ 0.1 pc when the velocity dispersion is sound speed with ~ 10 K. These results suggest that the typical size of filaments is due to attenuation of turbulent motion in filaments, which finally settles down to the sound speed.

A molecular cloud includes dense regions, dense cores. If a dense core includes a infrared source, it means that star formation is activated in the dense core, while if there is no infrared source, it means that there is no star formation activity in the dense core; the former and the latter are called protostellar core and starless core, respectively. The size, number density of molecular hydrogen, and mass of dense cores are < 0.1 pc in radius, $\sim 10^5 \text{ cm}^{-3}$, and $0.2 - 20 M_{\odot}$, respectively. For example Taurus Molecular Cloud has 55 H^{13}CO dense cores and 44 of them were not detected by Infrared Astronomical Satellite

(*IRAS*), i.e., starless cores (Onishi et al., 2002). Protostellar cores tend to show column density more concentrated on the center and larger velocity width in the central direction than starless cores. Starless cores also provide cool but dense environment where molecules are freeze-out on dust grains, which is an important condition for chemical studies. Tafalla et al. (2004) observed the two starless cores L1498 and L1517B in various chemical species and discussed their abundance relative to molecular hydrogen by estimating total hydrogen mass from dust continuum observations. As a result nitrogen compounds, N_2H^+ (1 – 0) and NH_3 (1, 1), show similar distributions to the dust continuum emission while CO isotopologues, C^{18}O (1 – 0), C^{18}O (2 – 1), C^{17}O (2 – 1) and sulfur compounds, CS (2 – 1), CS (3 – 2), C^{34}S (2 – 1) show freeze-out at the peaks of dust continuum emission. Because such freeze-out of molecules does not occur in protostellar cores, which is more evolved phase than starless cores, the depletion enables us to discuss core evolution.

Spitzer space telescope with higher sensitivity than *IRAS* added 24 infrared point sources in $70\ \mu\text{m}$. Particularly sources with low bolometric luminosity ($L_{\text{bol}} \sim 0.1 L_{\odot}$) are classified into Very Low Luminosity Objects (VeLLOs) and they are strong candidates of first hydrostatic cores; a representative VeLLO is L1521F IRS with $L_{\text{int}} = 0.07 L_{\odot}$ (Bourke et al., 2006). Onishi et al. (1999) detected blue-skewed line profiles in HCO^+ lines and single peak line profiles in H^{13}CO^+ lines toward a VeLLO, MC 27, using Caltech Submillimeter Observatory (CSO) 10 m single dish telescope. These results suggest that MC 27 has infall motion and thus that VeLLOs are in a very young phase where infall motion is dominant. On the other hand, L1544 includes no *Spitzer* source, although it shows chemical composition similar to that of the VeLLO L1521F IRS. In addition the number of VeLLOs compared to the number of protostars is much larger than predicted from the lifetime of first hydrostatic cores compared to that of protostars. For the reasons not all of VeLLOs are as young as hydrostatic cores. If the spectral energy distribution (SED) of a VeLLO has bolometric temperature T_{bol} higher than 70 K, i.e., its mean frequency is higher than that of a blackbody with 70 K, and if its chemical composition is

similar to protostars, then its low luminosity does not mean that the object is young but that its mass is low. In this point, although VeLLOs have low luminosity, they show a wide range of temperature. In contrast an object group called PACS Bright Red Sources (PBRs) show lower temperature than VeLLOs though they also show a wide range of luminosity. Recently first hydrostatic cores are, therefore, in the common part of the two groups: $L_{\text{bol}} < 0.05 L_{\odot}$ and $T_{\text{bol}} < 30$ K.

The first whole sky survey for protostars was carried out in 12, 25, 60, 100 μm by *IRAS* with a 60 cm mirror (Beichman et al., 1986). The detected infrared sources were considered to be T Tauri stars if they have a counterpart in optical wavelength while if they have no counterpart, they were considered to be protostars. This result provided a typical lifetime of $\sim 10^5$ yr for protostars based on the number ratio between T Tauri stars and protostars. Regarding this lifetime, if Jeans mass collapses within free-fall time with a constant mass accretion rate, the mass accretion rate can be estimated to be $\dot{M} \sim M_{\text{Jeans}}/t_{\text{ff}} = 5.37c_s^3/G$. Using 10 K, the mass accretion rate $\dot{M} \sim 1 \times 10^{-5} M_{\odot} \text{yr}^{-1}$ indicates that forming a star with $1 M_{\odot}$ takes 1×10^5 yr, which is consistent with the lifetime of protostars estimated from *IRAS* observations. The mass accretion rate also provides accretion luminosity $L_{\text{acc}} = GM_*\dot{M}/R_*$. If solar values (M_{\odot} , R_{\odot}) are assumed, the accretion luminosity is $\sim 300 L_{\odot}$, however, the luminosity observed toward protostars is a few L_{\odot} . This inconsistency is known as “luminosity problem” and widely accepted solutions are that mass accretion rates are not steady and that outflows can remove a part of energy from protostellar systems. Around half of dense cores identified by *IRAS* and *Spitzer* include no infrared source. These starless cores are considered to be an earlier phase than protostars and its lifetime is estimated to be $\sim 10^5$ yr. In addition the starless cores are located in filaments.

Disks in Keplerian rotation have been detected around T Tauri stars while observations toward protostars have detected disk-like envelopes or pseudo-disks. Keplerian disks have been identified even around protostars in the most recent observations. In 1990’s disks were identified by indirect evidence, such as line profiles where the redshifted part of jets

are hidden, large extinction suggestive of dust condensation, and flat SEDs in 10-100 μm . More direct evidence has been verified in more recent studies such as silhouettes of disks in optical wavelength with background bright objects and spatially resolved disks in radio continuum or dust extinction. For example O'dell & Wen (1994) and Smith et al. (2005) observed silhouettes of disks radiated by OB stars (proplyds), and Padgett et al. (1999) observed dark lanes in disks in near infrared scattered light. These observations enable us to investigate geometrical characteristics of disks. While investigating kinematics in disks requires to measure the direction of velocity gradient by observing molecular line emission. The presence of disks can also be confirmed by infrared excess. E-folding time of disks was estimated to be 2 – 3 Myr by statistically comparing infrared excess and ages of the disks (Bell et al., 2013; Hernández et al., 2007). Because infrared excess arises from the inner side of a disk, the fact that infrared excess decreases as the age increases indicates dissipation of the inner part of a disk. Furthermore infrared observations of scattered light and radio observations recently have identified disks with remarkable features, such as gaps and spiral arms.

YSOs from protostars to T Tauri stars are classified from Class 0 to III based on SEDs derived from infrared observations; the gradient of a SED in infrared wavelength is defined as $\alpha_{\text{IR}} = d \ln \lambda F_{\lambda} / d \ln \lambda = \ln \nu F_{\nu} / d \ln \nu$ and then Class 0 or I, Flat spectrum, Class II, and Class III are defined as $\alpha_{\text{IR}} \geq 0.3$, $-0.3 \leq \alpha_{\text{IR}} < 0.3$, $-1.6 \leq \alpha_{\text{IR}} < -0.3$, and $\alpha_{\text{IR}} \leq -1.6$, respectively (Williams & Cieza, 2011). Class 0 and Class I are distinguished by their bolometric temperature T_{bol} , which is the temperature of a blackbody having the same mean frequency: $T_{\text{bol}} = 1.25 \times 10^{-11} \int \nu F_{\nu} d\nu / \int F_{\nu} d\nu \text{ K Hz}^{-1}$ (Myers & Ladd, 1993). Class 0 is defined as α_{IR} and $T_{\text{bol}} \leq 30 \text{ K}$ (Williams & Cieza, 2011). Class 0 and Class I correspond to the protostellar phase; in a physical point of view, Class 0 has an envelope more massive than a central star while the envelope mass of Class I sources is smaller than the central stellar mass and similar to the disk mass. Class II and Class III physically correspond to Classical T Tauri stars (CTTSs) and Weak line T Tauri Stars (WTTSs), respectively, which are defined by equivalent width of H_{α} emission; CTTSs

have $EW_{H\alpha} > 10 \text{ \AA}$.

Observations of Continuum Emission from Disks

Optical and infrared observations target extinction and scattered light in observational studies on star formation while observations in millimeter/submillimeter continuum emission target thermal emission from astronomical objects. Dependency of flux density on wavelength, i.e., SED of a circumstellar disk gives us information about radial profiles of temperature and surface density in the disk because inner parts of the disk have higher temperature while outer parts of the disk have lower temperature. When only irradiation by a geometrically thin disk is considered, the predicted radial profile of temperature of the disk is $T(r) \propto r^{-3/4}$ and when radiative equilibrium between a star and a dust grain is assumed, the predicted radial profile is $T(r) \propto r^{-1/2}$. In addition to these fundamental prediction, disk surface can be warmer than the disk midplane because stellar UV photons may not reach the midplane when the disk is optically thick (Dullemond et al., 2002). Temperature smoothly changes from the surface to the midplane (Nomura et al., 2007). Furthermore when optical depth of the disk is larger in inner regions, the midplane can be heated by the surface more effectively in outer regions and cooling is less effective in outer regions, which can make the temperature gradient shallower (Chiang & Goldreich, 1997).

The first large survey observations toward PMSs in radio wavelength was carried out by Beckwith et al. (1990) using Institute de Radioastronomie Millimetrique (IRAM) 30 m single dish telescope. The targets are 1.3-mm continuum emission toward 86 PMSs in Taurus molecular cloud. The emission was detected toward 42% of their targets and, considering continuum sources below their sensitivity as well, they concluded that dust is commonly associated with PMSs. In addition, although the large 1.3-mm flux density implies large extinction, the fact that central stars with large 1.3-mm flux can be seen in optical wavelength suggests that the dust around PMSs has disk-like structures. Assuming that dust continuum emission is optically thin, the total disk mass including both dust and

gas can be estimated as

$$M_{\text{disk}} = \frac{d^2 F_\nu}{\kappa_\nu B_\nu(T_c)}, \quad (1.1)$$

where d , F_ν , κ_ν , B_ν , and T_c are distance, flux density, opacity, Planck function, and representative temperature, respectively. Their estimation of the disk mass of the PMSs is in the range of $\sim 1 \times 10^{-3} - 1 M_\odot$. They also concluded that the disk mass shows no evolution between Class II and Class III until 10^7 yr. SEDs of PMSs had been investigated in infrared wavelength before their observations in radio wavelength. Because dust continuum emission is optically thick in inner regions which infrared observations can investigate, those infrared observations can accurately estimate disk temperature while those cannot estimate disk mass accurately. In this sense, the radio observations by Beckwith et al. (1990) is quite important; they added optically thin millimeter data points, which enables us to accurately estimate disk mass, at least dust mass.

They also investigated other parameters in addition to the disk mass by comparing the observed SEDs with a disk model. The radial profile of temperature can be written with a power-law function based on the discussion above. They also adopted power-law functions for surface density. Among their free parameters, the innermost radius r_0 , the outermost radius R_d , the power-law index for surface density p , and inclination angle were fixed to be 0.01 AU, 100 AU, 1.5, and 0° , respectively, because these are difficult to constrain when the disk is not spatially resolved. Their model shows M_{disk} does not depend on R_d and p when R_d is smaller than 500 AU. The other free parameters are opacity κ_ν , a temperature profile (T_0, q) , and a coefficient for surface density Σ_0 . The temperature profile can be constrained well by shorter wavelength than 100 μm because continuum emission is optically thick in the wavelength. As a result q ranges from 0.5-0.75 with a peak at 0.65 toward the PMSs in Taurus region.

Once the temperature profile is constrained, M_{disk} can be estimated if κ_ν is determined. It is known, however, that the opacity has large uncertainty of 2-3 orders of

magnitude (Draine, 1989). κ_ν was directly measured around $30 \mu\text{m}$ and it is usually extrapolated to longer wavelength as $\kappa_\nu \propto \nu^\beta$. The power-law index β strongly depends on dust sizes and shapes of dust grains; $\beta \sim 2$ for dust grains smaller than wavelength while $\beta < 1$ for dust grains as large as wavelength. Beckwith et al. (1990) extrapolated the dust opacity in $250 \mu\text{m}$ with $\beta = 1$ (Hildebrand, 1989) as $\kappa_\nu = 0.1 (\nu/1 \text{ THz})^\beta \text{ cm}^2 \text{ g}^{-1} = 0.01 (\nu/1 \text{ THz})^\beta \text{ m}^2 \text{ kg}^{-1}$, where the opacity is the cross section of the unit gas mass implicitly assuming a gas-to-dust mass ratio, 100. Their model fitting shows that the disk mass ranges from $10^{-2.8}$ to $10^{-0.5} M_\odot$ with a peak at $0.02 M_\odot$, that the disk mass correlates with central stellar mass as $M_{\text{disk}}/M_* \sim 0.01$, and that the disk mass estimated by millimeter observations does not change in the time range of 10^{5-7} yr. On the other hand, observations of infrared excess show that the ratio of PMSs with infrared excess evolves as 80% at 1 Myr, 50% at 2 Myr, and 5% at 10 Myr, suggesting that inner disk mass, which is estimated by the infrared excess, is dissipated on the time scale of 1-10 Myr (Hernández et al., 2007; Haisch et al., 2001).

In 1990's the survey observations by Beckwith et al. (1990) was the largest continuum emission survey PMSs in the world. It was updated by even larger survey observations by Andrews & Williams (2005a) toward YSOs in Taurus-Auriga star forming region in submillimeter wavelength. The number of targets are 90 sources with James Clerk Maxwell Telescope (JCMT) 15 m single dish telescope in $450 \mu\text{m}$ and $850 \mu\text{m}$ with angular resolutions of $\sim 9''$ and $\sim 15''$, respectively, 39 sources with CSO 10 m in $350 \mu\text{m}$ with a angular resolution of $\sim 90''$, and others in archival data. The number is totally 153 YSOs including Class I, II, III, CTTS, WTTS, and binary systems, which is enough large to discuss statistics about circumstellar disks. They constrained Σ_0 , temperature at 1 AU T_1 , q , and β by model fitting to observed SEDs in the same way as (Beckwith et al., 1990). Because M_{disk} and β are degenerated together, $\beta = 1$ was assumed when the disk mass was estimated. The derived typical temperature profile, $T_1 \sim 178 \text{ K}$ and $q \sim 0.56$, is consistent with the results by Beckwith et al. (1990). The correlation between the observed flux density and the derived disk mass provides us typical temperature to estimate disk

mass from Equation (1.1), $T_c \sim 20$ K. The average disk mass is $M_{\text{disk}} = 5 \times 10^{-3} M_{\odot}$; without considering undetected objects, 37% of their targets have disk mass larger than minimum mass solar nebular (MMSN), i.e., $0.01 M_{\odot}$ and 79% have disk mass larger than one Jupiter mass. The spectral index $d \ln F_{\nu} / d \ln \nu$ is typically ~ 2 from submillimeter to millimeter wavelength. Although conversion from this index to the dust opacity β includes uncertainty (Beckwith & Sargent, 1991), dust particles appear to be grown more than those in interstellar medium because the derived spectral index indicates that $\beta < 2$ is required to explain more than half of their targets.

Comparison of the disks with the characteristics of central stars suggests disk mass decrease when central stars are older than 6 Myr. Regarding evolution, it was found that CTTSs tend to have less massive disks than WTTSs and heavy disks are not associated with Class III sources. The spectral index also tends to decrease from Class I to Class III. These results show that the difference between CTTSs and WTTSs defined by a mass accretion rate to central stars and the difference of Class defined by the shape of SEDs in infrared wavelength are related with the characteristics of outer disks observed by (sub)millimeter wavelength, suggesting that the inner and outer parts of disks evolve in the same way. In fact, sources detected in submillimeter without infrared excess, i.e., transition disks are less than 10% in their sample and thus the difference of dissipation time scales between the inner and outer parts should be ~ 0.1 Myr. Although the time scale in infrared regime can be explained by taking account of photoevaporation by stellar radiation as well as viscous accretion, these mechanisms cannot explain that the outer part is dissipated as fast as the inner part. An idea to solve this problem is grain growth. It is known that dust grains in the outer part grow earlier than the time scale on which the inner part is dissipated (Weidenschilling & Cuzzi, 1993). For this reason, the grain growth in the outer part makes the outer part harder to detect in (sub)millimeter wavelength while the inner part is dissipated, which can explain the apparent simultaneous dissipation of the inner and outer parts. The evolution of spectral index, i.e., the opacity β supports the dust grain growth. It is predicted by theoretical models on planet formation, such as core

accretion model and disk instability model, that forming a Jupiter-mass planet requires a protoplanetary disk with $\sim 0.05 M_{\odot}$ (Pollack et al., 1996; Boss, 1998). Exoplanet survey observations also show that more than 10% of the observed stars have gas planets (Marcy et al., 2005). Whereas, the typical mass derived by Andrews & Williams (2005a) is $M_{\text{disk}} \sim 5 \times 10^{-3} M_{\odot}$. This inconsistency implies that circumstellar disks have much dust which is not detected in (sub)millimeter wavelength.

Observations of Molecular Line Emission from Disks

Observing molecular line emission is important for research on star formation as well as other fields not only because it is useful to understand chemical evolution by measuring abundance of various chemical species but also because it enables us to investigate kinematics around YSOs by directly observing velocity fields through Doppler effect. In 1980's molecular line observations were conducted using single dish telescopes as dust continuum observations were. However, observations with single dish telescopes have several difficulties for research on circumstellar disks because of their large beam sizes. The single dish beams on tens arcsecond scales cannot spatially resolve circumstellar disks at all, whose typical size and distance are ~ 100 AU and a few 100 pc, respectively. Such large beams can also include molecular-cloud components around a disk, causing it difficult to distinguish the cloud components and the disk. Those cloud components can be ignored in dust continuum observations because those components are much less dense than disks. Those components, however, cannot be ignored in molecular line observations because the opacity of molecular line emission is much larger than that of dust continuum emission. Single dish observations toward disks in molecular line emission, therefore, require targets isolated from molecular clouds in space or in velocity. Even if such isolated targets are found, the emission from a disk will be significantly diluted by the large beam by 2-3 orders of magnitude. Even with such dilution, large integrated ranges of velocity increase signal-to-noise ratios in continuum observations. This cannot be applied, however, to molecular line observations because velocity ranges where molecular line

emission appears are much narrower than those for continuum emission. Fundamental characteristics of line profiles of rotating disks are well discussed by Beckwith & Sargent (1993). The line profiles show two remarkable features: (1) the profiles show a symmetrical shape with a double peak and (2) the double peak is located closer when the inclination angle i of the disk is smaller or closer to face-on. (1) can be explained by considering an area corresponding a (infinitesimal) range of line-of-sight (LOS) velocity. (2) is because the LOS velocity is proportional to $\sin i$.

Here I reproduce the two features by analytically considering only the projection of rotational velocity fields. Rotational velocity fields in the 2D XY plane can be written with a polar coordinate (r, ϕ) as $\mathbf{V}(\mathbf{r}) = -V_\phi(r) \sin \phi \mathbf{e}_X + V_\phi(r) \cos \phi \mathbf{e}_Y$, where \mathbf{e} is an unit vector. Inclination of a disk can be taken into account by rotating the XY plane around the Y axis. Then LOS velocity is $V_{\text{LOS}}(r, \phi) = \mathbf{V} \cdot \mathbf{e}_X \sin i = -V_\phi(r) \sin(\phi) \sin i$, where i is an inclination angle. To omit the normalization by the inclination angle, I define projected velocity $V(r, \phi)$ as $V(r, \phi) = -V_{\text{LOS}}(r, \phi) / \sin i$. The quantity that I would like to calculate is the area S satisfying $v < V(r, \phi) < v + dv$, where dv is a velocity resolution, as a function of velocity v , i.e., $dS(v) = \int \int_{v < V(r, \phi) < v + dv} r d\phi dr$. When dv is infinitesimal,

$$\begin{aligned} dS(v) &= \int \int_{v < V(r, \phi) < v + dv} r d\phi dr \approx \int \int_{v < V(r, \phi) < v + dv} \frac{r dr}{\partial V / \partial \phi} dV \\ &= dv \int \frac{r dr}{V_\phi(r) \cos \phi} = dv \int \frac{r dr}{\sqrt{V_\phi^2(r) - v^2}}. \end{aligned} \quad (1.2)$$

$V_\phi(r)$ is assumed to be $V_\phi(r) = V_{\text{out}}(r/r_{\text{out}})^{-p}$, where V_{out} and r_{out} are the outer velocity and the outer radius of the disk, respectively. For velocity smaller than the outer velocity ($v \leq V_{\text{out}}$), the integrated range is $0 < r < r_{\text{out}}$ while it is $0 < r < r_{\text{out}}(v/v_{\text{out}})^{-1/p}$ for

$v > V_{\text{out}}$ (see also Figure 1 of Beckwith & Sargent, 1993).

$$\begin{aligned} \frac{dS}{dv}(v) &= \int_0^{\min[r_{\text{out}}, r_{\text{out}}(v/V_{\text{out}})^{-1/p}]} \frac{r dr}{\sqrt{V_{\text{out}}^2 (r/r_{\text{out}})^{-2p} - v^2}} \\ &= \frac{[r_{\text{out}}(v/v_{\text{out}})^{-1/p}]^2}{2v} \int_0^{\min[(v/v_{\text{out}})^{2/p}, 1]} \frac{dr'}{\sqrt{r'^{-p} - 1}}. \end{aligned} \quad (1.3)$$

When the velocity field is Keplerian rotation, i.e., $p = 1/2$, the definite integral in Equation (1.3) can be analytically described as

$$\frac{dS}{dv} \propto u^{-5} \times \begin{cases} \frac{3\pi}{8} - \frac{1}{2}\sqrt{1-u^2}(2u^2+3) - \frac{3}{4}\text{Arctan}\left(\frac{\sqrt{1-u^2}(2u^2-1)}{2u^2(u^2-1)}\right) & (0 < u < 1) \\ \frac{3\pi}{4} & (1 < u), \end{cases} \quad (1.4)$$

where $u = v/V_{\text{out}}$. Although the discussion above did not include any intensity distribution nor any vertical structure of the disk, the fundamental characteristics discussed in Beckwith & Sargent (1993), such as the relation between the double peak and the outer radius, were reproduced well.

In order to observationally verify these theoretical prediction about circumstellar disks, several protoplanetary disks around T Tauri stars were observed with Nobeyama Radio Observatory (NRO) 45 m single dish telescope in CO (1 – 0) line emission. The targets were searched in regions where CO (1 – 0) were not detected by Five College Radio Astronomical Observatory (FCRAO) 14 m single dish telescope with an angular resolution of 45". As a result the molecular line emission was detected toward GG Tau, DM Tau, and other protoplanetary disks. Particularly GG Tau is the first example of molecular line detection toward T Tauri stars. Because the line profile of GG Tau shows a double peak, it was concluded that GG Tau has a rotating disk (Skrutskie et al., 1993). It was also confirmed that the double peak was not affected by off points by observing two off points at 1' East and at 1' West. The inclination angle and the optical depth of the disk were estimated from comparison with the model profile by Beckwith & Sargent (1993). After GG Tau, molecular emission from the protoplanetary disk around DM Tau was detected

in relatively optically thin ^{13}CO (1 – 0) as well as CO (1 – 0) line emissions, providing the disk mass $\sim 10^{-3} M_{\odot}$ (Handa et al., 1995). While, the mass estimated from dust continuum observations are $0.03 M_{\odot}$, suggestive of the freeze-out of CO molecules around DM Tau.

GG Tau, the first example of molecular line observations, have also been observed with radio interferometers, such as Nobeyama Millimeter Array (NMA), Owens Valley Radio Observatory (OVRO), and Plateau de Bure Interferometer (PdBI). Those interferometric observations spatially resolved the disk around GG Tau and revealed velocity gradients along the major axis of the disk, which are more direct evidence of rotation (Kawabe et al., 1993; Dutrey et al., 1994). PdBI observed ^{13}CO (1 – 0) line emission at the highest angular resolution in those days, $\sim 3''$, revealing a disk with an outer radius of 800 AU and the velocity gradient along the East-West direction, which can be interpreted as Keplerian rotation. Furthermore dust continuum observations found a hole at the central position with a radius of 180 AU. The hole was interpreted as a result of tidal force by an eccentric binary with $0.5 M_{\odot}$ and $0.65 M_{\odot}$. The disk mass was estimated to be $1.3 \times 10^{-3} M_{\odot}$ from ^{13}CO line emission by assuming temperature to be 15 K, while the mass estimated from dust continuum observations are $0.13 M_{\odot}$, suggesting that CO molecules are freeze-out around GG Tau.

In addition to GG Tau, DM Tau was observed by PdBI in CO (1 – 0) line emission (Guilloteau & Dutrey, 1998). The observations were compared with a Keplerian disk model in the Fourier (u, v) space, where a central stellar position, a position angle of the disk major axis, and a systemic velocity were fixed. Chi-squared fitting was performed; a few parameters were fixed at first to derive a temporary better model and subsequently the fixed parameters were searched by fixing the other parameters at the temporary better model. The derived index of temperature $q = 0.63$ suggests a flared disk due to central stellar radiation. The derived turbulence $dV = 0.07 \text{ km s}^{-1} \sim 0.3V_{\text{therm}}$ suggests that the disk is in hydrostatic equilibrium. In addition the inclination angle and the dynamical stellar mass were estimated to be $i = 33^{\circ}$ and $M_{*} = 0.50 M_{\odot}$, respectively, from

the observed Keplerian rotation. Central stellar mass can also be derived through evolution tracks in Hertzsprung-Russell Diagram (L_* , T_{eff}) predicted by several models. The evolutionary tracks, however, vary from model to model. The dynamical mass provides independent estimate to verify the evolutionary models (Simon et al., 2000), which is one of the most important points of dynamical mass.

After those studies of specific objects, survey observations toward PMSs were conducted with an interferometer, Submillimeter Array (SMA) (Andrews & Williams, 2007). The targets are 24 sources in Taurus-Auriga and Ophiucus-Scorpius molecular clouds. In addition to the SED fitting performed in single dish survey observations, visibility derived by the interferometric observations was also fitted with a model, which provides information about spatial structures much finer than that derived with single dish observations. Because the Fourier transform of a power-law function is also a power-law function, the product of surface density and temperature, i.e., $p + q$ can be estimated from observed visibility profiles. The authors fixed inclination angles, inner radii, and opacity. Their free parameters, a disk radius, a temperature profile (T_1, q), and a surface density profile (Σ_5, p), were estimated by both SED fitting and visibility fitting. T_1 and q have ranges of 100-300 K and 0.5-0.75, respectively. The disk radius has a single peak at 200 AU and the number of disks with radii smaller than 100 AU were significantly small. Disk mass has a single peak at $0.03 M_{\odot}$ and lower mass disks were also detected down to $1 \times 10^{-3} M_{\odot}$. The disk mass is overall larger than MMSN, whereas the surface density at 5 AU is smaller than MMSN. Although the median of the power-law index p is 0.5, it includes relatively large uncertainty. When an inclination angle of a disk is estimated from the ratio of the major- and minor-axes of the disk, the power-law index p is underestimated by 0.2-0.3. p is calculated from $p + q$ derived from the visibility fitting and q derived from the SED fitting; q has uncertainty of 0.2-0.3 while $p + q$ is constrained more precisely. In fact MMSN has $p = 1.5$ and $p = 1$ is predicted by a standard disk model, α -disk model. The authors, therefore, concluded that the derived p is consistent with α -disk model.

A standard model for circumstellar disks is the power-law profiles of temperature and surface density as shown in this section. Here I would like to investigate relation between the mass estimate described as Equation (1.1) and the power-law disk model. When dust continuum emission is optically thin, follows Rayleigh-Jeans law, $p + q < 2$, and the disk is face-on, flux density of a dust disk can be described as

$$F_\nu \simeq \int_0^{r_{\text{out}}} \frac{2k_B T_1 r^{-q}}{\lambda^2} \kappa_\nu \Sigma_1 r^{-p} \frac{2\pi r dr}{d^2} = \frac{2k_B T_{\text{out}}}{\lambda^2} \frac{2\pi r_{\text{out}}^2}{d^2} \frac{\kappa_\nu \Sigma_{\text{out}}}{2 - p - q}. \quad (1.5)$$

Using this equation, total mass of the disk is described as

$$M_{\text{disk}} \simeq \int_0^{r_{\text{out}}} \Sigma_1 r^{-p} 2\pi r dr = \frac{2\pi \Sigma_{\text{out}} r_{\text{out}}^2}{2 - p} \simeq \frac{d^2 F_\nu}{\kappa_\nu B_\nu(T_{\text{out}})} \frac{2 - p - q}{2 - p} \simeq \frac{d^2 F_\nu}{\kappa_\nu B_\nu(T(r_c))} \quad (1.6)$$

where $r_c = \left(\frac{2-p-q}{2-p}\right)^{1/q} r_{\text{out}}$. A typical pair, $p = 1$ and $q = 0.5$, provides $r_c = 0.25r_{\text{out}}$, indicating that T_c in Equation (1.1) is temperature at a moderately inner radius. In addition, if $p + q > 2$ and $p < 2$, the flux density strongly depends on the innermost radius of the disk while the mass is mainly determined by the outermost radius. Thus the relation between flux density and disk mass is not obvious in such a case.

1.1.3 Kinematics in Star Formation

Kinematics in star formation is mainly composed of mass accretion (infall), outflow, and rotation. The mass accretion is kinematical phenomenon that mass is transported by gravity from envelopes or ambient structures to disks and from the disks to central stars, which is the most important in star formation in the sense that mass accretion feeds mass to the central stars. The outflow was identified the earliest among the three and considered to be the most effective mechanism to remove angular momentum from young stellar systems. The rotation in young stellar systems is not only Keplerian rotation, where the centrifugal force is balanced with the gravity, but also rigid-body rotation or the rotation conserving angular momentum. The rotation conserving angular momentum is associated

with infall motion because its rotation law cannot support material against the gravity by a central star. The rotation is related with the outflow from the view point of angular momentum transfer. Furthermore rotating disks in YSOs are known to be a place for planet formation.

Mass accretion was identified for the first time in 1990's by indirect evidence from single dish observations in molecular line emission. The indirect evidence is called infall asymmetry; when inner regions of infalling gas have higher temperature, relatively optically thick line emission traces a slightly inner region at a blueshifted velocity channel than the redshifted counterpart, resulting in a symmetry that redshifted emission is weaker than blueshifted emission. The infall asymmetry, however, does not provide spatially resolved structures and in fact several examples of infall motion were revealed to be outflows by interferometric observations; a disk can hide the redshifted side of the associated bipolar outflow. After interferometers were developed in the latter 1990's, velocity fields in YSOs have been directly observed. Relatively optically thin molecular lines are used in interferometric observations so as to investigate the inside of YSOs. Infall asymmetry does not appear and thus infall motion and expanding motion cannot be distinguished from each other in such lines. However, dense cores, as well as disks, are not spherical but disk-like because the cores are supported by magnetic fields in the direction perpendicular to the magnetic fields (Girart et al., 2006). Those disk-like structures showing infall motion are called pseudo-disks. In this case, infall motion and expanding motion can be distinguished by considering the direction of associated outflows.

The first observational identification of outflows is supersonic bipolar motion from the protostar L1551 with velocity higher than escape velocity (Snell et al., 1980). Molecular outflows generally have velocity of several tens km s^{-1} , dynamical time on scales of 10^{3-5} yr, and length of 0.1-1 pc, which cannot be driven by stellar radiation only. The morphology of outflows is expressed with the ratio between the major length and the minor length; larger values indicate longer and narrower morphology. CO observations show the ratio $\sim 2 - 3$ while observations with dense tracer, such as SO, show the ratio

~ 10 . Molecular outflows are considered to be surrounding molecular gas entrained by a high-velocity jet. The central jets, primary jets, are quite thin and make bow shock at the head in jet driven model, while the primary jets are wide and make fan-like outflows in wind driven model. The difference of those models clearly appear in position velocity diagrams (Arce & Goodman, 2002). Molecular outflows are anticipated to rotate in the same direction as the associated disk so as to remove angular momentum from the system, which have been observationally confirmed toward several outflows. Several observations show Extremely High Velocity Outflows (EHVOs) and they are a candidate of primary jets.

Kinematics of dense cores and envelopes is dominated by infall motion on larger scales while rotation becomes dominant on smaller scales, in the simplest scenario. Infall velocity, as well as rotational velocity, has a radial profile. For example free-fall velocity has a radial profile proportional to $r^{-0.5}$. It is under heated discussion in the most recent studies how infalling rotating motion is transformed into Keplerian rotation at the boundary (Ohashi et al., 2014; Aso et al., 2015; Sakai et al., 2014; Oya et al., 2015) The outermost radius where rotational velocity is as large as Keplerian rotation is called the centrifugal radius, which is a candidate of the transitional point from infalling envelopes to Keplerian disks. When the disk is penetrated by strong magnetic fields, the magnetic fields may significantly remove angular momentum preventing a disk from forming (magnetic braking catastrophe). This problem has been solved in the most recent theoretical studies by adopting accurate conditions for calculation and/or considering non-ideal magnetic effects, such as Ohmic diffusion, Hall effect, and ambipolar diffusion (Tomida et al., 2015; Machida et al., 2014; Tsukamoto et al., 2015).

Infall Motion

Observational research on infall motion in protostars started in 1990's. In those days the way to investigate infall motion was detecting a characteristic line profile, infall asymmetry, in molecular line observations with single dish telescopes. When a spherical infalling

gas is observed in relatively optically thick molecular lines, given velocity corresponds to a shell with finite thickness due to thermal or turbulent velocity width. Because the molecular line is relatively optically thick, an inner part of the shell is observed in blueshifted velocity while an outer part of the shell is observed in redshifted velocity. This results in asymmetry that brightness temperature in blueshifted velocity is higher than the redshifted counterpart. In addition, the radial velocity gradient should be smaller in lower velocity and thus shells corresponding to lower velocity have larger width, resulting in self-absorption in the lower velocity. This asymmetry in line profiles is called infall asymmetry.

Infall velocity around the dense core B335 was in fact estimated by model fitting based on infall asymmetry (Zhou et al., 1993). Although infall asymmetry, which is composed of a double peak, cannot be distinguished from a pair of two components with different velocities in the same line of sight, a relatively optically thin line can solve this problem because such lines show a single peak with no self-absorption toward a single component. For this reason Mardones et al. (1997) observed two optically thicker CS ($2-1$) and H₂CO ($2_{12}-1_{11}$) lines and an optically thinner N₂H⁺ ($1-0$) line. Optically thicker lines have a stronger peak on the blueshifted side while optically thinner lines have a single peak at its systemic velocity. Based on this fact they defined skewness δV as $\delta V = (V_{\text{thick}} - V_{\text{thin}})/\Delta V_{\text{thin}}$, where V_{thick} , V_{thin} , and ΔV_{thin} are the stronger peak velocity of an optically thick line, the peak velocity of an optically thin line, and velocity width of the optically thin line; negative δV or blueskew indicates infall asymmetry while redskew indicates expanding motion. The skewness was measured toward 47 objects. It was also confirmed that the observed skewness of line profiles is not due to chemical effects by observing two optically thicker lines, CS and H₂CO. The results show that the number of objects with blueskew is close to the redskew counterpart. The authors claim that Class 0 sources have blueskew more significantly than Class I sources.

Infall asymmetry was also observed toward starless cores. Lee et al. (2004) observed 94 starless cores in CS ($3-2$) and DCO⁺ ($2-1$). Optically thicker CS shows infall

asymmetry and optically thinner DCO^+ shows single peaks. Infall velocity was measured toward 10 cores showing infall motion the most clearly to be $\sim 0.07 \text{ km s}^{-1}$, which is clearly slower than a typical value for protostars, $\sim 1 \text{ km s}^{-1}$. Starless cores in general show low infall velocity, $\sim 0.1 \text{ km s}^{-1}$ and the infall velocity is overall uniform on $\sim 10^4$ AU scales. In contrast higher velocity is concentrated within 1000 AU in protostars. Although research on infall motion was improved by the skewness, infall asymmetry is still indirect evidence because it cannot spatially resolve velocity fields. In fact interferometric observations of B335 in CS (5 – 4), which is the same molecule used to derive infall asymmetry, revealed a bipolar outflow going in the East-West direction. This result cautions us that infall asymmetry does not necessarily indicate infall motion (Wilner et al., 2000).

Observational studies of infall motion with interferometers started in 1990's. Interferometric observations can directly investigate infall motion. Optically thin molecular lines are used to investigate velocity fields through whole gas in such observations. If observed dense cores are spherical, infall motion cannot be distinguished from expanding motion by observations in optically thin lines. However, dense cores are in general supported by magnetic fields and thus have disk-like structures perpendicular to the magnetic fields. This fact enable us to distinguish infall motion from expanding motion by taking account of the direction of outflows. The disk-like structures and the outflows can also be distinguished from each other because they are perpendicular to each other and because optically thin lines does not trace outflows. In an axisymmetric disk-like structure, infall motion causes a velocity gradient along the minor axis of the structure while rotation causes a velocity gradient along the major axis. Infall motion and rotation, therefore, can be distinguished from each other as well.

One of the earliest observational studies of infall motion using interferometers was conducted with Nobeyama Millimeter Array (NMA) (Hayashi et al., 1993). The classical T Tauri star HL Tau was observed in ^{13}CO (1 – 0) with an angular resolution of $\sim 5''$. The authors revealed an extended structure perpendicular to the associated jet and blue- and

redshifted emissions on the far and near sides, respectively, indicative of infall motion. A small velocity gradient was detected along the major axis of the structure; $V_{\text{rot}} = 0.2 \text{ km s}^{-1}$ at 700 AU from the central star and $V_{\text{inf}} = 1.0 \text{ km s}^{-1}$ at 1400 AU. The fact of $V_{\text{inf}} > V_{\text{rot}}$ indicates dynamical infall. The authors also estimated the mass accretion rate to be $\dot{M} = 0.9 \times 10^{-5} M_{\odot} \text{ yr}^{-1}$.

Another example is L1551 IRS 5, toward which infall motion and slow rotation was detected (Momose et al., 1998). The observations can be interpreted as a combination of free-fall and rotation conserving its angular momentum, i.e., $V_{\text{rot}} \propto r^{-1}$ and was compared with a model based on stream lines in gravitational potential (Ulrich, 1976). Observed PV diagrams can be reproduced by a flared disk-like structure with a bipolar cavity in the polar direction, the stellar mass $M_* = 0.5 M_{\odot}$, and the mass accretion rate $\dot{M} = 6 \times 10^{-6} M_{\odot} \text{ yr}^{-1}$. This mass accretion rate is roughly similar to the mass accretion rate $7.7 \times 10^{-6} M_{\odot} \text{ yr}^{-1}$ required by the stellar mass and its bolometric luminosity, $L_{\text{bol}} = 30 L_{\odot}$.

The protostar L1527 IRS was observed with interferometers as well (Ohashi et al., 1997). This protostar is classified between Class 0 and Class I and has $L_{\text{bol}} \sim 1.9 L_{\odot}$ and $T_{\text{bol}} = 56 \text{ K}$. A pair of fan-like outflows going in the East-West direction is identified (Tamura et al., 1996), showing that L1527 IRS is close to the edge-on configuration. $\text{C}^{18}\text{O} (1-0)$ line shows an extended structure perpendicular to the outflow and rotation is detected from a velocity gradient along the extended direction. Although it is difficult to detect velocity gradients along the minor axis direction, the fact that emission is located on both North and South sides of the central stellar position suggests that the kinematics around L1527 IRS includes not only rotation but also infall motion. The infall motion was estimated to be $\sim 0.3 \text{ km s}^{-1}$ at 2000 AU. The central stellar mass was estimated to be $0.1 M_{\odot}$ from the rotational velocity $\sim 0.05 \text{ km s}^{-1}$ at 2000 AU. The mass infall rate $1.1 \times 10^{-6} M_{\odot} \text{ yr}^{-1}$ was estimated from the infall velocity and total gas mass. The dynamical time $M_*/\dot{M} \sim 10^5 \text{ yr}$ is consistent with the Class 0/I phase.

In addition to protostars, infall motion of starless cores have been investigated with

interferometric observations. Tafalla et al. (1998) observed the starless core L1544 using Berkeley Illinois Maryland Association (BIMA) in CCS molecular line. They detected an extended structure on 3×10^4 AU scale, which is larger than protostellar envelopes by an order of magnitude. CCS line shows a ring-like structure where emission is weaker at the peak position of continuum emission, suggestive of freeze-out of CCS molecules. The observed PV diagrams along the major- and minor axes were reproduced by a model of a infalling rotating ring.

Rotation and Angular Momentum

Angular momentum on envelope scales is smaller than that on dense core scales. For example L1527 IRS shows specific angular momenta of 5.0×10^{-4} km s⁻¹ pc at 2000 AU and 5.1×10^{-3} km s⁻¹ pc at 16000 AU; TMC-1A shows specific angular momenta of 2.5×10^{-3} km s⁻¹ pc at 580 AU and 1.0×10^{-2} km s⁻¹ pc at 27000 AU. This tendency requires that angular momentum is transferred to the outside. Specific angular momentum j and the radius r of a dense cores was found to have the relation $j \propto r^{1.6}$ on $> 10^4$ AU scales from measurement of velocity width and sizes toward 24 dense cores (Goodman et al., 1993). The relation changes to a constant, $j \sim 10^{-3}$ km s⁻¹ pc, on envelope scales (Ohashi et al., 1997). Because infalling envelopes are anticipated to conserve angular momentum, the relation between angular momentum and radii suggests that infall motion occurs when a dense core is smaller than $r \sim 0.03$ pc = 6000 AU.

Specific angular momentum of B335 was measured on 100-10⁴ AU scales, showing smaller specific angular momentum at inner radii (Yen et al., 2011). In addition more evolved objects tend to show larger specific angular momentum in the region of $j = \text{const.}$; $< 10^{-3}$ km s⁻¹ pc in Class 0 phase, $\sim 10^{-3}$ km s⁻¹ pc in Class I phase, and a few 10^{-3} km s⁻¹ pc in Class II phase (Yen et al., 2011). These results can be understood with “inside-out collapse model” (Shu et al., 1987; Terebey et al., 1984) where a small infalling region in the inner most region of a core with rigid-body rotation ($j \propto r^{1.5}$) expands to the outer regions and angular momentum of the infalling region increases as

larger angular momentum is transferred from the outer regions. The angular momentum transfer from the outer regions is terminated when protostellar envelopes are dissipated in the Class II phase. In fact such dissipation on a < 1000 AU scale occurs in a protostellar object, L43, between Class I and II (Koyamatsu et al., 2014). This might constrain the final angular momentum and the final radius of a growing disk as well as the final central stellar mass; these limit might depend on a couple of conditions of each star forming region.

Outflow

Outflows from YSOs were observationally identified by Snell et al. (1980) for the first time as supersonic motion from the protostar L1551 in Taurus molecular cloud. The authors concluded that it was not infall motion but outflow because the velocity of the supersonic motion is much larger than escape velocity, which is on the same order of free-fall with typical inclination angles. Subsequently numerous outflows have been identified in 1980's by observing CO molecular line emission.

It is known from low mass stars to high mass stars that sources with larger bolometric luminosity have more massive outflows and larger mass ejection rates (Wu et al., 2005; Caratti o Garatti et al., 2015). This relation also indicates relation between mass accretion rates and mass ejection rates. Observations toward V380 Ori NE revealed that outflows can show precession (Davis et al., 2000). Possible explanations for such precession are that a common outflow of a binary precesses according to the orbital motion of the binary and that the direction of an outflow is bent by Lorentz force by magnetic fields perpendicular to the outflow (Ching et al., 2016). The precession of HH 211 was explained by a binary with the orbital radius ~ 2.3 AU and the orbital period ~ 43 yr (Lee et al., 2010). The two largest issues in outflow studies are the driving mechanism of outflows and outflow rotation. Strong candidates of the driving mechanism are X-wind model (Shu et al., 1994), where outflows are driven at the inner edge of a disk, and disk-wind model (Blandford & Payne, 1982), where outflows are driven in a wide range of a disk. In addition core

dissipation due to an outflow is reported toward a Class 0/I protostar, L1527 (Kiyokane et al., 2013).

Jet-like outflows were detected toward L1448C in CO (3 – 2) and SiO (8 – 7) line emissions (Hirano et al., 2010), revealing several emission knots in the jet-like outflows. The SiO emission is accelerated on the 10'' scale and highly collimated in all detected velocity range. While the CO emission shows the similar acceleration, its structure is shell-like in lower velocity and jet-like in higher velocity. The shell traced in the CO emission can be explained with a wide-angle wind model (Li & Shu, 1996), where the velocity field is approximately expressed as $z \propto r^2$, $V_r \propto r$, $V_z \propto z$. The difference between SiO and CO can also be found in PV diagrams along the outflow axis. The authors explain the SiO emission by jet driven model and the CO emission by the combination of the jet driven outflow traced in SiO and a wide-angle shell. A similar combination was also detected in CO (2 – 1) line emission toward HH211; lower velocity components show both jet-like and shell-like structures while higher velocity components show a jet-like structure alone (Gueth & Guilloteau, 1999). SiO line emission from the same object shows a smaller and more collimated jet. Furthermore a higher transition of SiO line emission, 5 – 4, tends to show more clumpy structures and be stronger near the central protostar than a lower transition, 1 – 0 (Hirano et al., 2006). The CO outflows are fainter near the central protostars. These distributions of SiO and CO suggest that density and temperature can change in the outflows.

Outflow rotation is important to investigate how large angular momentum outflows can transfer from a system, which is also related with disk evolution. Rotation of outflows has, however, not been identified well in observations although it always appears in magnetohydrodynamic simulations and is considered to be the strongest mechanism to transfer angular momentum. The rotation was investigated toward the outflow from HH212 in CO (2 – 1) and SiO (8 – 7) using PV diagrams cutting across the outflow axis, revealing a slight or almost no velocity gradient (Lee et al., 2008). If the slight velocity

gradient is real, the launching radius can be estimated as

$$\varpi_0 = 0.7 \text{ AU} \left(\frac{\varpi_\infty}{100 \text{ AU}} \right)^{2/3} \left(\frac{v_{\phi\infty}}{10 \text{ km s}^{-1}} \right) \left(\frac{v_{p\infty}}{100 \text{ km s}^{-1}} \right)^{-4/3} \left(\frac{M_*}{1M_\odot} \right)^{1/3}. \quad (1.7)$$

SiO (8 – 7) toward HH211 shows velocity gradients in both blue and red lobes in the same direction across the outflow axis, suggesting a launching point at $\lesssim 3 R_\odot = 0.014$ AU (Lee et al., 2007b, 2009). Another observational example is B59#11, whose outflow shows velocity gradients in the same direction as rotation of its Keplerian disk (Hara et al., 2013), while the velocity gradients can also be explained by a binary with a separation smaller than ~ 10 AU.

1.2 DISK FORMATION IN EARLY PHASES

1.2.1 Importance and Problems

Protoplanetary disks play key roles in the evolution of young stellar objects (YSOs). In the early stages of star formation, mass and angular momentum are transferred to the central stars through protoplanetary disks. In the later stages, these disks can become the sites of planet formation (e.g. Howard, 2013). Protoplanetary disks are ubiquitous around classical T Tauri stars (CTTSs) or Class II sources and have been observed in thermal dust continuum and molecular line emissions at millimeter and submillimeter wavelengths since the 1990s. Keplerian rotation is revealed for several disks (Guilloteau & Dutrey, 1998; Guilloteau et al., 1999; Simon et al., 2000; Qi et al., 2004; Hughes et al., 2009; Rodriguez et al., 2010). In the evolutionary stages earlier than T Tauri stars, accreting protostars (Class I or 0 sources) that are still deeply embedded in protostellar envelopes are associated with disk-like structures that exhibit continuum and line emissions. These disk-like structures often show infall motions with little rotation (e.g. Ohashi et al., 1997; Momose et al., 1998; Brinch et al., 2009; Enoch et al., 2009, 2011; Jørgensen et al., 2009; Yen et al., 2010, 2011) and are called “pseudo-disks” (Galli & Shu, 1993a,b), although

pseudo-disks have not been firmly identified with observations. Recent high-sensitivity interferometric observations, however, have also revealed Keplerian disks around Class 0 and Class I protostars (Choi et al., 2010; Takakuwa et al., 2012; Tobin et al., 2012b; Yen et al., 2013).

Despite the discovery of Keplerian disks around some of protostars, their formation process from protostellar envelopes is still controversial both theoretically and observationally. Theoretical calculations of collapsing isothermal spheres with ideal, nonmagnetized conditions, such as “inside-out collapse” models (Terebey et al., 1984; Shu et al., 1987), provide a conventional picture of star and disk formation. According to these models, a central protostar forms with a Keplerian disk at the center of a slowly rotating dense molecular cloud core as the gas in the dense molecular cloud core dynamically infalls. The infalling gas conserves its specific angular momentum because the infalling motions are free-fall. Larger angular momentum is gradually transferred from the outer region of the dense core and is redistributed in the disk as time goes on. There are some observational studies confirming this tendency that a Keplerian disk develops later so that the rotational velocity and size of the disk become larger in later evolutionary stages of YSOs (e.g. Ohashi et al., 1997; Yen et al., 2013). Although these studies observationally suggest the growth of Keplerian disks in the course of YSO evolution, the dynamics of each source are not spatially resolved in these studies. This prevents us from directly investigating how a disk develops in a protostellar system.

Recent theoretical simulations for disk formation around protostars, including MHD calculations, are still under heated discussion. It is reported that such simulations have difficulties in transforming envelopes to Keplerian disks because of strong magnetic braking or fragmentation (Mellon & Li, 2008, 2009). However, Tomida et al. (2013, 2015) and Machida et al. (2011) point out that nonideal MHD effects can suppress angular momentum transport by magnetic fields and enable formation of circumstellar disks in the early phase of star formation (see also Joos et al., 2012). The formation of Keplerian disks is closely related to the dynamical transition from the infall motion in protostellar

envelopes to the Keplerian rotation. In fact, such a transition is being observationally revealed around several protostars by the most recent studies (Murillo et al., 2013; Chou et al., 2014; Ohashi et al., 2014; Takakuwa et al., 2014; Yen et al., 2014). The number of samples is, however, still too limited to perform any statistical study. In order for us to unveil the disk formation mechanism, it is essential to observe the two kinds of dynamics (infall and rotation) around protostars and increase the number of direct detections of the transition between the two.

Details of protostellar disks around protostars, such as their structures and dynamics are barely known because protostellar disks are deeply embedded in protostellar envelopes, making it difficult to observationally study protostellar disks without any confusion with protostellar envelopes. It is therefore critical whether or not disks and envelopes in protostellar systems can be distinguished from each other by observations to study protostellar disks in detail. One promising way to achieve this goal is to distinguish them kinematically by inspecting their rotational motion, i.e., envelopes that often have infall motion are expected to have rotation proportional to r^{-1} , while disks are expected to have Keplerian rotation proportional to $r^{-0.5}$. Once envelopes and disks are kinematically distinguished, disk radii can also be kinematically estimated. Another important aspect to identify Keplerian rotation in disks around protostars is that it allows us to estimate dynamical masses of central protostars directly with no assumption. Such direct estimation of the dynamical mass enables us to examine whether or not infall motions around protostar are free-fall otherwise it has been always assumed that they are free-fall.

It is not clear whether protostellar disks are similar to T Tauri disks structurally, as well as kinematically. Physical structures of T Tauri disks, such as radial dependences of surface density and temperature have been investigated well, suggesting that their radial power-law profiles of surface density and temperature are described well as $\Sigma \propto r^{-p}$ with $p \sim 1$ regardless of exponential tails and $T \propto r^{-q}$ with $q \sim 0.5$, respectively. Their scale height described as $H \propto r^h$ was also investigated, finding that they are in hydrostatic equilibrium (HSEQ) with a power-law index of $h = 1.25$. On the other hand, similar

studies to investigate physical structures of protostellar disks have not been performed yet except for very limited cases (e.g., Wolf et al., 2008; Tobin et al., 2013). Understanding physical structures of protostellar disks would be important to see whether disks and their surrounding envelopes can be geometrically distinguished from each other. If this is the case, we can have two independent ways (kinematically or geometrically) to identify disks around protostars. In addition, investigating physical structures of protostellar disks can help us to understand disk formation process and also evolution process into T Tauri disks. In particular recent observations of T Tauri disks have revealed irregular structures such as spirals, gaps, and central holes, which might be related to planet formation. Tantalizing ring structures are discovered even in the disk around the class I/II young star HL Tau. It would be very important to understand when and how such structures are formed in these disks, and to answer this question, it is required to investigate structures of protostellar disks, which would be precursors of disks with irregular structures.

1.2.2 Related Methods in Previous Works

In this thesis, the analysis of rotation curves of disks and envelopes around protostars is crucial to identify Keplerian rotations. In addition, the analysis of structures of disks and envelopes around protostars is also crucial. In this subsection, methods for such analysis done in previous works are summarized.

Rotating motion of a disk like structure can be detected as velocity gradient along the major axis of the structure, while infall motion of a disk like structure can be detected as velocity gradient along the minor axis of the structure. For this reason PV diagrams along major axes were investigated by Yen et al. (2013) in order to identify Keplerian rotation around protostars with less contamination from other kinds of motion, such as infall motion; they observed C^{18}O ($2-1$) line emission with an angular resolution of $\sim 4''$. Figure 1.1 shows PV diagrams derived by Yen et al. (2013). They determined representative points cutting both velocity and position directions. Figure 1.2 shows those representative

points in $\log R - \log V$ planes for four protostars. Those points were fitted with power-law functions, $V_{\text{rot}} \propto r^p$. Their results suggest that Class I protostars, TMC-1A and L1489 IRS, show power-law indices close to Keplerian law while Class 0 protostars, L1448-mm and L1527 IRS, show steeper power-law indices close to -1 , i.e., rotation conserving its specific angular momentum. They also found, however, that the power-law indices can be estimated to be shallower than real values in this analysis, depending on several factors, such as observational angular resolutions.

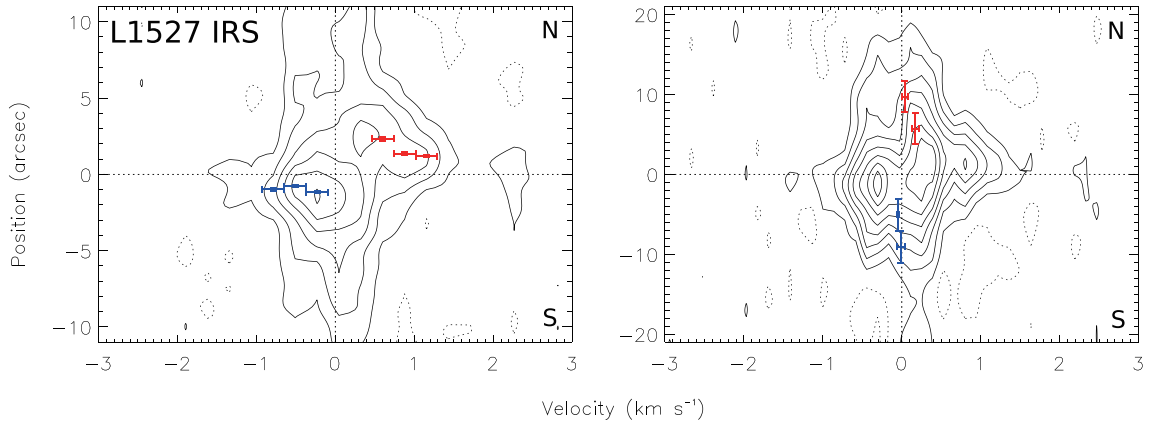


Figure 1.1 Representative points in PV diagrams derived by Yen et al. (2013). The PV diagrams are derived in $\text{C}^{18}\text{O} (2 - 1)$ emission of the protostar L1527 IRS with a cut perpendicular to the associated outflow direction. The left and right panels are produced with the combination of compact+subcompact SMA configurations and only the subcompact SMA configuration, respectively.

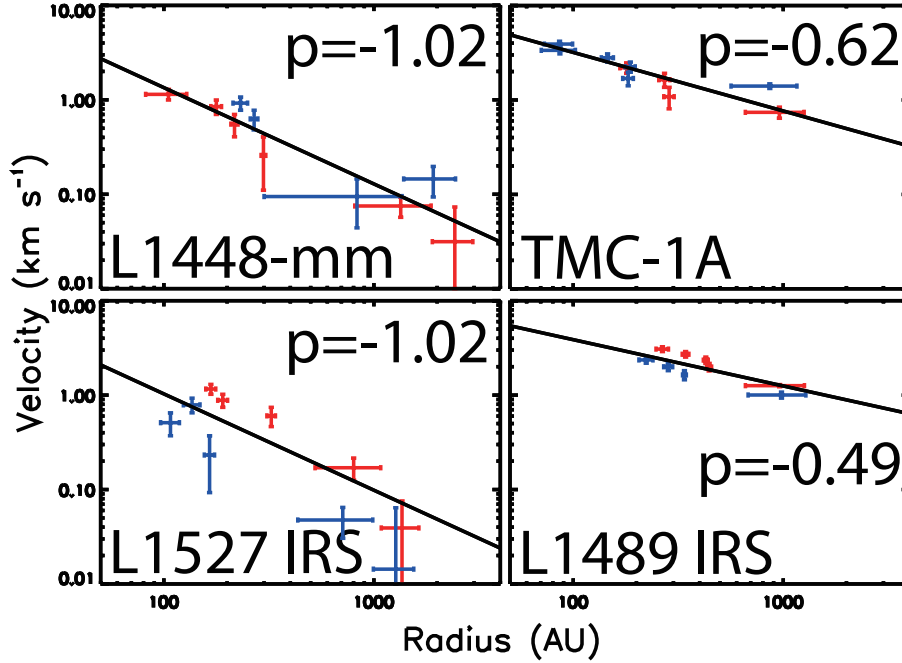


Figure 1.2 Representative points in the $\log R - \log V$ plane derived by Yen et al. (2013). The points correspond to ones in Figure 1.1. It is known that power-law indices can be artificially shallower than real values in the analysis in Yen et al. (2013), depending on several factors, such as observational angular resolutions.

In order for us to analyze structures of disks and envelopes around protostars, a conventional way is use their images. We should be, however, careful when we make such analysis based on images obtained with interferometers because imaging process for interferometric observations includes nonlinear process, such as CLEAN and MEM. This is because interferometers originally observe visibility, which is Fourier transform of brightness distribution of the observed target, and it is impossible to sample visibility in the whole uv plane. Several previous works using interferometers to study structures of disks and envelopes performed model fittings directly to visibility data to avoid the nonlinear effects. Figure 1.3 shows examples of visibility observed by Jørgensen et al. (2009) and Looney et al. (2003). Those visibilities were derived by azimuthally averaging, implicitly assuming that the observed structures are spherically symmetric. These studies with model fitting to visibility revealed mass ratio, or flux ratio, between disks and envelopes

for several protostars. However, it was difficult to determine detailed structures of disks, which are not spherically symmetric, with the averaged visibility data.

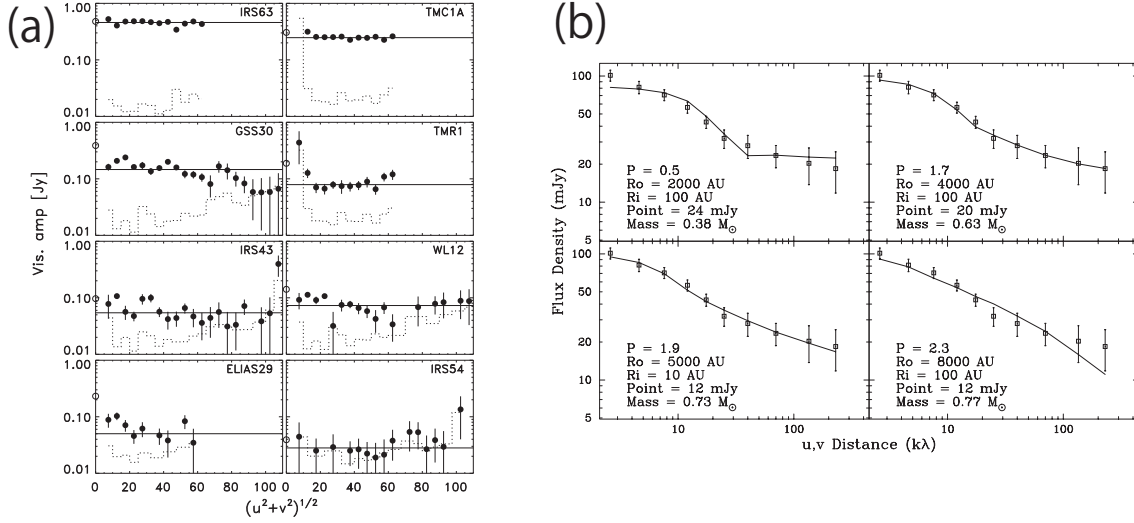


Figure 1.3 Visibility profiles of protostars used for model fitting. (a) 1.1 mm continuum visibility observed with SMA by Jørgensen et al. (2009). (b) 2.7 mm continuum visibility observed with BIMA by Looney et al. (2003).

1.2.3 This Thesis

The main objectives of this thesis are (1) to investigate kinematics of disks and envelopes in protostellar phases, (2) to investigate structures of disks and envelopes in protostellar phases, and (3) to identify new targets in younger phases of star formation for future studies. In order to accomplish these three objectives, two protostars, TMC-1A and L1527 IRS in the Taurus star forming region, have been observed. In addition, several millimeter sources newly found in the Serpens Main star forming region with SMA also have been observed. All the observations made for this thesis were carried out with Atacama Large Millimeter/submillimeter Array (ALMA) providing unprecedented sensitivity and angular resolutions. The observations have been made mainly in CO 2 – 1 isotopologues and thermal dust continuum at 1.3 mm.

This thesis consists of five chapters, including this Chapter 1 for introduction. Chapter 2 presents the observations of TMC-1A, describing the following four parts; (1) to iden-

tify a Keplerian disk around the protostar; (2) to determine the disk size and the central stellar mass of the protostar; (3) to investigate rotation and infall motion in the envelope surrounding the disk; and (4) to examine relations among those kinematical quantities.

Chapter 3 presents the observations of the protostar L1527 IRS that is younger than TMC-1A, describing the following three results; (1) to constrain radial and vertical structures of the disk around the protostar; (2) to investigate relation between structures and kinematics of the disk; and (3) to examine the origin of the derived structures. In order to investigate the structures of the disk, the continuum visibility data without azimuthal averages because is clearly not spherically symmetric.

Chapter 4 presents the observations of the Serpens Main star forming region, describing (1) to select new YSOs based on the previous wide-field observations using SMA, (2) to determine their evolutionary stages based on mm and infrared observations using *Spitzer* and *Herschel*, and (3) to identify and examine a possible extremely young object.

Chapter 5 presents the summary of this thesis, proposing a possible scenario of disk formation based on the results presented in this thesis.

Chapter 2

ALMA CYCLE 0 OBSERVATIONS OF TMC-1A

2.1 ABSTRACT

We have observed the Class I protostar TMC-1A with the Atacama Millimeter/submillimeter Array (ALMA) in the emissions of ^{12}CO and C^{18}O ($J = 2 - 1$) and 1.3 mm dust continuum. Continuum emission with a deconvolved size of $0''.50 \times 0''.37$, perpendicular to the ^{12}CO outflow, is detected. It most likely traces a circumstellar disk around TMC-1A, as previously reported. In contrast, a more extended structure is detected in C^{18}O , although it is still elongated with a deconvolved size of $3''.3 \times 2''.2$, indicating that C^{18}O traces mainly a flattened envelope surrounding the disk and the central protostar. C^{18}O shows a clear velocity gradient perpendicular to the outflow at higher velocities, indicative of rotation, while an additional velocity gradient along the outflow is found at lower velocities. The radial profile of the rotational velocity is analyzed in detail, finding that it is given as a power law $\propto r^{-a}$ with an index of ~ 0.5 at higher velocities. This indicates that the rotation at higher velocities can be explained as Keplerian rotation orbiting a protostar with a dynamical mass of $0.68 M_{\odot}$ (inclination corrected). The additional velocity gradient of C^{18}O along the outflow is considered to be mainly infall motions in the envelope.

Position-velocity diagrams made from models consisting of an infalling envelope and a Keplerian disk are compared with the observations, revealing that the observed infall velocity is ~ 0.3 times smaller than the free-fall velocity yielded by the dynamical mass of the protostar. Magnetic fields could be responsible for the slow infall velocity. A possible scenario of Keplerian disk formation is discussed.

2.2 INTRODUCTION

In order to investigate the expected transition from the infall motion to Keplerian rotation, we made observations of the Class I protostar TMC-1A (IRAS 04365+2535) with the Atacama Large Millimeter/Submillimeter Array (ALMA) in $^{12}\text{CO } J = 2 - 1$ (230.5380 GHz), $\text{C}^{18}\text{O } J = 2 - 1$ (219.5604 GHz), and 1.3 mm continuum emission. As its name suggests, our target TMC-1A is in the Taurus molecular cloud, which is one of the closest star-forming regions ($d = 140$ pc). Its bolometric luminosity $L_{\text{bol}} = 2.7 L_{\odot}$ and bolometric temperature $T_{\text{bol}} = 118$ K (Kristensen et al., 2012) indicate that TMC-1A is a typical Class I protostar. The systemic velocity of TMC-1A was measured at $V_{\text{LSR}} = 6.4$ km s $^{-1}$ by Terebey et al. (1989).

A molecular outflow ($t_{\text{dyn}} \sim 2.5 \times 10^3$ yr) is associated with TMC-1A (Hirano et al., 1995; Chandler et al., 1996; Tamura et al., 1996). Interferometric observations detected a dense gas condensation toward the protostar with its velocity gradient perpendicular to the outflow axis (Ohashi et al., 1996, 1997). Furthermore, Submillimeter Array (SMA) observations of this protostellar envelope show that higher-velocity components ($|V| \gtrsim 1.4$ km s $^{-1}$) are located closer to the central protostar than the lower-velocity components ($|V| \lesssim 0.8$ km s $^{-1}$), suggesting a differential rotation of the envelope (Yen et al., 2013). Their analysis, using the position-velocity (PV) diagram with a cut perpendicular to the outflow axis to obtain information purely about rotation by avoiding contamination from outflowing or infalling gas, showed that TMC-1A has a shallower rotational velocity profile ($p = -0.6 \pm 0.1$ with $v \propto r^p$) and higher rotation velocity (1.0 – 4.0 km s $^{-1}$)

than their other samples, such as L1527 IRS and L1448-mm, on a 1000 AU scale. They suggest that TMC-1A should have a Keplerian disk ($p = -0.5$) with $M_* = 1.1 \pm 0.1 M_\odot$ and a large angular momentum should have been transferred into the disk from the surrounding envelope. This result can be understood in terms of the conventional analytical model with inside-out collapse. Based on this model, the rotation profile indicates that TMC-1A is in an evolutionary stage at $t \sim 5 \times 10^5$ yr after the onset of collapse. A similar analysis to Yen et al. (2013) was applied to the visibilities of TMC-1A data obtained with the Plateau de Bure Interferometer (Harsono et al., 2014). They measured gas kinematics in the uv domain and suggested that the rotational velocity profile in the inner part ($r < 80 - 100$ AU) is explained with the power-law index of $p = -0.5$ (i.e. Keplerian disk) while the outer part is explained with $p = -1$. They also estimated the size of the disk by removing a spherical-infalling envelope component from the continuum emission toward TMC-1A, although it was not well constrained ($R_{\text{disk}} = 80 - 220$ AU). These pieces of previous work indicate that TMC-1A is in the disk-developing phases and hence is a good target to investigate the formation process of Keplerian disks around protostars.

Our observations and data reduction are described in Sec.2.3. In Sec.2.4, we present the continuum and molecular-line results. In Sec.2.5, we analyze velocity structures of the C^{18}O line, in particular rotating motions, while we discuss infalling motions around TMC-1A in more detail in Sec.2.6. In Sec.2.7, we present a summary of the results and our interpretation. In addition, an investigation into the analysis using a PV diagram and a comparison of flattened and spherical envelope models are presented in Appendix 2.8.1 and 2.8.2.

2.3 ALMA OBSERVATIONS

We observed our target, TMC-1A, during Cycle 0 using ALMA on 2012 November 6. The configuration is “extended” with 23 antennas. Extended configuration covers projected uv distances from 16 to 285 m (11.7-208.7 k λ in $\text{C}^{18}\text{O } J = 2 - 1$). This minimum

baseline resolves out more than 50% of the flux if a structure is extended more than $7''.7$ (Wilner & Welch, 1994), corresponding to ~ 1100 AU at the distance to TMC-1A. The coordinates of map center are $\alpha(\text{J2000})=4^{\text{h}}39^{\text{m}}35^{\text{s}}.010$, $\delta(\text{J2000})=25^{\circ}41'45''.500$. ^{12}CO ($J = 2 - 1$) and C^{18}O ($J = 2 - 1$) lines and 1.3 mm continuum emission in Band 6 were observed for 63 minutes (on source). In order to derive high-velocity resolutions for molecular line observations, we configured the correlator in Frequency Division Mode (FDM) for four spectral windows. Each spectral window has 3840 channels covering 234 MHz bandwidth. Emission-free channels are used to make the continuum map centered at 225 GHz. The total integrated frequency width of the continuum map is ~ 920 MHz. The observed visibilities were Fourier transformed and CLEANed with Common Astronomy Software Applications (CASA). In this process, we adopted Briggs weighting with the robust parameter of 0.5 and binned two channels; thus, the frequency (velocity) resolution in this chapter is 122 kHz, corresponding to 0.16 km s^{-1} in ^{12}CO ($J = 2 - 1$) and 0.17 km s^{-1} in C^{18}O ($J = 2 - 1$). We also set CLEAN boxes to enclose only positive emission in dirty maps. The synthesized beam sizes of the CLEANed maps are $1''.02 \times 0''.90$ for the ^{12}CO line, $1''.06 \times 0''.90$ for the C^{18}O line, and $1''.01 \times 0''.87$ for the continuum. J0522-364, J0510+180, and Callisto were observed as the passband, gain, and flux calibrator, respectively. In regard to the flux calibrator Callisto, models of solar system objects were updated from Butler-Horizons-2010 to Butler-JPL-2012 for CASA 4.0 after the delivery of our data, and the fractional difference (2012/2010 - 1) was reported. Following the value (Callisto: -0.15 , 241 GHz), we multiplied the delivered intensities by 0.85. The rms noise levels are measured in channels where emission is detected to take the noise due to spatial filtering artifacts and the thermal noise into account. The parameters of our observations mentioned above (and others) are summarized in Table 2.1.

Table 2.1. Summary of the observational parameters (TMC-1A)

Interferometer and Date	CO $J = 2 - 1$	C ¹⁸ O $J = 2 - 1$	Continuum
	ALMA (Extended), 2012 Nov.6		
Target	TMC-1A		
Coordinate center	R.A. (J2000)=4 ^h 39 ^m 35 ^s .010 Decl. (J2000)=25°41'45".500		
Frequency	230.5380 GHz	219.5604 GHz	225.4336 GHz
Primary beam	27".3	28".6	27".9
Projected baseline length	15.9 – 285.7 m		
Synthesized beam (P.A.)	1".02 × 0".90 (−178°)	1".06 × 0".90 (−176°)	1".01 × 0".87 (+0°.87)
Velocity resolution	0.16 km s ^{−1}	0.17 km s ^{−1}	923 MHz
Noise level (no emission)	5.6 mJy beam ^{−1}	4.6 mJy beam ^{−1}	—
Noise level (detected channel)	20 mJy beam ^{−1}	7.1 mJy beam ^{−1}	0.96 mJy beam ^{−1}
Passband calibrator	J0522-364		
Flux calibrator	Callisto		
Gain calibrator	J0510+180		

2.4 RESULTS

2.4.1 Continuum and ¹²CO

Figure 2.1 shows the 225 GHz continuum emission in TMC-1A observed with ALMA. Strong continuum emission with a weak extension to the west is detected. Though the size of the continuum emission is almost similar to the beam size (1".01 × 0".87), its deconvolved size can be estimated from a 2D Gaussian fitting to be $0".50 \pm 0".03 \times 0".37 \pm 0".05$, P.A. = $73^\circ \pm 16^\circ$. The peak position is also measured from the Gaussian fitting to be $\alpha(2000)=4^{\text{h}}39^{\text{m}}35^{\text{s}}.20$, $\delta(2000)=+25^\circ41'44".35$, which is consistent with previous measurements (Yen et al. 2013). The measured continuum peak position is used as the central protostar position of TMC-1A in this chapter. The peak intensity and the total flux density of the continuum emission derived from a Gaussian fitting are 148.5 ± 2.2 mJy beam^{−1} and 182.1 ± 2.6 mJy, respectively. The dust mass calculated with the total flux density is $M_{\text{dust}} = (4.2 \pm 0.9) \times 10^{-4} M_{\odot}$ assuming a standard opacity coefficient $\kappa(1 \text{ THz}) = 10.0 \text{ cm}^2 \text{ g}^{-1}$ (Beckwith et al., 1990), an opacity index $\beta = 1.46$, and a dust temperature $T_c = 28 \text{ K}$ (Chandler et al., 1998), which is a temperature estimated from a fitting to the

spectral energy distribution of TMC-1A at $\lambda \gtrsim 20 \mu\text{m}$. Thus, the gas mass is estimated to be $4.2 \times 10^{-2} M_{\odot}$ if assuming that the gas/dust mass ratio is 100.

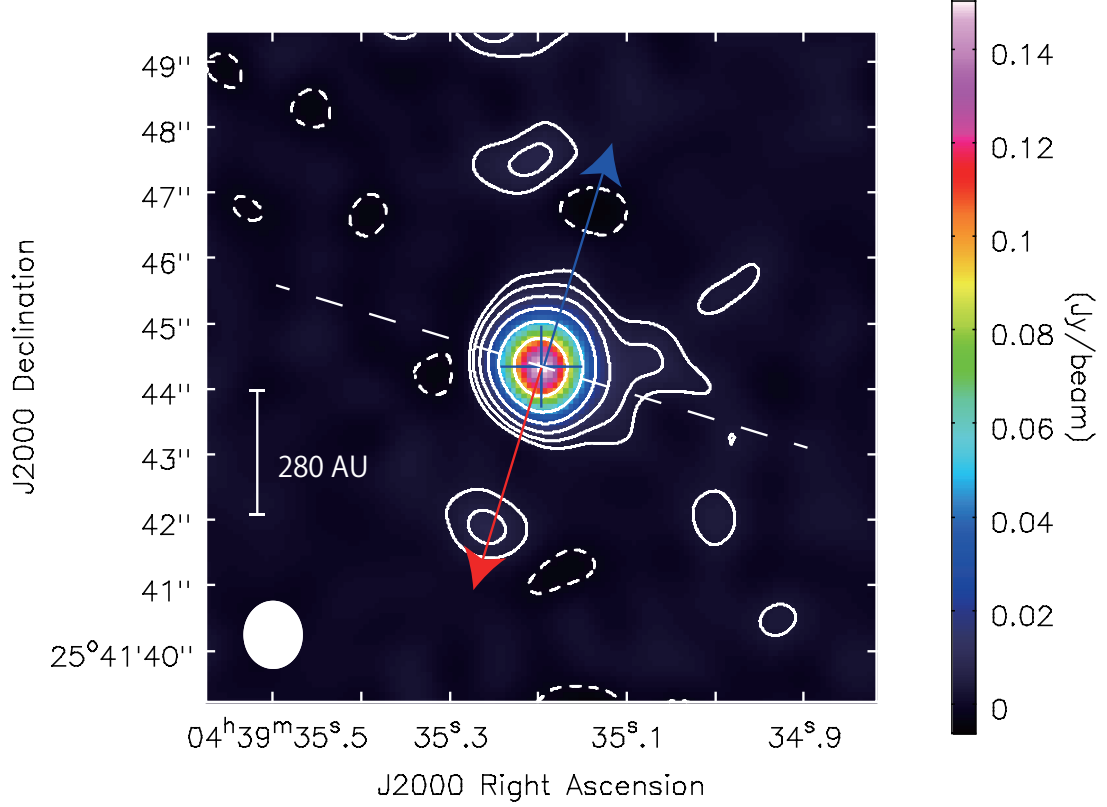


Figure 2.1 Continuum emission map of TMC-1A observed with ALMA. Contour levels are $-3, 3, 6, 12, 24, \dots \times \sigma$, where 1σ corresponds to $0.96 \text{ mJy beam}^{-1}$. A plus sign shows the position of the continuum emission peak. A filled ellipse at the bottom left corner denotes the ALMA synthesized beam; $1''.01 \times 0''.87$, P.A. = $+0^{\circ}87$. The deconvolved size of the continuum emission is $0''.50 \pm 0''.03 \times 0''.37 \pm 0''.05$, P.A. = $+73^{\circ} \pm 16^{\circ}$, and the elongation direction (73°) is shown with a white dashed line. Blue and red arrows show the direction of the molecular outflow from TMC-1A observed in the ^{12}CO ($J = 2 - 1$) line (Figure 2.2).

Figure 2.2 shows the integrated intensity (moment 0) and the intensity-weighted mean velocity (moment 1) maps of the ^{12}CO ($J = 2 - 1$) emission toward TMC-1A, presented, respectively in contour and in color. The ^{12}CO emission is detected at more than the 3σ level at a velocity ranging from -9 km s^{-1} to 12 km s^{-1} in local standard of rest (LSR) frame, except for the velocity from 5 km s^{-1} to 7 km s^{-1} , where the ^{12}CO emission is most likely resolved out. This resolved-out velocity range is around the systemic velocity $V_{\text{sys}} = 6.4 \text{ km s}^{-1}$. The emission shows a bipolar structure and a shell-like shape. The overall shape and velocity gradient seen in the maps indicate that the ^{12}CO emission clearly traces a molecular outflow going in the north-south direction. The position angle of the outflow axis is measured to be -17° by eye based on the direction of the velocity gradient and the shape of the ^{12}CO emission, as indicated with the dashed line in Figure 2.2, which is consistent with previous papers (e.g. -10° ; Chandler et al., 1996) and perpendicular to the elongation direction of the continuum emission. The blue lobe is detected more clearly than the red lobe. As suggested by the previous ^{12}CO ($J = 1 - 0$) observation (Tamura et al. 1996), an accelerated motion along the outflow axis can be seen, especially in the blue lobe on $\sim 1000 \text{ AU}$ scale as shown in Figure 2.3, where the PV diagram of the ^{12}CO emission along the outflow axis is presented. Essentially, the velocity increases out along the outflow axis (“Hubble law”) from the central protostar. On the other hand, across the outflow axis, the higher-velocity component is located closer to the outflow axis. This feature across the outflow axis has been observed in other outflows as well and can be understood by an outflow driven by a parabolic wide-angle wind (e.g. Lee et al., 2000). In addition to the ^{12}CO component tracing the outflow, there seems to be another ^{12}CO component near the central star, which shows an elongated structure almost perpendicular to the outflow axis. This additional component also has a velocity gradient along its extension. The geometrical and kinematical structures of this additional ^{12}CO component are similar to those of C^{18}O ($J = 2 - 1$), as will be shown later.

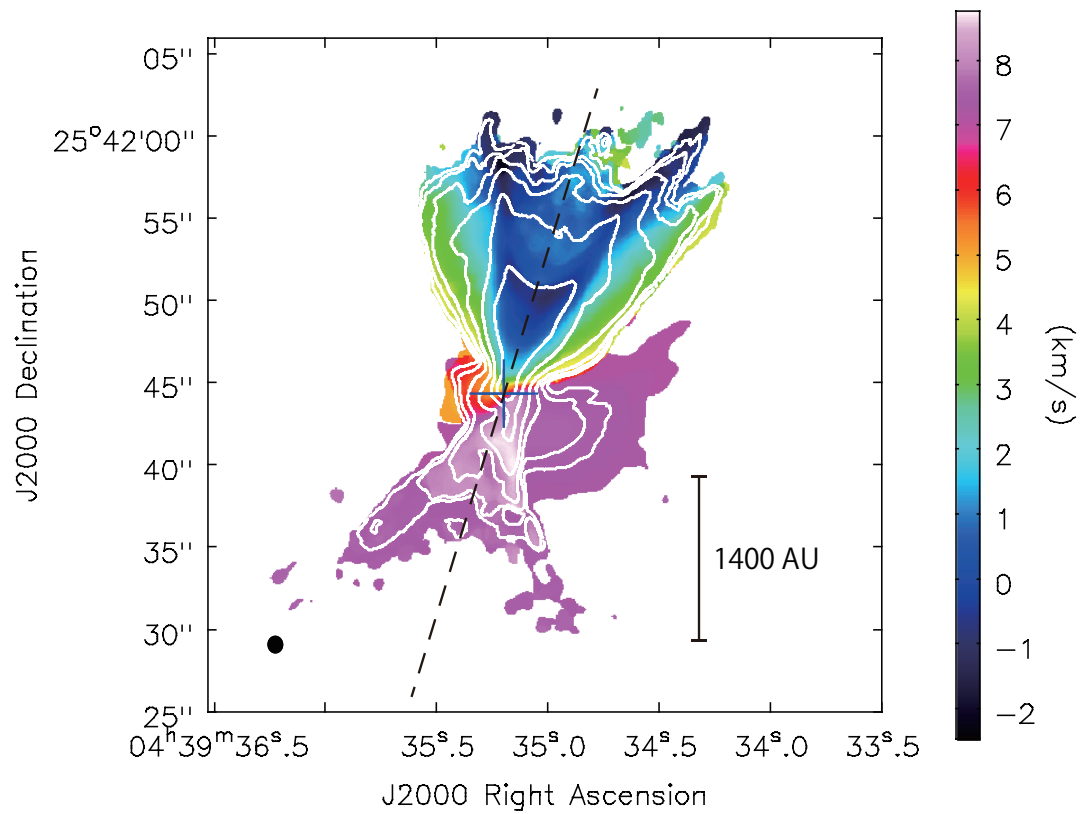


Figure 2.2 Moment 0 (white contours) and 1 (color) maps of the ^{12}CO ($J = 2 - 1$) emission in TMC-1A. Contour levels of the moment 0 map are $-3, 3, 6, 12, 24, \dots \times \sigma$, where 1σ corresponds to $0.034 \text{ Jy beam}^{-1} \text{ km s}^{-1}$. A plus sign shows the position of the central protostar (continuum emission peak). A filled ellipse at the bottom left corner denotes the ALMA synthesized beam; $1''.02 \times 0''.90$, P.A. = -178° . ^{12}CO clearly traces the molecular outflow from TMC-1A, and the axis of the outflow ($\sim -17^\circ$) is shown with a dashed line.

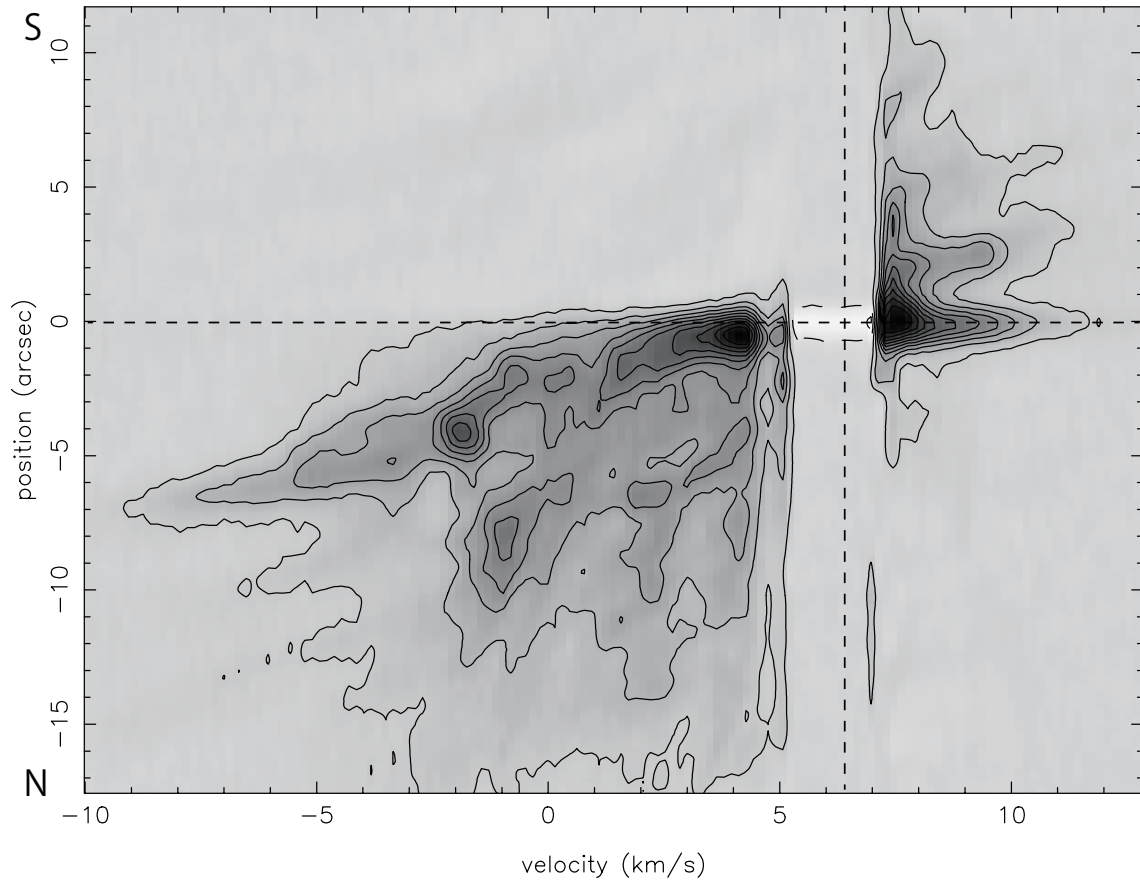


Figure 2.3 PV diagrams of the ^{12}CO ($J = 2 - 1$) emission in TMC-1A along the outflow axes ($\text{PA} = -17^\circ$). Contour levels are 6σ spacing from 3σ ($1\sigma = 20 \text{ mJy beam}^{-1}$). Central vertical dashed lines show the systemic velocity ($V_{\text{sys}} = 6.4 \text{ km s}^{-1}$), and central horizontal dashed lines show the central position.

The compactness of the continuum emission with its position angle perpendicular to the outflow axis suggests that the continuum emission arises from a compact disk and the major axis of the expected disk should be at P.A.= 73° direction (white dashed line in Figure 2.1). Although the uncertainty of the elongation direction of the continuum emission is relatively large ($\pm 16^\circ$), we hereafter adopt this position angle as the disk major axis around TMC-1A. The ratio of minor axis to major axis corresponds to the inclination angle of $i = 42^\circ$ and 55° if assuming a geometrically thin disk and $H/R = 0.2$, respectively.

2.4.2 $\text{C}^{18}\text{O } J = 2 - 1$

$\text{C}^{18}\text{O } (J = 2 - 1)$ is detected at more than a 3σ level at LSR velocities ranging from 2.7 to 10.4 km s^{-1} . In Figure 2.4, the moment 0 (MOM0) map integrated over this velocity range is shown in white contours, overlaid on the moment 1 (MOM1) map shown in color. The overall distribution of the C^{18}O integrated intensity exhibits an elongated structure almost perpendicular to the molecular outflow, with a peak located at the protostar position. The deconvolved size of MOM0 map is $3''.3 \pm 0''.1 \times 2''.2 \pm 0''.1$ with P.A.= $67^\circ \pm 2^\circ$. This morphology showing elongation perpendicular to the outflow axis (P.A.= -17°) indicates that the C^{18}O emission mainly traces a flattened envelope around TMC-1A, as was also suggested by Yen et al. (2013). In addition, there are weak extensions to the north, the northwest, and the east. The overall velocity gradient is seen from northeast to southwest, which is almost perpendicular to the outflow axis. These results are quite consistent with previous observations in $\text{C}^{18}\text{O } (J = 2 - 1)$ using SMA (Yen et al. 2013) although their map did not show the weak extensions detected in our ALMA observations.

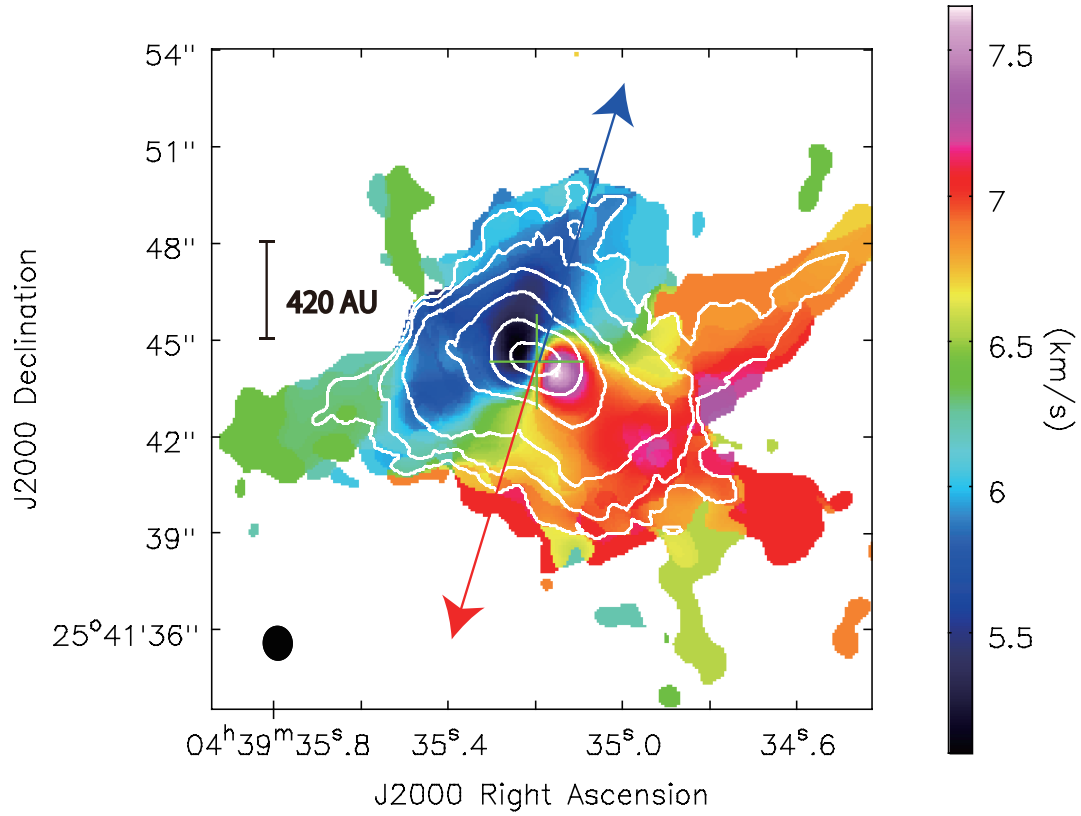


Figure 2.4 Moment 0 (white contours) and 1 (color) maps of the C¹⁸O ($J = 2 - 1$) emission in TMC-1A. Contour levels of the moment 0 map are $-3, 3, 6, 12, 24, \dots \times \sigma$, where 1σ corresponds to $8.1 \text{ mJy beam}^{-1} \text{ km s}^{-1}$. A plus sign shows the position of the central protostar (continuum emission peak). A filled ellipse at the bottom left corner denotes the ALMA synthesized beam; $1''.06 \times 0''.90$, P.A. = -176° . Blue and red arrows show the direction of the molecular outflow from TMC-1A observed in ¹²CO ($J = 2 - 1$) line (Figure 2.2).

In order for us to see more detailed velocity structures, channel maps shown in Figure 2.5 are inspected. At high velocities, $V_{\text{LSR}} \leq 4.9 \text{ km s}^{-1}$ and $\geq 7.9 \text{ km s}^{-1}$ (which are blueshifted and redshifted, respectively, by more than 1.5 km s^{-1} with respect to the systemic velocity of 6.4 km s^{-1}), there is compact emission with strong peaks located nearby the protostar position. The sizes of these emissions are smaller than $\sim 3''$ or 420 AU. The peaks of these emissions are located on the east side of the protostar at blueshifted velocities, while those for redshifted velocities are located on the west side, making a velocity gradient from east to west. This direction is roughly perpendicular to the outflow axis (P.A. = -17°). On the other hand, at lower blueshifted and redshifted velocities ($5.0 \text{ km s}^{-1} \leq V_{\text{LSR}} \leq 6.0 \text{ km s}^{-1}$), extended structures become more dominant. At lower blueshifted velocities, structures elongated from northwest to southeast with additional extensions to the northeastern side and the southern side appear, while at lower redshifted velocities, structures elongating to the southwest become more dominant. At velocities close to the systemic velocity, weak emission appears in even more extended structures to the east, south, west, and north, which seem to form an X-shaped structure as a whole. A similar X-shaped structure can also be seen in MOM0 and MOM1 maps, although they are less obvious because of a dilution effect after the channel integration.

Since the C^{18}O emission shows both compact emission at higher velocities and extended emission at lower velocities (whose origin and nature may be different from each other), integrated channel maps of blueshifted and redshifted emission, as presented in Figure 2.6, were made for further investigation. Figure 2.6a shows channel maps integrated for the high-velocity ($|\Delta V| > 2.0 \text{ km s}^{-1}$) compact emission, and Figure 2.6b shows those integrated for the low-velocity ($|\Delta V| < 1.0 \text{ km s}^{-1}$) extended emission, where ΔV indicates the relative velocity to the systemic velocity. The maps of the high-velocity component show a very compact structure as a natural consequence of the integration of compact emission seen in the original channel maps shown in Figure 2.5. The dashed line in Figure 2.6a passing the two peaks of blue- and redshifted components gives us a direction of the velocity gradient at the high velocities (P.A. = 72°), which is

almost perpendicular to the outflow direction. In contrast to the high-velocity component, the maps of the low-velocity component are extended to ~ 800 AU scale at the 4σ level. This figure also shows a clear velocity gradient in the direction of northeast-southwest as shown with a dashed line (P.A. = 49°) passing the two peaks of blue- and redshifted components in Figure 2.6b. This direction of the velocity gradient of the low-velocity component is not perpendicular to the outflow axis and apparently different from that of the velocity gradient seen in the high-velocity component. These differences seen between the high-velocity and low-velocity components will be discussed in more detail later.

The ratio of the brightness temperature between the C^{18}O and ^{12}CO emission tells us that C^{18}O is most likely optically thin, although it is difficult for us to estimate the optical depth of the C^{18}O emission at V_{LSR} between 5 and 7 km s^{-1} , where ^{12}CO is completely resolved out. We note that when the ratio between the C^{18}O and ^{12}CO emission is calculated, the spatial filtering has to be taken into account. In the case discussed here, however, the ^{12}CO emission is significantly more extended than the C^{18}O emission, and as a result, the ^{12}CO emission should be resolved out more than the C^{18}O emission. This suggests that the ratio of the C^{18}O emission to the ^{12}CO emission should be overestimated, and as a result, the optical depth of the C^{18}O emission should be overestimated. When C^{18}O is optically thin and under the condition of local thermodynamic equilibrium (LTE), total gas mass is estimated from the total flux of C^{18}O . The peak intensity and the total flux of the C^{18}O emission are 842 ± 82 $\text{mJy beam}^{-1} \text{ km s}^{-1}$ and 7.20 ± 0.70 Jy km s^{-1} , respectively. The gas mass calculated with the total flux is $M_{\text{gas}} = 4.4 \times 10^{-3} M_{\odot}$ assuming the excitation temperature $T = 28$ K (Chandler et al. 1998) and the abundance of C^{18}O relative to H_2 of $X(\text{C}^{18}\text{O}) = 3.0 \times 10^{-7}$ (Frerking et al., 1982). The gas mass derived from the C^{18}O flux is one order of magnitude smaller than that from dust continuum flux density, $4.2 \times 10^{-2} M_{\odot}$ assuming gas/dust=100 (see the result for Class II disks by Williams & Best, 2014), though both mass estimations include a lot of uncertain factors, such as optical depth, temperature, non-LTE effects, and gas/dust mass ratio. Additionally, the

molecular abundance of $C^{18}O$ might be decreased because of freeze-out of CO onto dust grains.

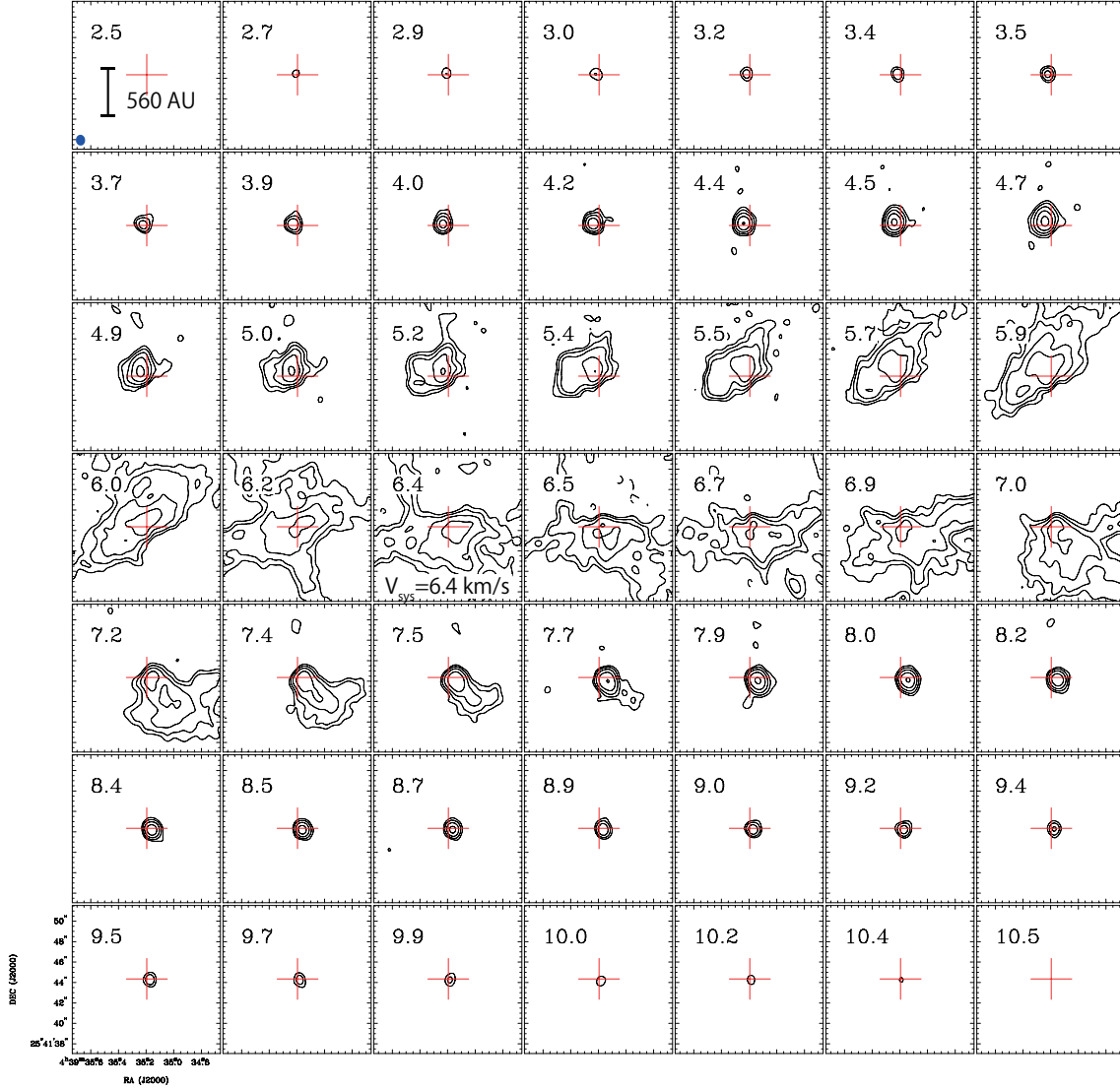


Figure 2.5 Channel maps of the $C^{18}O$ ($J = 2 - 1$) emission in TMC-1A. Contour levels are $-3, 3, 6, 12, 24, \dots \times \sigma$ where 1σ corresponds to $7.1 \text{ mJy beam}^{-1}$. Plus signs show the position of the central protostar (continuum emission peak). A filled ellipse in the top left panel denotes the ALMA synthesized beam; $1''.06 \times 0''.90$, P.A. = -176° . LSR velocities are shown at the top left corner of each panel, and the systemic velocity is 6.4 km s^{-1} .

2.5 ANALYSIS

2.5.1 C¹⁸O Velocity Gradient

As shown in the previous section, the C¹⁸O emission arising mainly from the flattened envelope of the TMC-1A protostar shows a very clear velocity gradient. In this section, the nature of the velocity gradient is investigated in more detail.

One remarkable characteristic of the velocity gradient is that its direction changes between high and low velocities, as shown in Figure 2.6. In order for us to investigate such a tendency more systematically (channel by channel), the mean position of the C¹⁸O emission at each channel is measured and plotted in Figure 2.7. The mean position is measured as $\mathbf{x}_0(v) = \int \mathbf{x}I(\mathbf{x}, v)d^2x / \int I(\mathbf{x}, v)d^2x$, where the sum is calculated with pixels having an intensity more than 6σ (σ is the rms noise level of C¹⁸O). For channels at $|\Delta V| < 0.5 \text{ km s}^{-1}$, the mean positions are not measured because very complex structures appear at those channels, such as the “X shape.” Points corresponding to higher velocities are plotted with smaller point sizes in Figure 2.7 and green points correspond to $|\Delta V| > 2.4 \text{ km s}^{-1}$. This figure demonstrates the difference between high and low velocities seen in Figure 2.6 more systematically, i.e., the mean positions for higher velocities are mostly along the major axis of the disk (dashed line, E-W) and near the center. Those for lower velocities depart from the major axis and are located far from the center. This displacement changes the direction of the velocity gradient between higher and lower velocities. Figure 2.7 suggests that the motion in the inner (high-velocity) part is dominated by rotation of the disk because the velocity gradient is almost along the major axis of the disk. In contrast to the motion in the inner part, the motion in the outer (low-velocity) part is considered to include additional motions to rotation, which give a tilt in the velocity gradient with respect to the disk major axis.

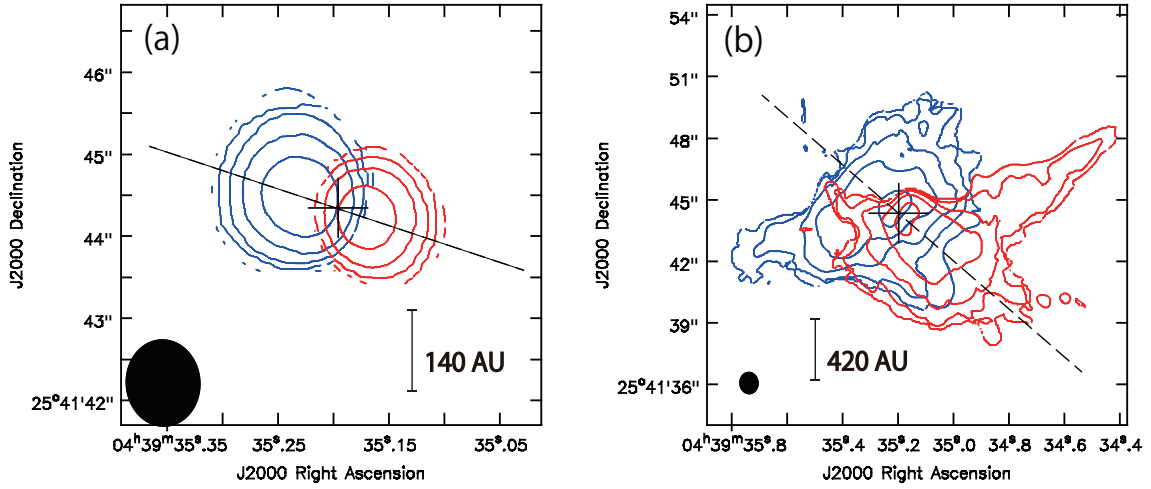


Figure 2.6 Maps of blueshifted (blue contours) and redshifted (red contours) emission of (a) high-velocity ($|\Delta V| > 2.0 \text{ km s}^{-1}$) and (b) low-velocity ($|\Delta V| < 1.0 \text{ km s}^{-1}$) components of C^{18}O ($J = 2 - 1$) emission in TMC-1A as observed with ALMA. Contour levels are $-2, 2, 4, 8, 16, 32 \times \sigma$ where 1σ corresponds to 2.9 and $4.1 \text{ mJy beam}^{-1}$ for (a) and (b), respectively. Plus signs in both panels show the position of the central protostar (continuum emission peak). Filled ellipses at the bottom left corner in both panels are the same in Figure 2.4. The dashed line passing peaks of blueshifted and redshifted maps in each panel shows the direction of the velocity gradient.

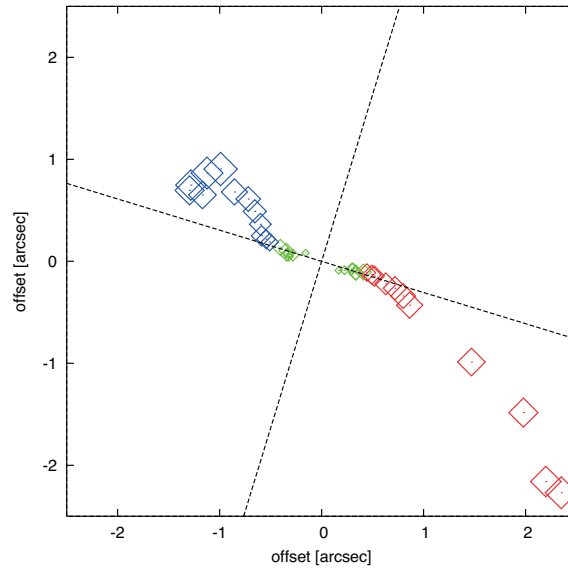


Figure 2.7 2D mean positions of the C^{18}O ($J = 2 - 1$) emission in TMC-1A. Each point indicates a 2D mean position at each channel weighted with the intensity and 6σ cutoff (σ is the rms noise level of C^{18}O emission). Error bars are not plotted but are smaller than the point size. Dashed lines show the major and the minor axis of the disk (73° and -17° , respectively) and the intersection is the position of the central protostar (continuum emission peak). The point size becomes smaller as the value of $|V - V_{\text{sys}}|$ becomes higher, and green points correspond to a velocity range of $|\Delta V| > 2.4 \text{ km s}^{-1}$.

In order for us to examine velocity gradients along the disk major axis in more detail, the PV diagram cutting along the disk major axis shown in Figure 2.8a is inspected here. This figure shows that the velocity gets higher as the position gets closer to the central star. As we discussed above, the PV diagram along the disk major axis is naturally considered to represent a velocity gradient due to rotation of the disk and/or the disk-like flattened envelope. There is a feature of the so-called spin-up rotation where emission peaks get closer to the central position (horizontal dashed line) as the velocity increases, while emission peaks depart from the center at low velocities. Keplerian rotation ($V_{\text{rot}} \propto R^{-1/2}$) is one form of spin-up rotation, and rotation that conserves its specific angular momentum ($V_{\text{rot}} \propto R^{-1}$) also shows a similar spin-up feature. However, it is generally not easy to distinguish such rotation patterns by comparing them with the PV diagram along the disk major axis. Further analysis to determine the powers of rotational velocity will be presented in the following section.

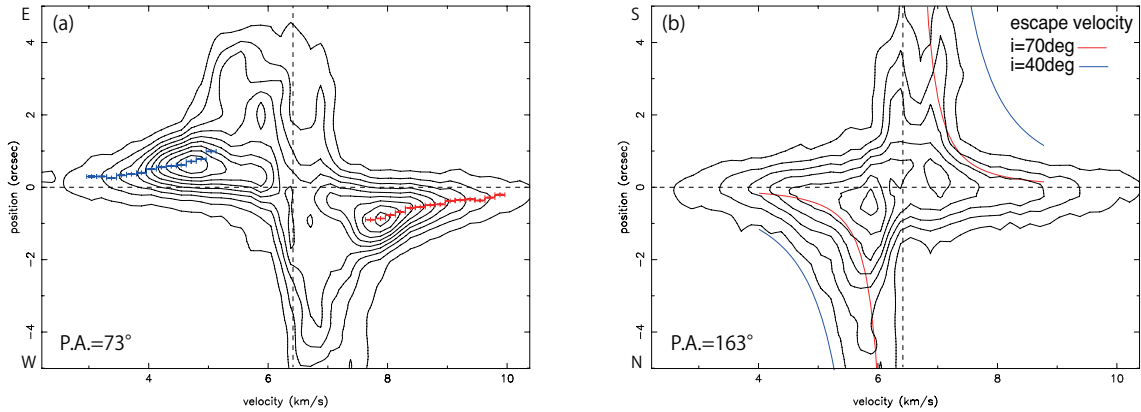


Figure 2.8 PV diagrams of the C^{18}O ($J = 2 - 1$) emission in TMC-1A along (a) the major axis and (b) the minor axis (the major axis corresponds to the white dashed line in Figure 2.1, PA = 73°). These PV diagrams have the same angular and velocity resolutions as those of the channel maps shown in Figure 2.5. Contour levels are 6σ spacing from 3σ ($1\sigma = 7.1 \text{ mJy beam}^{-1}$). Central vertical dashed lines show the systemic velocity ($V_{\text{sys}} = 6.4 \text{ km s}^{-1}$), and central horizontal dashed lines show the central position. Points with error bars in the panel (a) are mean positions derived along the position (vertical) direction at each velocity. Curves in the panel (b) show escape velocities along the outflow-axis direction for $i = 70^\circ$ and 40° .

2.5.2 Rotation Profile

In order for us to characterize the nature of the rotation, detailed analysis of the PV diagram is presented in this section. The nature of the rotation can be characterized by its rotation profile obtained from the PV diagram by measuring a representative position at each velocity channel in the diagram. The representative position at each velocity channel is defined as the 1D mean position weighted by the intensity, i.e., $x_m(v) = \int xI(x, v)dx / \int I(x, v)dx$, where the sum is done with pixels having an intensity more than 6σ (σ is the rms noise level of C¹⁸O). The measured mean positions are superposed on Figure 2.8a with error bars. The error bar along the direction of the position is derived by the fitting, while the one along the direction of the velocity is the velocity resolution of the C¹⁸O observations. The mean position is not measured at low velocities ($|\Delta V| < 1.2 \text{ km s}^{-1}$), where the emission shows extended structures, which is unsuitable for this analysis. We also note that a similar analysis was performed by Yen et al. (2013).

Figure 2.9 shows the mean positions of the PV diagram along the major axis on a $\log R - \log V$ diagram. The abscissa shows the mean positions measured as offset positions from the central protostar, which corresponds to the zero position on the PV diagram, assuming that the distance of TMC-1A is 140 pc. The ordinate is the relative-projected velocity assuming that the systemic velocity is 6.4 km s^{-1} . Because there is no systematic separation between the blue- and red-shifted components, we consider that the central position and the systemic velocity are plausible in order to measure the relative position and velocity. Figure 2.9 shows clear negative correlation between radius and velocity, demonstrating that the rotation velocity can be expressed as a power-law function of the radius (spin-up rotation). Importantly, there seems to be a break point at $R \sim 70 - 80 \text{ AU}$, where the power changes. We performed a χ^2 fitting to Figure 2.9 with a double power model as follows:

$$V_{\phi p}(R) = \begin{cases} V_b(R/R_b)^{-p_{\text{in}}} & (R \leq R_b) \\ V_b(R/R_b)^{-p_{\text{out}}} & (R > R_b) \end{cases}. \quad (2.1)$$

The powers, p_{in} and p_{out} , and the break point (R_b, V_b) are free parameters. The best-fit parameter set is $(R_b, V_b, p_{\text{in}}, p_{\text{out}}) = (67 \text{ AU}, 2.4 \text{ km s}^{-1}, 0.54 \pm 0.14, 0.85 \pm 0.04)$, where the errors for R_b and V_b are $\sim 1\%$, giving reduced $\chi^2 = 1.6$. Because this reduced χ^2 is close to the unity, we consider that the best fit is reasonable. The error of each parameter is derived by dispersing the data points randomly within the error bars of $\log R$ and $\log V$. We adopted a Gaussian distribution for the error of $\log R$ and a rectangular distribution for the error of $\log V$ because the error of $\log V$ is based on the velocity resolution of the observations. Another fitting to the mean positions is performed with a single power law. The best-fit parameter set for this single power law is $(R_b, p) = (64 \text{ AU}, 0.69 \pm 0.02)$, giving reduced $\chi^2 = 2.0$. In the single-power case, V_b is fixed at 2.4 km s^{-1} and (R_b, V_b) does not give a break. Although more parameters usually make a fitting better or χ^2 smaller, in our case, the best fit with a double power law provides a smaller “reduced” χ^2 than that with a single power law, even taking into account the difference in the number of parameters between two fittings (four for the double power law and two for the single power law). This suggests that the rotation profile of TMC-1A can be fitted with the double power law better than the single power law. The best-fit result suggests that the inner part and the outer part follow different rotation laws. The power of the inner part is roughly equal to $1/2$ for the case of Keplerian rotation, suggesting that the inner/higher-velocity part is dominated by Keplerian rotation. By contrast, the outer/lower-velocity part, showing a slope steeper than Keplerian, cannot be supported by rotation against the gravity yielded by the central protostar, as we will discuss later. It is interesting to note that p_{out} is equal to -0.85 , which is significantly different from -1 for the case where the specific angular momentum is conserved. This result could suggest that the specific angular momentum is proportional to $r^{0.15}$.

By using the break point $(R_b, V_b) = (67 \text{ AU}, 2.4 \text{ km s}^{-1})$, the dynamical mass of the central protostar and the specific angular momentum at R_b , which are not inclination corrected, can be calculated at $M_{*p} = M_* \sin^2 i = 0.43 M_\odot$ and $j_p = j \sin i = 7.7 \times 10^{-4} \text{ km s}^{-1} \text{ pc}$, respectively. We should note, however, that the analysis using certain

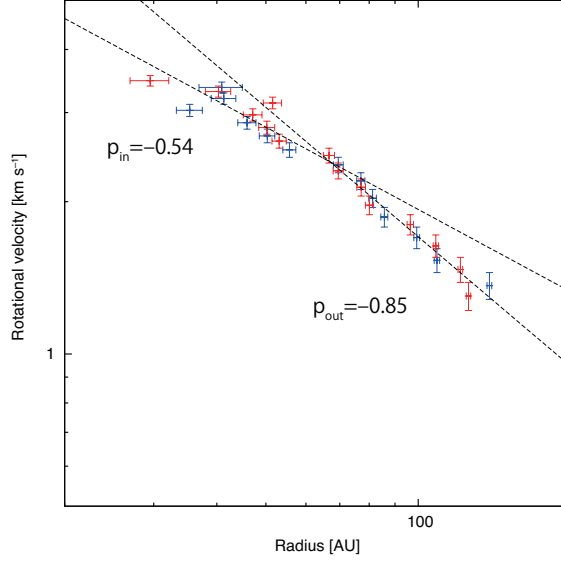


Figure 2.9 Mean positions of the PV diagram along the major axis plotted on $\log R - \log V$ plane. The ordinate is not deprojected. Blue and red points show blueshifted and redshifted components, respectively. Dashed lines show the best-fit lines with a double power law. In addition to the inner and outer power, the “break” radius and velocity are included as free parameters. The best-fit parameters are $R_b = 67$ AU, $V_b = 2.4$ km s $^{-1}$, $p_{\text{in}} = 0.54 \pm 0.14$, and $p_{\text{out}} = 0.85 \pm 0.04$. The error for (R_b, V_b) is $\sim 1\%$.

representative points on a PV diagram presented here may systematically underestimate R_b when the spatial resolution is not high enough, as discussed in Appendix 2.8.1. Taking this point into consideration, the real break radius can be estimated to be ~ 90 AU from the apparent break radius of 67 AU. $R_b \sim 90$ AU leads to $M_{*p} \sim 0.6 M_{\odot}$ and $j_p \sim 1 \times 10^{-3}$ km s $^{-1}$ pc.

2.5.3 Rotating Disk Models

In the previous section, the detailed analysis of the PV diagram cutting along the disk major axis was presented to characterize the nature of rotation, which suggests the existence of a Keplerian disk in the innermost part of the envelope. In this section, physical conditions of the Keplerian disk are investigated based on model fittings to the C 18 O channel maps. To quantify physical parameters of the disk around TMC-1A, we performed a χ^2 fitting to the C 18 O $J = 2 - 1$ channel maps based on a standard rotating disk model (e.g. Dutrey et al., 1994). When a standard disk model is compared with these observed C 18 O

channel maps, it is important to note that the observed C¹⁸O emission arises not only from the disk but also from the envelope having rotation and additional motions as discussed in Sec.2.5.1. Because of this, it is required that only the velocity channels where rotation is dominant should be used for comparison with a disk model. As shown in Figure 2.9, there is a velocity range showing the power-law index close to the Keplerian law, suggesting that the C¹⁸O emission in this range with $|\Delta V| > 2.4 \text{ km s}^{-1}$ is thought to arise from the possible Keplerian disk. We intend, therefore, to fit the channel maps within this velocity range, with rotating disk models.

We use a disk model with a code described in Ohashi et al. (2014). The model disk can be described with 10 parameters summarized in Table 2.2. The radial dependence of the disk temperature $T(R)$ and the disk surface density $\Sigma(R)$ are described as

$$T(R) = T_{100} \left(\frac{R}{100 \text{ AU}} \right)^{-q} \quad (2.2)$$

$$\Sigma(R) = \frac{(2-p)M_{200}}{2\pi(R_{\text{out}}^{2-p} - R_{\text{in}}^{2-p})} R^{-p} \quad (R < R_{\text{out}}), \quad (2.3)$$

where M_{200} is the mass within 200 AU (R_{out} will be fixed at 200 AU; see below for more details). The scale height of the disk $H(R)$ is given under the hydrostatic equilibrium condition as follows:

$$H(R) = \sqrt{\frac{2k_B T(R) R^3}{G m_0 M_{*p} / \sin^2 i}}, \quad (2.4)$$

where k_B , G , m_0 , and i are the Boltzmann constant, gravitational constant, mean molecular weight ($=2.37 m_H$), and inclination angle of the disk, respectively. In such a disk, its density distribution $\rho(R, z)$ is given as $\Sigma(R)/(\sqrt{\pi}H(R)) \exp(-z^2/H(R)^2)$, while the rotation profile of the disk is provided by

$$V_\phi(R) = \sqrt{\frac{GM_{*p} / \sin^2 i}{R_{\text{cent}}}} \left(\frac{R}{R_{\text{cent}}} \right)^{-v}, \quad (2.5)$$

Table 2.2. Fixed and free parameters of the model fitting (TMC-1A)

Fixed	i 65°	R_{in} 0.1 AU	R_{out} 200 AU				
Free	M_{*p} ^a	M_{200} ^b	p	T_{100}	q	R_{cent}	v
Best	$0.56^{+0.05}_{-0.05} M_{\odot}$	$3.6^{+1.5}_{-1.0} \times 10^{-3} M_{\odot}$	$1.46^{+0.3}_{-1.0}$	38^{+6}_{-5} K	$-0.02^{+0.04}_{-0.04}$	166^{+400}_{-120} AU	$0.53^{+0.05}_{-0.05}$

^a $M_{*p} = M_* \sin^2 i$, not inclination corrected.

^bThe mass within $R_{\text{out}} = 200$ AU. The mass of the Keplerian disk ($R_{\text{kep}} = 100$ AU) is calculated to be $2.5 \times 10^{-3} M_{\odot}$.

where R_{cent} is set to satisfy $V_{\phi}(R_{\text{cent}}) = \sqrt{GM_{*p}/\sin^2 i/R_{\text{cent}}}$ and gives a coefficient of the power law of $V_{\phi}(R)$. It is assumed that the turbulent line width is zero; that is, the profile function is defined by a thermal line width.

Among the 10 parameters, the first three parameters (i , R_{in} , R_{out}) are fixed, as shown in Table 2.2. Note that $R_{\text{out}}=200$ AU is assumed to cover a sufficiently large area for the fitting because our fitting to only the high-velocity inner part cannot constrain R_{out} well. In addition, $i = 65^\circ$ is also suitable to explain motions in the envelope, as discussed later in Sec.2.6.2. With the other seven free parameters (M_{*p} , M_{200} , p , T_{100} , q , R_{cent} , v), our model solves radiative transfers in 3D + velocity space to produce model channel maps (data cube). When solving the line transfers, we assume LTE and a typical abundance of C^{18}O relative to H_2 , $X(\text{C}^{18}\text{O}) = 3.0 \times 10^{-7}$. After solving the line transfers, model data cubes are convolved with the Gaussian beam, which has the same major axis, minor axis, and orientation as the synthesized beam of our observations. When the model is compared with the observations, the central position and the orientation (position angle, P.A.) of the disk are assumed to be the same as those of the continuum emission, and the systemic velocity is also assumed to be $V_{\text{sys}} = 6.4 \text{ km s}^{-1}$.

Reduced χ^2 is calculated to evaluate the validity of each model in the velocity range $|\Delta V| > 2.4 \text{ km s}^{-1}$. We use only pixels in channel maps (data cube) where observed emission is stronger than the 3σ level because if undetected pixels are included, where

noise is distributed around 1σ (reduced $\chi^2 \sim 1$), then the χ^2 value would be underestimated. We use the Markov Chain Monte Carlo method to find the minimum χ^2 efficiently.

Figure 2.10a shows the comparison of the best-fit disk model with the observations, and Figure 2.10b shows the residual obtained by subtracting the best-fit disk model from the observations. Reduced $\chi^2 = 0.72$ and Figure 2.10b indicate that our best-fit disk model reproduces, overall, the observations in the high-velocity region. The parameters of our best-fit disk model are summarized in Table 2.2. First of all, $v = 0.53$ suggests that the high-velocity component of C^{18}O emission from TMC-1A can be explained as a Keplerian disk better than other rotation laws, such as $V_\phi \propto R^{-1}$. Note that this power-law index is very consistent with p_{in} derived from the power-law fitting to the $\log R - \log V$ diagram in Sec.2.5.2. The central stellar mass (not inclination corrected) $M_{*p} = M_* \sin^2 i = 0.56 M_\odot$ is also consistent with that derived in Sec.2.5.2. With the best-fit M_{*p} , v , and $R_{\text{cent}} = 166 \text{ AU}$, the rotational velocity of our best-fit model is expressed as $1.5 \text{ km s}^{-1} (R/200 \text{ AU})^{-0.53}$. The mass within $R_{\text{out}} = 200 \text{ AU}$, $3.6 \times 10^{-3} M_\odot$ is similar to the total gas mass derived from the flux of C^{18}O , $M_{\text{gas}} = 4.4 \times 10^{-3} M_\odot$. With the best-fit M_{200} and $p = 1.46$, the surface density profile of our best-fit disk model is expressed as $0.069 \text{ g cm}^{-2} (R/200 \text{ AU})^{-1.46}$. The temperature seems roughly uniform ($q \simeq 0$) in our best-fit disk model. The temperature at the midplane can show such a radial profile when the inner region has a larger enough optical depth to cause a more effective cooling and a less effective heating by hot surface regions (Chiang & Goldreich, 1997). Another possibility is that the C^{18}O line traces a temperature at which C^{18}O molecules are evaporated off of dust grains.

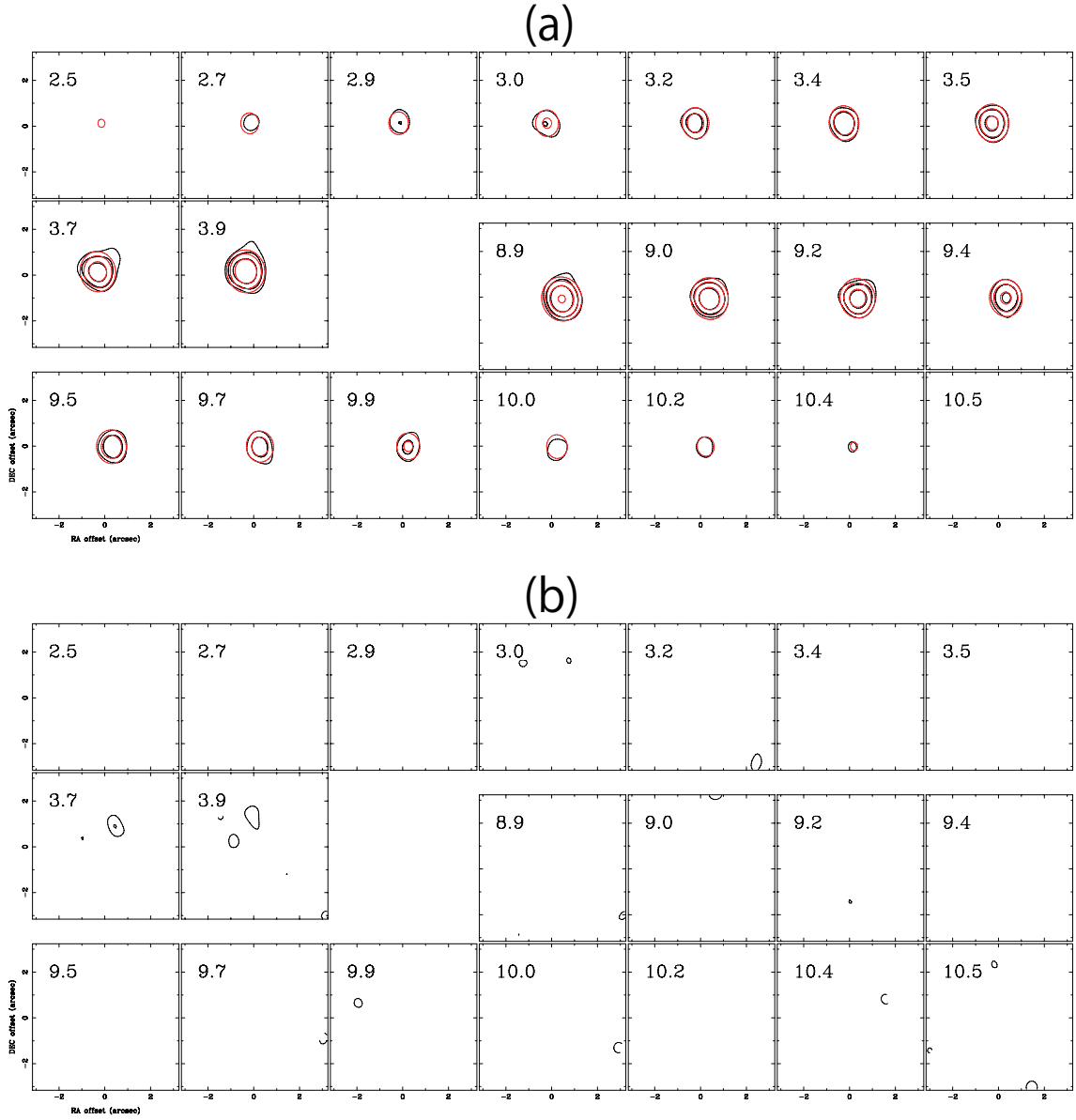


Figure 2.10 Channel maps, used in a χ^2 fitting with the rotating disk models of (a) the best-fit disk model (red contours) superposed on that of the observations of C^{18}O ($J = 2 - 1$) emission and (b) the residual obtained by subtracting the best-fit disk model from the observations. The systemic velocity is $V_{\text{LSR}} = 6.4 \text{ km s}^{-1}$. Contour levels are $-3, 3, 6, 12, 24, \dots \times \sigma$ where 1σ corresponds to $7.1 \text{ mJy beam}^{-1}$ for the panel (a) and $-3, -2, 2, 3, 4, \dots \times \sigma$ for the panel (b). The spatial scale is different from Figure 2.5.

The uncertainty of each parameter is defined by the range of the parameter where the reduced χ^2 is below the minimum plus one ($= 1.72$) when varying the parameter and fixing other parameters at those of the best-fit disk model. M_* and v , which are related to kinematics, have smaller uncertainty as compared to others. Another parameter related to kinematics, R_{cent} , has a large uncertainty because the rotational velocity is found to be close to the Keplerian rotation law.

It is important to investigate the effect of the inclination angle, which is fixed at $i = 65^\circ$ in our χ^2 fitting mentioned earlier. Figure 2.11 shows a distribution of the reduced χ^2 with different inclination angles of the disk. This plot is derived by changing the inclination angle i from 5° to 85° by 5° intervals, with the other parameters fixed at those of the best-fit disk model. Figure 2.11 shows that larger inclination angles between 45° and 75° give small reduced χ^2 , suggesting that it is difficult to give a constraint on the inclination angle in this model fitting. In Sec. 2.6.2, we examine the disk inclination angle further.

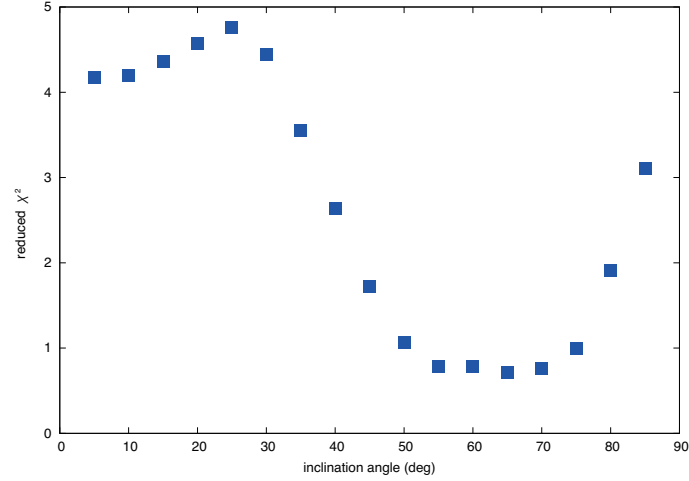


Figure 2.11 Distribution of the reduced χ^2 in terms of the inclination angle of the disk. All points have the same parameter set as the best-fit disk model except for the inclination angle. Larger inclinations ($45^\circ \leq i \leq 75^\circ$) give small reduced χ^2 (that is, good) models to explain the observations.

2.6 DISCUSSION

2.6.1 Velocity Gradient along the Disk Minor Axis

In the previous sections, detailed analyses of the motions for the inner part of the $C^{18}O$ envelope where rotation is dominant are presented, showing that there is a Keplerian disk at the innermost envelope. As shown in Sec. 2.5.1, the kinematics of the outer part of the envelope surrounding the Keplerian disk is described with not only rotation but also additional motions. In this section, the nature of the additional motions in the outer part of the envelope is discussed in detail.

There are two possibilities for the additional motions seen in the outer part. One is radial motion in the disk plane, and the other one is motion perpendicular to the disk plane. Either case is expected to form velocity gradients along the disk minor axis. In the latter case, outflowing motion going perpendicularly to the disk plane is the most natural one. On the other hand, in the former case, infalling motion or expanding motion in the disk plane can be considered, but these two can be distinguished from each other because the directions of their velocity gradients are opposite to each other. The geometry of the outflow having its blueshifted lobe located on the northern side of the central star tells us that the northern part of the disk plane is on the far side from the observers, while the southern part is on the near side. Since the northern part of the $C^{18}O$ emission is expected to have blueshifted emission, as mentioned in Sec. 2.4.2, the radial motion in the disk plane should be infall rather than expansion. Based on these considerations, the additional motion would be either an infall motion in the disk plane, an outflow motion going perpendicularly to the disk plane, or both.

The PV diagram along the disk minor axis shown in Figure 2.8b shows a velocity gradient with blueshifted and redshifted components located on the northern side and the southern side, respectively, at low velocities ($4.0 \text{ km s}^{-1} \lesssim V \lesssim 8.8 \text{ km s}^{-1}$). On the other hand, high-velocity ($V \lesssim 4.0 \text{ km s}^{-1}$, $8.8 \text{ km s}^{-1} \lesssim V$) components show

no significant velocity gradient along the disk minor axis, which is consistent with what was discussed with Figure 2.7. The velocity gradient seen at low velocities can be explained as either infall motion in the disk plane, outflow motion going perpendicularly to the disk plane, or both, as discussed above. It should be noted that a molecular outflow needs velocities sufficiently high enough to escape from the gravitational potential due to a central star. Such escape velocities are estimated as a function of the distance from the central star and are plotted in Figure 2.8b. When plotting the escape-velocity curves at the low velocities where there is a velocity gradient, the central mass (not inclination corrected) $M_{*p} = M_* \sin^2 i = 0.56 M_\odot$ was assumed based on the estimation of the dynamical central stellar mass (see Sec. 2.5.3). The inclination angle was also assumed to be $40^\circ < i < 70^\circ$ based on Chandler et al. (1996). Compared with the curve with $i = 70^\circ$, a part of the emission shows higher velocities than the escape velocities, suggesting an outflow motion. In fact, a part of the emission shown in channel maps (Figure 2.5) exhibits extensions or X-shaped structures, which spatially correspond to the molecular outflow traced by ^{12}CO . The significant part of the emission including the two peaks in Figure 2.8b, however, shows clearly slower velocities than the escape velocities. This suggests that the major part of the velocity gradient along the minor axis cannot be explained by outflow motions. We therefore consider that the velocity gradient along the disk minor axis in C^{18}O emission is mainly due to infall motion in the disk plane. Note that additional signature for the infall motion can be also seen in the major-axis PV diagram at lower velocities ($5.5 \text{ km s}^{-1} \lesssim V \lesssim 7.0 \text{ km s}^{-1}$): although the most of the blueshifted emission is located on the eastern side, a part of the blueshifted emission at lower velocities is located on the western side, and similarly a part of the redshifted emission at lower velocities is located on the side opposite to the western side, where the most of the redshifted emission is seen. These additional components in the diagram cannot be explained by rotation but can be explained by infall (e.g. Ohashi et al., 1997). In addition, we also note that L1551 IRS 5, a typical Class I protostar, also shows an infalling envelope with a velocity gradient along its disk minor axis (Momose et al., 1998). In the following subsections, details of

infall motions seen in C¹⁸O are discussed.

2.6.2 Nature of The Infall Motion

It is suggested that the inner high-velocity part of the C¹⁸O emission arises from a Keplerian disk and the parameters of the disk are derived by model fittings in Sec. 2.5.3. In addition to the rotation-dominant part, our results suggest that there is an infalling envelope surrounding the rotating disk. In order to investigate infall motions in the envelope, we make another model by adding an infalling envelope to the standard rotating disk model used in Sec. 2.5.3. Although the disk is basically described based on the best-fit disk model obtained in Sec. 2.5.3, it is necessary to define the transition radius between the disk and the infalling rotating envelope because the outer radius in the best-fit disk model is simply assumed to be 200 AU. A radius R_{kep} is set as a boundary between the infalling rotating envelope and the purely rotating disk. Within R_{kep} , all the parameters are the same as the best-fit disk model obtained in Sec. 2.5.3, except for the inclination angle (i), which was not fully determined in Sec. 2.5.3. The velocity field of the outer part ($R > R_{\text{kep}}$) is described as follows:

$$V_{\phi}(R) = V_{\phi}(R_{\text{kep}}) \left(\frac{R}{R_{\text{kep}}} \right)^{-v_{\text{out}}}, \quad (2.6)$$

$$V_r(r) = \alpha \sqrt{\frac{2GM_{*p} / \sin^2 i}{r}}. \quad (2.7)$$

Note that we distinguish the axial radius $R = \sqrt{x^2 + y^2}$ and the spherical radius $r = \sqrt{x^2 + y^2 + z^2}$ by using big and small letters, respectively. The infall-velocity vector points to the center, and the infall velocity $V_r(r)$ depends on z while the rotation velocity $V_{\phi}(R)$ does not depend on it. $V_{\phi}(R_{\text{kep}})$ is the rotation velocity at R_{kep} and is assumed to connect continuously to that of the inner disk. The infall velocity is set as a product of a constant coefficient α and the free-fall velocity. In terms of the geometry of the infalling envelope, we basically consider a flattened structure because of the shape of the C¹⁸O

integrated-intensity map (Figure 2.4). This flattened geometry of the infalling envelope is modeled by extrapolating the density and temperature structures from the inner disk ($R < R_{\text{kep}}$) to the outer radius of 900 AU, which is larger than the size of the C^{18}O integrated-intensity map. Hereafter, the models with a flattened envelope are called FE models.

It is important to note that in Sec. 2.5.3 the rotating disk models are fitted to the C^{18}O channel maps at higher velocities, while such fittings are not performed here. This is because models including the infalling envelope must be compared with the channel maps not only at higher velocities but also at lower velocities with complicated asymmetric structures. Such structures cannot be fitted by our simple axisymmetric models. For this reason, in this section we examine whether our models can reproduce the observed PV diagrams cutting along the major and minor axes (Figure 2.8), by comparing the following two parameters between them: (1) the mean position in the major-axis PV diagram measured in Section 2.5.2 (Figure 2.8a and Figure 2.9) and (2) the position of two peaks in the minor-axis PV diagram (Figure 2.8b). The first depends on the rotation velocity, while the second depends on the infall velocity within the disk plane.

It is also noted that the surface density of the envelope at radii more than 200 AU is reduced by a factor of two to reproduce relatively diffuse emission seen in PV diagrams at positions larger than $\sim 2''$. Because extended structures more than $\sim 8''$ are resolved out in our ALMA observations by 50%, we use the CASA task *simobserve* to include the spatial filtering. The synthesized beam derived with *simobserve* ($1''.03 \times 0''.81, -7.2$) is not exactly the same as that of the observations even though the same antenna positions and hour angles are configured. However, the difference is small, and there is no impact on our analysis.

Four parameters of the model mentioned above, v_{out} , R_{kep} , α , and the inclination angle of the disk i are changed to reproduce the observed PV diagrams. Figure 2.12 shows the comparison of different models (FE model A-F) and the observations. The FE model A is the case with $(v_{\text{out}}, R_{\text{kep}}, \alpha, i) = (0.85, 100 \text{ AU}, 0.3, 65^\circ)$. This FE model A can

reproduce both PV diagrams, whereas the other five models cannot reproduce either of them, as explained in detail below. Hereafter, we call the FE model A the “best-infall model”. We emphasize that the infall velocity is significantly smaller than the free-fall velocity in the best-infall model. More details of the slow infall velocity are discussed later.

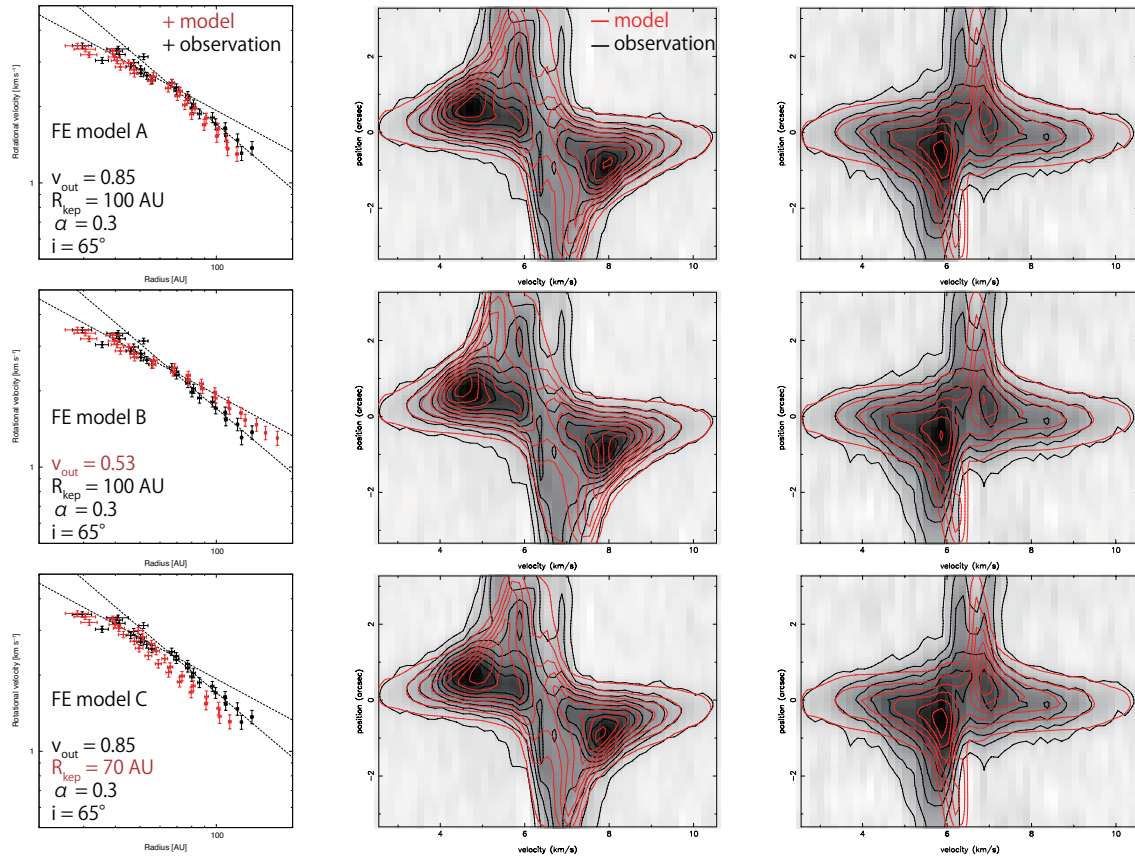


Figure 2.12 Comparisons of the observations and models with infall motions. The left column shows the mean position of the PV diagram along the major axis in $\log R - \log V$ diagrams. Red points indicate models, while black points indicate the observation, which is the same plot as Figure 2.9 except for the color. The middle and right columns show PV diagrams along the major and minor axis, respectively. The observations are in black contours and grayscales, while models are in red contours. Contour levels of the PV diagrams are the same as Figure 2.8. The same row includes the same model, and the parameters of each model are indicated in the left panel of each model. FE model A explains the observations most reasonably.

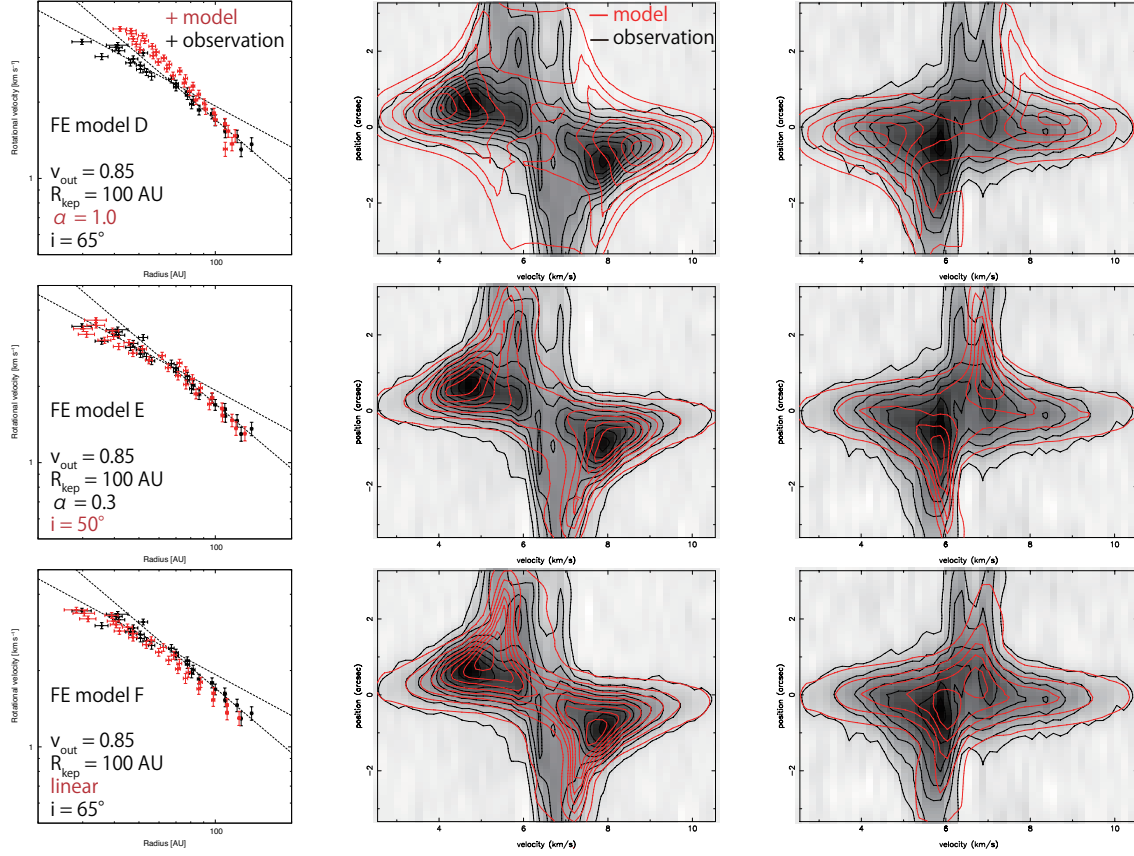


Figure 2.12 (Continued)

FE models B and C, which have a shallower v_{out} and a smaller R_{kep} , respectively, as compared with FE model A, show a clear difference in the $\log R - \log V$ diagram. The mean positions derived from FE model B are located above the observations in $R \gtrsim 70$ AU. On the other hand, the mean positions of FE model C clearly show smaller radii than the observations in $R \gtrsim 50$ AU.

FE models B and C exhibit similar PV diagrams along the minor axis to that of FE model A. However, FE models D and E, which have a larger infall velocity and a smaller inclination angle, respectively, as compared with FE model A, show a clear difference in the minor-axis PV diagram. The two peaks of FE model D show a clear offset from the observations along the “velocity” axis in the PV diagram. In addition, the $\log R - \log V$ diagram of FE model D is significantly different from the observations, in the sense that velocities at radii less than ~ 80 AU become larger than the observations, which can be

also seen in the major-axis PV diagram, where the two peaks in the model have larger velocities than the observations. On the other hand, the two peaks in the minor-axis PV diagram of FE model E show a clear offset along the “position” axis in the PV diagram.

The fact that FE model B, where the outer and inner power-law indices are the same as 0.53, cannot reproduce the observations indicates that the power-law index of the rotational velocity in the outer region is steeper than that in the inner region. The discrepancy between the observations and the FE model C with $R_{\text{kep}} = 70$ AU, at which the observed rotation profile appears to break, indicates that R_{kep} should be larger than the apparent breaking radius, as also discussed in Appendix 2.8.1 (see also Sec. 2.5.2). The discrepancy between the observations and FE model D, where the infall velocity is free-fall velocity, indicates that the infall velocity in the envelope should be smaller than the free-fall velocity. The fact that the FE model E with $i = 50^\circ$ cannot reproduce the observations indicates that the inclination angle of the disk is larger than $i = 50^\circ$. Although the inclination angle is not well constrained with the disk model, as shown in Sec. 2.5.3, it is constrained better in FE models because the peak positions in the minor-axis PV diagrams are sensitive to the inclination angle.

In addition, the power-law dependence of the infall velocity is investigated. Although, in FE model A, a conventional infall velocity law with the power-law index -0.5 is assumed, it would be possible that infall motions are decelerated and cease at the boundary radius because the inner region shows Keplerian rotation and no infall motion. Thus, we make FE model F with the same parameters as FE model A except for the infall velocity, which is linearly decelerated $V_r(r) = a(r - R_{\text{kep}})$ ($R > R_{\text{kep}}$), where a is a constant coefficient and set to be $a = 1.6 \times 10^{-3} \text{ km s}^{-1} \text{ AU}^{-1}$. Overall velocity structures seen in both PV diagrams made from FE model F seem to be consistent with the observations, even though the peaks in the minor-axis PV diagram of this FE model F are located at a smaller velocity than the observations and the two peaks are almost merged. This would suggest that the infall velocity may decelerate, although such a deceleration can happen only at the innermost region of an envelope.

From the parameters of the best-infall model, i.e., FE model A, $(v_{\text{out}}, R_{\text{kep}}, \alpha, i) = (0.85, 100 \text{ AU}, 0.3, 65^\circ)$, the infall velocity and mass infall rate \dot{M} can be estimated. First, the inclination-corrected central stellar mass is calculated at $M_* = 0.68 M_\odot$ from the inclination $i = 65^\circ$ and the best-fit $M_{*p} = M_* \sin^2 i = 0.56 M_\odot$ (best-fit disk model in Sec.2.5.3). Thus, from $\alpha = 0.3$, the infall velocity is estimated at $V_r = 0.74 - 1.04 \text{ km s}^{-1}$ at $R = 100 - 200 \text{ AU}$. Using the surface density of the best-infall model, the mass infall rate is estimated as

$$\dot{M} = 2\pi R V_r \Sigma = (1.5 - 3.0) \times 10^{-6} M_\odot \text{ yr}^{-1} (R = 100 - 200 \text{ AU}). \quad (2.8)$$

This value is comparable with a typical mass infall rate of protostars (e.g. Ohashi et al., 1997) and the mass flow rate $\dot{M}_{\text{flow}} = 1.5 \times 10^{-6} M_\odot \text{ yr}^{-1}$ of TMC-1A estimated by an observation of the molecular outflow (Chandler et al. 1996). The inclination-corrected central stellar mass $M_* = 0.68 M_\odot$ and the boundary radius $R_{\text{kep}} = 100 \text{ AU}$ also give us a specific angular momentum at the outer radius of the Keplerian disk, $j = 1.2 \times 10^{-3} \text{ km s}^{-1} \text{ pc}$, which is consistent with the specific angular momentum at 580 AU, $j = 2.5 \times 10^{-3} \text{ km s}^{-1} \text{ pc}$ within a factor of two (Ohashi et al., 1997). From $R_{\text{kep}} = 100 \text{ AU}$, the disk mass can be calculated to be $M_{\text{disk}} = \int \Sigma 2\pi R dR = 2.5 \times 10^{-3} M_\odot$, as well.

One might wonder whether a spherical geometry of the infalling envelope could explain the observations better, including the slower infalling velocities, even though the envelope has a flattened structure as shown in Sec. 2.4.2. We therefore consider models with a spherical envelope having bipolar cavities in addition to FE models discussed above as shown in Appendix 2.8.2. It is found that models with a spherical envelope cannot explain the observations better than FE models. More importantly, even if we adopt a model with a spherical envelope, the infall velocity should be significantly slower than the free-fall velocity. In addition, it might be possible that power-law index q for the temperature distribution in an envelope is not the same as that in a disk. A smaller value of q , i.e., -0.5 , is examined in the model, and it is found that it does not significantly change

the results discussed above.

2.6.3 Magnetic Pressure and Tension

In previous sections, we suggest that the infall velocity in the envelope around TMC-1A is ~ 0.3 times as large as the free-fall velocity, V_{ff} , yielded by the stellar mass, which is estimated from the Keplerian rotation. The slow infall velocity suggests the possibility that infalling material is supported by some kind of force against the pull of gravity. One possible mechanism is the magnetic effect. Dense cores where protostars form tend to have oblate shapes perpendicular to their associated magnetic fields. (e.g., NGC 1333 IRAS 4A; Girart et al., 2006). Thus, it is assumed that envelopes around protostars should also be penetrated by magnetic fields, and the magnetic force (pressure and tension) possibly slows infall motions. In this section we discuss whether the magnetic field expected to be associated with the envelope around TMC-1A can actually make the infall velocity as small as $0.3 V_{\text{ff}}$. Note that all the physical quantities in the following discussion are derived at a radius of 200 AU, which is rather arbitrary. The same estimations are also done at radii of 100 and 300 AU, providing results similar to that at 200 AU.

The magnetic flux density required to make the infall velocity as small as $0.3V_{\text{ff}}$ is estimated from the equation of motion including magnetic fields described below under a symmetric condition of $\partial/\partial\theta = 0$ and $\partial/\partial z = 0$ on the midplane:

$$\rho(R)V_r(R)\frac{dV_r}{dR} = -\frac{GM_*\rho(R)}{R^2} - \frac{1}{2\mu_0}\frac{dB^2}{dR} + \frac{B(R)^2}{\mu_0 R_{\text{curv}}(R)}, \quad (2.9)$$

where $\rho(R)$ and $V_r(R)$ indicates radial dependence of the mass density and infall velocity in the midplane of the envelope, respectively, whereas $R_{\text{curv}}(R)$ is the radial dependence of the curvature of magnetic field lines. μ_0 indicates the magnetic permeability in a vacuum. The second and third terms on the right-hand side indicate the magnetic pressure and the magnetic tension, respectively. A steady state is assumed here, and the gas and radiation pressures are ignored because they are too weak to support material against gravity

(i.e., the thermal energy is smaller than the gravitational potential by orders of magnitude at ~ 200 AU).

Although we do not know the configuration of magnetic fields around TMC-1A, it is reasonable for our order estimation to assume that R_{curv} is roughly equal to the scale height H , which is a typical spatial scale in the disk-like envelope. We also assume $B \propto \rho^{2/3}$, which corresponds to the case where gases spherically symmetrically collapse with magnetic fields. Then, with $\rho(R)$ and $V_r(R)$ derived from the best-infall model discussed in the previous section, the magnetic flux density required for $V_r = 0.3V_{\text{ff}}$ is estimated to be $B \sim 2$ mG. The magnetic flux density on the order of mG is somewhat larger than the typical value from Zeeman observations ($\lesssim 100 \mu\text{G}$). However, the Zeeman observations using a high-density tracer such as CN give us higher values, $\lesssim 1$ mG (Crutcher et al., 2010). In addition to single-dish observations, observations using SMA by Girart et al. (2006) toward NGC 1333 IRAS 4A at $\sim 1''$ angular resolution estimated the magnetic field strength in the plane of the sky to be $B_{\text{POS}} \sim 5$ mG by applying the Chandrasekhar-Fermi equation. These observations (see also Falgarone et al., 2008; Stephens et al., 2013) suggest that the magnetic field strength around TMC-1A can be possibly on the order of mG.

2.6.4 A Possible Scenario of the Keplerian Disk Formation

Over the past decade the number of protostellar sources associated with Keplerian disks has been increased with (sub)millimeter interferometric observations (see Table 3), and it is getting more feasible for us to discuss evolutionary processes of Keplerian disks around protostars based on these observations (e.g. Chou et al., 2014). We should, however, note that disk radii measured from such observations are subject to serious ambiguity, because the measured radii are likely affected by the effects of the sensitivity limits and the missing fluxes of the interferometric observations. In particular, some of these observations did not identify the transition from infalling motions to Kepler motions (see Column 9 in Table 3),

so that the estimated disk radii measured from such observations should be lower limits to the actual disk radii (see more details below). Indeed, Chou et al. (2014) attempted to discuss evolutionary processes of Keplerian disks around protostellar sources with those samples, but they could not identify any clear correlations and evolutionary sequences of the disks.

On the other hand, our series of ALMA observations of protostellar sources, L1527 IRS by Ohashi et al. (2014), TMC-1A in the present work, and L1489 IRS by Yen et al. (2014), all identified the transitions from infalling envelopes to disks and measured the power-law indices of the rotational profiles to verify that the disks are indeed in Keplerian rotation. In such observations, the disk radii are estimated better. Furthermore, recent high-resolution interferometric observations of L1551 NE (Takakuwa et al., 2014), L1551 IRS 5 (Chou et al., 2014), and VLA 1623A (Murillo et al., 2013) have also revealed transitions from infalling motions to Keplerian rotations. These observational results imply that transitions from infall motions to Keplerian rotations are ubiquitous in the protostellar phase. Statistical studies of such systems should provide important observational constraints on the ongoing growth process of Keplerian disks. Here, with our ALMA results, along with the other observational results showing transitions from infalling envelopes to Keplerian disks, we reexamine evolutionary processes of Keplerian disks around protostellar sources embedded in infalling envelopes.

In the following discussion, the bolometric temperature (T_{bol}) and the ratio of the bolometric to submillimeter luminosity ($= L_{\text{bol}}/L_{\text{submm}}$) are adopted as parameters tracing the evolution of protostars (Green et al., 2013). Figure 2.13 shows correlations between T_{bol} vs the central protostellar masses ($= M_*$), $L_{\text{bol}}/L_{\text{submm}}$ vs M_* , and M_* vs the radii of the Keplerian disks ($= R_{\text{kep}}$) for the protostellar sources associated with the Keplerian disks listed in Table 3. Note that the protostellar sources “with transitions” showing transitions from infall to Keplerian and “without transitions” are indicated with different marks. The sources with transitions exhibit correlations in all the T_{bol} vs M_* , $L_{\text{bol}}/L_{\text{submm}}$ vs M_* , and M_* vs R_{kep} plots, with the correlation coefficients of 0.97, 0.95, and 0.91, respectively.

The correlation coefficient for M_* vs R_{kep} will be 0.98 if assuming that VLA 1623A has $R_{\text{kep}} = 50$ AU, at which its rotational velocity profile shows a turnover point (Murillo et al., 2013). These results may suggest that the central protostellar masses increase as the protostellar evolution proceeds, and that the disk radii also grow as the central protostellar masses grow, although statistical significances are not high because the number of samples is small. On the other hand, inclusion of all the sample points almost diminishes the correlation in M_* vs R_{kep} with the correlation coefficient of 0.29. This poor correlation may be because R_{kep} is not measured accurately for the cases without transitions. The correlation between $L_{\text{bol}}/L_{\text{submm}}$ and M_* is not diminished (the correlation coefficient is 0.77) because measuring M_* does not depend on whether there is a transition, although the correlation of T_{bol} vs M_* is poor when all the samples are included (the correlation coefficient is 0.43). These results demonstrate that proper observational estimates of the central protostellar masses and the disk radii are essential to discuss evolutions of the protostars and disks.

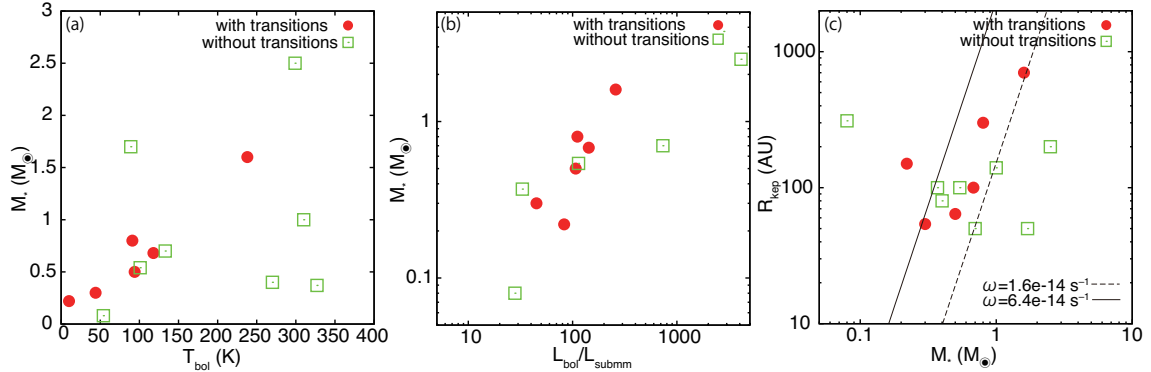


Figure 2.13 Correlation between (a) bolometric temperatures and central protostellar masses, (b) $L_{\text{bol}}/L_{\text{submm}}$ and central protostellar masses, and (c) central stellar masses and sizes of Keplerian disks around protostars. The data values are listed in Table 2.3. Red filled circles correspond to the protostars for which the transitions from infall motions to Keplerian rotations are identified well.

Table 2.3. Parameters of Keplerian disks around protostars

Source	$L_{\text{bol}} (L_{\odot})$	$T_{\text{bol}} (\text{K})$	$L_{\text{bol}}/L_{\text{submm}}^{\text{a}}$	$R_{\text{kep}} (\text{AU})^{\text{b}}$	$M_{*} (M_{\odot})^{\text{c}}$	$M_{\text{disk}} (M_{\odot})^{\text{d}}$	Class	Transition? ^e	References
NGC 1333 IRAS 4A2	1.9 ^f	51 ^f	28 ^f	310	0.08	...	0	no	1
VLA 1623A	1.1	10	83	150 ^g	0.22	...	0	yes	2,13
L1527 IRS	1.97	44	45	54	0.30	0.0028-0.013	0	yes	3,12,16
R CrA IRS 7B	4.6	89	...	50	1.7	0.024	I	no	4
L1551 NE	4.2	91	111	300	0.8	0.026	I	yes	5,14,17
L1551 IRS 5	22.1	94	107	64	0.5	0.07	I	yes	6,12,16
TMC1	0.9	101	114	100 ^h	0.54	0.025-0.06	I	no	7,12,16
TMC-1A	2.7	118	143	100	0.68	2.5×10^{-3}	I	yes	8,12,16
TMRI	2.6	140	734	50	0.7	0.01-0.015	I	no	7,16
L1489 IRS	3.7	238	259	700	1.6	$3-7 \times 10^{-3}$	I	yes	9,15,16
L1536	0.4	270	...	80	0.4	0.07-0.024	I	no	7,12
Elias 29	14.1	299	4215	200	2.5	$\lesssim 7 \times 10^{-3}$	I	no	10,12,16
IRS 43	6.0	310	...	140	1.0	8.1×10^{-3}	I	no	11,15
IRS 63	1.0	327	33	100	0.37	0.055	I	no	10,12,16

Table 2.3 (cont'd)

Source	$L_{\text{bol}} (L_{\odot})$	$T_{\text{bol}} (\text{K})$	$L_{\text{bol}}/L_{\text{submm}}^{\text{a}}$	$R_{\text{kep}} (\text{AU})^{\text{b}}$	$M_{*} (M_{\odot})^{\text{c}}$	$M_{\text{disk}} (M_{\odot})^{\text{d}}$	Class	Transition? ^e	References
--------	------------------------------	-----------------------------	--	---	--------------------------------	--	-------	--------------------------	------------

^a L_{submm} is defined as the luminosity measured at wavelengths longer than 350 μm .

^bOuter radius of the Keplerian disk.

^cCentral protostellar mass.

^dMass of the Keplerian disk.

^eFrag showing whether or not sources show transitions from infall motions to Keplerian rotations. “Yes” and “no” indicate sources with and without transitions, respectively.

^fBoth L_{bol} and L_{sub} are assumed to be a half of those derived toward the IRAS 4A binary system. T_{bol} is also assumed to be the same as that of the binary system.

^gMurillo et al. (2013) concluded that the Keplerian radius of VLA 1623A is 150 AU, although their UV-space PV diagram shows a turnover point of the rotational velocity profile at 50 AU. They argued that R_{kep} can be larger than 50 AU because of optical depth and absorption.

^hThe analysis using $\log R - \log V$ diagram gives us a breaking radius of ~ 90 AU. The results here are, however, not affected significantly even if 90 AU is adopted instead of 100 AU.

References: (1) Choi et al. 2010; (2) Murillo et al. 2013; (3) Ohashi et al. 2014; (4) Lindberg et al. 2014; (5) Takakuwa et al. 2014; (6) Chou et al. 2014; (7) Harsono et al. 2014; (8) this work; (9) Yen et al. 2014; (10) Lommen et al. 2008; (11) Eisner 2012; (12) Kristensen et al. 2012; (13) Murillo & Lai 2013; (14) Froebrich 2005; (15) Jørgensen et al. 2009; (16) Green et al. 2013; (17) Froebrich 2005

A simple interpretation of the positive correlation between M_* and R_{kep} is given by a conventional analytical picture of disk formation with “inside-out collapse” of envelopes, where the specific angular momenta increase linearly at outer radii (i.e., rigid-body rotation; Terebey et al., 1984; Shu et al., 1987; Yen et al., 2013). At the onset of the collapse, only the central part of the envelope with less angular momentum falls toward the center, and thus the mass of the protostellar source and the radius of the Keplerian disk are smaller. As the collapse proceeds outward, more material with larger angular momenta will be carried into the central region, raising the protostellar mass and radius of the Keplerian disk. In this picture, the dependence of R_{kep} on t (time) and M_* can be expressed as shown in Yen et al. (2013):

$$R_{\text{kep}} = \frac{\omega^2 r_{\text{inf}}^4}{GM_*(r_{\text{inf}})} = \frac{\omega^2 G^3 \dot{M}^3}{16c_s^8} t^3 = \frac{\omega^2 G^3}{16c_s^8} M_*^3, \quad (2.10)$$

where ω and c_s denote the angular velocity and the sound speed of the envelope, respectively, r_{inf} is the outermost radius of the infalling region, and \dot{M} is the mass infalling rate. A typical value of ω has been estimated as $\omega \sim 1 \text{ km s}^{-1} \text{ pc}^{-1} = 3.2 \times 10^{-14} \text{ s}^{-1}$ (Goodman et al., 1993). In Figure 2.13b lines of Eq.(2.10) with twice and half of the typical value of ω are drawn, with $c_s = 0.19 \text{ km s}^{-1}$ (i.e., $T_k = 10 \text{ K}$). Almost all the sources with transitions are within the area expected from Eq. 2.10, suggesting that the identified positive correlation between M_* and R_{kep} can be reproduced with the picture of the conventional analytical disk formation model with inside-out collapse.

More realistically, effects of magnetic fields on disk formation and growth, which are ignored in the model described above, must be taken into account (Li et al., 2014; Machida et al., 2014). Our ALMA observations of TMC-1A and L1527 IRS have found that the infalling velocities are a factor of a few slower than the corresponding free-fall velocities derived from the central protostellar masses, while in L1489 IRS the infalling velocity is consistent with the free-fall velocity. As discussed in the previous section, the slow infall velocities might be due to magnetic fields, while in the case of L1489 IRS, the magnetic

field may not be effective any more because the surrounding envelope that anchors the magnetic field is almost dissipated in the late evolutionary stage (Yen et al., 2014). The latest theoretical simulations by Machida & Hosokawa (2013), which include magnetic fields, have successfully demonstrated the growth of protostars and disks, as well as the deceleration of infall and the dissipation of envelopes in the late evolutionary stage. Their models also predict that, in the last phase of evolutionary stage, the growth of the central Keplerian disk stops while the protostellar mass itself is still growing (Visser et al., 2009; Machida & Hosokawa, 2013; Machida et al., 2014). Currently our observational samples do not show any clear evidence for such a saturation of the disk radius. Future large-scale ALMA surveys of a number of protostellar sources may reveal such a saturation, and a comprehensive observational picture of disk formation and growth around protostellar sources.

2.7 CONCLUSIONS

Using ALMA in Cycle 0, we observed a Class I protostar in Taurus star-forming region TMC-1A in the 1.3 mm dust continuum, ^{12}CO ($J = 2 - 1$), and C^{18}O ($J = 2 - 1$) lines. The main results are summarized below.

1. The 1.3 mm dust continuum shows a strong compact emission with a weak extension to the west. The gas mass of the dust emission is estimated from its flux density to be $M_{\text{dust}} = 4.2 \times 10^{-2} M_{\odot}$ assuming an opacity $\kappa_{1.3 \text{ mm}} = 1.2 \text{ cm}^2 \text{ g}^{-1}$, $T_c = 28 \text{ K}$, and a gas/dust mass ratio of 100, which is ten times larger than the gas mass estimated from the C^{18}O flux.

2. The ^{12}CO line traces the molecular outflow with the axis perpendicular to the elongation of the 1.3 mm continuum emission. Velocity gradients are seen both along and across the outflow axis. The velocity is accelerated along the outflow axis (Hubble law). Across the outflow axis, the higher-velocity component is located closer to the axis, which can be explained by an outflow driven by a parabolic wide-angle wind.

3. The C^{18}O emission shows the velocity gradient along the major axis of the disk traced in the 1.3 mm continuum emission. This velocity gradient is due to rotation. The power-law indices of the radial profile of the rotation velocity are estimated from fittings to the major-axis PV diagram to be $p_{\text{in}} = 0.54$ for the inner/high-velocity component and $p_{\text{out}} = 0.85$ for the outer/low-velocity component. This indicates the existence of the inner Keplerian disk surrounded by the outer infalling envelope.

4. In order to investigate the nature of the Keplerian disk, χ^2 fittings are performed to the C^{18}O channel maps at high velocities with the rotating disk models. In the model fitting, the power-law index of the rotational velocity (v) is included as a free parameter. The reduced χ^2 is minimized at $v = 0.53$, which is very consistent with p_{in} , and confirms that the rotational velocity at high velocities can be explained by Keplerian rotation. The dynamical mass (not inclination corrected) derived from our best-fit disk model is $M_* \sin^2 i = 0.56 M_{\odot}$.

5. In addition to the velocity gradient along the major axis, there is another velocity gradient along the minor axis, which can be interpreted as infalling motions. In order to investigate the nature of the infall motion, the observed PV diagrams along both major and minor axes are compared with models consisting of an infalling envelope and a Keplerian disk. The Keplerian disk size and the inclination angle are estimated to be 100 AU and $i = 65^\circ$, respectively, and the infall velocity is found to be 0.3 times as large as the free-fall velocity yielded by the dynamical mass of the central protostar. Possible reasons for the infall motions to be slower than the free-fall velocity are magnetic pressure and magnetic tension. The magnetic field strength yielding the slow infall velocity is estimated to be ~ 2 mG.

6. Based on observations, including our series of ALMA observations, which show transitions from infalling envelopes to Keplerian disks, evolutionary processes of Keplerian disks around protostellar sources are examined. Those samples exhibit correlations in T_{bol} vs M_* , $L_{\text{bol}}/L_{\text{submm}}$ vs M_* , and M_* vs R_{kep} . This may suggest that the central protostellar masses and disk radii increase as protostellar evolution proceeds.

2.8 APPENDIX

2.8.1 Analytic Consideration of Our Method to Derive Rotational Profiles from Observed PV Diagrams

In section 2.5.2 we adopted two independent methods to derive the rotational profile of the disk around TMC-1A; one is a method using the observed PV diagram along the major axis introduced by Yen et al. (2013), and the other is a full three-dimensional χ^2 fitting of a rotating disk model to the observed C^{18}O channel maps in the high-velocity ($> 2.4 \text{ km s}^{-1}$) regions. The former method yields the rotational profile of $2.4 (\text{km s}^{-1}) \times (R/67 \text{ AU})^{-0.54 \pm 0.03}$, and the latter $2.4 (\text{km s}^{-1}) \times (R/87 \text{ AU})^{-0.53 \pm 0.1}$. Thus, while the derived rotational power-law indices are consistent with each other and suggest Keplerian rotation, the rotational radius at a certain velocity derived from the former method is $\sim 23\%$ lower than that from the latter method. This implies that the former method underestimates the central stellar mass and the rotational angular momentum by $\sim 23\%$. In this appendix, these uncertainties inherent in the method using the PV diagrams are analyzed. For simplicity, we consider a geometrically thin, uniform disk with a pure rotational motion and discuss the effects of the finite velocity and spatial resolutions. The effect of the internal gas motion in the disk can be absorbed into the effect of the finite velocity resolution. We do not consider any radial motion in the disk here, since the effects of the radial motions on the estimates of the rotational profiles have already been discussed by Yen et al. (2013).

The on-plane coordinates of the model disk are described with the 2D polar coordinates system (R, ϕ) and the projected coordinates on the plane-of-the-sky 2D Cartesian (x, y) , where the x -axis is defined as the major axis of the ellipse of the disk projected on the sky. The disk inclination angle from the plane of the sky ($\equiv i$) is defined such that $i = 0$ means face-on, and thus $x = R \cos \phi$ and $y = R \sin \phi \cos i$. The radial profile of the rotation velocity of the disk is expressed as $V_\phi(R) = V_1(R/R_1)^{-v}$, and the iso-velocity

curve at a given line-of-sight velocity ($\equiv V_{\text{LOS}}$) projected onto the plane of the sky is described as $V_{\text{LOS}} = V_\phi(R) \cos \phi \sin i$. This curve passes through the origin $(x, y) = (0, 0)$ and $(R_o, 0)$, where $R_o = R_1(V_{\text{LOS}}/V_1/\sin i)^{-1/v}$. R_o gives the outermost point located in the major axis at a given V_{LOS} and curves at different V_{LOS} do not intersect with each other. The curves exhibit a symmetrical shape with respect to the major axis, and around the systemic velocity the curves show the well-known “butterfly” shapes. The curves at different V_{LOS} correspond to the velocity channel maps in the case of the infinite spatial and velocity resolutions, and the PV diagram along the major axis forms the rotation curve of $V_{\text{LOS}} = V_\phi(R) \sin i$ exactly. In cases of finite spatial and velocity resolutions, the iso-velocity curve on the plane of the sky must have widths depending on the velocity resolution ($\equiv \Delta V$), where the maximum width is seen along the major axis. Such iso-velocity regions are convolved with the spatial beam, defined as the circular Gaussian with the FWHM beam size of θ ($\equiv \exp[-4 \ln 2(x^2 + y^2)/\theta^2]$). The spatial convolution skews the mean position along the major axis ($\equiv x_m$) at a given V_{LOS} .

In realistic cases of central disks, our method adopts only high-velocity (typically greater than a few times kilometers per second), fast-rotating parts of the PV diagrams, and the amount of the positional shifts within a typical velocity resolution ($\sim 0.1 \text{ km s}^{-1}$) is much smaller than a typical spatial resolution. The iso-velocity curve (i.e., $V_{\text{LOS}} = V_\phi(R) \cos \phi \sin i$) can be rewritten in terms of y as

$$\frac{y}{R_o \cos i} = \pm \sqrt{\left(\frac{x}{R_o}\right)^{2/(v+1)} - \left(\frac{x}{R_o}\right)^2}. \quad (2.11)$$

Thus, the width of the iso-velocity region along the y direction at a given $x (< R_o)$ and ΔV can be written as

$$\Delta y \simeq \frac{\partial y}{\partial V_{\text{LOS}}} \Delta V = \frac{\partial y}{\partial R_o} \frac{dR_o}{dV_{\text{LOS}}} \Delta V = \frac{R_o^{v+1} \Delta V \cos i}{(v+1)V_1 R_1^v \sin i} \frac{\left(\frac{x}{R_o}\right)^{2/(v+1)}}{\sqrt{\left(\frac{x}{R_o}\right)^{2/(v+1)} - \left(\frac{x}{R_o}\right)^2}} \quad (2.12)$$

where $(\Delta V/V_{\text{LOS}})^2$ or higher-order components are ignored. On the major axis ($y = 0$), the intensity distribution ($\equiv I$) spatially convolved along the y -axis is then described as

$$I_{\theta_n}(z) \propto \Delta y \exp \left[-4 \ln 2 \left(\frac{y}{\theta} \right)^2 \right] \propto \frac{z^{\frac{1}{v+1}}}{\sqrt{1-z^{v+1}}} \exp \left[-4 \ln 2 \left(\frac{z^{\frac{1}{v+1}} \sqrt{1-z^{v+1}}}{\theta_n} \right)^2 \right] \quad (2.13)$$

where $z = x/R_o$ is the normalized spatial coordinate along the major axis and $\theta_n = \theta/R_o/\cos i$ is the normalized beam width along the minor axis. In Eq.(2.13), Δy^2 or higher-order components are ignored because Δy is an infinitesimal proportional to ΔV . The spatial convolution along the x -axis (the major-axis direction) does not change the mean position mathematically. Then, the skewness of the mean position along the major axis due to the finite resolution ΔV and θ can be expressed as

$$z_m = \frac{x_m}{R_o} = \frac{\int_0^1 I_{\theta_n}(z) z dz}{\int_0^1 I_{\theta_n}(z) dz}, \quad (2.14)$$

where z_m is the normalized mean position; z_m can be derived as a function of θ_n , which depends on R_o (or V_{LOS}) because θ is a constant. Figure 2.14 shows the dependence of z_m on $1/\theta_n$ in the case of $v = 1/2$ (Keplerian rotation). This figure shows that large $1/\theta_n$ gives $z_m \simeq 1$, and thus the relevant radius can be derived accurately if the spatial resolution is high enough as compared with the emission size. On the other hand, small $1/\theta_n$ gives $z_m \simeq 0.760 < 1$, which means that the correct radius cannot be derived from the mean positions. However, if the beam size is very large ($1/\theta_n < 1.0$), the dependency of z_m on $1/\theta_n$ (i.e. R_o) is small, indicating $x_m = \text{const.} \times R_o$. This means that the power-law index can be derived correctly by using the mean positions, although the radii themselves are underestimated. These results also indicate that the estimates of the central stellar masses or angular momenta are affected at most $< 23\%$.

In our case of TMC-1A, the size of the synthesized beam (FWHM $\sim 1''$) corresponds to $1/\theta_n \simeq R_o/2''.4 = R_o/330 \text{ AU}$ with $i = 65^\circ$ and $d = 140 \text{ pc}$. Figure 2.14 shows that the power-law index of the rotational velocity is expected to be estimated correctly at $R < 330$

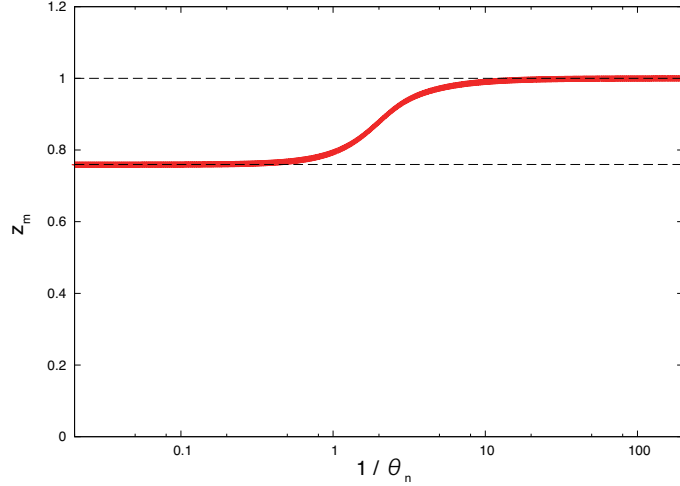


Figure 2.14 The dependency of the normalized mean position $z_m = x_m/R_o$ on the normalized beam width $1/\theta_n = R_o \cos i/\theta$ in the case with $v = 1/2$ (Keplerian rotation).

AU for TMC-1A. In an intermediate situation, the degree of the underestimation of the radii depends on the relevant radius; thus, the power-law indices must also be distorted. These considerations imply that effects of the spatial and velocity resolutions, as well as those of the radial velocities, should be taken into account to derive the rotational profiles from the observed PV diagrams.

2.8.2 Comparison between the Flattened and Spherical Envelope Models

In Sec. 2.6.2, we have constructed models consisting of a Keplerian disk and a flattened envelope (FE model) to interpret the observed gas motions, and we have found that the envelope is infalling toward the disk with the infalling velocity slower than the free-fall velocity yielded by the mass of the central star. The interpretation of gas motions is, however, dependent on the assumed geometry of the envelope (e.g. Tobin et al., 2012a), and it is thus possible that the identified infalling motion slower than the free fall could be due to the effect of the assumed envelope geometry. To qualitatively assess the effects of the different geometries of the envelopes, we have also constructed models consisting

of a spherical envelope and a Keplerian disk. Hereafter we call them SE models.

The density structure of the spherical envelope in the SE models we adopted is a solution of the rotating and infalling envelope modeled by Terebey et al. (1984), with the temperature profile of $T(r) = 38.0 \text{ K } (r/100 \text{ AU})^{0.02}$, the mass infalling rate of $\dot{M} = 10^{-5} M_{\odot}/\text{yr } (M_*/0.5 M_{\odot})^{0.5}$, the central stellar mass $M_* = 0.68 M_{\odot}$, and the outermost radius $R = 900 \text{ AU}$. To mimic the cavity created by the associated outflow, artificial bipolar cavities in a conical shape with the opening angle of 20° are added in the spherical envelope, and within $R < R_{\text{kep}} = 100 \text{ AU}$ the same disk as that of FE models is located. To simplify the comparison of the observed gas kinematics between FE and SE models, the rotational velocity in the spherical envelope is assumed to be only the function of the distance from the rotational axis, with the same radial profile as that of the flattened envelope models, and the infalling motion is assumed to be isotropic. As in the case of FE models, we adopt two types of infalls in SE models: a reduced infall $V_r = 0.3V_{\text{ff}}$, and free fall ($V_r = V_{\text{ff}}$), where the free-fall velocity is derived from the central stellar mass of $0.68 M_{\odot}$. The former and latter models are named as SE models A and D, respectively. The corresponding FE models are FE models A (our best-fit model) and D.

Figure 2.15a and b compare the PV diagrams along the major and minor axes of FE model A (red contours) and SE model A (gray scale), and Figure 2.15c and d compare FE model D (red contours) and SE model D (gray scale), respectively. These figures show some slight differences between SE and FE models as described below. As shown in Figure 2.15d, the minor-axis PV diagram of SE model D shows two peaks at $V \sim 5 \text{ km s}^{-1}$ and $\sim 8 \text{ km s}^{-1}$, while two velocity peaks in FE model D are $\sim 1 \text{ km s}^{-1}$ faster than them. In addition, FE model A/D shows only blueshifted emission at positions $\lesssim -1''$ in the minor-axis PV diagram and only redshifted emission at $\gtrsim 1''$, whereas SE model A/D shows blue- and redshifted emission on both positive and negative sides. In spite of these slight differences, FE model A and SE model A, as well as FE model D and SE model D, show overall similar PV diagrams along both major and minor axes; therefore, we conclude that SE models cannot explain the observations better than FE

models. It is important to note that when SE models A and D are compared with the observations, it is found that SE model A can explain the observations better than SE model D, suggesting that the infall velocity should be significantly slower than the free-fall velocity even in the case with a spherical envelope.

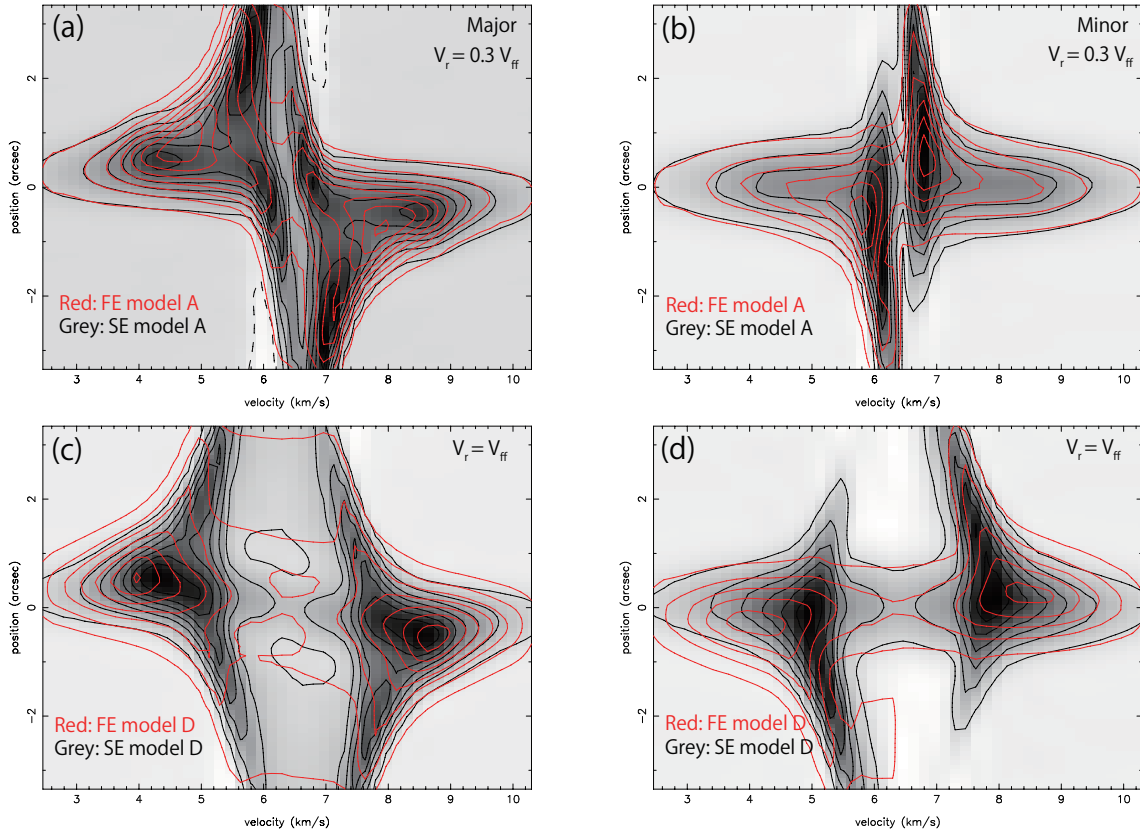


Figure 2.15 Comparison FE model A/D in Sec. 2.6.2 (red contours) and SE model A/D in Appendix 2.8.2 (black contours and grayscales). The right and left columns show PV diagrams along the major and minor axes, respectively. The contour levels are the same as Figure 2.8 and Figure 2.12.

Chapter 3

ALMA CYCLE 1 OBSERVATIONS OF L1527 IRS

3.1 ABSTRACT

We have newly observed the Class 0/I protostar L1527 IRS using Atacama Large Millimeter/submillimeter Array (ALMA) during its Cycle 1 in 220 GHz dust continuum and C^{18}O ($J = 2 - 1$) line emissions with a ~ 2 times higher angular resolution ($\sim 0''.5$) and ~ 4 times better sensitivity than our ALMA Cycle 0 observations. Continuum emission shows elongation perpendicular to the associated outflow, with a deconvolved size of $0''.53 \times 0''.15$. C^{18}O emission shows similar elongation, indicating that both emissions trace the disk and the flattened envelope surrounding the protostar. The velocity gradient of the C^{18}O emission along the elongation due to rotation of the disk/envelope system is re-analyzed, identifying Keplerian rotation proportional to $r^{-0.5}$ more clearly than the Cycle 0 observations. The Keplerian-disk radius and the dynamical stellar mass are kinematically estimated to be $\sim 74 \pm 2$ AU and $\sim 0.45 M_{\odot}$, respectively. The continuum visibility is fitted by models without any annulus averaging, revealing that the disk is in hydrostatic equilibrium. The best-fit model also suggests a density jump by a factor of ~ 5 between the disk and the envelope, suggesting that disks around protostars can be geometrically

distinguishable from the envelope. Importantly, the disk radius geometrically identified with the density jump is consistent with the one kinematically estimated. Possible origin of the density jump due to the mass accretion from the envelope to the disk is discussed. C^{18}O observations can be reproduced by the same geometrical structures derived from the dust observations, with possible C^{18}O freeze-out and localized C^{18}O desorption.

3.2 INTRODUCTION

L1527 IRS (IRAS 04365+2557) is one of youngest protostars, whose disks have been studied. L1527 IRS, located in one of closest star-forming regions, Taurus Molecular Cloud ($d = 140$ pc), has bolometric luminosity $L_{\text{bol}} = 2.0 L_{\odot}$ and bolometric temperature $T_{\text{bol}} = 44$ K (Kristensen et al., 2012), indicating that L1527 IRS is a relatively young protostar. The systemic velocity of L1527 IRS in the local standard of rest (LSR) frame was estimated to be $V_{\text{LSR}} \sim 5.7$ km s $^{-1}$ from C^{18}O $J = 1 - 0$ observations with Nobeyama 45 m single-dish telescope (Ohashi et al., 1997), while N_2H^+ $J = 1 - 0$ observations with Five College Radio Astronomy Observatory (FCRAO) 14 m and Institut de Radioastronomie Millimetrique (IRAM) 30 m single-dish telescopes, estimated it to be $V_{\text{LSR}} \sim 5.9$ km s $^{-1}$ (Caselli et al., 2002; Tobin et al., 2011). We adopt $V_{\text{LSR}} = 5.8$ km s $^{-1}$ for the systemic velocity of L1527 IRS in this chapter, which is reasonable as will be shown later.

On a ~ 30000 AU scale, a bipolar outflow associated with this source were detected in the east-west direction by FCRAO single-dish observations in ^{12}CO $J = 1 - 0$ molecular line emission (Narayanan et al., 2012) and by James Clerk Maxwell Telescope (JCMT) single-dish observations in ^{12}CO $J = 3 - 2$ molecular line emission (Hogerheijde et al., 1997). Their results show that the blue and red robes of the outflows are on the eastern and western sides, respectively. On the other hand, inner parts (~ 8000 AU scale) of the outflow mapped with Nobeyama Millimeter Array (NMA) in ^{12}CO $J = 1 - 0$ show the opposite distribution, i.e., stronger blueshifted emission on the western side and stronger

redshifted emission on the eastern side (Tamura et al., 1996). Mid-infrared observations toward L1527 IRS with Spitzer Space Telescope shows bright bipolar scattered light nebulae along the outflow axis in the ~ 20000 AU scale (Tobin et al., 2008). They fitted a protostellar envelope model to near- and mid-infrared scattered light images and spectral energy distribution (SED). As a result the inclination angle of the envelope around L1527 IRS was estimated to be $i = 85^\circ$, where $i = 90^\circ$ means the edge-on configuration. By expanding the studies by Tobin et al. (2008), Tobin et al. (2013) fitted a model composed of an envelope and a disk to (sub)millimeter continuum emissions and visibilities observed with SMA and CARMA as well as infrared images and SED. Their best-fitting model suggests a highly flared disk structure ($H \propto R^{1.3}$, $H = 48$ AU at $R = 100$ AU).

The first interferometric observations of the envelope surrounding L1527 IRS were reported by Ohashi et al. (1997), identifying an edge-on flattened envelope elongated perpendicularly to the associated outflow, in their $\text{C}^{18}\text{O } J = 1 - 0$ map obtained with NMA at an angular resolution of $\sim 6''$. It was found that kinematics of the envelope can be explained with dynamical infall motion ($\sim 0.3 \text{ km s}^{-1}$) and slower rotation ($\sim 0.05 \text{ km s}^{-1}$) at 2000 AU. Its mass infalling rate was also estimated to be $\dot{M} \sim 1 \times 10^{-6} M_\odot \text{ yr}^{-1}$. Higher-resolution ($\sim 1''$) observations using Submillimeter Array (SMA) and Combined Array for Research in Millimeter Astronomy (CARMA) in $^{13}\text{CO } J = 2 - 1$ line were carried out toward this source by Tobin et al. (2012b). They measured offset of emission from the central protostar at each channel and fitted the position-velocity data by assuming Keplerian rotation. According to their best-fit result, the mass of L1527 IRS was estimated to be $M_* = 0.19 \pm 0.04 M_\odot$ and the disk radius was also estimated to be 150 AU. It should be noted, however, that no other kinds of rotation, such as the one conserving its angular momentum, were compared with the observations in their work, even though such rotation would be expected in the infalling envelope surrounding L1527 IRS.

In order to investigate the rotational velocity around L1527 IRS without assuming Keplerian rotation, a radial profile of the rotational velocity V_{rot} was measured by Yen

et al. (2013) from their SMA observations in $\text{C}^{18}\text{O } J = 2 - 1$ line with the angular resolution of $4''.2 \times 2''.5$. In their analysis, the rotation profiles are derived from Position-Velocity (PV) diagrams cutting along a line perpendicularly to the outflow axis. The rotation profile of L1527 IRS was measured at $r \gtrsim 140$ AU to be $V_{\text{rot}} \propto r^{-1.0 \pm 0.2}$, which is clearly different from Keplerian rotation $V_{\text{rot}} \propto r^{-1/2}$. Further investigation of the rotation profile around L1527 IRS was performed with much higher sensitivity as well as higher angular resolution provided by Atacama Large Millimeter/submillimeter Array (ALMA) (Ohashi et al., 2014). The rotation profile obtained in $\text{C}^{18}\text{O } J = 2 - 1$ at a resolution of $\sim 0''.9$ mostly shows velocity inversely proportional to the radius being consistent with the results obtained by Yen et al. (2013), while it also suggests a possibility that the profile at $\lesssim 54$ AU can be interpreted as Keplerian rotation with a central stellar mass of $\sim 0.3 M_{\odot}$. In addition, it is found that infall velocity in the envelope is slower than the free fall velocity yielded by the expected central stellar mass (Ohashi et al., 2014).

In this chapter we report new ALMA Cycle 1 observations of L1527 IRS in $\text{C}^{18}\text{O } (J = 2 - 1)$ and 220 GHz continuum, with a ~ 2 times higher angular resolution and a ~ 4 times higher sensitivity as compared with our previous ALMA cycle 0 observations, which allow us to give a much better constraint on the rotation profile of the disks and the envelope, and also their geometrical structures. Our observations and data reduction are described in Section 3.3. In Section 3.4, we present the continuum and molecular-line results. In Section 3.5, we analyze rotation velocity measured by the C^{18}O line and perform χ^2 fitting to explain the continuum visibility using a model. In Section 3.6, we investigate the validity and consistency of the model that reproduces the observations the best. We present a summary of the results and our interpretation in Section 3.7.

3.3 ALMA OBSERVATIONS AND DATA REDUCTION

We observed our target, L1527 IRS, during Cycle 1 using ALMA on 2014 July 20. The observations composed of two tracks in the same day with a separation of ~ 40 minutes.

Each track was ~ 30 minutes including overhead. J0510+1800 was observed as the passband, gain, and flux calibrator for the former track and J0423-013 was observed as the flux calibrator for the latter track. Thirty-four antennas were used in the first track, while one antenna was flagged in the latter track. The antenna configuration covers projected baseline length from 17 to 648 m (13-474 $k\lambda$ in uv -distance at the frequency of $C^{18}O$ $J = 2 - 1$). This minimum baseline resolves out more than 50% of the flux when a structure is extended more than $7''.1$ (Wilner & Welch, 1994), corresponding to ~ 990 AU at a distance of L1527 IRS. The coordinates of the map center during the observations were $\alpha(J2000) = 04^{\text{h}}39^{\text{m}}53^{\text{s}}.90$, $\delta(J2000) = 26^{\circ}03'10''.00$. $C^{18}O$ $J = 2 - 1$ line and 220 GHz continuum emission in Band 6 were observed for $6.9+6.7=14$ minutes (on source). To derive high-velocity resolutions for molecular line observations, we configured the correlator in Frequency Division Mode for two spectral windows. Each spectral window has 3840 channels covering 234 MHz bandwidth. Emission-free channels in the lower side band are used to make the continuum map centered at 220 GHz. The total bandwidth of the continuum map is ~ 234 MHz.

All the mapping process was carried out with Common Astronomy Software Applications (CASA). Because the original map center during the observations was not coincident with the continuum peak position estimated from 2D Gaussian fitting in the uv -domain by $0''.54$, the phase center of the observed visibilities was shifted from the original phase center with *fixvis* in CASA, making the map center of the resultant maps in this chapter the same as the continuum peak position. The visibilities were Fourier transformed and CLEANed. In this process we adopted superuniform weighting with $n_{\text{pixel}} = 2$ and binned two frequency channels; the resultant frequency resolution in this chapter is 122 kHz, corresponding to 0.17 km s^{-1} in the velocity resolution at the frequency of $C^{18}O$ $J = 2 - 1$. We set a $30'' \times 30''$ area centered on the map center as a CLEAN box with a threshold of 3σ . The synthesized beam sizes of the CLEANed maps are $0''.50 \times 0''.40$ for the $C^{18}O$ line, and $0''.47 \times 0''.37$ for the continuum emission.

We also performed self-calibration for the continuum observations using tasks in

Table 3.1. Summary of the ALMA observational parameters (L1527 IRS)

Date	2014.Jul.20	
Target	L1527 IRS	
Coordinate center	R.A. (J2000)=4 ^h 39 ^m 53 ^s .9 Dec. (J2000)=26°03'10''0	
Projected baseline length	17.4 - 647.6 m	
Primary beam	28''6	
Passband calibrator	J0510+1800	
Flux calibrator	J0423−013, J0510+1800	
Gain calibrator	J0510+1800	
	Continuum	C ¹⁸ O $J = 2 - 1$
Frequency	219.564200	219.560358
Synthesized beam (P.A.)	0''47 × 0''37 (−0.4°)	0''50 × 0''40 (3.1°)
Velocity resolution	234 MHz	0.17 km s ^{−1}
1 σ	0.2 mJy beam ^{−1}	2.6 mJy beam ^{−1}

CASA (*clean*, *gaincal*, and *applycal*), and the obtained calibration table for the continuum observations was applied to the C¹⁸O observations. The self-calibration has improved the rms noise level of the continuum map by a factor of 2-3, while the noise level of the C¹⁸O map has been improved by less than a few percent. The noise level of the C¹⁸O map was measured in emission-free channels. The parameters of our observations mentioned above and others are summarized in Table 3.1.

3.4 RESULTS

3.4.1 220 GHz Continuum

Figure 3.1 shows the 220 GHz continuum emission in L1527 IRS observed with ALMA. Strong compact continuum emission is detected. The emission is clearly elongated in the north-south direction and shows weak extensions to the northwest and the southeast. The 6 σ contour in Figure 3.1 shows a full width of $\sim 2'' = 280$ AU along the north-south direction. Its deconvolved size derived from a 2D Gaussian fitting is 531 ± 2 mas \times 150 ± 2 mas, P.A. = $1.5^\circ \pm 0.2^\circ$. This major-axis direction is almost perpendicular to the direction of the associated outflow, indicating that the continuum emission traces a dust

disk and/or a flattened dust envelope around L1527 IRS. Compared with the synthesized beam size ($0''.47 \times 0''.37$, P.A. = -0.4°), the major axis of the emission is fully spatially resolved. The aspect ratio, 0.28, is a half of (i.e. thinner than) the ratio reported by Ohashi et al. (2014) with lower angular resolutions than this work. The peak position is also measured from the Gaussian fitting to be $\alpha(2000) = 04^{\text{h}}39^{\text{m}}53^{\text{s}}.88$, $\delta(2000) = +26^\circ03'09''.55$, which is consistent with previous measurements (Yen et al., 2013; Ohashi et al., 2014). We define this peak position and the major-axis direction as the central protostellar position of L1527 IRS and the orientation angle of its dust disk/envelope respectively in this chapter. The peak intensity and the total flux density of the emission derived from the Gaussian fitting are 101.4 ± 0.2 mJy beam $^{-1}$ and 164.6 ± 0.5 mJy, respectively, while the total flux density is 176 mJy when measured in the whole region of Figure 3.1. By assuming that the dust continuum emission is optically thin and dust temperature is isothermal, total mass can be calculated with the total flux density (Andrews & Williams, 2005b). The total fluxes derived above correspond to a mass of $M_{\text{gas}} \sim 0.013 M_{\odot}$ by assuming a dust opacity of $\kappa(220 \text{ GHz}) = 0.031 \text{ cm}^2 \text{ g}^{-1}$ (Tobin et al., 2013), a dust temperature of 30 K (Tobin et al., 2013), and a standard gas to dust mass ratio, g/d, of 100.

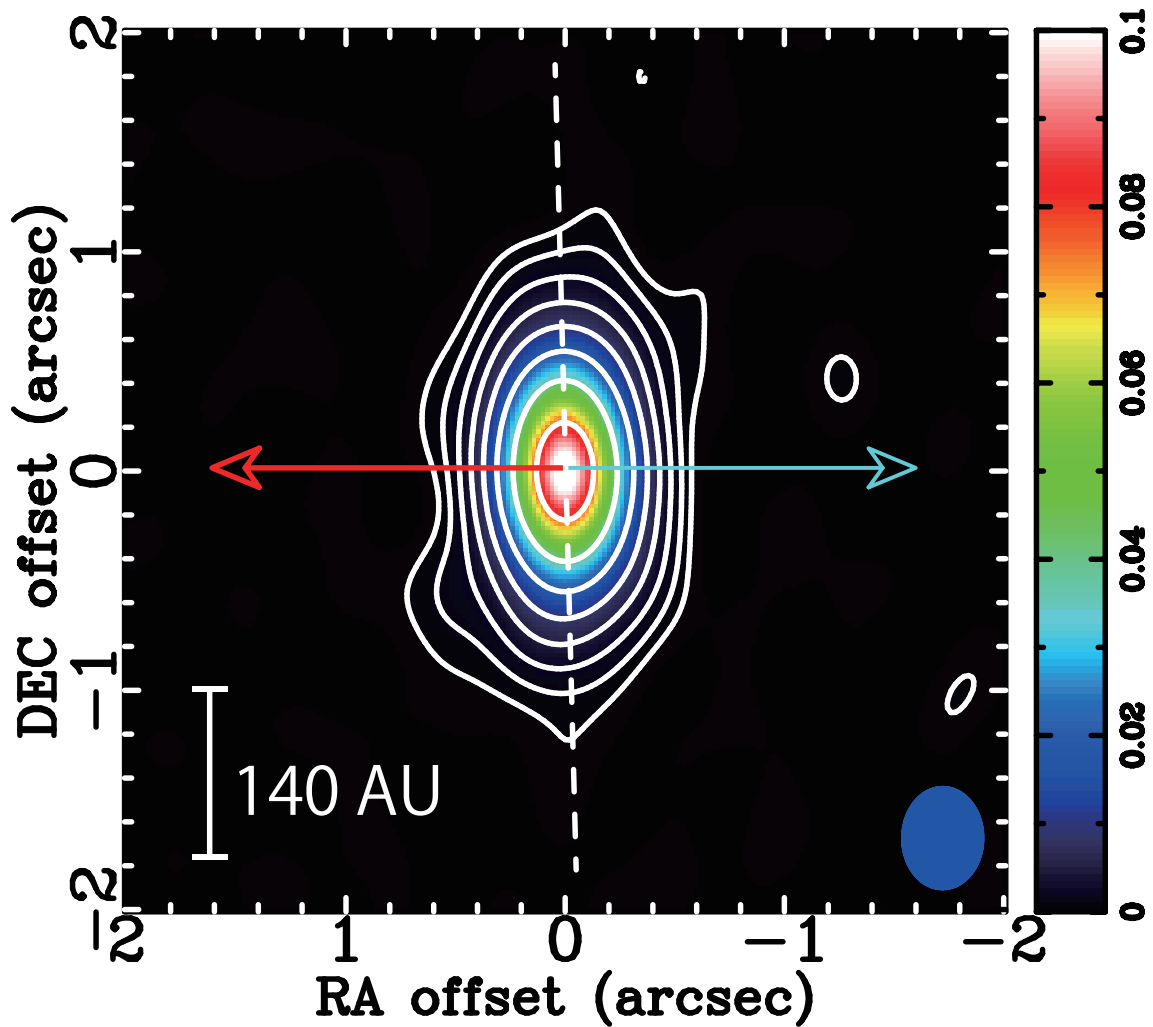


Figure 3.1 Continuum emission map of L1527 IRS. Contour levels are $-3, 3, 6, 12, 24, \dots \times \sigma$, where 1σ corresponds to $0.2 \text{ mJy beam}^{-1}$. A blue filled ellipse at the bottom right corner denotes the ALMA synthesized beam; $0''.47 \times 0''.37$, P.A. = -0.4° . The elongation direction (1.5°) is shown with a white dashed line. Blue and red arrows show the direction of the molecular outflow (east-west) from single-dish observations toward L1527 IRS in $^{12}\text{CO } J = 1 - 0$ (Narayanan et al., 2012).

3.4.2 C¹⁸O J=2-1

The C¹⁸O $J = 2 - 1$ emission was detected above 3σ level at the relative velocity range from -3.3 to 3.2 km s⁻¹ in the LSR frame with respect to the systemic velocity $V_{\text{LSR}} = 5.8$ km s⁻¹. Figure 3.2 shows the total integrated intensity (moment 0) map in white contours and the intensity-weighted-mean velocity (moment 1) map in color; both are derived from the above velocity range with 3σ cutoff. The moment 0 map overall shows an elongated structure perpendicular to the outflow axis, centered at the protostellar position. In more detail, lower contours ($\sim 3-6\sigma$) show extensions to north-northeast, north-northwest, south-southeast, and south-southwest. The moment 0 map also shows two local peaks on the northern and southern sides of the central protostar with a separation of $\sim 1''$. This double peak is due to a “continuum subtraction artifact”; the continuum emission is absorbed by extended C¹⁸O gas around the systemic velocity and the extended C¹⁸O emission is resolved out. at the position of central star, which is clearly seen in the channel maps (Figure 3.3). Regardless of the double peak, the map was fitted with single 2D Gaussian to measure the overall structure of the C¹⁸O emission; a deconvolved size of the C¹⁸O emission is estimated to be $2''.17 \pm 0''.04 \times 0''.88 \pm 0''.02$, with P.A. = $-1.8^\circ \pm 0.7^\circ$. Peak integrated intensity and total flux measured in the whole region of Figure 3.2 are 0.20 Jy beam⁻¹ km s⁻¹ and 2.2 Jy km s⁻¹. The moment 1 map shows a velocity gradient in the north-south direction, which is perpendicular to the outflow axis. The morphology of C¹⁸O emission indicates that it traces a flattened gas envelope and/or a gas disk around L1527 IRS and thus the velocity gradient seen in the C¹⁸O emission is mainly due to their rotation, as already suggested by Ohashi et al. (2014) and Yen et al. (2013). Because the C¹⁸O emission shows more complicated structure than the continuum emission, we assume the orientation angle of the gas disk/envelope to be the same as that of the dust disk/envelope in this chapter.

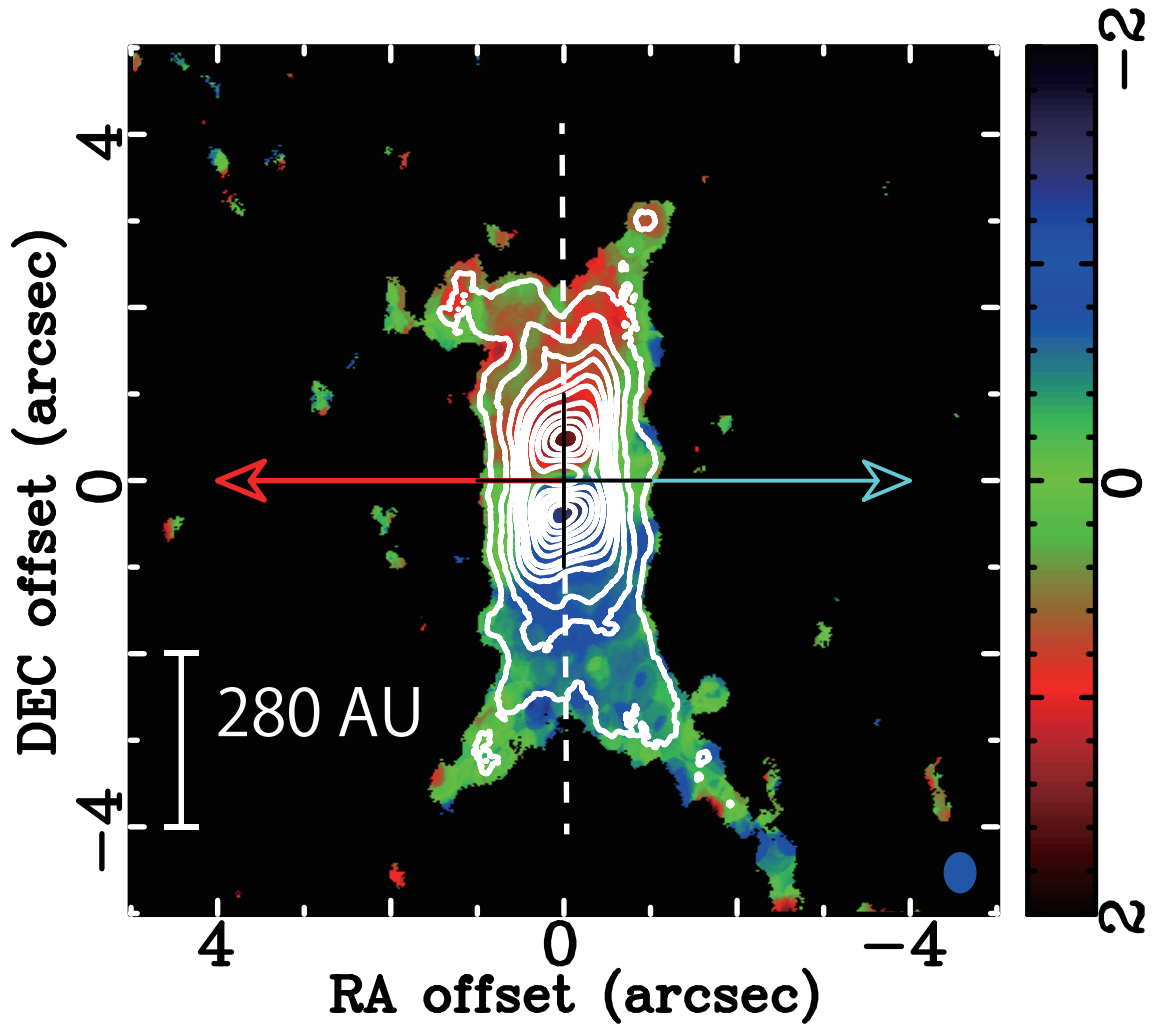


Figure 3.2 Integrated intensity map (moment 0; white contours) and mean velocity map (moment 1; color) of the $\text{C}^{18}\text{O } J = 2 - 1$ emission in L1527 IRS, where the velocity is relative LSR velocity with respect to the systemic velocity $V_{\text{LSR}} = 5.8 \text{ km s}^{-1}$. Contour levels of the integrated intensity map are from 5σ to 30σ in steps of 5σ and then in steps of 10σ , where 1σ corresponds to $2.3 \text{ mJy beam}^{-1} \text{ km s}^{-1}$. A central black plus sign shows the position of the central protostar (continuum emission peak). A blue filled ellipse at the bottom right corner denotes the ALMA synthesized beam; $0''.50 \times 0''.40$, P.A. = 3.1° . Blue/red arrows and a white dashed line show the direction of the molecular outflow and the major-axis direction of the continuum emission, respectively, as shown in Figure 3.1.

Figure 3.3 shows channel maps of the C^{18}O emission, which enable us to investigate velocity structures in more detail. In higher blue- and redshifted velocities ($|V| \gtrsim 1.6 \text{ km s}^{-1}$), emissions show overall circular shapes and their sizes at 3σ level are smaller than $\sim 1''.5$. The emission peaks are located on the southern side in the blueshifted range while on the northern side in the redshifted range, making a velocity gradient from the south to the north as seen in Figure 3.2. In a middle velocity range ($0.4 \lesssim |V| \lesssim 1.5 \text{ km s}^{-1}$), more complicated structures can be seen. For example, at $-1.15, -0.98, 0.85, 1.02 \text{ km s}^{-1}$, the emissions appear to be composed of a strong compact ($\sim 1''$) structure close to the protostar and a more extended ($> 2''$) structure, resulting in a plateau structure. The extended emissions are located mainly on the southern side in the blueshifted range while mainly on the northern side in the redshifted range. Furthermore some blueshifted channels (-0.65 and -0.48 km s^{-1}) show an extension from the protostar to the northwest. In the other lower velocities, emissions are strongly resolved out and negative emission can be seen from 0.02 to 0.35 km s^{-1} . This redshifted negative emission is due to a continuum subtraction artifact with an extended infalling envelope around L1527 IRS (Ohashi et al., 2014). The higher angular resolution than Ohashi et al. (2014) can make the negative emission deeper and result in a double peak in Figure 3.2 that did not appear in Ohashi et al. (2014).

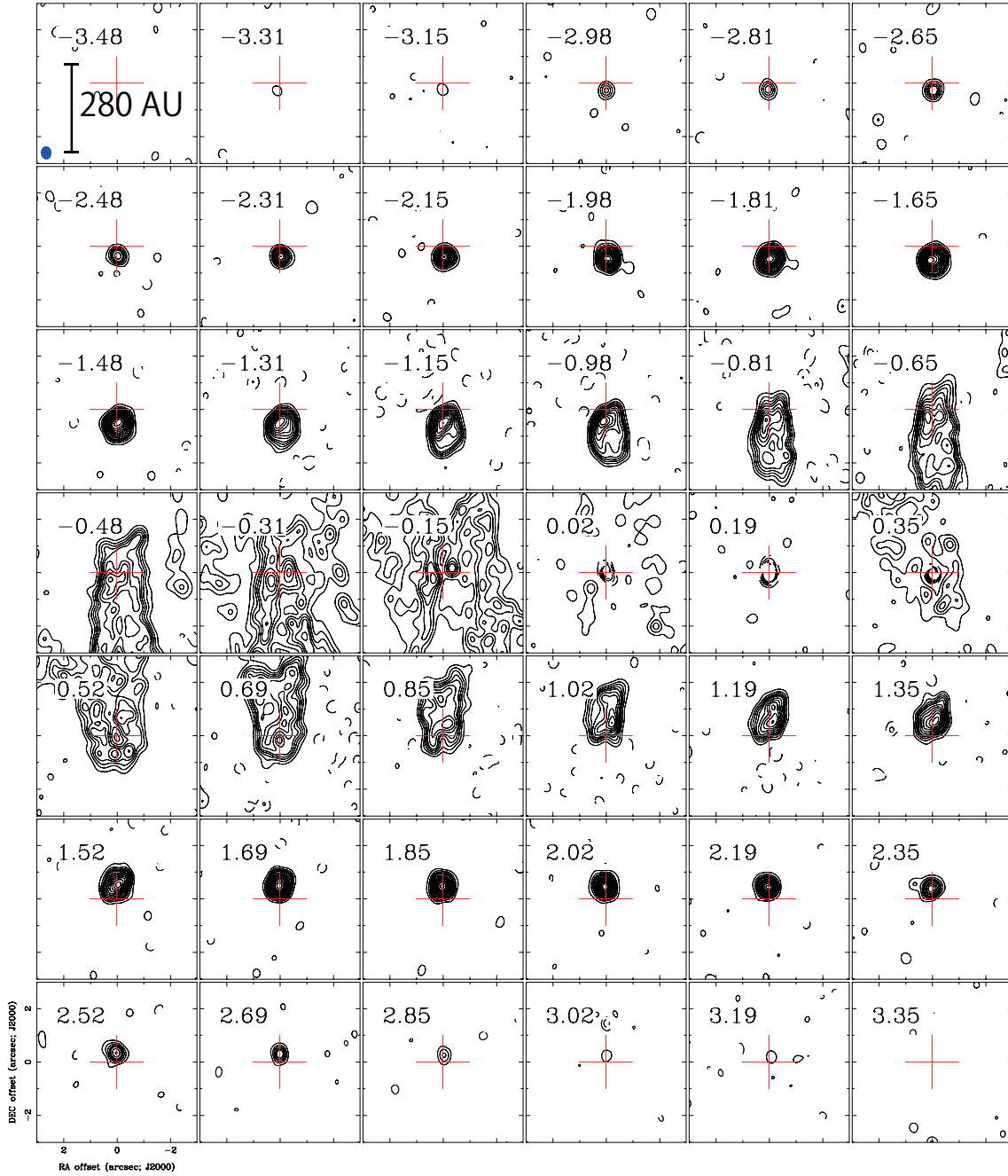


Figure 3.3 Channel maps of the $\text{C}^{18}\text{O } J = 2-1$ emission in L1527 IRS. Contour levels are from 3σ to 15σ in steps of 3σ and then in 5σ , where 1σ corresponds to $2.6 \text{ mJy beam}^{-1}$. A central red plus sign in each panel shows the position of the central protostar (continuum emission peak). A blue filled ellipse in the top left panel denotes the ALMA synthesized beam; $0''.50 \times 0''.40$, P.A. = 3.1° . Relative LSR velocity with respect to the systemic velocity $V_{\text{LSR}} = 5.8 \text{ km s}^{-1}$ is shown at the top left corner of each panel.

In the moment 1 map and channel maps, L1527 IRS shows a velocity gradient from the south to the north. The PV diagrams along the major and minor axes are considered to represent a velocity gradient due to rotation and radial motion, respectively, toward disk-like structures as discussed in previous work. Figure 3.4a and b show PV diagrams of the C^{18}O emission cutting along the major and minor axes, respectively. The overall velocity gradient from the south to the north can be confirmed in the PV diagram along the major axis. In more detail, the so-called “spin up” rotation can also be seen in $|V| \gtrsim 1.5 \text{ km s}^{-1}$, that is, an emission peak at a velocity channel is closer to the central position at higher velocity. We will analyze the dependence of rotational velocity on radial distance from the central position in Section 3.5.1. In $0.6 \lesssim |V| \lesssim 1.4 \text{ km s}^{-1}$, a strong compact emission and a more extended emission appear to be superposed, which corresponds to the plateau structures seen in the channel maps (Figure 3.3). In the PV diagram along the minor axis, there are four strong peaks in the western redshifted and blueshifted components, and the eastern blueshifted and redshifted ones in $|V| \lesssim 1.5 \text{ km s}^{-1}$ while the emission is mainly concentrated on the central position in the higher velocity range. The western blueshifted component extends to higher velocities than the eastern blueshifted one, and also the eastern redshifted component extends to higher velocities than the western redshifted one. These extensions can be interpreted as a small velocity gradient from the west to the east, which was detected in observations in CS $J = 5 - 4$ line emission and considered to be due to infalling motion in the protostellar envelope by Oya et al. (2015).

3.5 ANALYSIS

3.5.1 Rotation Profile

In the previous section we identified rotation in the C^{18}O gaseous component tracing either a flattened envelope, disk, or both. In this section the radial profile of the rotation will be investigated with the PV diagram along the major axis (Figure 3.4) so as to characterize

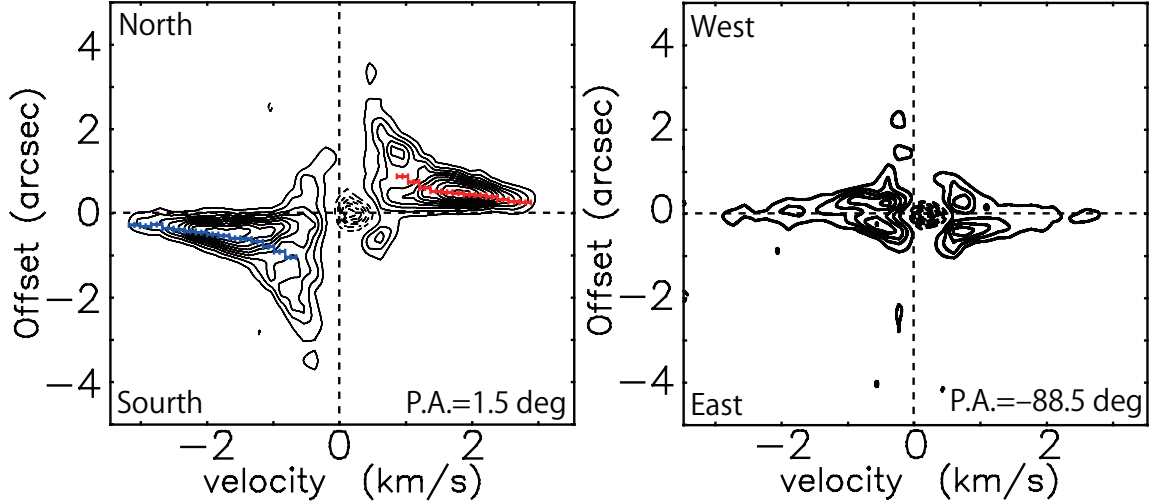


Figure 3.4 Position Velocity diagrams of the $\text{C}^{18}\text{O } J = 2 - 1$ emission in L1527 IRS along (a) the major axis and (b) the minor axis of the continuum emission (the major axis corresponds to the white dashed line in Figure 3.1, P.A. = 1.5°). These PV diagrams have the same angular and velocity resolutions as those of the channel maps shown in Figure 3.3. Contour levels are 5σ spacing from 3σ , where 1σ corresponds to $2.6 \text{ mJy beam}^{-1}$. Central vertical dashed lines show the systemic velocity and central horizontal dashed lines show the protostellar position. Blue and red points with error bars in panel (a) are mean positions derived along the position (vertical) direction at each velocity.

the nature of the observed rotation. The method used in this section to obtain the radial profile of rotational velocity is based on the analyses presented by Yen et al. (2013) and also explained by Aso et al. (2015) in detail. The representative position at each velocity channel of the PV diagram along the major axis is measured as the intensity-weighted 1D mean position, $x_m(v) = \int xI(x, v)dx / \int I(x, v)dx$. Pixels having intensity more than 5σ are used to calculate the sum. The error bar of each representative position is also derived by considering propagation of errors. The derived representative positions are overlaid with error bars on the PV diagram along the major axis (Figure 3.4) and also plotted in a $\log R - \log V$ plane (Figure 3.5). The abscissa of Figure 3.5 is calculated from the offset position in the PV diagram by assuming that the distance of L1527 IRS is 140 pc. Figure 3.5 shows a clear negative correlation that the rotational velocity is higher at the position closer to the central protostar, i.e., differential rotation. Furthermore the $\log R - \log V$ diagram in Figure 3.5 exhibits two different linear regimes with a break radius of ~ 60 AU. The data points in the $\log R - \log V$ plane are, therefore, fitted by a double power-law

function with four free parameters: inner and outer power-law indices p_{in} and p_{out} , respectively, and a break point (R_b, V_b) (see Equation (1) in Aso et al., 2015). The best-fit parameter set is $(R_b, V_b, p_{\text{in}}, p_{\text{out}}) = (56 \pm 2 \text{ AU}, 2.31 \pm 0.07 \text{ km s}^{-1}, 0.50 \pm 0.05, 1.22 \pm 0.04)$, giving a reasonable reduced χ^2 of 1.6. For comparison, χ^2 fitting with a single power function is also performed, where V_b is fixed at 2.31 km s^{-1} . The best-fit parameter set for this case is $(R_b, p) = (49.5 \pm 0.3 \text{ AU}, 0.88 \pm 0.01)$, giving reduced $\chi^2 = 4.0$. These reduced χ^2 suggest that the radial profile of rotational velocity is characterized by the double power function better than any single power function. In addition, to examine whether the LSR velocity of L1527 IRS we adopt, 5.8 km s^{-1} , is reasonable, we also carried out fitting including the systemic velocity as another free parameter, which was fixed to be 5.8 km s^{-1} above, confirming that the adopted systemic velocity is the most reasonable to fit the $\log R - \log V$ diagram.

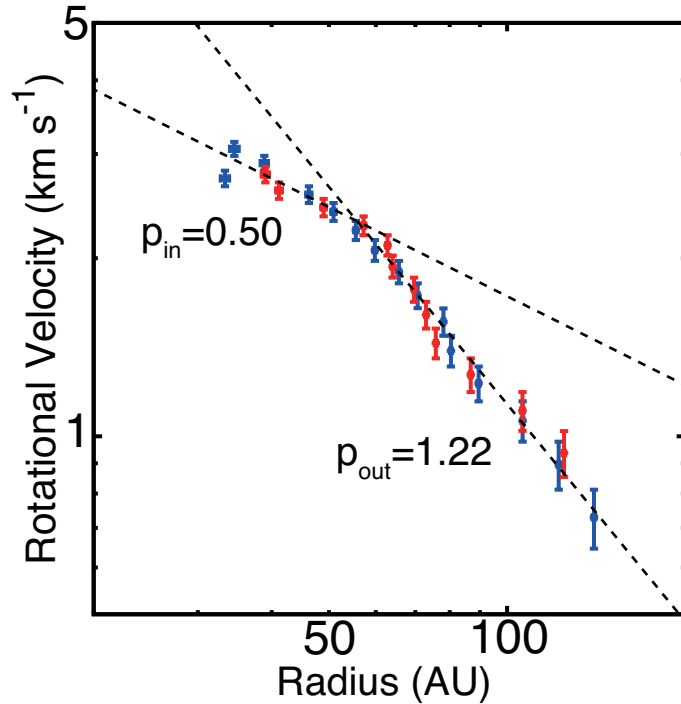


Figure 3.5 Mean positions of the PV diagram along the major axis plotted on a $\log R - \log V$ plane. The ordinate is not deprojected. Blue and red points show bluishifted and redshifted mean positions in Figure 3.4a, respectively. Dashed lines show the best-fit lines with a double power law.

The best-fit inner power-law index is almost equal to Keplerian rotation law ($p = 1/2$), suggesting that the inner/higher-velocity component of the $C^{18}O$ emission traces a Keplerian disk. In fact, the Keplerian rotation was marginally detected in Ohashi et al. (2014). On the other hand, the best-fit outer power-law index is roughly equal to that of rotation conserving its angular momentum ($p = 1$), which is steeper than the Keplerian rotation law, and thus suggests that the rotation in the envelope around the disk cannot support material against the gravity yielded by the central protostar. This is consistent with the fact that the envelope is in infalling motion, as was confirmed by the redshifted negative emission in the channel maps (Figure 3.3, see also Ohashi et al., 2014). The best-fit result is quite consistent with that obtained for our previous Cycle 0 observations of L1527 IRS (Ohashi et al., 2014), while the higher angular resolution and sensitivity of the Cycle 1 observations has enabled us to sample twice as many data points within the break radius in the $\log R - \log V$ diagram as the previous work, making the break in the rotation profile more definite with more precise measurements of the radius of the break and the inner power-law index. The radius of the identified Keplerian disk can be estimated from the best-fit break radius. Because L1527 IRS has an edge-on configuration, we are required to take into account a factor of underestimation reported by Aso et al. (2015). With this underestimation taken into account, the Keplerian disk radius is estimated to be $\sim 74 \pm 2$ AU. From the best-fit break velocity together with this disk radius, the central protostellar mass M_* of L1527 IRS and a specific angular momentum j at the outermost radius of the Keplerian disk can also be estimated to be $M_* \sim 0.45 M_\odot$ and $j \sim 8.3 \times 10^{-4} \text{ km s}^{-1} \text{ pc}$, respectively, where the inclination angle is assumed to be $i = 85^\circ$ (Tobin et al., 2013; Oya et al., 2015).

3.5.2 Structures of the Keplerian Disk

As shown in the previous section, a Keplerian disk has been kinematically identified by the $C^{18}O$ results. This disk around the protostar L1527 IRS seems to be kinematically

quite similar to those around T Tauri stars (Guilloteau & Dutrey, 1998; Simon et al., 2000; Rodriguez et al., 2010). A tantalizing question is whether this disk is also geometrically similar to those around T Tauri stars. Because this disk is almost edge-on, it is also possible to investigate the vertical structures of the disk. In this subsection geometrical structures of the Keplerian disk are investigated.

Continuum Visibility distribution

To investigate the disk structures, we have performed direct model fitting to the observed continuum visibility data, which is free from any non-linear effects associated with interferometric imaging. Figure 3.6 shows distributions of the continuum visibilities in three panels, where red and blue points denote the same groups; the red points are located near the major axis ($\pm 15^\circ$ on the uv -plane) while the blue points are located near the minor axis. Note that all the visibilities of each baseline in each track for ~ 30 minutes are averaged in these plots. That is the reason why any trajectory due to Earth's rotation is not drawn on the uv -plane (Figure 3.6a). It should be stressed that although all the visibilities of each baseline are averaged, further azimuthal average has not been done in our analysis as being obvious in Figure 3.6a. This is because information on not spherically symmetric structures such as disks is missed with azimuthally averaged visibilities, as explained below in more detail.

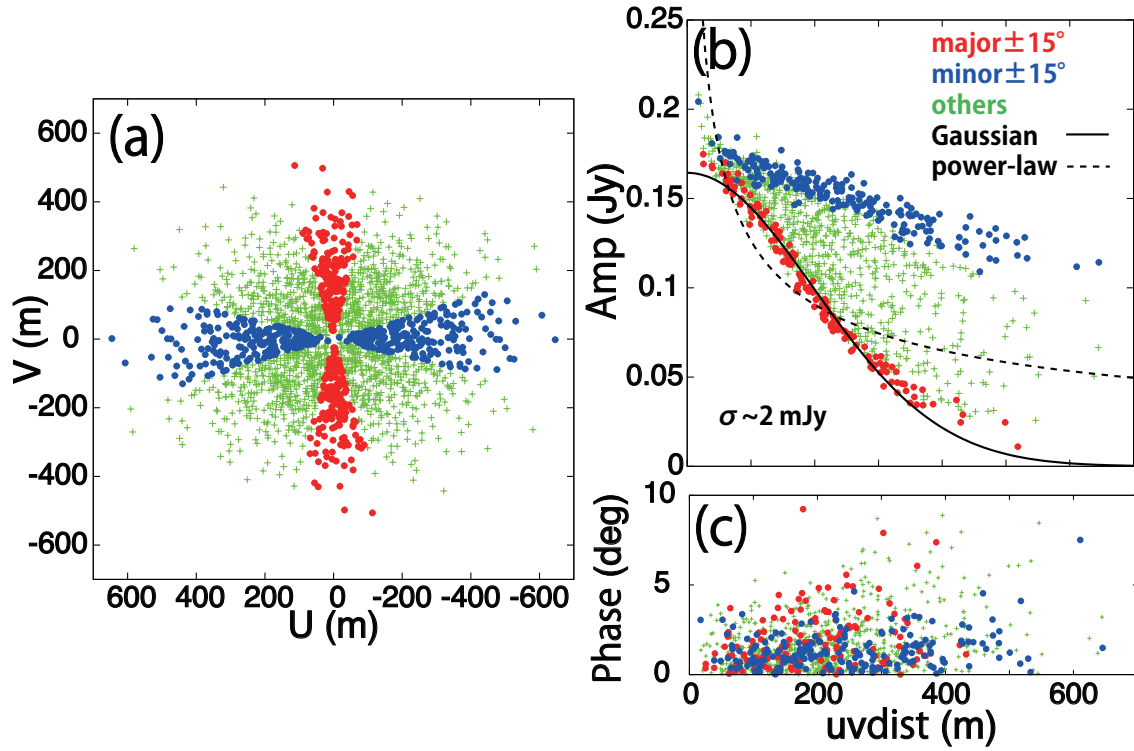


Figure 3.6 Continuum visibility averaged over scans. The two observational tracks are not averaged together. 1 m corresponds to $0.73 \text{ k}\lambda$ at the observed frequency. (a) Data points on the uv -plane. Both of each conjugate pair are plotted. (b) Distribution of the visibility amplitude. An error bar of the amplitude for each point is ~ 2 mJy. (c) Distribution of the visibility phase. Only one of each conjugate pair with a positive phase is plotted. Blue and red circles denote data points near the major- and minor-axis directions, respectively; in other words, $\text{Arctan}(U/V) = 1.5^\circ \pm 15^\circ, -88.5^\circ \pm 15^\circ$, respectively. Green crosses denote the other data points. Solid and dashed curves are the best-fit Gaussian and power-law profiles, respectively, to the data points near the major axis (red points).

Figure 3.6b exhibits a trend that the visibility amplitudes are higher at shorter uv -distances. The total flux density 176 mJy measured in the image space (Figure 3.1) appears consistent with an amplitude at zero uv -distance, which can be derived from visual extrapolation of the amplitude distribution. Figure 3.6b also exhibits the data points appearing to scatter more widely at longer uv -distances. This is clearly not due to the error of each data point, which is ~ 2 mJy but due to the structures of the continuum emission. In more detail, blue and red points have the highest and lowest amplitudes at each uv -distance, respectively. Considering Fourier transform, these distributions of the blue and red points indicate that structures of the continuum emission are largest along the major axis and smallest along the minor axis in the image domain, which is consistent with the image of the continuum emission shown in Figure 3.1. Similarly the scattering of the green points between the blue and red points is due to structures along directions at different azimuthal angles. In addition, the data points near the major axis (red points) are also compared with two simple functions in Figure 3.6b: Gaussian and power-law profiles. Best-fit profiles are $0.16 \text{ Jy} \exp(-4 \ln 2(\beta/234 \text{ m})^2)$ and $0.13 \text{ Jy} (\beta/100 \text{ m})^{-0.48}$, respectively, where β denotes the uv -distance. The power-law profile cannot explain the observations at all. Although the Gaussian profile matches the observations better, this profile is not necessarily realistic for circumstellar-disk structures (Harsono et al., 2014, and references therein) and also the comparison shows systematic deviation; the points are higher than the Gaussian profiles in $< 100 \text{ m}$ and $> 300 \text{ m}$ while they are lower in $\sim 200 \text{ m}$. Figure 3.6c exhibits that most phases of the visibility are smaller than $\lesssim 5^\circ$, which corresponds to $\lesssim 0''.04$ where uv -distance is larger than 100 m. This indicates that emission is centered at the protostellar position at most spatial frequencies. Red points and blue points appear to be well mixed in Figure 3.6c, which means that the distribution of phases in the azimuthal direction is roughly uniform.

As clearly demonstrated in Figure 3.6b, the analysis of visibility without azimuthal average in a uv -plane is quite powerful to investigate spatially resolved not spherically symmetric structures such as disks, except for face-on cases. No such analysis has been

done in previous studies mostly because of insufficient sensitivity of their continuum observations. Exceedingly high sensitivity as well as high angular resolution of ALMA allows us to perform such data analyses.

Model fitting

Our analysis of the disk structures is performed by χ^2 fitting of models to the continuum visibilities shown in Figure 3.6b. It should be noted that the full size of the continuum emission at 6σ level in Figure 3.1, ~ 280 AU (see Section 3.4.1) is twice the disk size expected from the radius kinematically estimated in Section 3.5.1. This suggests that the continuum emission arises not only from the disk but also from the envelope. Hence our models should include envelope structures as well as disk structures. Because the envelope around L1527 IRS shows a flattened morphology, the model we use in this section is based on a standard disk model (e.g., Dutrey et al., 1994) but modified to express a flattened dust envelope as well as a dust disk, as described below. We used the code described in Ohashi et al. (2014). The model includes 12 parameters summarized in Table 3.2. The radial dependence of temperature $T(R)$ and scale height $H(R)$ are described as $T(R) = T_1(R/1 \text{ AU})^{-q}$ and $H(R) = H_1(R/1 \text{ AU})^h$, respectively. This means that the scale height in our model is not assumed to be in HSEQ. To express dust disk and dust envelope structures, the radial dependence of surface density $\Sigma(R)$ is described by a combination of inner and outer profiles formulated as

$$\Sigma(R) = \frac{(2-p)M_{\text{disk}}}{2\pi(R_{\text{out}}^{2-p} - R_{\text{in}}^{2-p})} R^{-p} \times \begin{cases} 1 & (R \leq R_{\text{out}}) \\ S_{\text{damp}} & (R > R_{\text{out}}) \end{cases}, \quad (3.1)$$

where M_{disk} is a disk mass (mass within R_{out}) determined from $g/d=100$ and S_{damp} is a damping factor of the surface density for the outer dust envelope. R_{out} is the outer radius of the disk defined as the boundary between the disk and the envelope. In our model, mass density distribution $\rho(R, z)$ is determined from the scale height $H(R)$ and the sur-

Table 3.2. Fixed and Free Parameters of the Model Fitting (L1527 IRS)

Fixed	i	R_{in}	T_1	q	$\kappa(220 \text{ GHz})$	g/d
	85°	0.1 AU	403.5 K	0.5	$0.031 \text{ cm}^2 \text{ g}^{-1}$	100
Free	M_{disk}	R_{out}	p	S_{damp}	H_1	h
Best	$1.3^{+0.3}_{-0.4} \times 10^{-2} M_\odot$	$84^{+16}_{-24} \text{ AU}$	$1.7^{+0.1}_{-0.3}$	$0.19^{+0.03}_{-0.09}$	$0.11^{+0.02}_{-0.03} \text{ AU}$	$1.2^{+0.1}_{-0.1}$

face density $\Sigma(R)$ as $\Sigma/(\sqrt{2\pi}H) \exp(-z^2/2H^2)$ within the outermost radius of 1000 AU. Our model adopts the same power-law index of density for both disk and envelope, which is supported by theoretical simulations by Machida et al. (2010) without magnetic fields (see their Figure 5). Some of the parameters are fixed as shown in Table 3.2. Radio observations are considered to be not sensitive to temperature distribution because most observed continuum emissions are optically thin, which makes it hard to constrain temperature distribution by mm-continuum observations. Therefore, we fixed the temperature distribution in our model based on observations including infrared wavelengths (Tobin et al., 2008, 2013), which are more sensitive to temperature than radio observations. The inclination angle of the dust disk/envelope is fixed at $i = 85^\circ$ and the eastern side is on the near side for the observers (Oya et al., 2015). The other six quantities are free parameters ($M_{\text{disk}}, R_{\text{out}}, p, S_{\text{damp}}, H_1, h$). When radiative transfers were solved in 3D space to produce a model image, the following condition and quantities were assumed: local thermodynamic equilibrium (LTE), $g/d = 100$, and a dust opacity of $0.031 \text{ cm}^2 \text{ g}^{-1}$ calculated from a opacity coefficient of $\kappa(850 \mu\text{m}) = 0.035 \text{ cm}^2 \text{ g}^{-1}$ and an opacity index of $\beta = 0.25$ (Tobin et al., 2013).

After a model image was calculated from the radiative transfers, model visibility was obtained by synthetic observations through the CASA tasks *simobserve* and *listvis*. In the synthetic observations, the phase center was set at the center of the model image and the orientation (P.A.) was assumed to be the same as that of the observed continuum emission. Following the two observational tracks, we performed the synthetic observations without artificial noise twice with the same antenna configurations as the observations.

Then model visibilities were derived at the same points on the uv -plane as the observations. Using the model visibility and the observed continuum visibility, reduced χ^2 was calculated to evaluate the validity of each model. Without azimuthally averaging visibilities, all 1089 data points were used to calculate the reduced χ^2 defined as

$$\chi^2_{\nu} = \frac{1}{\sigma^2(2N_{\text{data}} - N_{\text{par}} - 1)} \sum_i \left[(\text{Re}V_i^{\text{obs}} - \text{Re}V_i^{\text{mod}})^2 + (\text{Im}V_i^{\text{obs}} - \text{Im}V_i^{\text{mod}})^2 \right] \quad (3.2)$$

where σ , V_i^{obs} , V_i^{mod} , N_{data} , and N_{par} are the standard deviation of noise in the observed visibility amplitude, the observed visibility, model visibility, the number of data points, and the number of free parameters, respectively; $N_{\text{data}} = 1089$ and $N_{\text{par}} = 6$ as mentioned above. N_{data} is multiplied by two because each visibility includes two independent values, real and imaginary parts. Using the distribution of reduced χ^2 in the parameter space, the uncertainty of each parameter is defined as the range of the parameter where the reduced χ^2 is below the minimum plus one ($= 6.6$) when all parameters are varied simultaneously. We also used the Markov Chain Monte Carlo method to find the minimum χ^2 efficiently.

Figure 3.7a represents a comparison of the observed continuum visibility with our best-fit model showing that the best-fit model overall reproduces the observations. The reduced χ^2 of the best-fit model is 5.6, which corresponds to a residual of $\sim 2.4\sigma$ on average. It is also confirmed that the best-fit model can reproduce the observations in an image space, as shown in Figure 3.8. Note that the model image in Figure 3.8a was not made through the synthetic observation using CASA but was simply made based on the best-fit parameters in Table 3.2 with convolution using the synthesized beam of our observations. This is because the synthetic observations using CASA produce a beam that is slightly different from the actual observations. Synthetic observation is not very crucial for this comparison, but convolution with the beam exactly same as the synthesized beam used in the actual observations is more crucial because model image is relatively compact as compared to the synthesized beam. The residual shown in Figure 3.8b was obtained by

subtracting the best-fit model, in the image space, from the observations, indicating that almost no significant residual can be seen in the image space.

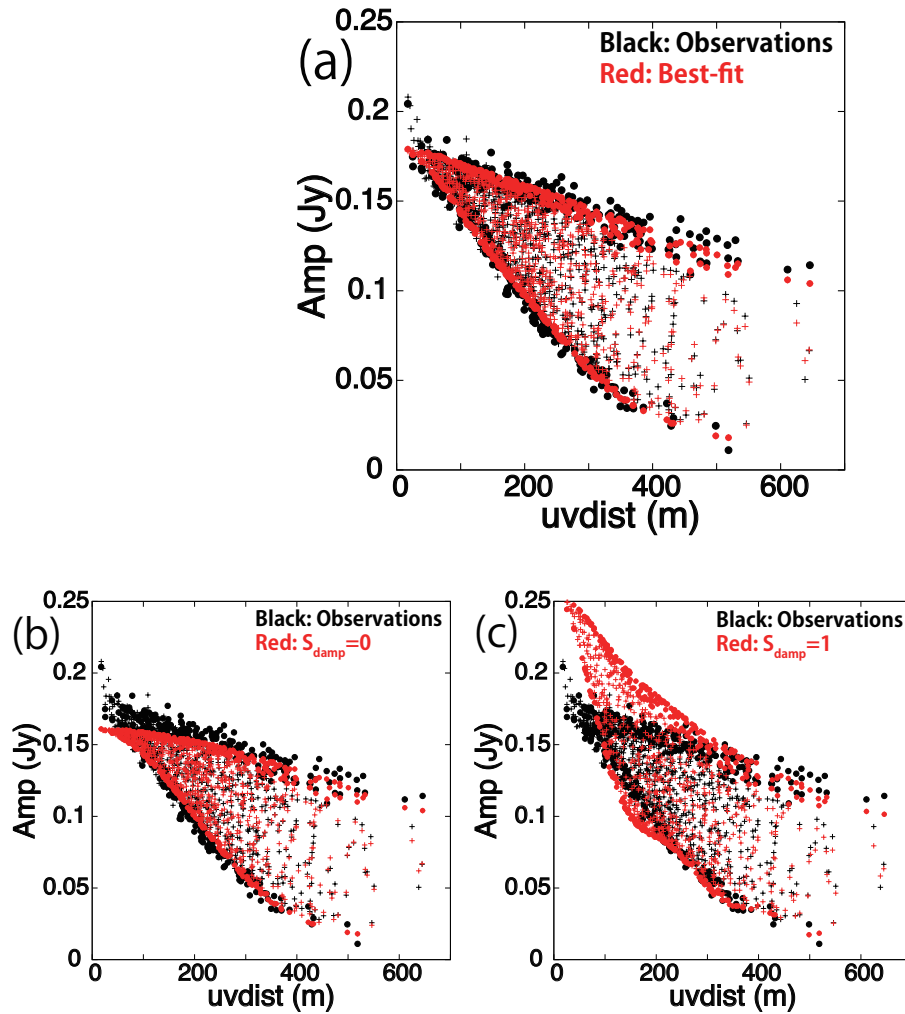


Figure 3.7 The observed continuum visibility (black circles and crosses) and (a) the best-fit model, (b) the model with $S_{\text{damp}} = 0$, and (c) the model with $S_{\text{damp}} = 1$, denoted with red circles and crosses. For the models in panel (b) and (c), parameters except for S_{damp} are fixed at those of the best-fit model. The observations are the same plot as Figure 3.6(b) except for the color, and thus the circles denotes the data points near the major- and minor-axis directions while crosses denote the other data points for both the observations and models.

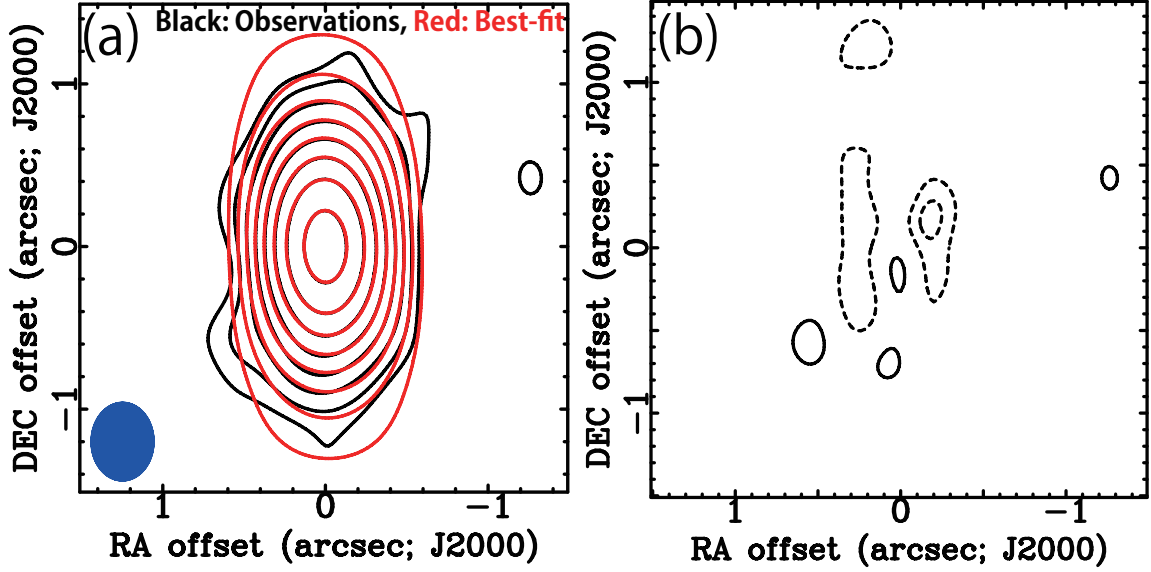


Figure 3.8 (a) The observed continuum image (black contours) and the best-fit model (red contours). (b) The residual obtained by subtracting the best-fit model from the observations. Contour levels are $-3, 3, 6, 12, 24, \dots \times \sigma$ for panel (a) and $-3, 3, 6, 9, \dots \times \sigma$ for panel (b), where 1σ corresponds to $0.2 \text{ mJy beam}^{-1}$. A blue filled ellipse at the bottom right corner in panel (a) denotes the ALMA synthesized beam; $0''.47 \times 0''.37$, P.A. = -0.4° . The spatial scale is different from Figure 3.1.

The parameters of the best-fit model are summarized in Table 3.2. The damping factor $S_{\text{damp}} = 0.19_{-0.09}^{+0.03}$, which is not zero but significantly smaller than the unity, suggests that the observed continuum emission arises from both a dust disk and a dust envelope with a significant jump of the column density between them. A much larger or smaller value than 0.19 cannot explain the observed visibilities as shown in Figure 3.7b and 3.7c. The former and the latter show models with $S_{\text{damp}} = 0$ and 1, respectively, where the other parameters are the same as those of the best-fit model. In Figure 3.7b and 3.7c visibility amplitude of models at longer uv -distance ($\gtrsim 300 \text{ m}$) appears to be similar to the observations in both cases, whereas visibility amplitude of the models with $S_{\text{damp}} = 0$ and 1 are lower and higher than the observations, respectively, at shorter uv -distance ($\lesssim 300 \text{ m}$). One might wonder a jump of dust opacity, as well as surface density, could also explain the observations. It is observationally confirmed, however, that the opacity index β does not change between on scales 100 AU and 1000 AU, based on observed dependency of spectral index on uv -distance (Tobin et al., 2013), and possible uncertainty of $\Delta\beta, \sim 0.2$,

adds only $\sim 8\%$ to the relative uncertainty of S_{damp} . The damping factor S_{damp} could also be directly affected by the power-law index of surface density p in the outer envelope, which was fixed to be the same as that of the inner disk. An analytical envelope model with a constant mass accretion rate provides a density profile $\rho \propto r^{-1.5}$ (Terebey et al., 1984), corresponding to a surface density profile $\Sigma \propto r^{-0.5}$. The case with this shallower index is discussed in Appendix 3.8.1, indicating that the difference does not change our conclusions significantly. Further discussion on the significant jump of the surface density between the dust disk and envelope will be presented in Section 3.6.

The best-fit value of $R_{\text{out}} = 84_{-24}^{+16}$ AU is close to the Keplerian disk radius kinematically derived from the C^{18}O results; the discrepancy between the two values are within their errors. This result suggests that the dust disk identified geometrically by this model fitting is consistent with the kinematically identified gaseous Keplerian disk. The power-law index of the surface density, $p = 1.7_{-0.3}^{+0.1}$, is a bit steeper than the typical value for T Tauri disks, ~ 1.0 (Andrews & Williams, 2007; Hughes et al., 2008; Andrews et al., 2010) while similar steep p has been found toward a few other protostars as well (e.g., Yen et al., 2014; Aso et al., 2015).

The power-law index of the scale height, $h = 1.2_{-0.1}^{+0.1}$, corresponds to that for HSEQ ($h = 1.25$) within the error range. To examine whether the best-fit model is indeed in HSEQ, the scale height of the disk at a certain radius can be compared directly with that in HSEQ. The scale height of the best-fit model at $R = R_{\text{out}}$ is calculated to be ~ 20 AU while the scale height of a disk in HSEQ is estimated to be ~ 15 AU at the same radius when the central stellar mass is $M_* = 0.45 M_{\odot}$ as kinematically estimated from the rotation profile (see Section 3.5.1), the temperature is 44 K as estimated from the temperature profile we used in the model, and a mean molecular weight is $2.37 m_{\text{H}}$. This comparison suggests that the disk around L1527 IRS is most probably in HSEQ. Note that Tobin et al. (2013) suggested a highly flared disk around L1527 IRS, which has a scale height of 38 AU at R_{out} . We consider that their estimated scale height is higher than ours because their observations included infrared wavelength, which may be contaminated by

scattered light making the disk geometrically thick in appearance.

The best-fit model shows that the disk around L1527 IRS has a mass and a radius similar to those of T Tauri disks. The scale height is also similar to that of T Tauri disks in the sense that it is in HSEQ. This indicates that the disk around L1527 IRS is geometrically as well as kinematically similar to T Tauri disks, although we also note that the power-law index of the surface density of the disk is steeper than that of T Tauri disks.

3.6 DISCUSSION

3.6.1 Possible Origin of the Surface Density Jump

A jump of the surface density between the envelope and the Keplerian disk around L1527 IRS has been found by our model fittings to the continuum visibility. In fact, such a density jump can be qualitatively confirmed in numerical simulations of disk evolution (Machida et al., 2010) and a similar density jump by a factor of ~ 8 is suggested to reproduce continuum emission arising from the disk around HH 212 (Lee et al., 2014a). These results suggest that disks around protostars may be not only kinematically but also geometrically distinguishable from their surrounding envelopes. It is important to note that the disk radius of L1527 IRS geometrically estimated with the density jump is fairly consistent with the radius kinematically estimated, suggesting that the density jump may be physically related with kinematical transition from infalling motions to Keplerian rotation. In this section, the possible origin of the surface density jump is quantitatively discussed.

Surface density of the disk at the boundary ~ 84 AU can be calculated from our best-fit model to be $\Sigma_{\text{disk}} = 0.42 \text{ g cm}^{-2}$ with Equation 3.1 and the best-fit parameters shown in Table 3.2. This surface density is within the typical range derived for Class II YSO disks in Taurus (Andrews & Williams, 2007) and Ophiuchus (Andrews et al., 2009, 2010). On the other hand, volume density of the envelope at the boundary can be

calculated from the best-fit model to be $\rho_{\text{env}} = 1.0 \times 10^{-16} \text{ g cm}^{-3}$, which corresponds to the number density of $n_{\text{env}} = 2.5 \times 10^7 \text{ cm}^{-3}$. For embedded young stars in Taurus-Auriga molecular cloud, a typical density distribution of protostellar envelopes can be described as $\sim (0.3 - 10) \times 10^{-13} \text{ g cm}^{-3} (R/1 \text{ AU})^{-2}$ (Kenyon et al., 1993), which provides $(0.04 - 1.4) \times 10^{-16} \text{ g cm}^{-3}$, corresponding to $(0.1 - 3.5) \times 10^7 \text{ cm}^{-3}$, at the boundary, R_{out} . This indicates that the envelope density in the best-fit model is also reasonable when compared with other observations

Because the disk around L1527 IRS is considered to still grow with mass accretion from the envelope, as discussed in Ohashi et al. (2014), a possible origin of the density jump may be mass accretion from the envelope to the disk, resulting in radial pressure equilibrium between the infalling envelope and the Keplerian disk. The gravity of a central protostar causes material in the envelope to infall dynamically and thus the material has radial infall velocity $u_r(R)$ as a function of radius. Because this radial velocity should be supersonic, radial pressure from the envelope to the disk at R_{out} can be assumed to be dominated by dynamic pressure $\rho_{\text{env}} u_r^2(R_{\text{out}})/2$, where ρ_{env} is density of the envelope at the boundary. On the other hand, material in the disk has almost no radial motion because the material is in Keplerian rotation. Radial pressure from the disk to the envelope can thus be assumed to be dominated by thermal pressure $\rho_{\text{disk}} c_s^2$, where ρ_{disk} and c_s are density of the disk and sound speed, respectively, at the boundary. On the assumption of the equilibrium of the two pressure, the predicted density jump can be written as $S_{\text{damp}} = \rho_{\text{env}}/\rho_{\text{disk}} = 2c_s^2/u_r^2$. The sound speed at the boundary can be calculated from our best-fit model to be $c_s = 0.39 \text{ km s}^{-1}$. Regarding the infall velocity, we assume u_r to be the product of a constant coefficient α and free fall velocity $\sqrt{2GM_*/R_{\text{out}}}$, i.e., $u_r = \alpha\sqrt{2GM_*/R_{\text{out}}}$, as was discussed by Ohashi et al. (2014). By using $M_* = 0.45 M_{\odot}$ and $R_{\text{out}} = 84 \text{ AU}$, this infall velocity can be calculated to be $3.1\alpha \text{ km s}^{-1}$. In order to explain $S_{\text{damp}} = 0.19$, α should be ~ 0.4 , which is consistent with the range of α (0.25-0.5) Ohashi et al. (2014) found. This quantitative discussion suggests that mass accretion from the envelope to the disk is a possible origin of the density jump we found.

3.6.2 Structures of the $C^{18}O$ gas disk

In the previous sections the structures of the disk and the envelope around L1527 IRS have been discussed based on the continuum observations tracing the disk and the envelope. $C^{18}O$ emission, on the other hand, also traces them, as was discussed in Ohashi et al. (2014). Because it can be reasonably assumed that gas and dust are well coupled and mixed in the protostellar phase in contrast to the T Tauri phase where gas and dust can be decoupled because of grain growth, it is important to examine whether the structures of the disk and the envelope revealed in the dust observations can also be valid for those traced in $C^{18}O$ emission.

In order to answer the question mentioned above, in this section, models for $C^{18}O$ are constructed based on the best-fit dust model derived from the fitting to the continuum visibility shown in Section 3.5.2, and models are compared with the $C^{18}O$ observations. The models of $C^{18}O$ have the same profiles of the surface density, temperature, and scale height as those of the best-fit dust model derived from the fitting to the continuum visibility shown in Section 3.5.2. The surface density profile has a jump at a radius of 84 AU, which is the boundary between the disk and the envelope, as was suggested by the best-fit dust model. In addition to these constraints on structures, $C^{18}O$ models also require velocity fields, which cannot be constrained by the continuum observations. For velocity fields, we assume that $C^{18}O$ models follow the radial profile of the rotation derived from the $C^{18}O$ observations in Section 3.5.1, and that of infall introduced in Section 3.6.1. Note that we adopt 74 AU as the radius where the rotation profile has a break even though the geometrical boundary between the disk and the envelope is set at 84 AU in radius, as mentioned above. These geometrical and kinematical structures of the $C^{18}O$ models are fixed in the following discussion. Importantly the $C^{18}O$ models still depend on the fractional abundance of $C^{18}O$ relative to H_2 , $X(C^{18}O)$, as discussed later.

In order to compare models and observations, $C^{18}O$ data cubes are calculated from the models described above. It should be noted that the $C^{18}O$ emission obviously traces

more extended structures arising from outer parts of the envelope, as compared with the dust emission. Because structures of the disk and the envelope adopted for C¹⁸O model are based on the continuum emission detected within a radius of $\sim 1''$ (see Figure 3.1), comparisons between C¹⁸O models and observations should be made only within a radius of $1''$. According to the C¹⁸O velocity channel maps shown in Figure 3.3, the C¹⁸O emission arises within a radius of $\sim 1''$ when $|V_{\text{LSR}}| > 2.0 \text{ km s}^{-1}$, and only C¹⁸O emission having these LSR velocities is discussed in comparisons between the models and the observations. When C¹⁸O data cubes are calculated from the models, radiative transfers, including both dust and C¹⁸O opacities, are also solved in 3D and velocity space, and then dust continuum emission is subtracted to derive the final model cubes. The model data cubes calculated from the radiative transfers are convolved with a Gaussian beam having the same major and minor axes, and orientation as the synthesized beam of our observations.

Figure 3.9a shows a comparison of moment 0 maps between a model and the observations. In this model, a constant C¹⁸O abundance of 4×10^{-8} is adopted. In this case, significant residuals at 9σ level are left, as shown in Figure 3.9b. Inner regions show negative residuals while outer regions show positive residual, demonstrating that the model C¹⁸O is too strong in inner regions while it is too weak in outer regions, as compared with the observations. Note that neither a higher nor a lower constant value than 4×10^{-8} of the C¹⁸O abundance improves the model. Although there are a couple of factors to change the C¹⁸O intensity in the model, the abundance of C¹⁸O is the only one that changes the intensity of C¹⁸O if we still remain the same physical structures of the disk in the model, i.e., in order to make the C¹⁸O intensity weaker in inner regions and stronger in outer regions in the model, the C¹⁸O abundance might be lower in inner regions and higher in outer regions. For instance, if the C¹⁸O abundance in outer regions ($R > 84 \text{ AU}$) is the same as the one in interstellar medium (ISM), 5×10^{-7} (Lacy et al., 1994; Jørgensen et al., 2005; Wilson & Rood, 1994), and the abundance in the inner regions ($R < 84 \text{ AU}$) decreases by a factor of ~ 20 due to the freeze-out of C¹⁸O molecules, the observations can

be explained by the model. T Tauri disks are, however, usually considered to have temperature profiles having higher temperature in inner regions (e.g., Andrews & Williams, 2007), and the disk around L1527 IRS is also considered to have such a temperature profile as Tobin et al. (2013) suggested. With such a temperature profile, it would be difficult for the disk to have a lower $C^{18}O$ abundance in the inner regions because of the molecular freeze-out.

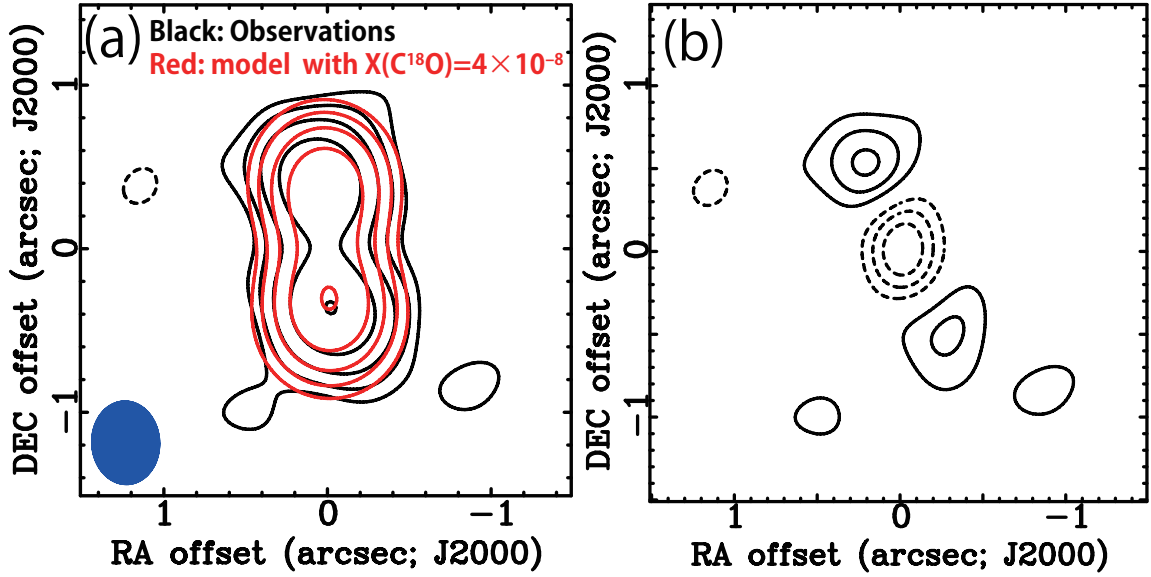


Figure 3.9 Comparison of $C^{18}O$ moment 0 maps integrated over $|V| > 2.0 \text{ km s}^{-1}$. (a) Observations in black contours and a model with $X(C^{18}O) = 4 \times 10^{-8}$ in red contours. (b) The residual obtained by subtracting the model from the observations. Contour levels are $-3, 3, 6, 12, 24, \dots \times \sigma$ in panel (a) and $-3, 3, 6, 9, 12, \dots \times \sigma$ in panel (b), where 1σ corresponds to $1.8 \text{ mJy beam}^{-1} \text{ km s}^{-1}$. A blue filled ellipse at the bottom right corner denotes the ALMA synthesized beam; $0''.50 \times 0''.40$, P.A. = 3.1° .

One possible $C^{18}O$ abundance distribution that can explain the observations is the one with a local enhancement of the $C^{18}O$ molecule, as has been suggested for the SO molecular abundance around L1527 IRS by Ohashi et al. (2014); they suggested that the SO abundance is locally enhanced around L1527 IRS because of accretion shocks making the dust temperature sufficiently high for SO molecules freeze-out on dust grains to be desorbed. An example of such a $C^{18}O$ abundance distribution is a constant abundance of 2×10^{-8} with the ISM abundance only radii between 80 and 88 AU. Figure 3.10 shows the comparison between the model with this $C^{18}O$ abundance distribution and the obser-

vations, suggesting that the model with this $C^{18}O$ abundance distribution can reproduce the observations with reasonably small residual.

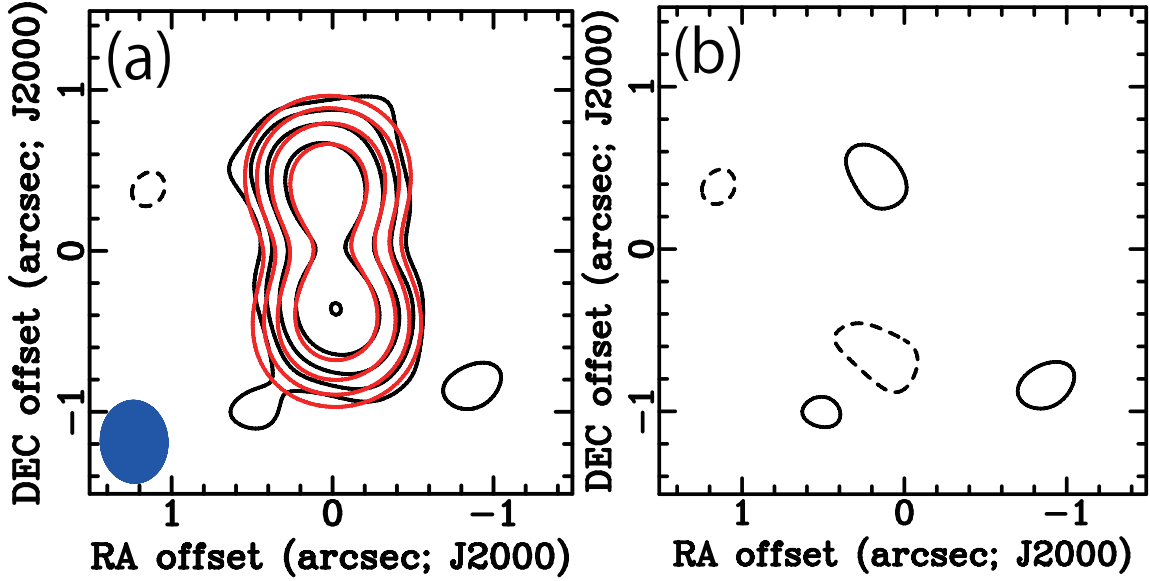


Figure 3.10 The same figures as Figure 3.9 but the model has enhancement of $C^{18}O$ abundance: $X(C^{18}O) = 5 \times 10^{-7}$ in 80-88 AU and $X(C^{18}O) = 2 \times 10^{-8}$ in the other regions.

As was explained for the case of the SO abundance distribution around L1527 IRS by Ohashi et al. (2014), the constant lower $C^{18}O$ abundance can be explained as freeze-out of $C^{18}O$ molecules due to low temperature, while the $C^{18}O$ abundance can be locally enhanced because of accretion shocks making dust temperature high enough for frozen-out $C^{18}O$ molecules to be back to gas phase. In fact, freeze-out of CO was reported toward the protoplanetary disks (Qi et al., 2004; Favre et al., 2013; Bell et al., 2013). The freeze-out can change abundance of CO by a factor of 10-100 (Aikawa et al., 2015). It is noted that the temperature within 300 AU is not below the sublimation temperature of the CO molecule (~ 20 K) according to the temperature profile used in our model. We should also note, however, that there would be a temperature gradient along the vertical direction, and the temperature profile in the model refers to the temperature averaged along the vertical direction. In protoplanetary disks, midplane temperature is expected to be ~ 4 times lower than disk-surface temperature on a ten AU scale in theoretical and observational studies (Gorti & Hollenbach, 2008; Woitke et al., 2009; Williams &

Best, 2014), suggesting that the midplane temperature can be ~ 2.5 times lower than the averaged temperature. On the other hand accretion shocks near the boundary between the disk and the envelope around L1527 IRS would also be expected because materials in the envelope still have infall motions. We note, however, that the local enhancement of the C^{18}O abundance discussed here cannot be directly shown in the observed C^{18}O map because of the limited angular resolution of the present observations. It is therefore difficult for us to find a unique solution of the C^{18}O abundance distribution for the model that can explain the observations. Nevertheless the above discussion suggests that the disk geometrical structures derived from the dust continuum observations can also explain the disk structures traced in C^{18}O .

3.7 CONCLUSIONS

We have observed the Class 0/I protostar L1527 IRS in Taurus star-forming region with ALMA during its Cycle 1 in 220 GHz continuum and $\text{C}^{18}\text{O } J = 2 - 1$ line emissions to probe the detailed structures of the disk and the envelope around L1527 IRS. The 220 GHz continuum emission spatially resolved with an angular resolution of $\sim 0''.5 \times 0''.4$ shows a similar elongated structure in the north-south direction. Its deconvolved size is estimated from a 2D Gaussian fitting to be $\sim 0''.53 \times 0''.15$, showing a significantly thinner structure than those previously reported on the same target. The $\text{C}^{18}\text{O } J = 2 - 1$ emission overall shows an elongated structure in the north-south direction with its velocity gradient mainly along the same direction. The integrated intensity map shows a double peak with the central star located between the peaks, due to a continuum subtraction artifact. The elongation of the continuum as well as C^{18}O clearly indicates that these emissions trace the disk/envelope system around L1527 IRS and the velocity gradient along the elongation is naturally considered to be due to rotation of the system, as was previously suggested.

The radial profile of rotational velocity of the disk/envelope system obtained from the position-velocity diagram of the C^{18}O emission cutting along the major axis of the con-

tinuum emission was fitted with a double power-law, providing the best-fit result with a power-law index for the inner/higher-velocity (p_{in}) of 0.50 and that for the outer/lower-velocity component (p_{out}) of 1.22. This analysis clearly suggests the existence of a Keplerian disk around L1527 IRS, with a radius kinematically estimated to be $\sim 74 \pm 2$ AU. The dynamical mass of the central protostar is estimated to be $\sim 0.45 M_{\odot}$.

In order to investigate structures of the disk/envelope system, χ^2 model fittings to the continuum visibility without any annulus averaging have been performed, revealing a density jump between the disk and the envelope, with a factor of ~ 5 higher density on the disk side. The disk radius geometrically identified with the density jump is consistent with the Keplerian disk radius kinematically estimated, suggesting that the density jump may be related to the kinematical transformation from infalling motions to Keplerian motions. One possible case to form such a density jump is that dynamical pressure due to infalling motions in the envelope is balanced with thermal pressure in the disk at the boundary between the envelope and the disk. If this is the case, to form the density jump with a factor of ~ 5 requires the infall velocity in the envelope to be ~ 0.4 times slower than the free fall velocity yielded by the central stellar mass. In addition to the density jump, it was found that the disk is roughly in hydrostatic equilibrium. The geometrical structures of the disk found from the χ^2 model fittings to the continuum visibility can also reproduce the C^{18}O observations as well, if C^{18}O freeze-out and localized desorption possibly occurring within $\sim 1''$ from the central star are taken into account.

3.8 APPENDIX

3.8.1 Shallower Index for Outer Envelope

In Section 3.5.2 the best-fit model provides several parameters of the disk and the envelope. Among the parameters, the damping factor S_{damp} is degenerated with the power-law index of surface density for the outer envelope, which is fixed to the same index as that of the inner disk in Section 3.5.2. While this condition is supported by theoretical simulations (Machida et al., 2008), we also investigate the case with a different index $p_{\text{env}} = 0.5$ for the outer envelope in this appendix. The density profile is predicted by an analytical envelope model with a constant mass accretion rate. The damping factor S_{damp} is redefined with this power-law index as follows:

$$\Sigma(R) = \Sigma(R_{\text{out}})S_{\text{damp}} \left(\frac{R}{R_{\text{out}}} \right)^{-0.5} \quad (R > R_{\text{out}}), \quad (3.3)$$

where $\Sigma(R_{\text{out}})$ is the surface density at $R = R_{\text{out}}$ defined by Equation 3.1. To focus on the effect of the shallower index on S_{damp} , we fix all other parameters to be those of the best-fit model in Section 3.5.2. In this case, the damping factor is estimated to be $S_{\text{damp}} = 0.08_{-0.04}^{+0.03}$, which is smaller than that of the best-fit model in Section 3.5.2, with a reduced $\chi^2 = 5.9$. The smaller S_{damp} of 0.08 corresponds to $\alpha = 0.6$ defined in Section 3.6.1. Although this coefficient is larger than the case of the best-fit model in Section 3.5.2 ($\alpha = 0.4$) and not quite consistent with the results by Ohashi et al. (2014), it is still smaller than the unity. Figure 3.11 shows comparison of this alternative model and the observations. The C^{18}O model has $X(\text{C}^{18}\text{O}) = 5 \times 10^{-7}$ in $R = 80\text{-}88$ AU and $X(\text{C}^{18}\text{O}) = 1 \times 10^{-8}$ at the other radii. Although the model provides slightly larger residuals in the image domain, it reproduces the observations overall as well as the best-fit model in Section 3.5.2. Therefore, even if the shallower index is adopted, it does not change our conclusions that infall motion in the envelope around L1527 IRS is slower than the free-fall and basically the C^{18}O emission can also be explained by the same

structures as the dust continuum emission.

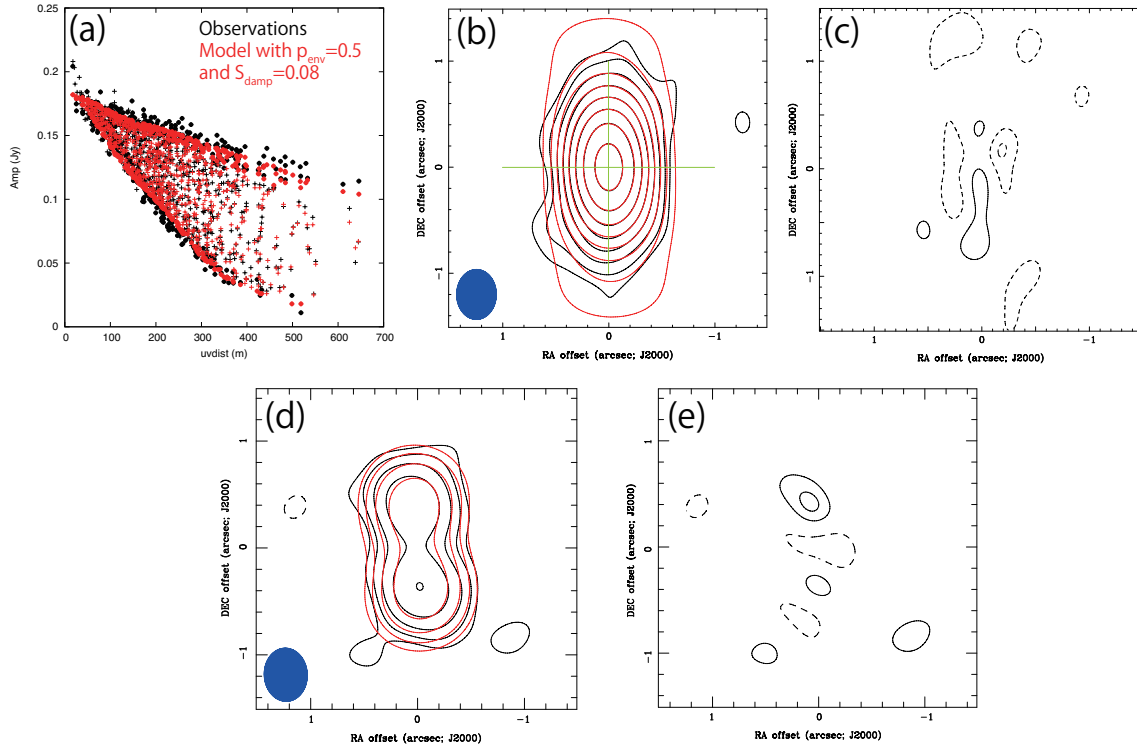


Figure 3.11 Comparison of the continuum and C^{18}O observations and the alternative model with $p_{\text{env}} = 0.5$, $S_{\text{damp}} = 0.08$, and $\alpha = 0.6$. Panels (a), (b), (c), (d), and (e) are the same figures as Figure 3.7a, Figure 3.8a, Figure 3.8b, Figure 3.10a, and Figure 3.10b, respectively, but with $p_{\text{env}} = 0.5$, $S_{\text{damp}} = 0.08$, and $\alpha = 0.6$. The C^{18}O model has $X(\text{C}^{18}\text{O}) = 5 \times 10^{-7}$ in 80-88 AU and $X(\text{C}^{18}\text{O}) = 1 \times 10^{-8}$ at the other radii.

Chapter 4

ALMA CYCLE 3 OBSERVATIONS OF SERPENS MAIN CLUSTER

4.1 ABSTRACT

In order to extend the targets for our research into objects in earlier star formation phases, we have observed five regions in Serpens Main star forming region with Atacama Large Millimeter/submillimeter Array (ALMA) during its Cycle 3 in 1.3-mm dust continuum, ^{12}CO ($J = 2 - 1$) line, and C^{18}O ($J = 2 - 1$) line emissions with an angular resolution of $\sim 0''.5$, which corresponds to ~ 210 AU at the distance of Serpens Main. The five regions were chosen based on 1.3-mm continuum and ^{12}CO ($J = 2 - 1$) mosaicking observations using Submillimeter Array (SMA) and $70\ \mu\text{m}$ continuum observations using *Herschel*; three of them have no counterpart in infrared wavelength including $70\ \mu\text{m}$, suggesting that those sources are in an extremely earlier phase, first hydrostatic cores (FHSC). The ALMA observations have identified twelve sources in 1.3-mm continuum emission, some of which are spatially resolved from the 1.3-mm continuum sources identified with the SMA observations. All of them have been found to have associated ^{12}CO outflows, with a few exceptions. We have measured their bolometric temperature and bolometric luminosity, as well as internal luminosity using *Spitzer* and *Herschel* data,

revealing an extremely cold (23 K) and low luminosity ($0.05 L_{\odot}$) source, SMM11a, which would be a new FHSC candidate. The inclination angle of its ^{12}CO outflow was estimated from simple model fittings to the integrated intensity map and position-velocity diagrams suggesting that its inclination angle is $\sim 80^{\circ}$. In addition to its low bolometric temperature and luminosity, its outflow and chemical properties also support that SMM11a is a strong candidate of FHSC. Furthermore the observed visibility suggests that the degree of spherical symmetry decrease in the course of evolution. SMM11a will be one of the best targets to investigate disk formation in the FHSC phase.

4.2 INTRODUCTION

Disk formation around protostars has been investigated with observations toward two specific targets, the Class I protostar TMC-1A and the younger Class 0/I protostar L1527 IRS, in Taurus molecular cloud in previous Chapters. Our results suggested that more evolved protostars tend to have a larger disk. The Class 0 protostar B335 is also reported to have no disk larger than > 10 AU with a possibility that its age is as young as ~ 0.05 Myr. On the other hand theoretical simulations predict that much younger objects, ~ 500 yr after the first core formation, can have a disk on a 100-AU scale depending on initial rotation (Machida et al., 2014). It is thus required as the next step for us to find other remarkable targets so as to extend the research into various, particularly earlier, evolutionary phases for further understanding of disk formation.

Serpens Main, which consists of the two subcluster NW and SE on a 0.1 pc scale, is located at low declination $\delta \sim +1^{\circ}$. The distance of this region is 429 pc (Dzib et al., 2011). Gas density in this region is $\sim 10^4 \text{ cm}^{-3}$ and in average and column density of H_2 molecules is $> 10^{22} \text{ cm}^{-2}$ (Enoch et al., 2007). The NW subcluster have a uniform velocity field and a homogeneous 10 K gas temperature while the SE subcluster has a large-scale velocity gradient and its temperature is in 10-20 K (Duarte-Cabral et al., 2010). Previous observations with JCMT (Davis et al., 1999; Casali et al., 1993)

identified ten submillimeter continuum condensations (SMM1, SMM2, ...) and recent *Spitzer/Herschel* observations found infrared sources associated with them (e.g., Enoch et al., 2009; Dunham et al., 2015). A Class 0 source in SMM1 condensation and another Class 0 source in SMM9 in condensation have names of FIRS1 and S68N, respectively. FIRS1 is a intermediate-mass protostar with a highly collimated molecular jet where ionization of an outflow cavity was directly detected by ALMA observations (Hull et al., 2016). An outflow associated with S68N was observed with the 15-m Swedish-ESO Submillimetre Telescope (SEST) in $^{12}\text{CO } J = 2 - 1$ with a angular resolution of $23''$ and other molecules. Serpens Main also includes Class II and Class III objects more dispersed than protostars, implying two main episodes of star formation. The time difference of formation between the pre-main sequence stars and the protostars are estimated 2 Myr (Harvey et al., 2007; Kaas et al., 2004). Duarte-Cabral et al. (2011) suggests that cloud-cloud collision may have triggered the most recent episode of star formation; such collision can also explain differences of temperature and age dispersion between the tow subclusters. The difference between the two subclusters have also been investigated with interferometric observations. Lee et al. (2014b) observed Serpens Main with CARMA in $\text{N}_2\text{H}^+ J = 1 - 0$ line emission and studied gas structures using dendrogram technique. The emission shows filamentary structures from SE subcluster with lengths of ~ 0.2 pc and subsonic velocity dispersions except for the central region of the subcluster. The typical width of the filaments, ~ 0.036 pc, is three times smaller than the characteristic value derived from *Herschel* observations. The statistics derived from dendrogram analysis suggests complexity of hierarchical structure in SE subcluster.

In this Chapter we report new ALMA Cycle 3 observations of Serpens Main in $^{12}\text{CO } J = 2 - 1$ line, $\text{C}^{18}\text{O } J = 2 - 1$ line, and 1.3-mm continuum emissions. *Spitzer* and *Herschel* images of this region are also inspected to investigate evolutionary phases. Sample selection based on SMA archival data and our ALMA observations, as well as data reduction, are described in Section 4.3. In Section 4.4, we present the continuum and ^{12}CO outflows, which are also compared with the infrared images. In Section 4.5, we

focus on a remarkable 1.3-mm source, SMM11a; its outflow property, C¹⁸O abundance, and morphology in 1.3-mm continuum emission will be investigated in detail. We present a summary of the results and our interpretation in Section 4.6.

4.3 SAMPLES AND ALMA OBSERVATIONS

4.3.1 Samples

Our sample selection is based on SMA archival data of a blind survey toward Serpens Main cluster carried out with the mosaicking mode (PI: Jonathan P. Williams) in 1.3-mm continuum and ¹²CO $J = 2 - 1$ line emissions. Figure 4.1 shows the entire region of Serpens Main cluster with JCMT 850- μ m map and Herschel 70- μ m map. The SMA mosaicking observations are toward the northwestern subcluster and the southeastern subcluster. The two subclusters include widely known submillimeter continuum condensations identified by JCMT observations, which labeled with the numbers in Figure 4.1. Figure 4.2 shows four parts of the SMA observations overlaid on Herschel 70 μ m images. Positions of YSOs identified by *Spitzer* (Dunham et al., 2015) are also plotted in this figure. We label the SMA 1.3-mm sources as shown in this figure, such as SMM11a. SMM9a is known as the Class 0 protostar S68N (Eiroa & Casali, 1992). The sources except for SMM9d appears to be associated with ¹²CO emission and the sources except for SMM9a and SMM9b are not identified as a *Spitzer* YSO. Furthermore SMM11a and SMM9d, and possibly SMM4a, has no counterpart in *Herschel* 70 μ m. The detection in 1.3 mm indicates that there is dust with high (column) density while the deficit in 70 μ m indicates that the dust does not have high temperature ($\lesssim 50$ K); these results suggest that the sources are in very early phases of star formation. For these reasons, we chose SMM11a, SMM4a, and SMM9d as our targets and also observed SMM9a and another Class 0 protostar in SMM2 condensation for comparison.

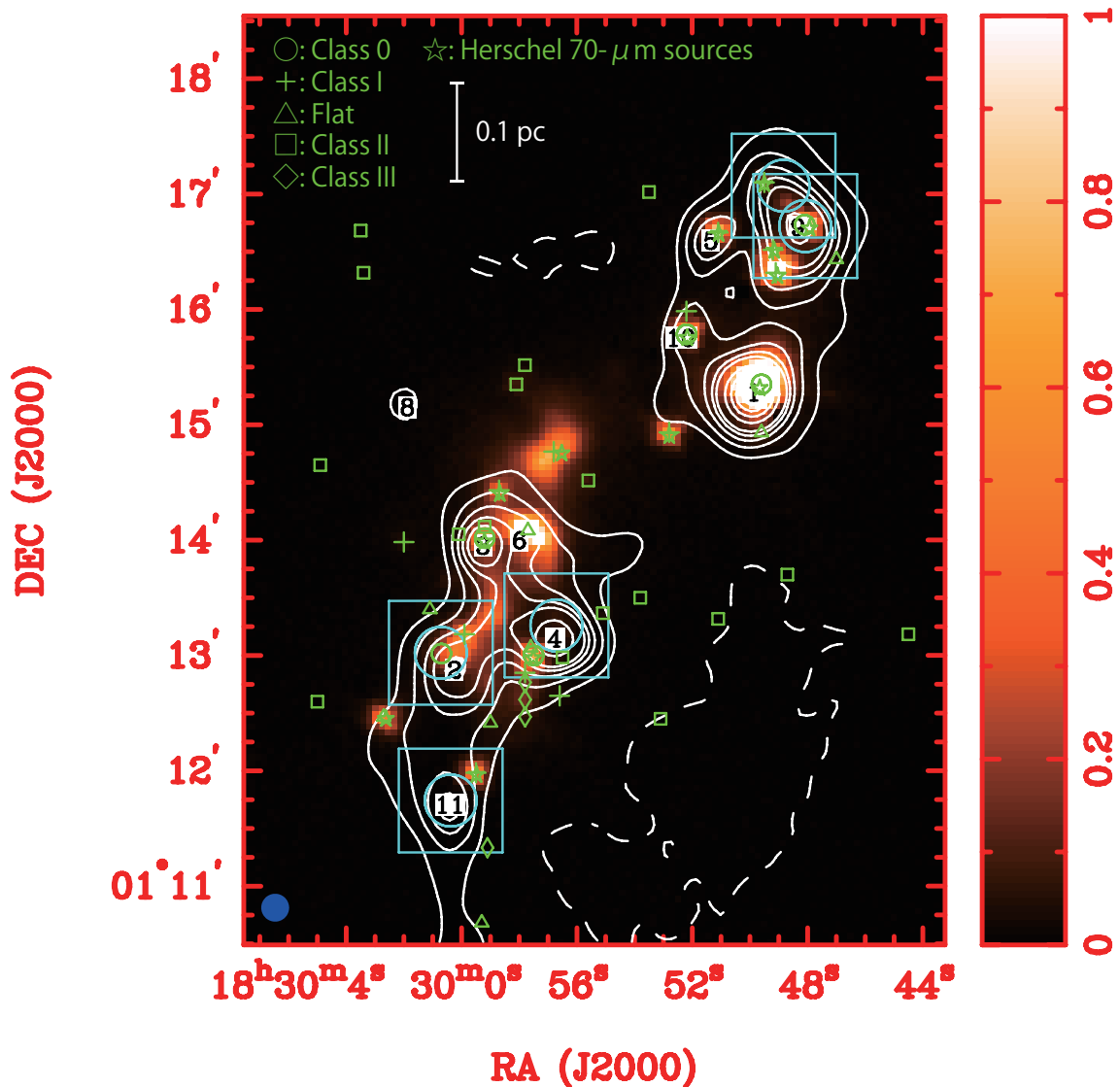


Figure 4.1 JCMT 850- μm contour map of Serpens Main cluster overlaid on Herschel 70- μm image. Contour levels are from 3σ to 15σ with 3σ spacing and from 15σ with 15σ spacing, where 1σ corresponds to $0.15 \text{ Jy beam}^{-1}$. The unit of 70- μm image is Jy pixel^{-1} and the pixel size is $3''.2$. Green marks except for pentagrams indicate YSO positions identified by *Spitzer* observations; the classification is based on extinction corrected a spectral index α' and extinction corrected bolometric temperature T'_{bol} in Dunham et al. (2015). The pentagrams indicates positions of Herschel 70- μm sources (Bressert, 2012). Submillimeter continuum condensations (Davis et al., 1999) are labeled with numbers in white boxes. Cyan circles and squares indicate FWHM of primary beams and mapped regions, respectively, in our ALMA observations. Blue ellipse at the bottom left corner denotes the JCMT beam size ($14''$).

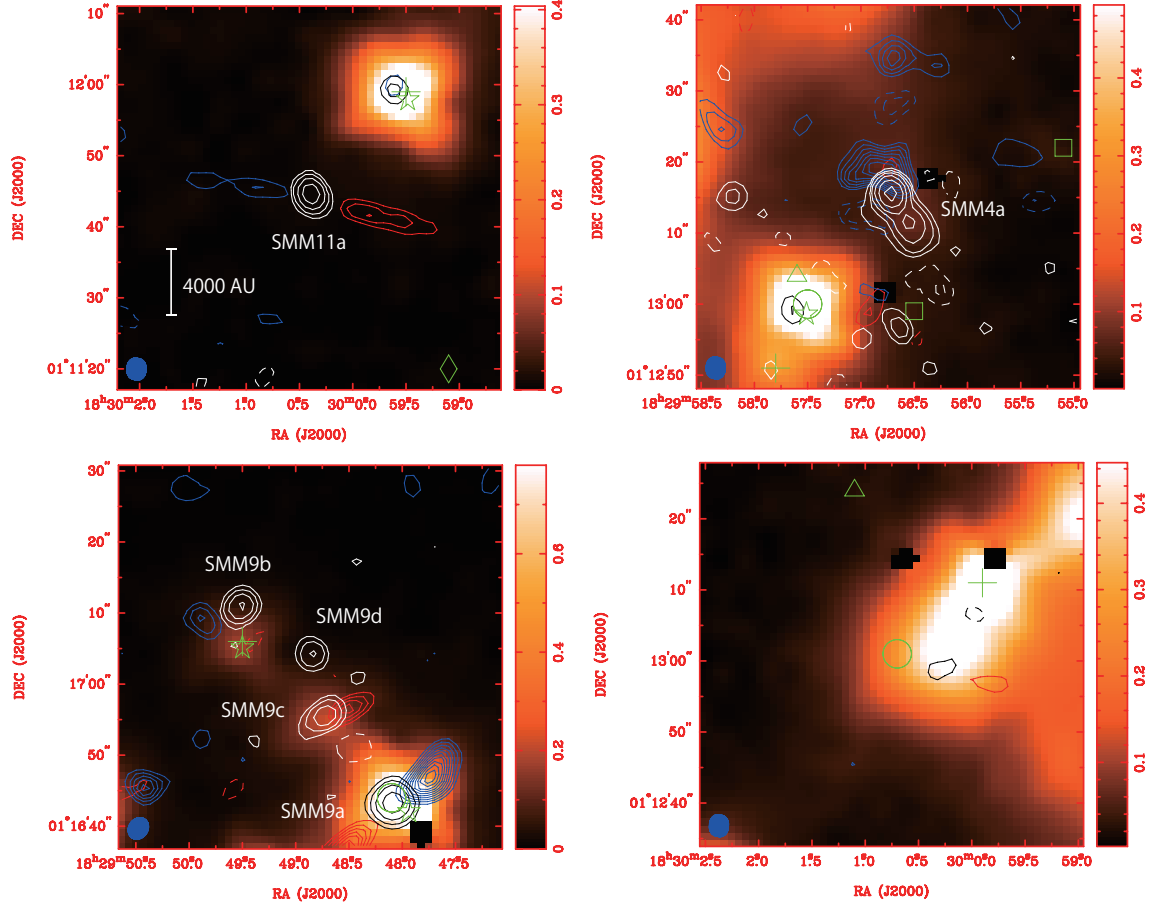


Figure 4.2 Four parts of SMA mosaicking observations overlaid on Herschel $70 \mu\text{m}$ images. White/black contours, blue contours, and red contours are 1.3-mm continuum emission, blue lobes of $^{12}\text{CO } J = 2 - 1$ line emission, and red lobes of $^{12}\text{CO } J = 2 - 1$ line emission. Contour levels are $-10, -5, 5, 10, 20, 40, \dots \times \sigma$, where 1σ corresponds to $2 \text{ mJy beam}^{-1} \text{ km s}^{-1}$ for the continuum emission and 2σ spacing from 5σ for the ^{12}CO emission. Blue filled ellipse at the bottom left corner denotes SMA synthesized beam; $3''.2 \times 2''.7$ (-36°) for the continuum emission and $3''.1 \times 2''.5$ (-31°) for the ^{12}CO continuum emission. Green marks are the same as those in Figure 4.1. Labels, such as SMM11a, indicate SMA 1.3-mm source names labeled in this chapter.

4.3.2 ALMA Observations and Data Reduction

We observed five regions in Serpens Main cluster during Cycle 3 using ALMA on 2016 May 19 and 21. Observing time including overhead was ~ 43 min and ~ 72 min while on-source time was 4.5 min and 9.0 min in the first and the second days, respectively. J1751+0939 and Titan were observed as the passband calibrator and the flux calibrator,

respectively. J1830+0619 and J1824+0119 were observed as the gain calibrator. The numbers of antenna were 37 and 39 in the first and the second days, respectively, and the antenna configuration of the second day was more extended than that of the first day. The antenna configuration covers projected baseline length from 15 to 613 m (11-460 k λ in uv -distance at 225 GHz). This minimum baseline resolves out more than 50% of the flux when a structure is extended more than 8'' (Wilner & Welch, 1994), corresponding to ~ 3400 AU at a distance of Serpens Main cluster. The five pairs of the map-center coordinates were $\alpha(\text{J2000}) = 18^{\text{h}}30^{\text{m}}00^{\text{s}}.38$, $\delta(\text{J2000}) = 1^{\circ}11'44''.55$, $\alpha(\text{J2000}) = 18^{\text{h}}29^{\text{m}}56^{\text{s}}.71$, $\delta(\text{J2000}) = 1^{\circ}13'15''.60$, $\alpha(\text{J2000}) = 18^{\text{h}}29^{\text{m}}48^{\text{s}}.83$, $\delta(\text{J2000}) = 1^{\circ}17'04''.30$, $\alpha(\text{J2000}) = 18^{\text{h}}29^{\text{m}}48^{\text{s}}.08$, $\delta(\text{J2000}) = 1^{\circ}16'43''.30$, and $\alpha(\text{J2000}) = 18^{\text{h}}30^{\text{m}}00^{\text{s}}.72$, $\delta(\text{J2000}) = 1^{\circ}13'01''.40$. Although two of them are relatively close to each other, the distance is roughly the same as FWHM of the primary beam ($\sim 27''$). Spectral windows for ^{12}CO ($J = 2 - 1$) and C^{18}O ($J = 2 - 1$) line emissions had 3840 and 1920 channels covering 117 and 59 MHz hand width, respectively. Two other spectral windows for continuum emission covered 216-218 GHz and 232-234 GHz; the central frequency of the two continuum spectral windows were 225 GHz.

Table 4.1. Summary of the ALMA observational parameters (Serpens)

Date	2016.May.19, 21			
Projected baseline length	15 - 613 m			
Primary beam	27''			
Passband calibrator	J1751+0939			
Flux calibrator	Titan			
Gain calibrator	J1830+0619, J1824+0119			
Continuum frequency, bandwidth, Beam (P.A.)	225 GHz, 4 GHz, 0'':58 × 0'':47 (−86°)			
CO ($J = 2 - 1$) frequency, Beam (P.A.)	230.538000 GHz, 0'':62 × 0'':51 (−83°)			
C ¹⁸ O ($J = 2 - 1$) frequency, Beam (P.A.)	219.560358 GHz, 0'':65 × 0'':52 (−85°)			
	SMM11b	SMM4c	SMM9d	SMM2
Coordinate center (J2000)	18 ^h 30 ^m 00 ^s .38 1°11'44''.55	18 ^h 29 ^m 56 ^s .71 1°13'15''.60	18 ^h 29 ^m 48 ^s .83 1°17'04''.30	18 ^h 30 ^m 00 ^s .72 1°13'01''.40
1 σ of continuum map	74 μ Jy beam ^{−1}	150 μ Jy beam ^{−1}	56 μ Jy beam ^{−1}	63 μ Jy beam ^{−1} 41 μ Jy beam ^{−1}

All the mapping process was carried out with Common Astronomical Software Applications (CASA). The visibilities were Fourier transformed and CLEANed. In this process we adopted Briggs weighting with the robust parameter of 0.0. We set a $54'' \times 54''$ area centered on the map centers as a CLEAN box with a threshold of 3σ . Multi-scale CLEAN was used for the line maps to converge CLEAN with the 3σ threshold, where CLEAN components were a point source or a $\sim 1''.5$ Gaussian source. The synthesized beam sizes of the CLEANed maps are $\sim 0''.58 \times 0''.47$ (-86°) for the continuum emission, $\sim 0''.62 \times 0''.51$ (-83°) for the CO line emission, and $\sim 0''.65 \times 0''.52$ (-85°) for the C¹⁸O line emission.

We also performed self-calibration for the continuum data using tasks in CASA (*clean*, *gaincal*, and *applycal*). We determined the best solutions by gradually decreasing *solint*, i.e. how many scans are averaged, in the iterative self-calibration process. The obtained calibration tables for the continuum observations were applied to the line data. The self-calibration has improved the rms noise level of the continuum maps by a factor of ~ 2 . The noise level of the line maps were measured in emission-free channels. The parameters of our observations mentioned above and others are summarized in Table 4.1.

4.4 RESULTS

4.4.1 ALMA 1.3-mm continuum and ¹²CO line

Our ALMA observations are toward five SMA 1.3-mm sources (SMM11a, SMM4a, SMM9d, SMM9a, and SMM2) as shown with cyan circles and boxes in Figure 4.1. ALMA 1.3-mm continuum and ¹²CO line emissions in each direction are inspected in this subsection. When integrated intensity maps and mean velocity maps of ¹²CO emission were drawn, the velocity range 8-10 km s⁻¹ were not used because the ¹²CO emission is affected by self-absorption and strongly resolved-out in the velocity range. Additionally 5σ cutoff was used to make the mean velocity maps. Below, we mainly focus on 1.3-mm

sources within the ALMA primary beam (FWHM $\sim 27''$) for each direction. Corresponding Spitzer $24\ \mu\text{m}$ and Herschel $70\ \mu\text{m}$ images are also shown for comparison.

SMM11a— Figure 4.3a shows the 1.3-mm continuum emission toward SMM11a in Serpens Main cluster observed with ALMA. Strong compact emission from SMM11a was confirmed near the mapping center, which have not been identified as a YSO by *Spitzer*. Extension in the north-south direction can also be seen on a $\sim 5''$ scale. Regarding the extension, this area is a part of a tail-like structure in the north-south direction (Figure 4.1). Its deconvolved size derived from 2D Gaussian fitting shows an approximately circular structure slightly elongated in the east-west direction (P.A. = 80°). All Gaussian fitting in this subsection used emission above the 3σ level. The total flux density was also measured in a primary-beam corrected map using pixels with emission stronger than 3σ level in the not-corrected map. The results of Gaussian fitting and flux density measurement are shown in Table 4.3 in more detail, including gas mass derived from the flux density where dust temperature $T_{\text{dust}} = 30\ \text{K}$, dust opacity $(\kappa_{850\mu\text{m}}, \beta) = (0.035\ \text{cm}^2\ \text{g}^{-1}, 1)$ (Andrews & Williams, 2005a), and gas-to-dust mass ratio 100 were assumed. In addition two compact emissions separated by $\gtrsim 1''$ were detected in the northwest of the mapping center outside the primary beam. The two correspond to the position of a Class I source and a Herschel $70\text{-}\mu\text{m}$ source though neither Spitzer nor Herschel can spatially resolve the two emissions. The northeastern one of the two has ~ 3 times larger flux density than the other one. Figure 4.3b shows the ^{12}CO line emission toward SMM11a. This source has a bipolar outflow going the east-west direction. Both blue and red lobes are clearly detected and have a length of $\sim 15''$ and a width of $\sim 3''$. The velocity structure of this outflow will be discussed in more detail in Section 4.5.1. In the northwest of SMM11a, another bipolar outflow is detected, associated with the two continuum emissions in Figure 4.3a.

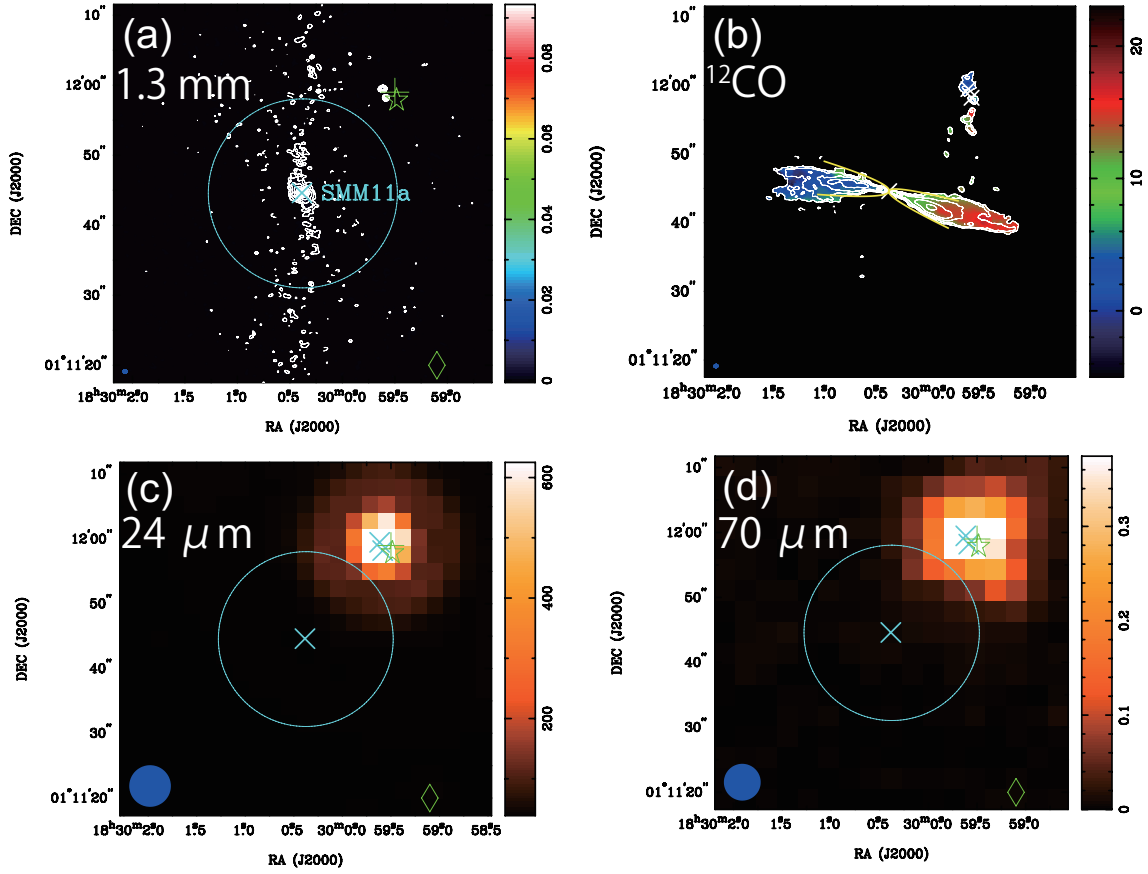


Figure 4.3 (a) ALMA 1.3-mm continuum emission map toward SMM11a. Contour levels are $-6, -3, 3, 6, 12, 24, \dots \times \sigma$. A blue filled ellipse at the bottom left corner denotes the ALMA synthesized beam. 1σ and the beam size are in Table 4.1. Green marks and cyan circle are the same as those in Figure 4.1. Cyan x mark indicates the peak position derived from Gaussian fitting (Table 4.3). Label, SMM11a, indicates ALMA 1.3-mm source name labeled in this chapter. (b) ALMA ^{12}CO line emission map toward SMM11a. White contours show integrated intensity map while the color map shows mean velocity. Integrated velocity range is from -5 to 23 km s^{-1} except for $8\text{--}10 \text{ km s}^{-1}$ where ^{12}CO emission is affected by self-absorption. Contour levels are $-10, -5, 5, 10, 20, 40, \dots \times \sigma$, where 1σ corresponds to $24 \text{ mJy beam}^{-1} \text{ km s}^{-1}$. A blue filled ellipse at the bottom left corner denotes the ALMA synthesized beam. Yellow curves show the best-fit parabolic models for emission within $10''$ in radius (see Section 4.5.1 in more detail). (c) *Spitzer* $24 \mu\text{m}$ image. Blue filled ellipse at the bottom left corner denotes FWHM of the PSF ($6''.4$). The brightness unit is Jy sr^{-1} . (d) *Herschel* $70 \mu\text{m}$ image. The FWHM of PSF is $5''.7$. The brightness unit is Jy pixel^{-1} , where 1 pixel is $3''.2 \times 3''.2$.

SMM4a— Figure 4.4a shows the 1.3-mm continuum emission toward SMM4a. The SMA source has been divided by ALMA into a strong compact emission and a relatively weak, extended emission. We label these 1.3-mm sources as SMM4a1 and SMM4a2, respectively. A bridge-like structure between the two can be seen at the 3σ level. SMM4a1 has the strongest 1.3-mm flux density among the sources in Table 4.3. In addition compact emission was detected in the southeast of the mapping center outside the primary beam. This emission corresponds to the position of a Class 0 source and a Herschel 70- μm source. Figure 4.4b shows the ^{12}CO line emission toward SMM4a. A bipolar outflow was detected, going from SMM4a2 to the north and the south. The blue and red lobes have sizes of $\sim 15''$ and $\sim 20''$, respectively and the red lobe is has narrower width than the blue lobe. The figure also shows another outflow from SMM4a1 to the north with a width of $\sim 5''$, merging into the blue lobe of the outflow from SMM4a2, whereas no red lobe from SMM4a1 is detected.

SMM9d— Figure 4.5a shows the 1.3-mm continuum emission toward SMM9d. Emission in this area has much more complicated structures in the other areas. SMM9d has been divided by ALMA into multiple components. A filament-like structure can be seen from the mapping center to the southwest. Three components were detected in SMM9d by Gaussian fitting; we label them as SMM9d1, SMM9d2, and SMM9d3 as shown in Figure 4.5. SMM9d1 and SMM9d2 were simultaneously fitted. There might be more components in SMM9d though it is not obvious in the present observations. Strong emission with X-shaped structure can be seen under SMM9d, which corresponds to SMM9c. SMM9b has been divided by ALMA into two strong emissions; we label these components as SMM9b1 and SMM9b2 as shown in Figure 4.5. SMM9c2 corresponds to the position of a Class I source and a Herschel 70- μm source. Except for SMM9c2, none of the sources within the primary beam is identified as a YSO by *Spitzer*. The compact strong emission in the southwest of the mapping center is SMM9a, located at another mapping center and inspected in more detail in the following. Figure 4.5b shows the ^{12}CO line emission toward SMM9d. A clear bipolar outflow from SMM9c was detected,

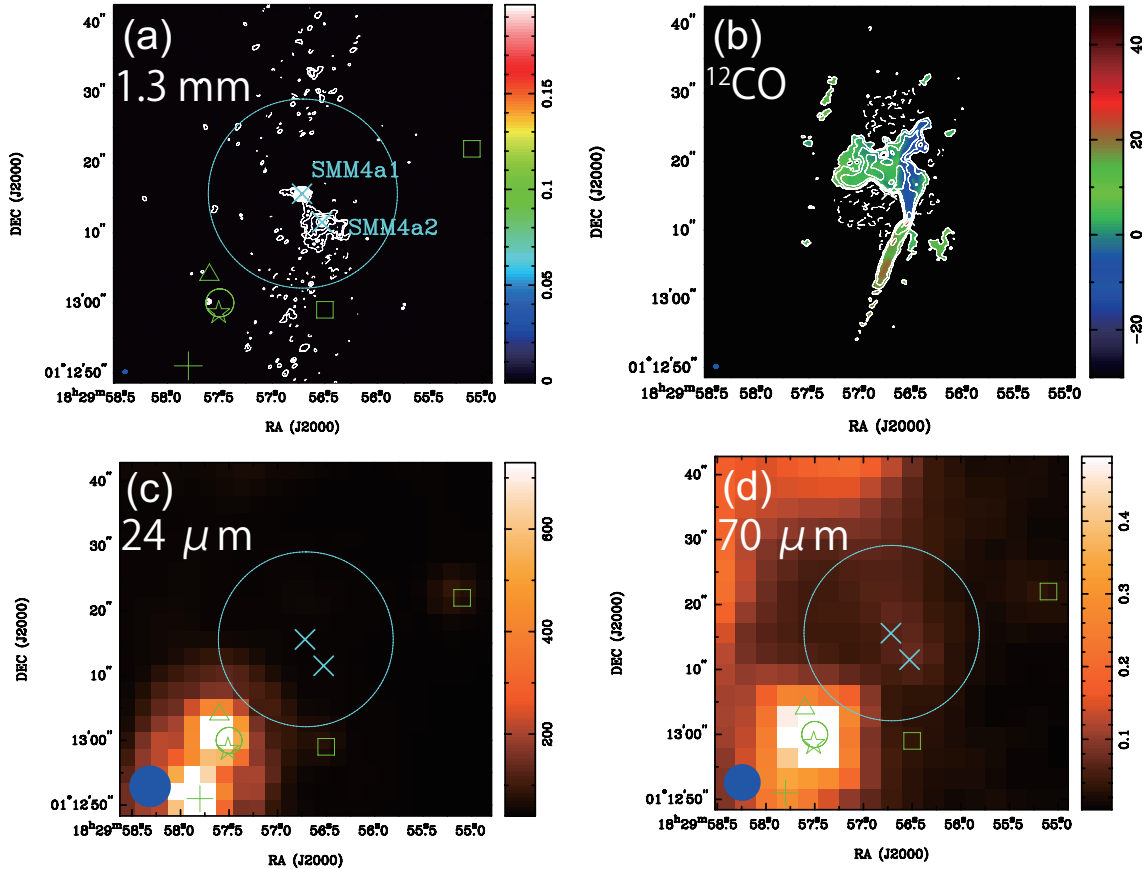


Figure 4.4 The same figure as Figure 4.3 but toward SMM4a. (b) Integrated velocity range is from -30 to 48 km s^{-1} except for $8\text{--}10 \text{ km s}^{-1}$. 1σ is $65 \text{ mJy beam}^{-1} \text{ km s}^{-1}$.

going in the northwest-southeast direction. The length and the width of the outflow from SMM9c are $\sim 10''$ and $\sim 1''.5$, respectively. SMM9b1 and SMM9b2 also have ^{12}CO emission associated with them. Because ^{12}CO emission around SMM9d is weak and extended, it is not obvious which components of SMM9d have ^{12}CO emission associated with them. In addition

SMM9a— Figure 4.6a shows the 1.3-mm continuum emission toward SMM9a. Strong emission with complicated structures was detected, showing extension to the northwest, northeast, east, and south directions. There is also a hole in the northeast of the strong emission. The filament-like structure in the north of SMM9a was inspected above and can be seen more clearly in Figure 4.5. In addition compact emission was detected in the southeast of SMM9a, which corresponds to the position of a Class I source and

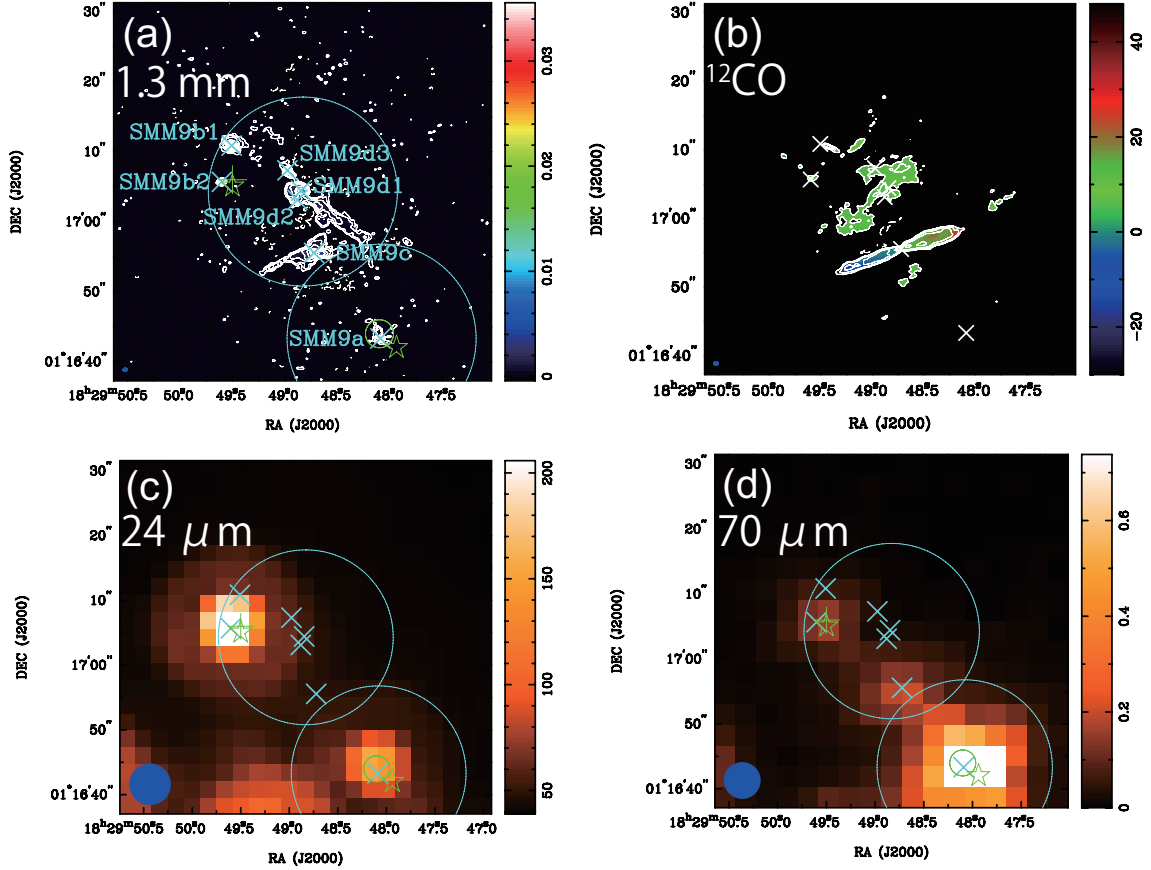


Figure 4.5 The same figure as Figure 4.3 but toward SMM9d. (b) Integrated velocity range is from -30 to 48 km s^{-1} except for $8-10 \text{ km s}^{-1}$. 1σ is $60 \text{ mJy beam}^{-1} \text{ km s}^{-1}$.

a Herschel $70\text{-}\mu\text{m}$ source. Another compact emission was detected in the southwest of SMM9a, which corresponds to the position of a flat-spectrum source. Figure 4.6b shows the ^{12}CO line emission toward SMM9a. A large bipolar outflow from SMM9a was detected, going in the northwest-southeast direction. The length and the width of each lobe are $\sim 15\text{-}20''$ and $\sim 8''$, respectively. The bipolar outflow from SMM9c can also be seen in this figure. The ^{12}CO emission shows another component on a $\sim 10''$ scale between the outflows of SMM9a and SMM9c around the systemic velocity.

SMM2— Figure 4.7a shows the 1.3-mm continuum emission toward SMM2 condensation. Two compact emissions separated by $\sim 4''$ were detected near the mapping center. We label the two 1.3-mm sources as SMM2a1 and SMM2a2 as shown in Figure 4.7. SMM2a2 has weaker emission and corresponds to the position of a Class 0 source

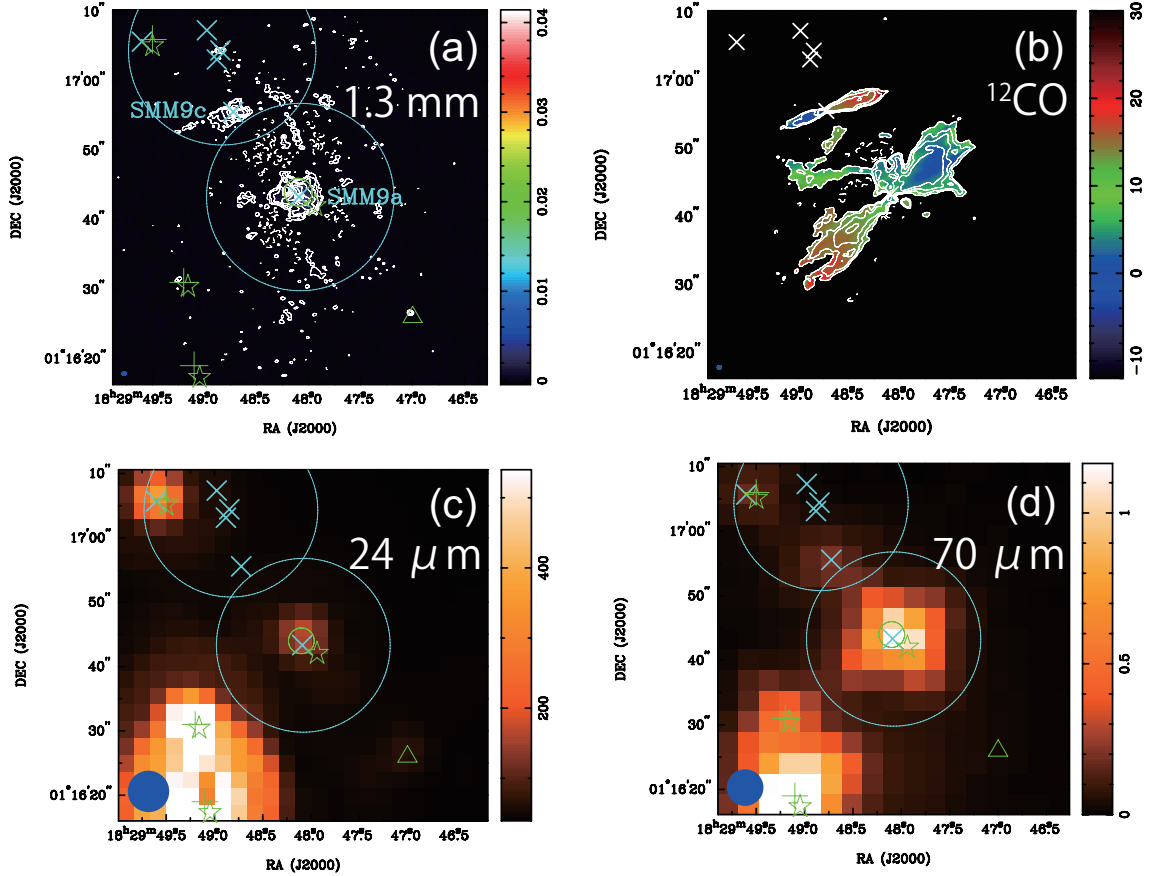


Figure 4.6 The same figure as Figure 4.3 but toward SMM9a. (b) Integrated velocity range is from -12 to 30 km s^{-1} except for $8-10$ km s^{-1} . 1σ is 42 $\text{mJy beam}^{-1} \text{km s}^{-1}$.

while SMM2a2 has not been identified as a YSO by *Spitzer*. The two have the weakest emission among the sources in Table 4.3. Because of the weakness, only a possible upper limit of deconvolved size was derived for SMM2a1 and even such an upper limit could not be derived for SMM2a2, i.e., point source in the present observations. The emission in the west of the two is extended on a $5''$ scale, which appears bright in $70 \mu\text{m}$ (Figure 4.7d). In addition compact emission was detected in the northwest of the two outside the primary beam, which corresponds to the position of a Class I source. Figure 4.7b shows the ^{12}CO line emission toward SMM2 condensation. This figure shows a blueshifted component in the northwest of SMM2a2 on a $\sim 15''$ scale, surrounding SMM2a2. Another component can be seen passing SMM2a1 in the east-west direction on a $\sim 20''$ scale, showing a velocity gradient where red- and blueshifted emissions are on the eastern and western

sides of SMM2a1. In addition the Class I source detected in 1.3-mm has ^{12}CO emission associated with it.

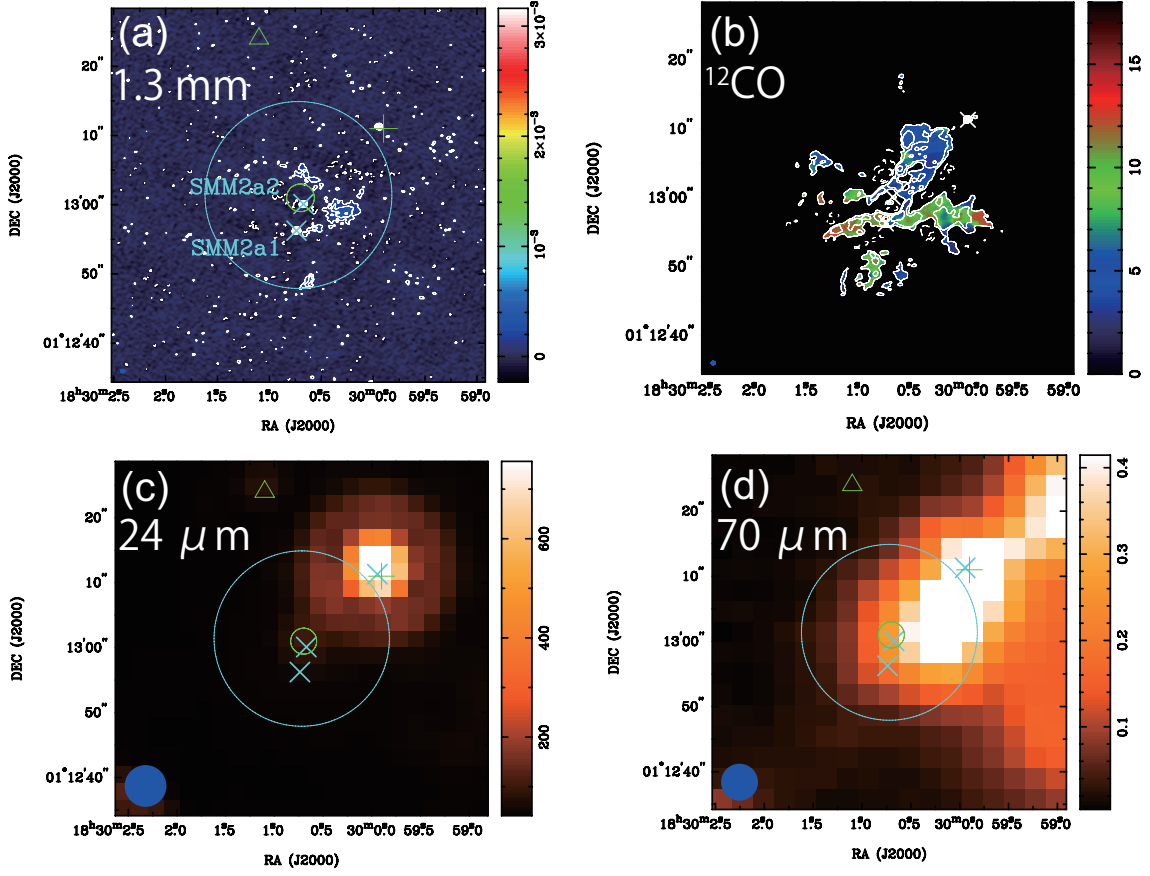


Figure 4.7 The same figure as Figure 4.3 but toward SMM2 condensation. (b) Integrated velocity range is from 0 to 18 km s^{-1} except for 8-10 km s^{-1} . 1σ is 22 $\text{mJy beam}^{-1} \text{km s}^{-1}$.

4.4.2 Near and Mid-infrared emission

Twelve 1.3-sources have been identified within ALMA primary beams in Section 4.4.1 and nine of them have not been identified as a YSO by *Spitzer*. It is, therefore, important to measure flux density in near and mid-infrared wavelength in order to investigate the evolutionary phase of the ALMA 1.3-mm sources. For this purpose we used *Spitzer* IRAC (3.6, 4.5, 5.8, 8.0 μm) and MIPS (24 μm) and *Herschel* PACS 70 μm data of Serpens Main cluster. First, we determined an average sky level and a noise level by the following iterative process. (1) Measure mean μ (Jy pixel^{-1}) and standard deviation σ (Jy pixel^{-1})

using the all pixels, (2) Exclude pixels where emission is lower than $\mu - 3\sigma$ or higher than $\mu + 3\sigma$, (3) Measure μ and σ using only the surviving pixels, and (4) Repeat (2) and (3) until the two values converge. Secondly, we measured the flux density within an aperture centered on the ALMA-source positions, whose radius is FWHM of point spread function (PSF) (Aniano et al., 2011), i.e., the diameter of the aperture is twice larger than the FWHM. The average sky level μ was subtracted at this point. The aperture covers four times larger area than the FWHM and thus includes 16 independent points from the point of view of Nyquist sampling. For this reason we define 3σ detection limit as $\sqrt{16} \times 3\sigma$ (Jy) using σ derived above. Thirdly we measured bolometric temperature T_{bol} and bolometric luminosity L_{bol} using the flux density derived above. The bolometric temperature was calculated from flux-weighted mean frequency (Myers & Ladd, 1993). The bolometric luminosity was calculated by Trapezoidal integral with the distance $d = 429$ pc (Dzib et al., 2011). When the flux density is lower than the 3σ detection limit, the limit was used instead in the calculation of T_{bol} and L_{bol} . Figure 4.8 shows the derived SEDs and the derived T_{bol} and L_{bol} are shown in Table 4.3. The bolometric temperature of SMM9c2 is higher than 70 K while that of SMM9a and SMM2a2 is lower than 70 K. This is consistent with the fact that SMM9c2 is classified as Class I while SMM9a and SMM2a2 are classified as Class 0 (Chen et al., 1995), supporting the validity of our results. Our method, however, cannot remove contamination from neighboring sources particularly in longer wavelength; FWHM of the PSF in 24 and 70 μm is $\sim 6''$. Although SMM11a is separated from the nearest Class I source by $\sim 20''$, the emission in 24 and 70 μm appears contaminated by the emission from the Class I source. Nevertheless, its bolometric temperature $T_{\text{bol}} = 23$ K and bolometric luminosity $L_{\text{bol}} = 0.050 L_{\odot}$ are already the lowest among the sources in Table 4.3 before the contamination is removed.

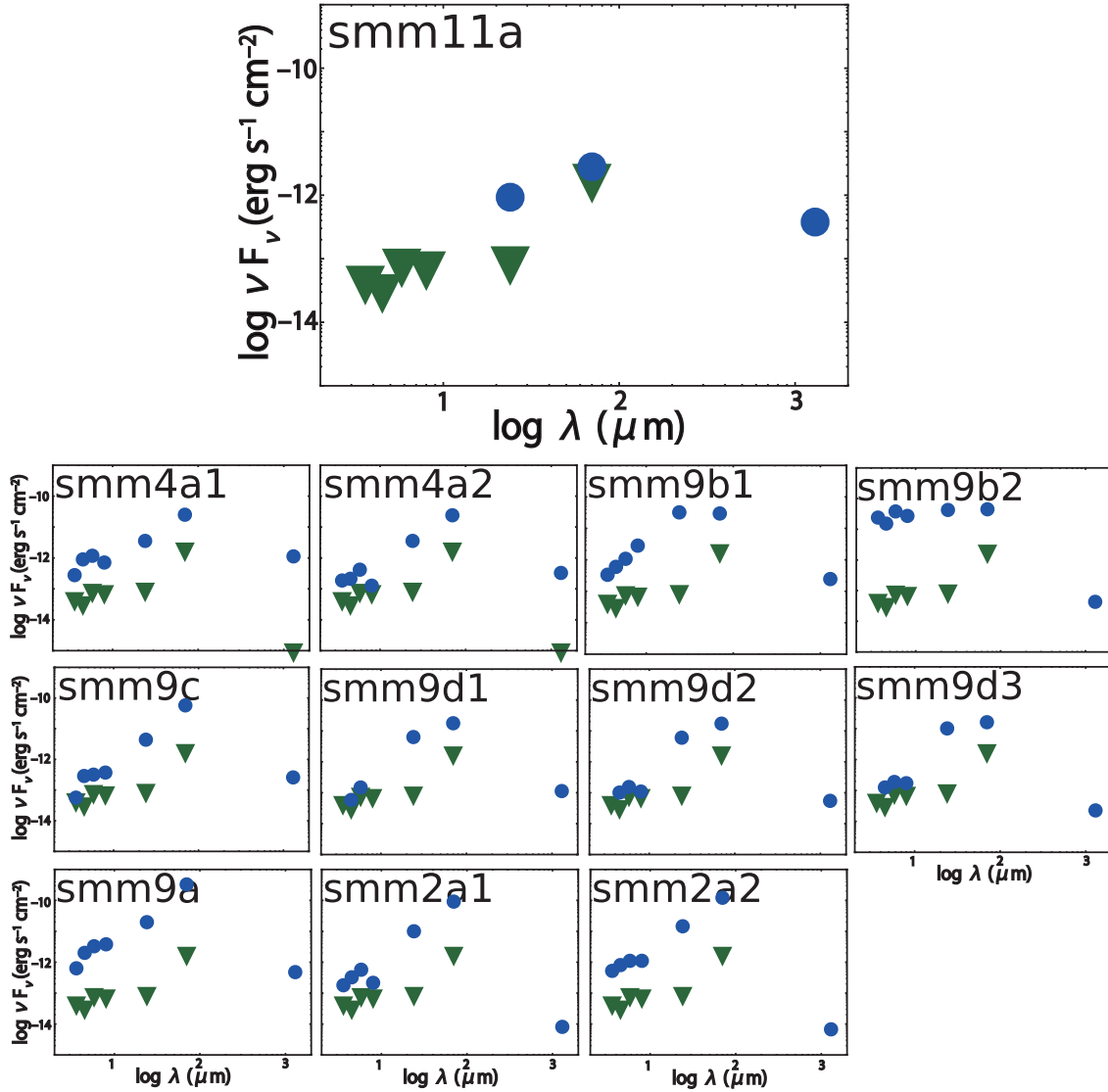


Figure 4.8 SEDs of the ALMA 1.3-mm sources derived from *Spitzer* IRAC (3.6, 4.5, 5.8, 8.0 μm), MIPS 24 μm , and Herschel PACS 70 μm data. Blue points denote the measured flux density while green points denote the 3σ detection limit (see the text in more detail). Bolometric temperature T_{bol} and bolometric luminosity L_{bol} calculated from this figure are shown in Table 4.3.

Table 4.2. ALMA 1.3-mm sources

Name	R.A. (J2000)	Dec. (J2000)	Size ^a (P.A.)	$F_{1.3\text{ mm}}$ (mJy)	M_{gas}^b (M_{\odot})	Class ^c	T_{bol} (K)	L_{bol} (L_{\odot})	^{12}CO outflow? Y/N/?
SMM11a	18 ^h 30 ^m 00 ^s :3856	1°11'44"6093	0'':37 × 0'':31 (80°)	164	0.16	—	23	0.050	Y
SMM4a1	18 ^h 29 ^m 56 ^s :7179	1°13'15"5788	0'':75 × 0'':46 (145°)	487	0.49	—	37	0.29	Y
SMM4a2	18 ^h 29 ^m 56 ^s :5261	1°13'11"5072	0'':70 × 0'':54 (94°)	142	0.14	—	49	0.24	Y
SMM9b1	18 ^h 29 ^m 49 ^s :5079	1°17'10"8671	0'':37 × 0'':34 (86°)	106	0.11	—	78	0.51	Y
SMM9b2	18 ^h 29 ^m 49 ^s :6015	1°17'05"6855	0'':70 × 0'':61 (98°)	18.7	0.019	I	150	0.87	Y
SMM9c	18 ^h 29 ^m 48 ^s :7230	1°16'55"5634	1'':21 × 0'':56 (87°)	112	0.11	—	53	0.52	Y
SMM9d1	18 ^h 29 ^m 48 ^s :8466	1°17'04"4312	1'':32 × 0'':65 (90°)	49.1	0.049	—	60	0.20	?
SMM9d2	18 ^h 29 ^m 48 ^s :8817	1°17'03"1221	1'':16 × 0'':59 (88°)	23.7	0.024	—	62	0.19	?
SMM9d3	18 ^h 29 ^m 48 ^s :9770	1°17'07"3296	0'':47 × 0'':28 (19°)	9.81	0.098	—	72	0.21	?
SMM9a	18 ^h 29 ^m 48 ^s :0908	1°16'43"3310	0'':73 × 0'':51 (38°)	207	0.021	0	56	2.9	Y
SMM2a1	18 ^h 30 ^m 00 ^s :7386	1°12'56"2481	< 0'':13 × 0'':10	3.51	3.5×10^{-3}	—	58	0.82	Y
SMM2a2	18 ^h 30 ^m 00 ^s :6725	1°13'00"0918	point source	2.92	2.9×10^{-3}	0	59	1.1	Y

^aDeconvolution size derived from 2D Gaussian fit.

^b $\kappa(1.3\text{ mm}) = 0.023\text{ cm}^2\text{ g}^{-1}$, $T_{\text{dust}} = 30\text{ K}$, and $d = 429\text{ pc}$ are assumed.

^cBased on extinction corrected α' and T_{bol} in Dunham et al. (2015).

4.5 DISCUSSION

The low bolometric temperature $T_{\text{bol}} = 23$ K and the low bolometric luminosity $L_{\text{bol}} = 0.05 L_{\odot}$ of SMM11a suggest a possibility that the source is in the earliest phase of star formation, first hydrostatic cores (FHSCs). The phase of FHSC was first theoretically predicted by Larson (1969) as the phase between starless and protostellar phases, while there is still no determinative observation to identify FHSCs. In theoretical studies, the FHSC is defined as the phase at which adiabatic collapse starts because the density is high enough to be opaque to radiation ($\rho_c \gtrsim 10^{-13}$ g cm $^{-3}$ or $n_c \gtrsim 10^{10}$ cm $^{-3}$; Larson, 1969). Recent theoretical studies also predict maximum mass, lifetime, internal luminosity¹ and radius to be $0.01 - 0.1 M_{\odot}$, $500-5 \times 10^4$ yr, $10^{-4} - 0.1 L_{\odot}$, and 5-100 AU, respectively (Boss & Yorke, 1995; Masunaga et al., 1998; Omukai, 2007), depending on various conditions, such as magnetic fields (Commerçon et al., 2012) and rotation (Saigo & Tomisaka, 2006; Saigo et al., 2008; Tomida et al., 2010). Particularly, simulations of rotating FHSCs suggest that those FHSCs can transform into Keplerian disks around protostars (Bate, 2011; Machida & Matsumoto, 2011).

An observable indication of FHSCs predicted by theories is SED, which is characterized by dust emission with a temperature of 10-30 K, predicting emission at wavelength shorter than 20-50 μm is lower than detection limits of present telescopes, such as *Spitzer* and *Herschel* (Boss & Yorke, 1995; Masunaga et al., 1998; Omukai, 2007; Saigo & Tomisaka, 2011). SMM11a has been detected as a point source in neither 24 nor 70 μm (Figure 4.3), as well as 3.6, 4.5, 5.8, nor 8.0 μm . Furthermore, its bolometric temperature $T_{\text{bol}} = 23$ K is consistent with the predicted temperature range. The bolometric temperature and the bolometric luminosity $L_{\text{bol}} = 0.05 L_{\odot}$ are also as low as those of known FHSC candidates, L1451-mm (30 K, $0.05 L_{\odot}$; Pineda et al., 2011), CB 17 MMS (16 K, $0.04 L_{\odot}$; Chen et al., 2012) and L1448 IRS2E ($0.1 L_{\odot}$; Chen et al., 2010). Internal luminosity of SMM11a can be estimated from 70 μm flux density to be $L_{\text{int}} = 0.043 L_{\odot}$

¹Internal luminosity does not include the luminosity due to external heating by interstellar radiation field and envelopes.

using an empirical law (Equation (2) in Dunham et al., 2008), which is also as low as the predicted luminosity and those of known FHSC candidates in Table 4.3. For these reasons, we suggest SMM11a as a new FHSC candidate. The properties of its ^{12}CO outflow, C^{18}O abundance, and continuum visibility will be discussed in this section in order to verify whether the source is a FHSC.

4.5.1 ^{12}CO outflows

Figure 4.3b shows that the eastern and western lobes of the ^{12}CO outflow from SMM11a have different axes and thus the two lobes are separately investigated in this subsection. In addition the emission associated with the closest Class I source to SMM11a is ignored in the following analyses. First we used the integrated intensity map to determine the orientation angle of each lobe. With a given orientation angle, the reflected map across the direction was subtracted from the original map and the best orientation angle was determined by minimizing the residual, where only pixels over 3σ were used. As a result the orientation angle of the eastern and western lobes were estimated to be P.A.= 79° and -110° , respectively. Figure 4.9 shows two Position Velocity (PV) diagrams along the position angles P.A.= 79° and -110° . In Figure 4.9a, blueshifted components are mainly located on the eastern side as was seen in Figure 4.3b. Emission at $V_{\text{LSR}} \sim 2 \text{ km s}^{-1}$ is absorbed in a wide spatial range showing negative parts, which can be explained by the resolved out effect if there is extended emission behind the emission associated with SMM11a. In fact our observations using the 22-m Mopra Radio Telescope in $^{13}\text{CO } J = 1-0$ line shows extended emission in the velocity range (Observation ID: MC142011). In addition to the blueshifted component, relatively small redshifted components are located on the eastern side as well. The same combination can also be seen in Figure 4.9b; larger redshifted and smaller blueshifted components are located on the western side. Those combinations suggest that the outflow axes lie almost on the plane of the sky. Subsequently we determined the morphology, velocity structure, and inclination angle of

the two lobes based on Appendix A in Yen et al. (2016). They adopted the wind-driven-shell model (Shu et al., 1991; Lee et al., 2000), where the velocity field can be described as

$$z = c_0 R^2, \quad V_R = v_0 R, \quad V_z = v_z z, \quad (4.1)$$

where z , R , V_R , V_z , c_0 , and v_0 are the distance along the outflow axis, the distance perpendicular to the outflow axis, velocity along the R direction, velocity along the z direction, coefficient in the unit of arcsec^{-1} , and coefficient in the unit of $\text{km s}^{-1} \text{arcsec}^{-1}$, respectively. When the outflow inclines, the projected shape is also a parabola and can be described as

$$z' = c_0 \sin i R'^2 - \frac{\cos^2 i}{4c_0 \sin i}, \quad (4.2)$$

where z' and R' are the projected distance along and across the outflow axis, respectively, and i is an inclination angle ($i = 0^\circ$ is pole-on). The second term in the right hand side in Equation (4.2) can be ignored when the outflow axis lies almost in the plane of the sky, and thus the equation also indicates that the two parameters c_0 and i are degenerated. For this reason we determined $c_0 \sin i$ before i and v_0 as described below. Pixels over 3σ in the observations and the inside of the model curve were set to be the unity while other regions were set to be zero as was performed by Yen et al. (2016). In addition we only use pixels within $10''$ in radius because the shape of the outflow is more like bow shock in the outer region, which cannot be explained by the wind-driven-shell model. The model was subtracted from the integrated intensity map and the residual was minimized. The best-fit parameters are $c_0 \sin i = 1.7_{-0.4}^{+0.2}$ and $2.3_{-0.6}^{+0.4} \text{arcsec}^{-1}$ for the eastern and western lobes. The error bars were 5% P-value ranges, which were estimated from χ^2 by assuming reduced χ^2 is the unity for the best-fit value. The pair of best-fit parabolas are overlaid on Figure 4.3b, which reproduce the overall shape of both lobes. Next the PV diagrams

(Figure 4.9) is used to determine the other parameters i and v_0 . The model curve is below.

$$z'' = \frac{V_{\text{LOS}} \sin i}{v_0 \cos i} + \frac{\sin i}{2c_0 \cos^2 i} \left(1 \pm \sqrt{1 + \frac{4c_0 V_{\text{LOS}} \cos i}{v_0 \sin^2 i}} \right), \quad (4.3)$$

where z'' and V_{LOS} correspond to the position and velocity coordinates of a PV diagram along a projected outflow axis with the units of arcsec and km s^{-1} . Note that systemic velocity of SMM11a is estimated to be 9.1 km s^{-1} from our C^{18}O results in Section 4.5.2. Again pixels over 3σ in the observations and the inside of the model curve were set to be the unity while other regions were set to be zero, and only pixels within $10''$ in radius were used to derive residuals. The best-fit parameters and 5% P-value ranges are $i = 79_{-2}^{+0}$, $v_0 = 3.6_{-0.2}^{+0.4} \text{ km s}^{-1} \text{ arcsec}^{-1}$ for the eastern lobe and $i = 87_{-16}^{+0}$, $v_0 = 3.8_{-2.2}^{+0.2} \text{ km s}^{-1} \text{ arcsec}^{-1}$ for the western lobe. The best-fit curves are overlaid on Figure 4.9, which reproduce the velocity structure of both lobes, overall. These results support that the outflow axes lie almost on the plane of the sky and also suggest a dynamical time of the outflows, $\sim 600 \text{ yr}$.

The outflow properties related with mass are also derived as defined by Dunham et al. (2011). The mass of outflow M_{flow} , momentum P_{flow} , and kinetic energy E_{flow} were directly derived from the observed data cube using pixels over 3σ in the same velocity range as used to make the integrated intensity map ($-5 - 23 \text{ km s}^{-1}$), without inclination correction. It is assumed that ^{12}CO line emission is in local thermodynamic equilibrium (LTE) and optically thin, and the temperature 20 K was adopted (Dunham et al., 2011), when total flux is converted to mass. Then characteristic velocity $v = P_{\text{flow}}/M_{\text{flow}}$, dynamical time $\tau_d = R_{\text{lobe}}/v$, force $F_{\text{flow}} = P_{\text{flow}}/\tau_d$, and mechanical luminosity $L_{\text{flow}} = E_{\text{flow}}/\tau_d$ were calculated from the three quantities. The results are listed in Table 4.3 with those of known FHSC candidates, where the quantities of both lobes are combined. Among the candidates in Table 4.3, Per-Bolo 58 and CB17 MMS have the properties close to SMM11a, although the quantities of SMM11a are not inclination-corrected to compare with those of the FHSC candidates, which are not inclination-corrected. If the outflow

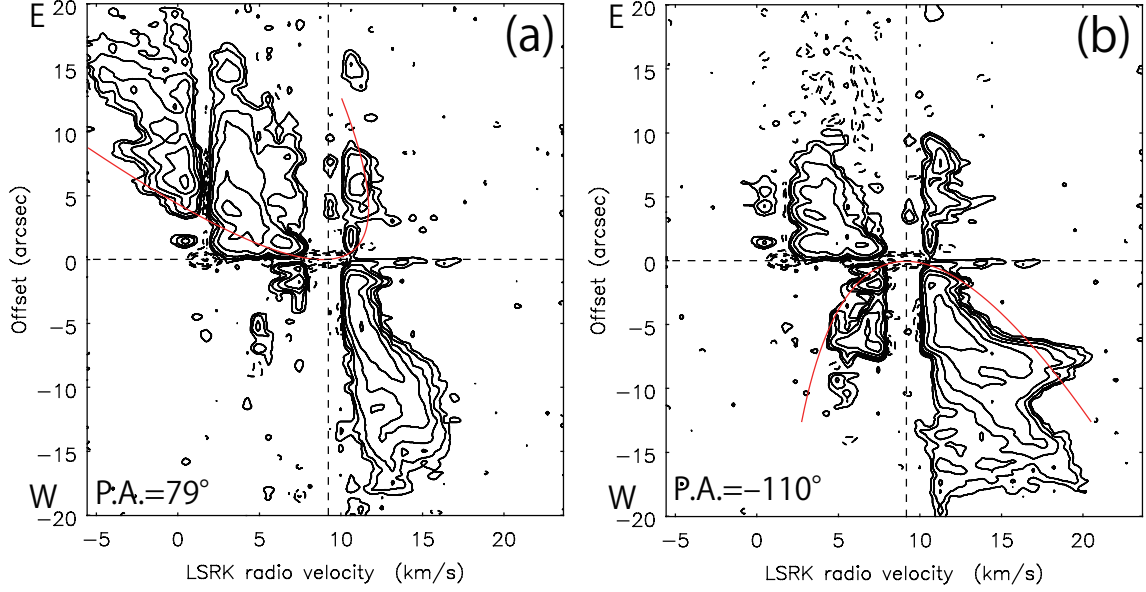


Figure 4.9 Position Velocity diagram of the $^{12}\text{CO } J = 2 - 1$ emission in SMM11a along two axes: (a) P.A.= 79° and (b) P.A.= -110° . Slices over the beam width ($0''.55$) were averaged. Velocity resolution is 0.63 km s^{-1} . Contour levels are $-6, -3, 3, 6, 12, 24, \dots\sigma$, where 1σ corresponds to $3.6 \text{ mJy beam}^{-1}$. Central vertical and horizontal dashed lines show the systemic velocity 9.1 km s^{-1} and the continuum peak position. Red curves shows the best-fit parabolic models.

from SMM11a has only a velocity component along the outflow axis with inclination angle $i \sim 80^\circ$, a projection factor $\cos 80^\circ = 0.17$ is smaller than the average value $\langle \cos i \rangle = 0.5$ by a factor of 3. However, this factor is not larger than deviation among the sources. We conclude, therefore, that the outflow property of SMM11a is close to those of the known FHSC candidates.

Table 4.3. Comparison of outflow properties of SMM11a and known FHSC candidates.

Quantity	Unit	SMM11a	Per-Bolo 58	L1448 IRS2E	CB 17 MMS	L1451-mm
Internal Luminosity (L_{int})	$10^{-2} L_{\odot}$	4.3	1.2	< 10	< 7	< 3
Lobe Size (R_{lobe})	10^3 AU	6.4	6.2	9.6	8.0	0.55
Mass (M_{flow})	$10^{-4} M_{\odot}$	7.3	2.0	20	7.9	0.12
Momentum (P_{flow})	$10^{-3} M_{\odot} \text{ km s}^{-1}$	3.5	0.56	50	1.9	0.017
Kinetic Energy (E_{flow})	10^{41} erg	2.1	0.51	120	0.43	0.0031
Luminosity L_{flow}	$10^{-4} L_{\odot}$	2.8	0.42	500	0.25	0.013
Force (F_{flow})	$10^{-7} M_{\odot} \text{ km s}^{-1} \text{ yr}^{-1}$	5.6	0.56	250	1.3	0.083
Characteristic velocity v	km s^{-1}	4.8	2.9	25	2.4	1.3
Dynamical Time (τ_d)	10^3 yr	6.3	10	1.8	14	2.0
References		this work	Dunham et al. (2011)	Chen et al. (2010)	Chen et al. (2012)	Pineda et al. (2011)

4.5.2 C¹⁸O abundance

Figure 4.10 shows C¹⁸O emission detected by ALMA; white contours show the integrated intensity map and color shows the mean velocity map. The detected area above 3σ level is smaller than that of the 1.3-mm continuum emission (cyan contours). Integrated intensity map shows two local peaks on the eastern and western sides of the continuum peak position with a separation of $\sim 1'' = 429$ AU. Integrated intensity at the continuum peak position is $30 \text{ mJy beam}^{-1} \text{ km s}^{-1}$ and total flux of the C¹⁸O emission is $240 \text{ mJy km s}^{-1}$. By comparing these values with the peak intensity (90 mJy beam^{-1}) and total flux density (130 mJy) of the continuum emission, respectively, the fractional abundance of C¹⁸O relative to H₂, $X(\text{C}^{18}\text{O})$, can be estimated. We also consider sizes of the two emissions and continuum subtraction without assuming that the two emissions are optically thin. When the common temperature is 15-30 K, the derived abundance is $\sim (1-2) \times 10^{-10}$, which is lower than a typical interstellar value 5×10^{-7} (Lacy et al., 1994; Wilson & Rood, 1994) by nearly 4 orders of magnitude. This fractional abundance suggests that the temperature is enough low for CO molecules to be freeze-out. In fact theoretical chemical simulation (Aikawa, 2013) shows CO molecules are freeze-out in the FHSC phase; the abundance of CO molecules is lower than the typical interstellar value by 4 orders of magnitude at a few AU from the first core and the abundance is further smaller a range from a few 10 AU to ~ 100 AU, which is quite consistent with our observations. Similar depletion of a carbon-bearing molecule, H¹³CO⁺, was reported for the FHSC candidate Barnard 1-bN (Huang & Hirano, 2013). In addition the C¹⁸O fractional abundance is estimated to be $(1-2) \times 10^{-9}$ at the two local peaks, which is ~ 20 times higher than one at the continuum peak. This can be interpreted as desorption due to heating by the associated outflows because the two peaks are located along the outflow axes (magenta contours), indicating that the C¹⁸O is affected by the outflows in the direction.

In addition to the alignment of the two local peaks along the outflow direction, the overall velocity gradient of the C¹⁸O emission is also similar to that of the ¹²CO outflow

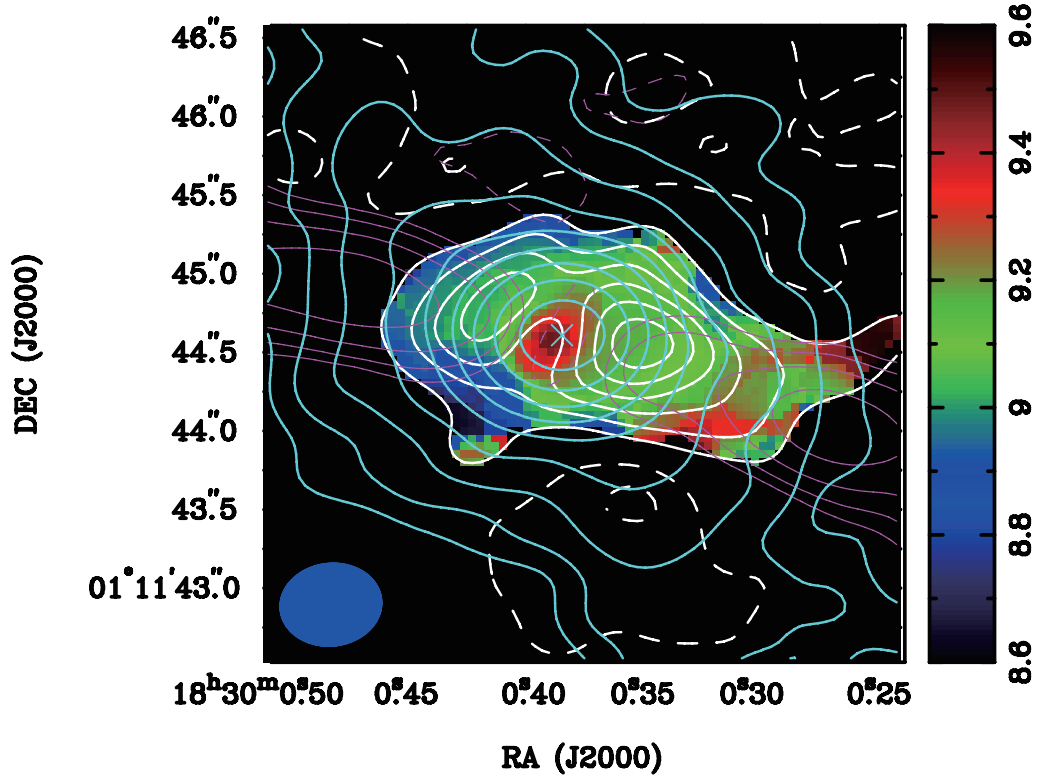


Figure 4.10 Integrated intensity map (moment 0; white contours) and mean velocity map (moment 1; color) of the C^{18}O $J = 2 - 1$ emission in SMM11a overlaid on the 1.3-mm continuum (cyan contours) and ^{12}CO line (moment 0; magenta contours) emissions. Contour levels of the C^{18}O integrated intensity map are from 3σ in steps of 3σ , where 1σ corresponds to $3.5 \text{ mJy beam}^{-1} \text{ km s}^{-1}$. Integrated velocity range of C^{18}O emission is from 8.3 to 9.9 km s^{-1} . Contour levels of the 1.3-mm continuum and the ^{12}CO map are the same as Figure 4.3a and 4.3b, respectively. A central cyan x mark shows the peak position of the 1.3-mm continuum emission. A blue filled ellipse at the bottom left corner denotes the ALMA synthesized beam.

as shown in Figure 4.10. To investigate the velocity structure in more detail, channel maps of the C^{18}O emission (Figure 4.11) are inspected here. The extended structure along the outflow axes can be confirmed in the channels from 8.9 - 9.1 km s^{-1} . We measured distribution of total flux in a $4'' \times 1''$ box at each channel, i.e. line profile, and determined the systemic velocity of SMM11a to be 9.1 km s^{-1} and FWHM to be 0.8 km s^{-1} by Gaussian fitting to a line profile. Although there is a tendency in the channel maps that emission is located on both eastern and western sides of the continuum peak position in blueshifted velocity while emission is located mainly on the eastern side in redshifted velocity, velocity gradient is not obvious either along or across the outflow axes. A PV

diagram cutting across the outflow axes (P.A. $=-15.5^\circ$) is analyzed so as to focus on the velocity gradient across the outflow axes, which is considered to originate from rotation. Figure 4.12 shows the PV diagram of the $C^{18}O$ emission. Velocity gradient is not obvious though a local peak can be seen in blueshifted velocity on the northern side and another local peak can be seen in redshifted velocity on the southern side. We also measured 1D mean position $\int Ixdx / \int Idx$ at each velocity channel using pixels over 3σ level in the same method as Aso et al. (2015). The mean positions are, however, dispersed and show no systematic velocity gradient. We thus determined an upper limit of specific angular momentum from the mean positions to be $\lesssim 1 \times 10^{-4} \text{ km s}^{-1} \text{ pc}$, which is several times lower than a typical value for Class 0 protostars (Yen et al., 2011).

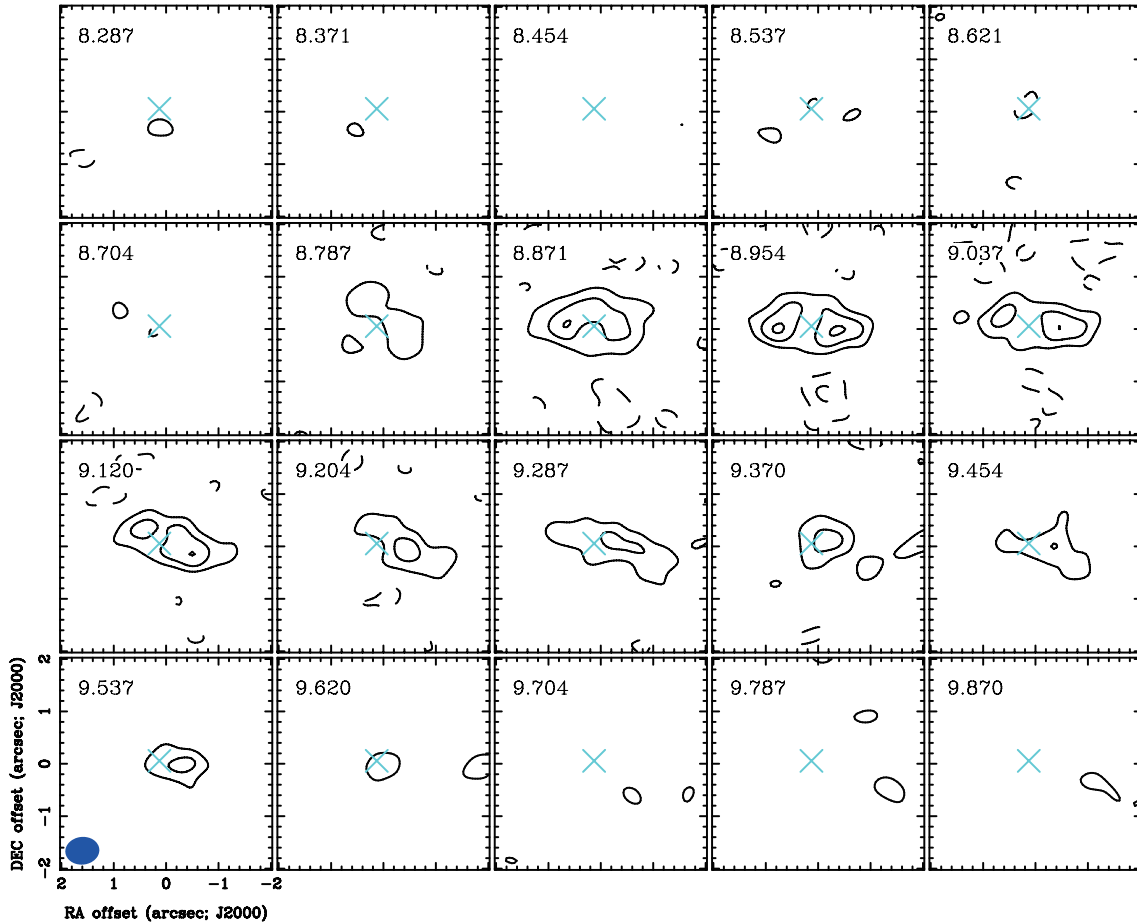


Figure 4.11 Channel maps of the $\text{C}^{18}\text{O } J = 2 - 1$ emission in SMM11a. Contour levels are from 3σ in steps of 3σ , where 1σ corresponds to 11 mJy beam^{-1} . A central x mark in each panel shows the continuum peak position. A blue filled ellipse in the bottom left panel denotes the ALMA synthesized beam. LSR velocity is shown at the top left corner of each panel.

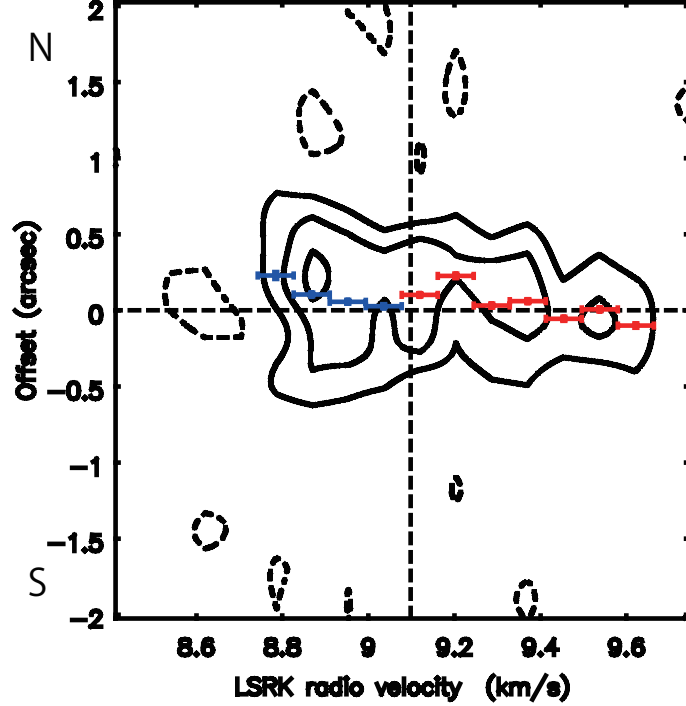


Figure 4.12 Position Velocity diagram of the $\text{C}^{18}\text{O } J = 2 - 1$ emission in SMM11a across the outflow axes (P.A. $=-15.5^\circ$). Slices over the beam width ($0''.55$) were averaged. Velocity resolution is 0.083 km s^{-1} . Contour levels are from 3σ in steps of 3σ , where 1σ corresponds to 8 mJy beam^{-1} . Central vertical and horizontal dashed lines show the systemic velocity 9.1 km s^{-1} and the continuum peak position. Blue and red points with error bars are 1D mean positions derived along the position (vertical) direction at each velocity.

4.5.3 Continuum visibility

To investigate structures of continuum emission of SMM11a, visibility distribution is analyzed in this subsection, which is free from any non-linear effects associated with interferometric imaging. Figure 4.13 shows distributions of the observed 1.3-mm continuum visibility. Each data point corresponds to one baseline and the visibility is averaged over an observational track for $\lesssim 50$ min. For this reason no trajectory due to Earth's rotation appears in the uv -plane (Figure 4.13a). Blue and red points in all panels denote the data points close to the major- (P.A. $=80^\circ \pm 15^\circ$) and the minor (P.A. $=-10^\circ \pm 15^\circ$) axes of the continuum emission, respectively; the axes were derived from Gaussian fitting to the continuum image in Section 4.4.1. We note that, although these visibility includes flux

from the two components on the northwest of SMM11a (see Figure 4.3a), the total flux density of the two components is 8 mJy, which is ~ 10 times smaller than the smallest amplitude in Figure 4.13 and thus negligible. Figure 4.13b shows amplitude distribution as a function of uv -distance in the linear space. It shows a negative correlation that visibility amplitude is stronger at shorter uv -distance. In more detail blue points have slightly stronger amplitude than red points at the same uv -distance, overall, which is consistent with the result that the deconvolution size of continuum image is extended along the major axis. While, the blue and red points are mostly overlapped at uv -distance longer than 50 m, which is also consistent with the aspect ratio of the deconvolution size is close to the unity (~ 1.2). This result and the ^{12}CO outflows from SMM11a lying almost on the plane of the sky (Section 4.5.1) suggest that the dust structure of SMM11a is closer to a sphere than a disk on scales from $\sim 5''$ to $\sim 0.5''$ or from 2000 to 200 AU. Figure 4.13c shows the amplitude distribution in the log-log plane. This figure shows red points have stronger amplitude than blue points at uv -distance shorter than $\lesssim 50$ m, which corresponds to spatial wavelength of $\sim 5''$. In fact the continuum image (Figure 4.3a) is extended in such a large scale along the north-south direction, which is closer to the minor axis direction of the deconvolved size. The data points at the middle range from 50 to 300 m are concentrated on a straight line, while those at longer uv -distance appear to deviate from the straight line in Figure 4.13c. Figure 4.13d shows visibility phase distribution as a function of uv -distance. Its phase center is the peak position of the continuum image. Most of the phase are smaller than $\lesssim 5^\circ$ and the three colors are mixed better than those in the amplitude plots. Although phase can be affected by the two northwestern components more than amplitude, the discussion below depends only on the amplitude distribution.

To investigate the straight line and deviation in Figure 4.13c in more detail, we fitted the amplitude distribution with three different functions. The first one is Gaussian function; the best-fit curve is $0.13 \text{ Jy} \exp(-\ln 2(\beta/380 \text{ m})^2)$ where β is uv -distance, which is consistent with the deconvolution size of the continuum image ($\text{FWHM} \sim 0''.3$) and plotted in Figure 4.13b and 4.13c with dashed-dotted curves. The best-fit Gaus-

sian function significantly deviates from the observations at shorter ($\lesssim 80$ m) and longer ($\gtrsim 350$ m) uv -distance. The second one is a power-law function; the best-fit curve is $0.12 \text{ Jy } (\beta/100 \text{ m})^{-0.30}$, where 100 m was a fixed parameter, and plotted in the panels with dashed curves. The best-fit power-law function is consistent with the observations at shorter and middle uv -distance whereas it significantly deviates from the observations at longer ($\gtrsim 350$ m) uv -distance. The last one is the combination of Gaussian and power-law functions; the best-fit curve is $0.031 \text{ Jy } \exp(-\ln 2(\beta/370 \text{ m})^2) + 0.089 \text{ Jy } (\beta/100 \text{ m})^{0.33}$ and plotted in the two panels with solid curves. The best-fit combination curve is consistent with the observations at all uv -distance. Because Fourier transform is linear process, these results suggest that the dust structure around SMM11a can be interpreted as a combination of a dense compact component with the radius of ~ 70 AU and an extended, power-law component. Half width at half maximum (HWHM) of Gaussian component corresponds to $\text{FWHM} \sim 0''.32$ or a radius of ~ 70 AU and its amplitude corresponds to a mass of $\sim 0.03 M_{\odot}$ if dust temperature $T_{\text{dust}} = 30$ K, dust opacity $(\kappa_{850\mu\text{m}}, \beta) = (0.035 \text{ cm}^2 \text{ g}^{-1}, 1)$ (Andrews & Williams, 2005a), and gas-to-dust mass ratio 100 are assumed. The radius and mass provide average number density of H_2 molecules, $\sim 3 \times 10^9 \text{ cm}^{-3}$, which is ~ 10 times smaller than the critical density between isothermal and adiabatic states (Masunaga et al., 1998; Matsumoto & Hanawa, 2011). On the other hand, if temperature and volume density have spherical power-law profiles with indices of p and q , respectively, the index of the power-law component, 0.33, corresponds to $p + q \sim 2.7$ (Looney et al., 2003). This is steeper than the case of an infalling envelope with no rotation where the mass accretion rate is a constant ($p = 1.5$) and temperature is determined only from flux from the central object ($q = 0.5$).

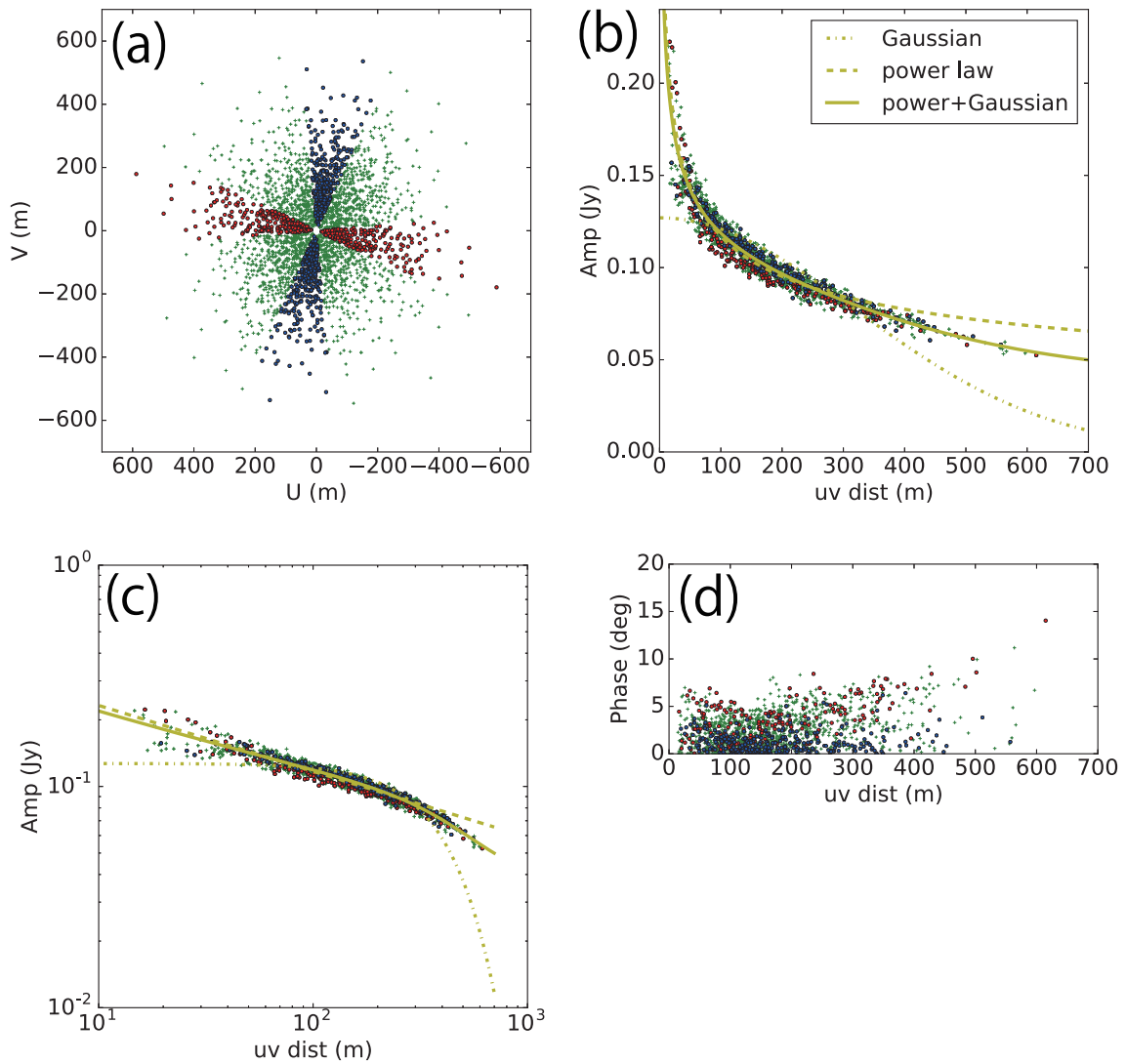


Figure 4.13 Continuum visibility averaged over scans. 1 m corresponds to $0.73 \text{ k}\lambda$ at the observed frequency. (a) Data points on the uv -plane. Both of conjugate pair are plotted. (b) Distribution of the visibility amplitude. An error bar of the amplitude for each point is $\sim 1 \text{ mJy}$. Note that the visibility also includes flux density of the two components on the northwest of SMM11a, 8 mJy . (c) The same distribution as (b) but in the log-log plane. (d) Distribution of the visibility phase. Only one of each conjugate pair with a positive phase is plotted. Red and blue circles denote data points near the major- and minor-axis directions of the continuum image, or $\text{Arctan}(U/V) = 80^\circ \pm 15^\circ$ and $\text{Arctan}(U/V) = -10^\circ \pm 15^\circ$, respectively. Green crosses denote the other data points. Dashed-dotted, dashed, and solid curves show the best-fit curves with Gaussian, power-law, and power-law+Gaussian functions, respectively.

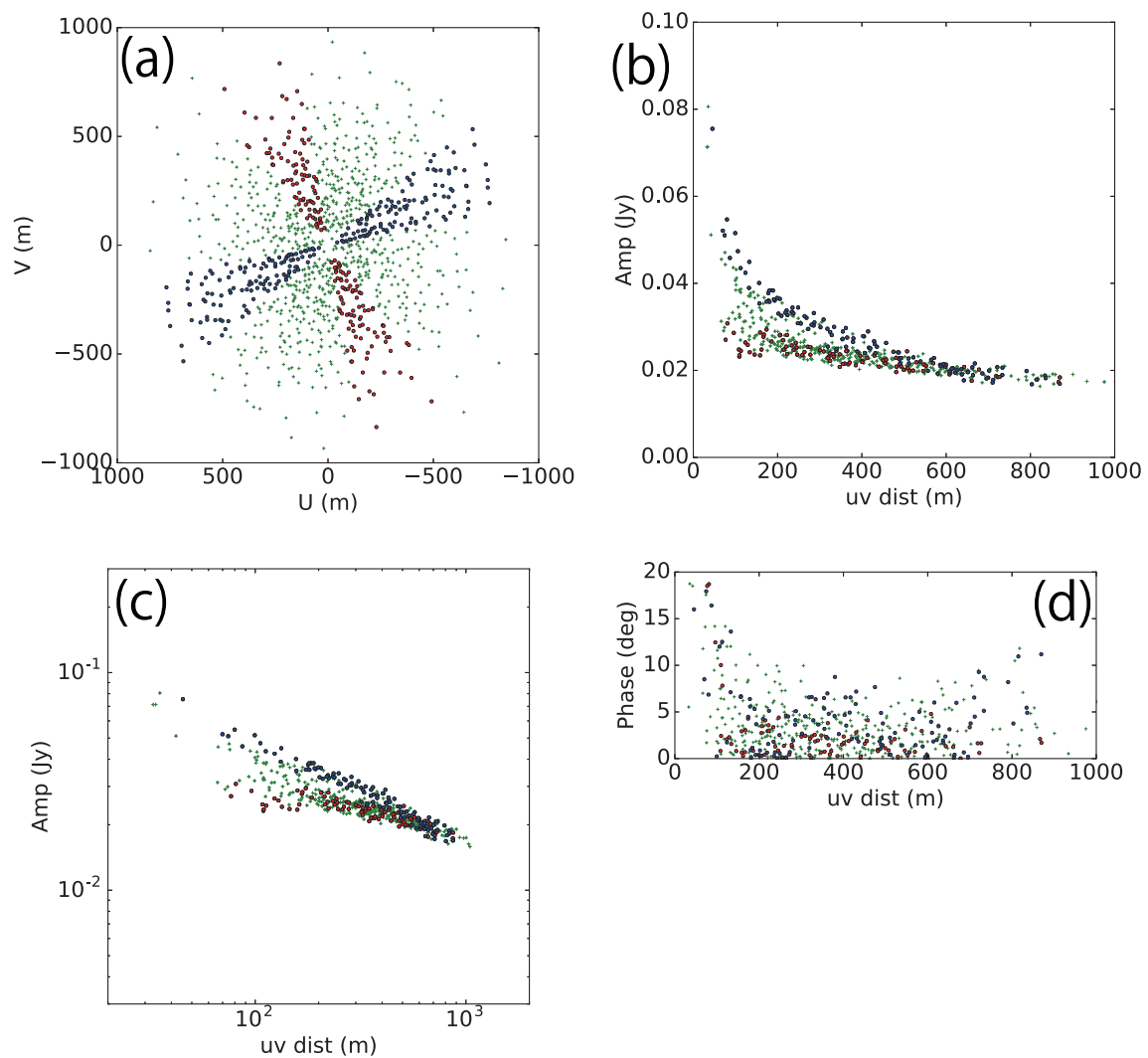


Figure 4.14 The same figures of the Class 0 protostar B335 as Figure 4.13. The distance of B335 is 130 pc. An error bar of the amplitude for each point is ~ 2 mJy.

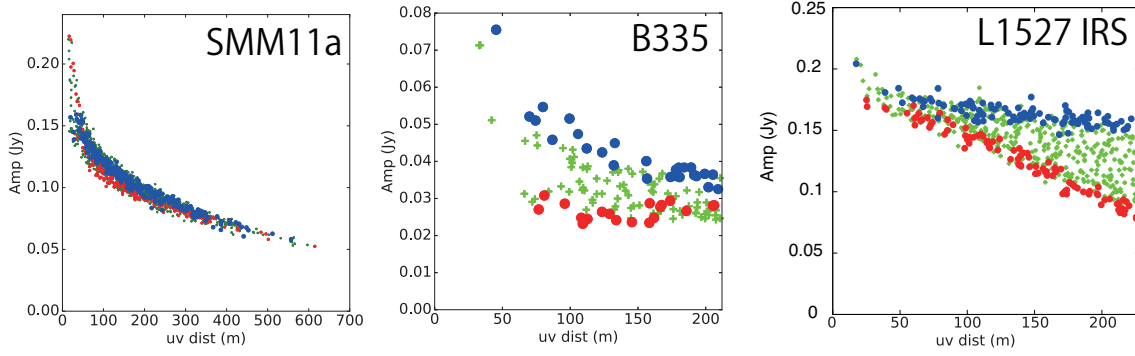


Figure 4.15 Comparison of visibility distributions. X-axes are scaled so as to compare visibility distributions on the same physical scale by taking account of the distance of each object. The distances of SMM11a, B335, and L1527 IRS are 429, 130, and 140 pc, respectively.

The visibility distribution of the Class 0/I protostar L1527 IRS was investigated in Section 3.5.2 and the visibility shows significantly different profiles along the major- and minor axes (Figure 3.6b) at uv -distance longer than > 100 m or on scales smaller than < 400 AU at the distance of L1527 IRS, 140 pc. Figure 4.14 shows another example, visibility distribution of the Class 0 protostar B335. The observed frequency is 225 GHz and the data is reported in Yen et al. (2015) in more detail. The red and blue points in Figure 4.14b and 4.14c are separated at uv -distance shorter than < 400 m, or spatial scales larger than > 90 AU at the distance of B335, 130 pc. These two protostars, as well as SMM11a, are known to have outflows lying almost on the plane of the sky ($i \gtrsim 80^\circ$). Thus the difference between the major- and minor axes is not due to the difference of inclination angles but due to degrees of spherical symmetry. Our results show that SMM11a has the highest degree of spherical symmetry among the three sources; the three visibility distributions are compared on the same physical scale in Figure 4.15. On the other hand B335 has bolometric temperature higher than SMM11a, $T_{\text{bol}} = 36$ K (Kristensen et al., 2012), and L1527 IRS has the highest bolometric temperature among the three, $T_{\text{bol}} = 44$ K (Kristensen et al., 2012). Hence, our results may imply that the degree of spherical symmetry decreases in the course of evolution between the protostellar phase and the FHSC phase, although no statistics can be discussed only with the present observations.

We should also note that theoretical simulations show that morphology in FHSC and protostellar phases depends on the initial conditions, such as rotation, turbulence, and magnetic fields, as well as the evolutionary phase (Machida et al., 2008; Matsumoto & Hanawa, 2011). In fact no significant rotation was identified toward SMM11a (Section 4.5.2).

4.5.4 Possibility of Second Core

The aspects discussed in previous subsections suggest that SMM11a is a promising candidate of FHSC. On the other hand, our results also include uncertainties, which should be investigated before we conclude that SMM11a is a FHSC. Those uncertainties are discussed in this subsection.

First, SMM11a is more distant than other FHSC candidates. Figure 4.16 shows SED comparison of SMM11a, L1451-mm, and L1521F IRS. The SEDs of the three sources appear not to be significantly different when compared with a theoretical prediction by Saigo & Tomisaka (2011), if they were at the same distance. L1451-mm is a FHSC candidate at 250 pc with $L_{\text{int}} < 0.03 L_{\odot}$ while, L1521F IRS is a representative very-low-luminosity object (VeLLO) at 140 pc with $L_{\text{int}} < 0.07 L_{\odot}$. VeLLOs are defined as protostars identified by *Spitzer* with internal luminosities $L_{\text{int}} \leq 0.1 L_{\odot}$ (di Francesco et al., 2007), which are not considered to be FHSCs because they are detected as point sources in mid-infrared or shorter wavelength (e.g., Dunham et al., 2008; Bourke et al., 2006). In contrast, FHSC candidates have not been identified as point sources in the wavelength. Although SMM11a has not been identified as a point source in the wavelength, the VeLLO L1521F IRS may not be detected either if it was at the same distance as SMM11a, because the long distance of SMM11a causes effectively lower sensitivity than L1521F IRS and because the measured flux of SMM11a is contaminated by the neighbor Class I source. SMM11a has not been detected either in X ray (Giardino et al., 2007) nor in 6 cm (Ortiz-León et al., 2015) wavelengths, which trace magnetic activities after the sec-

ond collapse. However, the detection limits are affected by the long distance for the same reason. Therefore, observations with higher sensitivity and higher angular resolutions are necessary to rule out the possibility that SMM11a might be a VeLLO.

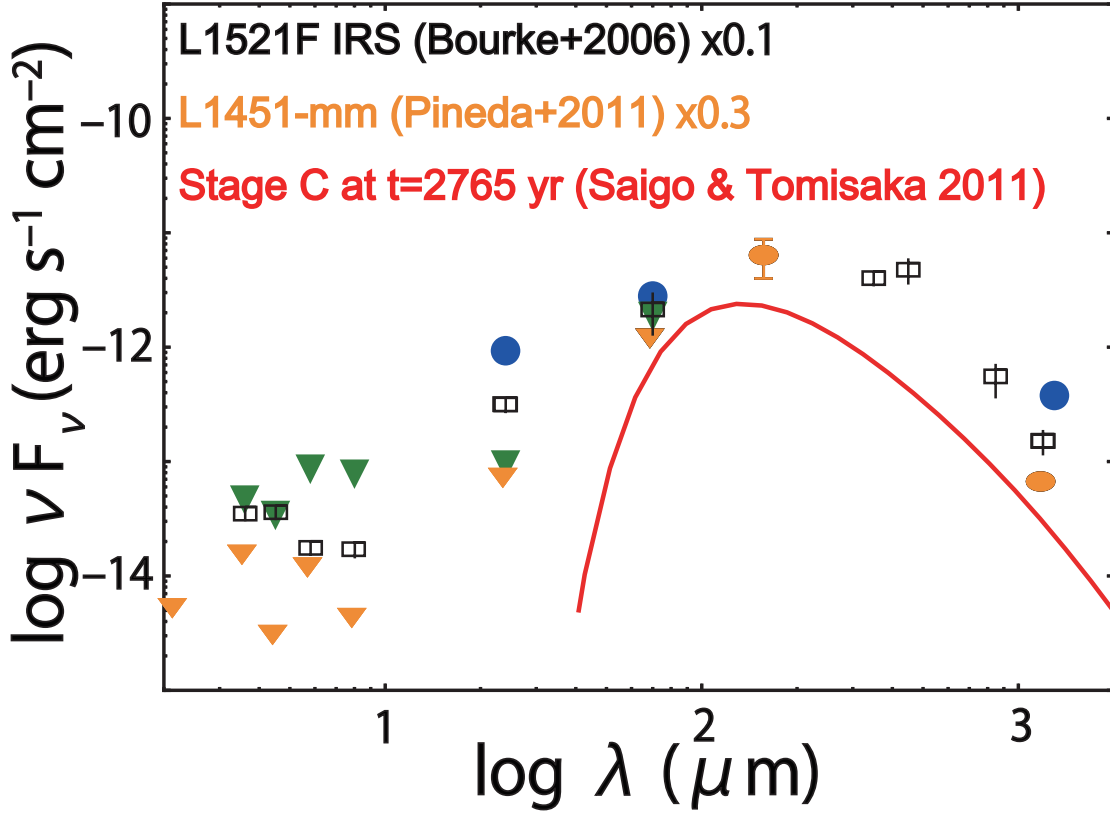


Figure 4.16 SED comparison of SMM11a, L1451-mm, and L1521F IRS with the same distance. L1451-mm is a known FHSC candidate (Pineda et al., 2011) while L1521F IRS is a VeLLO (Bourke et al., 2006). The fluxes of L1451-mm and L1521F are multiplied by 0.3 and 0.1 based on their distances 250 and 140 pc, respectively. Red curve is a theoretical SED of a FHSC by Saigo & Tomisaka (2011).

Secondly, SMM11a has the outflow with significantly higher velocity than predicted by theoretical simulations of FHSC. The model fitting to its outflows provided the coefficient $v_0 \sim 4 \text{ km s}^{-1} \text{ arcsec}^{-1}$, indicating a few 10 km s^{-1} at a few 1000 AU. On the other hand, theoretical simulations predict that FHSCs drive outflows with velocity at $\sim 5 \text{ km s}^{-1}$ (Machida et al., 2008). The predicted velocity is determined by the gravitational potential energy. For example, the gravitational potential energy with $0.16 M_\odot$ within $r < 30 \text{ AU}$ (Tomida et al., 2010) corresponds to $\sim 3 \text{ km s}^{-1}$. The potential en-

ergy cannot be much higher because central temperature cannot exceed the dissociation temperature of molecular hydrogen. We should, however, note that other known FHSC candidates may have high velocity outflows as well because their observed outflow velocities shown in Table 4.3 were not corrected with their inclination angles. It would be, therefore, important to determine those outflow velocities accurately from observations to fairly compare with theoretical prediction.

On the other hand, it is also difficult to explain SMM11a as a second core or a protostar as follows. If SMM11a is assumed to be a second core, $\sim 30 \text{ km s}^{-1}$ requires gravitational energy by central stellar mass of $M_* = V^2 R_*/2G \sim 0.01 M_\odot (R_*/4R_\odot)^1$. This central stellar mass corresponds to accretion luminosity of $L_{\text{acc}} = GM\dot{M}/R_* \sim 0.7 L_\odot (\dot{M}/10^{-5} M_\odot \text{ yr}^{-1})^1$ with a typical mass accretion rate for Class 0 protostars, $\dot{M} \sim 1 \times 10^{-5} M_\odot \text{ yr}^{-1}$ (Henriksen et al., 1997; Andre et al., 2000; Lee et al., 2007a,b; Yen et al., 2010), which is also consistent with the dynamical time $\sim 600 \text{ yr}$ derived from v_0 as $0.01 M_\odot/600 \text{ yr} = 1.7 \times 10^{-5} M_\odot \text{ yr}^{-1}$. The expected luminosity is larger than the observed value $L_{\text{bol}} = 0.05 L_\odot$ by an order of magnitude. In comparison, predicted accretion luminosity of FHSCs are not so large because mass is not centrally concentrated and also the accretion front is more distant from the center: for example, $L_{\text{acc}} = 0.03 L_\odot$ with $M_{\text{FC}} = 0.16 M_\odot$, $\dot{M}_{\text{FC}} = 4 \times 10^{-5} M_\odot \text{ yr}^{-1}$, and $R_{\text{FC}} = 30 \text{ AU}$ (Tomida et al., 2010).

4.6 CONCLUSION

We have observed five regions in Serpens Main cluster with ALMA during its Cycle 3 in 1.3-mm continuum, $^{12}\text{CO } J = 2 - 1$ line, and $\text{C}^{18}\text{O } J = 2 - 1$ line emissions on purpose to find objects in phases earlier than the protostellar phase. Twelve sources have been identified in 1.3-mm continuum emission within ALMA primary beams. ^{12}CO emission shows outflow from all of the 1.3-mm sources with a few exceptions. Ten of them have not been identified in infrared wavelength by either *Spitzer* nor *Herschel*, suggesting

that those are in an extremely early phase, first hydrostatic core (FHSC). To investigate evolutionary phases of the 1.3-mm sources, we measured flux density in 3.6, 4.5, 5.8, 8.0, and 24 μm using *Spitzer* data and one in 70 μm using *Herschel* data, as well as flux density in 1.3 mm, revealing that one of the 1.3-mm sources, SMM11a, has bolometric temperature, bolometric luminosity, and internal luminosity as low as those of known FHSC candidates. Although infrared flux of the other sources are not so faint nor red as SMM11a, flux measurement for those sources appear to be significantly affected by neighbor infrared sources particularly in 24 and 70 μm . SMM11a also has the clearest bipolar outflow among the 1.3-mm sources. For these reasons we propose that SMM11a is a new FHSC candidate.

We focused on the new FHSC candidate SMM11a and investigated its outflow properties, C^{18}O abundance, and morphology. Orientation angles of the two lobes of the outflow from SMM11a were separately estimated to be P.A.= 79° and P.A.= -110° by fitting the ^{12}CO integrated intensity map to reflected maps. To estimate inclination angles of the outflow, the integrated intensity map and position-velocity diagrams were fitted with the wind-driven-shell model. The derived inclination angles of the eastern and western lobes are $i = 79^\circ$ and 87° , respectively, i.e., the outflow from SMM11a has been found to lie almost on the plane of the sky. Other outflow properties, M_{flow} , P_{flow} , E_{flow} , v , τ_d , F_{flow} , and L_{flow} were also estimated from the ^{12}CO data cube and compared with those of known FHSC candidates. Those quantities of SMM11a without inclination correction are consistent with the other candidates and the effect of inclination is smaller than dispersion among the previously known candidates.

The C^{18}O integrated intensity map of SMM11a shows double peak on the eastern and western sides of the continuum peak position with a separation of $\sim 1'' = 429$ pc. The continuum peak intensity and the C^{18}O flux at the same position indicate that the C^{18}O molecules around SMM11a on a few 100 AU scale are freeze-out compared to interstellar medium by four orders of magnitude, which is quite consistent with theoretical prediction, and similar depletion of carbon-bearing molecules were reported in previous

studies on a FHSC candidate, Barnard-bN. In addition the local two peaks can be interpreted as desorption due to heating by the outflow.

The morphology was investigated using 1.3-mm continuum visibility. The visibility-amplitude profile can be fitted well with a combination of a power-law function and a Gaussian function. The profile also show that data points along the major- and minor axes of the continuum image are mostly overlapped on each other. This fact and the inclination angle of the associated outflow indicate that material around SMM11a is distributed with high degree of spherical symmetry. The visibility analysis toward two protostars with similar inclination angles, L1527 IRS and B335, may imply that the degree of spherical symmetry decreases in the course of evolution, although theoretical simulations predict that such morphology depends on initial conditions, such as rotation and magnetic fields, as well as evolutionary phases.

Chapter 5

CONCLUSIONS

In order to research disk formation around protostars, we observed a Class I protostar, TMC-1A, and a Class 0/I protostar, L1527 IRS, and previously identified 1.3-mm sources in Serpens Main cluster using ALMA during its Cycle 0, 1, and 3, respectively, in 1.3-continuum emission and CO isotopologues molecular line emissions. The main results are summarized below.

1. In the research on TMC-1A, 1.3-mm continuum, ^{12}CO ($J = 2 - 1$) line, and C^{18}O ($J = 2 - 1$) line emissions were observed. We investigated velocity gradients using an integrate intensity map and position velocity diagrams of the C^{18}O emission, revealing that the protostellar system can be divided into a Keplerian disk and an infalling rotating envelope. The disk was fitted well in the image domain with a standard disk model for more evolved, i.e., T-Tauri disks. Furthermore infall velocity in the envelope was found to be ~ 0.3 times slower than free fall velocity yielded by the central stellar mass derived from Keplerian rotation in the disk. Assuming that material is supported by magnetic fields in the envelope, we estimated the magnetic flux density required to explain the slow infall velocity to be ~ 2 mG.
2. In the research on L1527 IRS, 1.3-mm continuum and C^{18}O ($J = 2 - 1$) line emissions were observed. A Keplerian disk in an envelope was marginally identified in previous work. The disk was more clearly confirmed and its radius and central

stellar mass were estimated to be ~ 74 AU and $\sim 0.45 M_{\odot}$, respectively, in this paper. In addition to the kinematics, structures of the disk/envelope system has been investigated based on 1.3-mm continuum visibility, which shows clearly different profiles along the major- and minor axes. Therefore, we fitted the visibility with a disk+envelope model without azimuthal averaging. The best-fit model indicates that the disk is in hydrostatic equilibrium, which is similar to more evolved T-Tauri disks while its surface density profile is steeper than that of T-Tauri disks. It is also revealed that a density jump between the disk and the envelope by a factor of ~ 5 is required to explain the observations, which corresponds to infall velocity ~ 0.4 times slower than free fall when pressure equilibrium is taken into account. The $C^{18}O$ emission can also be explained by the same structures with depletion and local desorption of $C^{18}O$ molecules.

3. In the research on Serpens Main, 1.3-mm continuum and ^{12}CO ($J = 2 - 1$) line, and $C^{18}O$ ($J = 2 - 1$) line emissions were observed. Our ALMA observations detected the sources previously identified by mosaicking observations with SMA in 1.3-mm continuum emission, including protostars and sources with no counterpart in *Spitzer* nor *Herschel* observations. The sources have associated ^{12}CO outflows with a few exception. A source with the clearest ^{12}CO bipolar outflow, SMM11a, also has the lowest bolometric temperature 23 K and the lowest bolometric luminosity $0.050 L_{\odot}$, indicating that the source is a new first hydrostatic core (FHSC) candidate. The inclination angle of the outflow associated with SMM11a has been estimated to be $i \sim 80^{\circ}$ from simple fittings with a wind-driven-shell model. Other outflow properties, such as mass and momentum, are similar to those of known FHSC candidates. Furthermore $C^{18}O$ abundance is estimated to be smaller than the interstellar value by four orders of magnitude, which is consistent with theoretical simulations in the FHSC phase. Continuum visibility shows that SMM11a has more spherically symmetric morphology than two protostars, L1527 and B335.

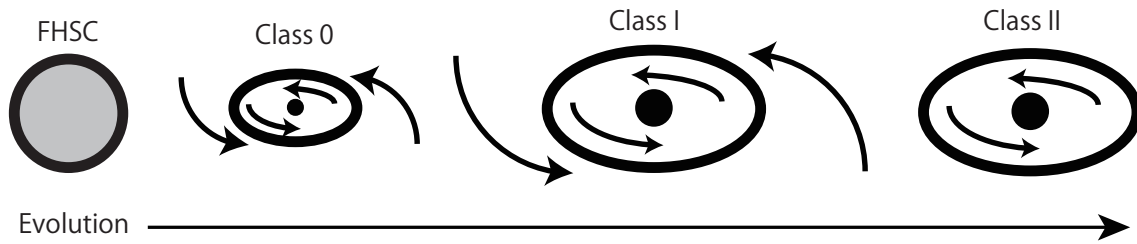


Figure 5.1 Summary of this thesis. The studies in this thesis based on observations have suggested that (1) envelopes are flattened between a very early phase of protostars and the phase of FHSCs, (2) disk sizes grow as central stellar mass increases, (3) infall motion in protostellar envelopes around protostellar disks is a few times slower than the free-fall, and (4) protostellar disks have similar characteristics to T Tauri disks from both kinematical and structural points of view.

As investigated in this thesis, disks have been identified around protostars in addition to more evolved phases, i.e., T-Tauri phases. Furthermore physical quantities, such as kinematics (rotation, infall) and structures (density, temperature) of those protostellar disks have also been investigated in detail as those of T-Tauri disks were. From a technical point of view, this thesis suggests a new method to distinguish protostellar disks from envelopes based on dust continuum emission; density jumps would enable us to estimate the same radius as the method based on PV diagrams of molecular line emission, which has been developed in these few years. In addition, the density jump could also enable us to estimate infall velocity in protostellar envelopes. This framework will be further developed by applying it for other protostars.

In the context of disk formation, the observational studies in this thesis have provided mainly four suggestions as shown in Figure 5.1: (1) envelopes are more spherical in the phase of first hydrostatic cores, while it becomes more flattened in the very early phase of protostars, (2) sizes of protostellar disks grow as central stellar mass increases, (3) infall motion in protostellar envelopes around protostellar disks are slower than the free-fall, and (4) protostellar disks have characteristics both kinematically and structurally similar to T Tauri disks. We should note that these suggestions still have some uncertainties because the sample sources that we have observed are still very limited, implying that suggestions are not statistically significant. Larger samples are needed for further discus-

sion, for example, about dependency of the above evolutionary tendency (2) on individual characteristics of each protostars, such as final mass, binary, cluster, and so on. Nevertheless, detailed studies on individual sources presented in this thesis are extremely important because the observational study of the disk formation is still an early stage, and detailed studies of individual sources will guide future statistical studies with larger samples. I consider, therefore, that the research in this thesis has made significant contributions to the research field of the disk formation.

Finally, I would like to make a couple of points for future works. The first point is that polarimetric observations on disk scales would be very important to verify whether magnetic fields is the external force making infall slower than free-fall in the above suggestion (3). The second point is that observations of SMM11a at high angular resolutions would be very important because presence of a disk on a few tens AU scale around SMM11a cannot be ruled out only with the current observations with the angular resolution corresponding to ~ 200 AU. Observations with higher angular resolutions without affected by freeze-out will constrain the disk size in the very early phase, which could approach the birth moment of protostellar disks.

Acknowledgments

When I was a senior at the University of Tokyo, I started astronomical research under the supervision of Prof. Masahiko Hayahis. Because I was interested in stellar-scale objects, he introduced a T-Tauri star, CW Tau, to me as the topic of my graduation research. Even though he belonged to the university only for about two years, he have supported me since the graduation research. I fully appreciate this encounter.

After graduating, I moved to ALMA building at National Astronomical Observatory of Japan in Mitaka city still belonging to the same graduate school, and met my current supervisor, Prof. Nagayoshi Ohashi. I also met friends then, Satoshi Ohashi, Toshiki Saito, and Kyoko Onishi, with whom I enjoyed much discussion about ALMA in various research fields. While I was being perplexed with a fact that my supervisor changed and the new supervisor worked in Hawaii, I also met other advisors Prof. Shigehisa Takakuwa and Dr. Hsi-Wei Yen; they were my advisors when I joined the summer student program held by Academia Sinica Institute of Astronomy and Astrophysics (ASIAA) in Taiwan. This is my first experience of long life, two months, outside Japan. I studied a T-Tauri star, Haro 6-33, learnt calibration process of SMA data, and experienced remote observations using SMA in the program. Prof. Takakuwa and Dr. Hsi-Wei have supported me since the program. I also keep in touch with friends I met in Taiwan, Daniel Lam, Yen-Chi Chen, Hong Jin Huang, Jing Hua Lin, and Mah Jingyi. In the next year, ALMA began showing its fantastic results and Prof. Ohashi introduced his ALMA data of a protostar, TMC-1A, to me. We have studied with ALMA since then. Dr. Kazuya Saigo gave me huge help about data reduction and modeling in the research on TMC-1A.

I moved to Subaru Telescope in Hawaii after getting a master's degree. In Hawaii, my supervisor, Prof. Nagayoshi Ohashi, taught me the importance of trying everything even if it looks useless but hard work. My life in the foreign country for about three years was supported by four seniors, Shin Koyamatsu, Yoshito Ono, Yuriko Saito, and Rizumu Shimakawa in the first half and by two members of staff in the last half, Yusei Koyama and Yoshito Onodera, who also gave me advice about infrared data reduction in my PhD thesis. I also appreciate fruitful advice from Prof. Jonathan Williams and Prof. Leonardo Testi, which deepen my understanding of infrared observations. Even after I moved to Hawaii, friends from the undergraduate school, Mitsuru Kokubo, Takuma Izumi, Kei Sano, Kazuma Mitsuda, Koh Takahashi, and Kazushi Okada, welcomed me as if nothing changed, which made my research life in Hawaii much more stable.

Last but not least, I leave inexpressible thanks for my parents who have supported me always understanding my life.

Thank you all,

Yusuke Aso

December 20, 2016

References

- Aikawa, Y. 2013, in *Astronomical Society of the Pacific Conference Series*, Vol. 476, *New Trends in Radio Astronomy in the ALMA Era: The 30th Anniversary of Nobeyama Radio Observatory*, ed. R. Kawabe, N. Kuno, & S. Yamamoto, 197
- Aikawa, Y., Furuya, K., Nomura, H., & Qi, C. 2015, *ApJ*, 807, 120
- Andre, P., Ward-Thompson, D., & Barsony, M. 2000, *Protostars and Planets IV*, 59
- Andrews, S. M., & Williams, J. P. 2005a, *ApJ*, 631, 1134
- . 2005b, *ApJ*, 631, 1134
- . 2007, *ApJ*, 659, 705
- Andrews, S. M., Wilner, D. J., Hughes, A. M., Qi, C., & Dullemond, C. P. 2009, *ApJ*, 700, 1502
- . 2010, *ApJ*, 723, 1241
- Aniano, G., Draine, B. T., Gordon, K. D., & Sandstrom, K. 2011, *PASP*, 123, 1218
- Arce, H. G., & Goodman, A. A. 2002, *ApJ*, 575, 928
- Aso, Y., et al. 2015, *ApJ*, 812, 27
- Bate, M. R. 2011, *MNRAS*, 417, 2036
- Beckwith, S. V. W., & Sargent, A. I. 1991, *ApJ*, 381, 250

—. 1993, *ApJ*, 402, 280

Beckwith, S. V. W., Sargent, A. I., Chini, R. S., & Guesten, R. 1990, *AJ*, 99, 924

Beichman, C. A., Myers, P. C., Emerson, J. P., Harris, S., Mathieu, R., Benson, P. J., & Jennings, R. E. 1986, *ApJ*, 307, 337

Bell, C. P. M., Naylor, T., Mayne, N. J., Jeffries, R. D., & Littlefair, S. P. 2013, *MNRAS*, 434, 806

Blandford, R. D., & Payne, D. G. 1982, *MNRAS*, 199, 883

Boss, A. P. 1998, *ApJ*, 503, 923

Boss, A. P., & Yorke, H. W. 1995, *ApJ*, 439, L55

Bourke, T. L., et al. 2006, *ApJ*, 649, L37

Bressert, E. W. 2012, PhD Thesis, University of Exeter, 1

Brinch, C., Jørgensen, J. K., & Hogerheijde, M. R. 2009, *A&A*, 502, 199

Caratti o Garatti, A., Stecklum, B., Linz, H., Garcia Lopez, R., & Sanna, A. 2015, *A&A*, 573, A82

Casali, M. M., Eiroa, C., & Duncan, W. D. 1993, *A&A*, 275, 195

Caselli, P., Benson, P. J., Myers, P. C., & Tafalla, M. 2002, *ApJ*, 572, 238

Chandler, C. J., Barsony, M., & Moore, T. J. T. 1998, *MNRAS*, 299, 789

Chandler, C. J., Terebey, S., Barsony, M., Moore, T. J. T., & Gautier, T. N. 1996, *ApJ*, 471, 308

Chen, H., Myers, P. C., Ladd, E. F., & Wood, D. O. S. 1995, *ApJ*, 445, 377

Chen, X., Arce, H. G., Dunham, M. M., Zhang, Q., Bourke, T. L., Launhardt, R., Schmalzl, M., & Henning, T. 2012, *ApJ*, 751, 89

- Chen, X., Arce, H. G., Zhang, Q., Bourke, T. L., Launhardt, R., Schmalzl, M., & Henning, T. 2010, *ApJ*, 715, 1344
- Chiang, E. I., & Goldreich, P. 1997, *ApJ*, 490, 368
- Ching, T.-C., Lai, S.-P., Zhang, Q., Yang, L., Girart, J. M., & Rao, R. 2016, *ApJ*, 819, 159
- Choi, M., Tatematsu, K., & Kang, M. 2010, *ApJ*, 723, L34
- Chou, T.-L., Takakuwa, S., Yen, H.-W., Ohashi, N., & Ho, P. T. P. 2014, *ArXiv e-prints*
- Commerçon, B., Levrier, F., Maury, A. J., Henning, T., & Launhardt, R. 2012, *A&A*, 548, A39
- Crutcher, R. M., Wandelt, B., Heiles, C., Falgarone, E., & Troland, T. H. 2010, *ApJ*, 725, 466
- Davis, C. J., Dent, W. R. F., Matthews, H. E., Coulson, I. M., & McCaughrean, M. J. 2000, *MNRAS*, 318, 952
- Davis, C. J., Matthews, H. E., Ray, T. P., Dent, W. R. F., & Richer, J. S. 1999, *MNRAS*, 309, 141
- di Francesco, J., Evans, II, N. J., Caselli, P., Myers, P. C., Shirley, Y., Aikawa, Y., & Tafalla, M. 2007, *Protostars and Planets V*, 17
- Draine, B. T. 1989, in *ESA Special Publication, Vol. 290, Infrared Spectroscopy in Astronomy*, ed. E. Böhm-Vitense
- Duarte-Cabral, A., Dobbs, C. L., Peretto, N., & Fuller, G. A. 2011, *A&A*, 528, A50
- Duarte-Cabral, A., Fuller, G. A., Peretto, N., Hatchell, J., Ladd, E. F., Buckle, J., Richer, J., & Graves, S. F. 2010, *A&A*, 519, A27
- Dullemond, C. P., van Zadelhoff, G. J., & Natta, A. 2002, *A&A*, 389, 464

- Dunham, M. M., Chen, X., Arce, H. G., Bourke, T. L., Schnee, S., & Enoch, M. L. 2011, *ApJ*, 742, 1
- Dunham, M. M., Crapsi, A., Evans, II, N. J., Bourke, T. L., Huard, T. L., Myers, P. C., & Kauffmann, J. 2008, *ApJS*, 179, 249
- Dunham, M. M., et al. 2015, *ApJS*, 220, 11
- Dutrey, A., Guilloteau, S., & Simon, M. 1994, *A&A*, 286, 149
- Dzib, S., Loinard, L., Mioduszewski, A. J., Boden, A. F., Rodríguez, L. F., & Torres, R. M. 2011, in *Revista Mexicana de Astronomia y Astrofisica Conference Series*, Vol. 40, *Revista Mexicana de Astronomia y Astrofisica Conference Series*, 231–232
- Eiroa, C., & Casali, M. M. 1992, *A&A*, 262, 468
- Eisner, J. A. 2012, *ApJ*, 755, 23
- Enoch, M. L., Corder, S., Dunham, M. M., & Duchêne, G. 2009, *ApJ*, 707, 103
- Enoch, M. L., Glenn, J., Evans, II, N. J., Sargent, A. I., Young, K. E., & Huard, T. L. 2007, *ApJ*, 666, 982
- Enoch, M. L., et al. 2011, *ApJS*, 195, 21
- Falgarone, E., Troland, T. H., Crutcher, R. M., & Paubert, G. 2008, *A&A*, 487, 247
- Favre, C., Cleeves, L. I., Bergin, E. A., Qi, C., & Blake, G. A. 2013, *ApJ*, 776, L38
- Frerking, M. A., Langer, W. D., & Wilson, R. W. 1982, *ApJ*, 262, 590
- Froebrich, D. 2005, *ApJS*, 156, 169
- Fujii, K., et al. 2014, *ApJ*, 796, 123
- Galli, D., & Shu, F. H. 1993a, *ApJ*, 417, 220

- . 1993b, *ApJ*, 417, 243
- Giardino, G., Favata, F., Micela, G., Sciortino, S., & Winston, E. 2007, *A&A*, 463, 275
- Girart, J. M., Rao, R., & Marrone, D. P. 2006, *Science*, 313, 812
- Goodman, A. A., Benson, P. J., Fuller, G. A., & Myers, P. C. 1993, *ApJ*, 406, 528
- Gorti, U., & Hollenbach, D. 2008, *ApJ*, 683, 287
- Green, J. D., et al. 2013, *ApJ*, 770, 123
- Gueth, F., & Guilloteau, S. 1999, *A&A*, 343, 571
- Guilloteau, S., & Dutrey, A. 1998, *A&A*, 339, 467
- Guilloteau, S., Dutrey, A., & Simon, M. 1999, *A&A*, 348, 570
- Haisch, Jr., K. E., Lada, E. A., & Lada, C. J. 2001, *ApJ*, 553, L153
- Handa, T., et al. 1995, *ApJ*, 449, 894
- Hara, C., et al. 2013, *ApJ*, 771, 128
- Harsono, D., Jørgensen, J. K., van Dishoeck, E. F., Hogerheijde, M. R., Bruderer, S., Persson, M. V., & Mottram, J. C. 2014, *A&A*, 562, A77
- Harvey, P., Merín, B., Huard, T. L., Rebull, L. M., Chapman, N., Evans, II, N. J., & Myers, P. C. 2007, *ApJ*, 663, 1149
- Hayashi, C., Nakazawa, K., & Nakagawa, Y. 1985, in *Protostars and Planets II*, ed. D. C. Black & M. S. Matthews, 1100–1153
- Hayashi, M., Ohashi, N., & Miyama, S. M. 1993, *ApJ*, 418, L71
- Henriksen, R., Andre, P., & Bontemps, S. 1997, *A&A*, 323, 549
- Hernández, J., et al. 2007, *ApJ*, 662, 1067

- Hildebrand, R. 1989, in IAU Symposium, Vol. 135, Interstellar Dust, ed. L. J. Allamandola & A. G. G. M. Tielens, 275
- Hirano, N., Hasegawa, T., Hayashi, M., Tamura, M., & Ohashi, N. 1995, *Ap&SS*, 224, 113
- Hirano, N., Ho, P. P. T., Liu, S.-Y., Shang, H., Lee, C.-F., & Bourke, T. L. 2010, *ApJ*, 717, 58
- Hirano, N., Liu, S.-Y., Shang, H., Ho, P. T. P., Huang, H.-C., Kuan, Y.-J., McCaughrean, M. J., & Zhang, Q. 2006, *ApJ*, 636, L141
- Hogerheijde, M. R., van Dishoeck, E. F., & van Langevelde, H. J. 1997, in IAU Symposium, Vol. 182, Herbig-Haro Flows and the Birth of Stars, ed. B. Reipurth & C. Bertout, 138
- Howard, A. W. 2013, *Science*, 340, 572
- Huang, Y.-H., & Hirano, N. 2013, *ApJ*, 766, 131
- Hughes, A. M., Wilner, D. J., Qi, C., & Hogerheijde, M. R. 2008, *ApJ*, 678, 1119
- Hughes, A. M., et al. 2009, *ApJ*, 698, 131
- Hull, C. L. H., et al. 2016, *ApJ*, 823, L27
- Inutsuka, S.-i., Inoue, T., Iwasaki, K., & Hosokawa, T. 2015, *A&A*, 580, A49
- Joos, M., Hennebelle, P., & Ciardi, A. 2012, *A&A*, 543, A128
- Jørgensen, J. K., Schöier, F. L., & van Dishoeck, E. F. 2005, *A&A*, 435, 177
- Jørgensen, J. K., van Dishoeck, E. F., Visser, R., Bourke, T. L., Wilner, D. J., Lommen, D., Hogerheijde, M. R., & Myers, P. C. 2009, *A&A*, 507, 861
- Kaas, A. A., et al. 2004, *A&A*, 421, 623

- Kawabe, R., Ishiguro, M., Omodaka, T., Kitamura, Y., & Miyama, S. M. 1993, *ApJ*, 404, L63
- Kenyon, S. J., Calvet, N., & Hartmann, L. 1993, *ApJ*, 414, 676
- Kiyokane, K., Saito, M., Saigo, K., Kurono, Y., Momose, M., Tsukagoshi, T., & NRO45m SF-Legacy Team. 2013, in *Astronomical Society of the Pacific Conference Series*, Vol. 476, *New Trends in Radio Astronomy in the ALMA Era: The 30th Anniversary of Nobeyama Radio Observatory*, ed. R. Kawabe, N. Kuno, & S. Yamamoto, 375
- Kokubo, E., & Genda, H. 2010, *ApJ*, 714, L21
- Koyamatsu, S., Takakuwa, S., Hayashi, M., Mayama, S., & Ohashi, N. 2014, *ApJ*, 789, 95
- Kristensen, L. E., et al. 2012, *A&A*, 542, A8
- Lacy, J. H., Knacke, R., Geballe, T. R., & Tokunaga, A. T. 1994, *ApJ*, 428, L69
- Lada, C. J., & Lada, E. A. 2003, *ARA&A*, 41, 57
- Larson, R. B. 1969, *MNRAS*, 145, 271
- Lee, C.-F., Hasegawa, T. I., Hirano, N., Palau, A., Shang, H., Ho, P. T. P., & Zhang, Q. 2010, *ApJ*, 713, 731
- Lee, C.-F., Hirano, N., Palau, A., Ho, P. T. P., Bourke, T. L., Zhang, Q., & Shang, H. 2009, *ApJ*, 699, 1584
- Lee, C.-F., Hirano, N., Zhang, Q., Shang, H., Ho, P. T. P., & Krasnopolsky, R. 2014a, *ApJ*, 786, 114
- Lee, C.-F., Ho, P. T. P., Bourke, T. L., Hirano, N., Shang, H., & Zhang, Q. 2008, *ApJ*, 685, 1026

- Lee, C.-F., Ho, P. T. P., Hirano, N., Beuther, H., Bourke, T. L., Shang, H., & Zhang, Q. 2007a, *ApJ*, 659, 499
- Lee, C.-F., Ho, P. T. P., Palau, A., Hirano, N., Bourke, T. L., Shang, H., & Zhang, Q. 2007b, *ApJ*, 670, 1188
- Lee, C.-F., Mundy, L. G., Reipurth, B., Ostriker, E. C., & Stone, J. M. 2000, *ApJ*, 542, 925
- Lee, C. W., Myers, P. C., & Plume, R. 2004, *Journal of Korean Astronomical Society*, 37, 257
- Lee, K. I., et al. 2014b, *ApJ*, 797, 76
- Li, Z.-Y., Krasnopolsky, R., Shang, H., & Zhao, B. 2014, *ApJ*, 793, 130
- Li, Z.-Y., & Shu, F. H. 1996, *ApJ*, 472, 211
- Lindberg, J. E., et al. 2014, *A&A*, 566, A74
- Lommen, D., Jørgensen, J. K., van Dishoeck, E. F., & Crapsi, A. 2008, *A&A*, 481, 141
- Looney, L. W., Mundy, L. G., & Welch, W. J. 2003, *ApJ*, 592, 255
- Machida, M. N., & Hosokawa, T. 2013, *MNRAS*, 431, 1719
- Machida, M. N., Inutsuka, S.-i., & Matsumoto, T. 2008, *ApJ*, 676, 1088
- . 2010, *ApJ*, 724, 1006
- Machida, M. N., Inutsuka, S.-i., & Matsumoto, T. 2011, *PASJ*, 63, 555
- Machida, M. N., Inutsuka, S.-i., & Matsumoto, T. 2014, *MNRAS*, 438, 2278
- Machida, M. N., & Matsumoto, T. 2011, *MNRAS*, 413, 2767
- Marcy, G. W., Butler, R. P., Vogt, S. S., Fischer, D. A., Henry, G. W., Laughlin, G., Wright, J. T., & Johnson, J. A. 2005, *ApJ*, 619, 570

- Mardones, D., Myers, P. C., Tafalla, M., Wilner, D. J., Bachiller, R., & Garay, G. 1997, ApJ, 489, 719
- Masunaga, H., Miyama, S. M., & Inutsuka, S.-i. 1998, ApJ, 495, 346
- Matsumoto, T., & Hanawa, T. 2011, ApJ, 728, 47
- Mellon, R. R., & Li, Z.-Y. 2008, ApJ, 681, 1356
- . 2009, ApJ, 698, 922
- Momose, M., Ohashi, N., Kawabe, R., Nakano, T., & Hayashi, M. 1998, ApJ, 504, 314
- Murillo, N. M., & Lai, S.-P. 2013, ApJ, 764, L15
- Murillo, N. M., Lai, S.-P., Bruderer, S., Harsono, D., & van Dishoeck, E. F. 2013, A&A, 560, A103
- Myers, P. C., & Ladd, E. F. 1993, ApJ, 413, L47
- Narayanan, G., Snell, R., & Bemis, A. 2012, MNRAS, 425, 2641
- Nomura, H., Aikawa, Y., Tsujimoto, M., Nakagawa, Y., & Millar, T. J. 2007, ApJ, 661, 334
- O'dell, C. R., & Wen, Z. 1994, ApJ, 436, 194
- Ohashi, N., Hayashi, M., Ho, P. T. P., Momose, M., Tamura, M., Hirano, N., & Sargent, A. I. 1997, ApJ, 488, 317
- Ohashi, N., Hayashi, M., Kawabe, R., & Ishiguro, M. 1996, ApJ, 466, 317
- Ohashi, N., et al. 2014, ApJ, 796, 131
- Omukai, K. 2007, PASJ, 59, 589
- Onishi, T., Mizuno, A., & Fukui, Y. 1999, PASJ, 51, 257

Onishi, T., Mizuno, A., Kawamura, A., Tachihara, K., & Fukui, Y. 2002, *ApJ*, 575, 950

Ortiz-León, G. N., et al. 2015, *ApJ*, 805, 9

Oya, Y., Sakai, N., Lefloch, B., López-Sepulcre, A., Watanabe, Y., Ceccarelli, C., & Yamamoto, S. 2015, *ApJ*, 812, 59

Padgett, D. L., Brandner, W., Stapelfeldt, K. R., Strom, S. E., Terebey, S., & Koerner, D. 1999, *AJ*, 117, 1490

Pineda, J. E., et al. 2011, *ApJ*, 743, 201

Pollack, J. B., Hubickyj, O., Bodenheimer, P., Lissauer, J. J., Podolak, M., & Greenzweig, Y. 1996, *Icarus*, 124, 62

Qi, C., et al. 2004, *ApJ*, 616, L11

Rodriguez, D. R., Kastner, J. H., Wilner, D., & Qi, C. 2010, *ApJ*, 720, 1684

Saigo, K., & Tomisaka, K. 2006, *ApJ*, 645, 381

—. 2011, *ApJ*, 728, 78

Saigo, K., Tomisaka, K., & Matsumoto, T. 2008, *ApJ*, 674, 997

Sakai, N., et al. 2014, *Nature*, 507, 78

Shu, F., Najita, J., Ostriker, E., Wilkin, F., Ruden, S., & Lizano, S. 1994, *ApJ*, 429, 781

Shu, F. H., Adams, F. C., & Lizano, S. 1987, *ARA&A*, 25, 23

Shu, F. H., Ruden, S. P., Lada, C. J., & Lizano, S. 1991, *ApJ*, 370, L31

Simon, M., Dutrey, A., & Guilloteau, S. 2000, *ApJ*, 545, 1034

Simon, T., Ayres, T. R., Redfield, S., & Linsky, J. L. 2002, *ApJ*, 579, 800

Skrutskie, M. F., et al. 1993, *ApJ*, 409, 422

- Smith, N., Bally, J., Shuping, R. Y., Morris, M., & Kassis, M. 2005, *AJ*, 130, 1763
- Snell, R. L., Loren, R. B., & Plambeck, R. L. 1980, *ApJ*, 239, L17
- Stephens, I. W., et al. 2013, *ApJ*, 769, L15
- Tafalla, M., Mardones, D., Myers, P. C., Caselli, P., Bachiller, R., & Benson, P. J. 1998, *ApJ*, 504, 900
- Tafalla, M., Myers, P. C., Caselli, P., & Walmsley, C. M. 2004, *A&A*, 416, 191
- Takakuwa, S., Saito, M., Lim, J., Saigo, K., Sridharan, T. K., & Patel, N. A. 2012, *ApJ*, 754, 52
- Takakuwa, S., Saito, M., Saigo, K., Matsumoto, T., Lim, J., Hanawa, T., & Ho, P. T. P. 2014, *ApJ*, 796, 1
- Tamura, M., Ohashi, N., Hirano, N., Itoh, Y., & Moriarty-Schieven, G. H. 1996, *AJ*, 112, 2076
- Terebey, S., Shu, F. H., & Cassen, P. 1984, *ApJ*, 286, 529
- Terebey, S., Vogel, S. N., & Myers, P. C. 1989, *ApJ*, 340, 472
- Tobin, J. J., Hartmann, L., Bergin, E., Chiang, H.-F., Looney, L. W., Chandler, C. J., Maret, S., & Heitsch, F. 2012a, *ApJ*, 748, 16
- Tobin, J. J., Hartmann, L., Calvet, N., & D'Alessio, P. 2008, *ApJ*, 679, 1364
- Tobin, J. J., Hartmann, L., Chiang, H.-F., Wilner, D. J., Looney, L. W., Loinard, L., Calvet, N., & D'Alessio, P. 2012b, *Nature*, 492, 83
- Tobin, J. J., et al. 2011, *ApJ*, 740, 45
- . 2013, *ApJ*, 779, 93

- Tomida, K., Machida, M. N., Saigo, K., Tomisaka, K., & Matsumoto, T. 2010, *ApJ*, 725, L239
- Tomida, K., Okuzumi, S., & Machida, M. N. 2015, *ApJ*, 801, 117
- Tomida, K., Tomisaka, K., Matsumoto, T., Hori, Y., Okuzumi, S., Machida, M. N., & Saigo, K. 2013, *ApJ*, 763, 6
- Tsukamoto, Y., Iwasaki, K., Okuzumi, S., Machida, M. N., & Inutsuka, S. 2015, *MNRAS*, 452, 278
- Ulrich, R. K. 1976, *ApJ*, 210, 377
- Visser, R., van Dishoeck, E. F., Doty, S. D., & Dullemond, C. P. 2009, *A&A*, 495, 881
- Weidenschilling, S. J., & Cuzzi, J. N. 1993, in *Protostars and Planets III*, ed. E. H. Levy & J. I. Lunine, 1031–1060
- Williams, J. P., & Best, W. M. J. 2014, *ApJ*, 788, 59
- Williams, J. P., & Cieza, L. A. 2011, *ARA&A*, 49, 67
- Wilner, D. J., Myers, P. C., Mardones, D., & Tafalla, M. 2000, *ApJ*, 544, L69
- Wilner, D. J., & Welch, W. J. 1994, *ApJ*, 427, 898
- Wilson, T. L., & Rood, R. 1994, *ARA&A*, 32, 191
- Woitke, P., Thi, W.-F., Kamp, I., & Hogerheijde, M. R. 2009, *A&A*, 501, L5
- Wolf, S., Schegerer, A., Beuther, H., Padgett, D. L., & Stapelfeldt, K. R. 2008, *ApJ*, 674, L101
- Wu, Y., Zhang, Q., Chen, H., Yang, C., Wei, Y., & Ho, P. T. P. 2005, *AJ*, 129, 330
- Yen, H.-W., Koch, P. M., Takakuwa, S., Krasnopolsky, R., Ohashi, N., & Aso, Y. 2016, *ArXiv e-prints*

Yen, H.-W., Takakuwa, S., Koch, P. M., Aso, Y., Koyamatsu, S., Krasnopolsky, R., & Ohashi, N. 2015, *ApJ*, 812, 129

Yen, H.-W., Takakuwa, S., & Ohashi, N. 2010, *ApJ*, 710, 1786

—. 2011, *ApJ*, 742, 57

Yen, H.-W., Takakuwa, S., Ohashi, N., & Ho, P. T. P. 2013, *ApJ*, 772, 22

Yen, H.-W., et al. 2014, *ApJ*, 793, 1

Zhou, S., Evans, II, N. J., Koempe, C., & Walmsley, C. M. 1993, *ApJ*, 404, 232

Zinnecker, H., & Yorke, H. W. 2007, *ARA&A*, 45, 481